ABSTRACT

Title of dissertation: DISSIPATIVE AND DISPERSIVE MEASUREMENTS OF A COOPER PAIR BOX

Zaeill Kim, Doctor of Philosophy, 2010

Dissertation directed by: Professor Frederick C. Wellstood
Department of Physics
Dr. Benjamin S. Palmer
Laboratory for Physical Sciences

The quantum states of an $Al/AlO_x/Al$ Cooper pair box (CPB) qubit were measured at temperatures below 100 mK.

Detailed spectroscopic measurements of the excited state of the CPB were made along with detailed measurements of the lifetime T_1 of the first excited state. The CPB states were probed using radio-frequency (rf) techniques to read out using either an rf - single-electron transistor (rf-SET) or a low-loss superconducting resonator.

Using an rf-SET, I measured the excited state spectrum of a CPB from 15 to 50 GHz. In this spectrum, a few anomalous avoided level crossings (ALC) were observed. These ALCs exhibited a strong gate voltage dependence and Josephson energy (E_J) dependence, consistent with a charge fluctuator coupled to the CPB island. A model Hamiltonian was used to fit the measured spectrum. Fitting parameters such as the charging energy $E_C/h = 12.1$ GHz and the Josephson energy E_J/h tuned between 2 GHz and 21 GHz for the CPB, and the well asymmetry, tunneling

amplitude, and the minimum hopping distance for each fluctuator were extracted. The tunneling rates ranged from less than 3.5 to 13 GHz, *i.e.* values between 5 % and 150 % of the well asymmetry, and the dipole moments yield a minimum hopping distance of 0.3 to 0.8 Å. I also made detailed measurements of the lifetime of the first excited state away from the CPB charge degeneracy point and found that the lifetime varied from less than 50 ns up to a few μs as the Josephson energy E_J decreased, consistent with a charge noise ($S_q \sim 10^{-11}\ e^2$/Hz around 37 GHz to $S_q \sim 10^{-12}\ e^2$/Hz around 27 GHz) coupled to the qubit. I also found that at frequencies where an ALC was observed in the spectrum, a decrease in T_1 occurred, suggesting that the discrete charge defects are a significant source of dissipation in the CPB.

I also designed and fabricated a "quasi-lumped element" thin-film superconducting Al microwave resonator on sapphire to be used for a dispersive read-out of the CPB. The resonator consists of a meandering inductor and an interdigitated capacitor coupled to a transmission line. At $T = 30$ mK and on resonance at 5.578 GHz, the transmission through the transmission line decreased by 15 dB and the loaded quality factor was 60,000. I measured the temperature dependence of the resonator frequency and loss at temperatures as high as 500 mK and found reasonable agreement with the Mattis-Bardeen theory.

Finally, I coupled a "quasi-lumped element" microwave resonator ($f_0 \simeq 5.443$ GHz), made of superconducting Al on sapphire, to an Al/AlO_X/Al CPB qubit. Most of my measurements were made in the dispersive regime where $E_J - hf_0$ is much larger than the coupling strength. In this case, the qubit causes a small

state-dependent frequency shift in the resonator's resonant frequency. By sending down a second microwave tone (the pump), I was able to excite the CPB qubit. In zero magnetic field with the CPB far detuned from the resonator, I measured a 50 kHz decrease in f_0 with the qubit in the ground state and biased near the degeneracy point of the CPB. The charging energy and Josephson energy of the CPB were determined from spectroscopy taken by saturating the CPB with a second microwave tone and measuring the transmission through the resonator. The first device had $E_C/h = 12.5$ GHz and maximum $E_J/h = 9$ GHz. The second device had $E_C/h = 6.24$ GHz and E_J/h tuned between 4 GHz and 8 GHz. By changing the external magnetic field, I could decrease the effective E_J of the CPB. From modeling, I extracted coupling strengths $g/2\pi = 11$ MHz and 5 MHz for the first and second device, respectively. Finally I did single and two-tone spectroscopy, and measured the relaxation and Rabi oscillations of the CPB. From the first device, I was able to obtain relaxation times T_1 of 10.3 μs at $E_J/h = 7$ GHz on the CPB degeneracy point and spectroscopic coherence times $T_2^* \sim 100$ ns. From the second device, I found relaxation times T_1 of 200 μs at $E_J/h = 4$ GHz to 4.5 GHz decreasing down to 4 μs around 8 GHz. There was also a depression in T_1 around the resonant frequency of the resonator. The Rabi decay times were found to be up to $T' \sim 330$ ns.

DISSIPATIVE AND DISPERSIVE MEASUREMENTS OF A COOPER PAIR BOX

by

Zaeill Kim

Dissertation submitted to the Faculty of the Graduate School of the
University of Maryland, College Park in partial fulfillment
of the requirements for the degree of
Doctor of Philosophy
2010

Advisory Committee:
Professor Frederick C. Wellstood, Chair/Advisor
Dr. Benjamin S. Palmer, Co-Advisor
Professor Steven M. Anlage
Professor Luis A. Orozco
Dr. Kevin D. Osborn
Professor Romel D. Gomez

Dedication

to my dear family.

Acknowledgements

I must thank my dissertation committee members: Prof. Frederick C. Wellstood, Dr. Benjamin S. Palmer, Prof. Steven M. Anlage, Prof. Luis A. Orozco, Dr. Kevin D. Osborn, and Prof. Romel D. Gomez.

How lucky I was to work for my co-advisor Dr. Ben Palmer at the Laboratory for Physical Sciences! No word can express my thanks to Ben. He was not only a great advisor but also merry fellow to me. To break through challenging experiments, he has no fears for being a path finder himself and encouraged me to be a good soldier. And whenever I got lost, he steered me in the right direction.

I am deeply indebted to my advisor Prof. Fred Wellstood. Fred always surprised me by new ideas and insight in physics. By questioning and answering himself, he shone a flash of light in a dark cloud. His writing reminds me of two great poets in China's Tang period: Li Bai who finished a poem really fast at once and Du Fu who kept rewriting a poem.

I would like to thank Dr. Kevin Osborn, who is the expert in the superconducting microwave resonator. Kevin helped me design the resonator. Invaluable discussion with Kevin resulted in the nice lumped-element resonator that brought me a short cut to graduation.

I would like to thank Dr. Marc Manheimer, who supported our experiments as the leader of the quantum computing program at the LPS. I did not appreciate that there were many kinds of unique beer besides Miller until he awoke me.

I am grateful to lab mates. I owe much to Vitaley Zaretskey, who has numerous

ideas and encyclopedic knowledge of experiments. Vitaley was very good at Labview programming and this helped me take data readily. He was also very careful and a perfectionist in experiments, except stretching his shoulder out too much. I also thank Baladitya Suri and Sergey Novikov, who joined the group in January 2010. Bala and Sergey helped me characterize my last device and found many interesting results. I wish they had joined the group earlier.

I am also grateful to Dr. Pierre Echternach, Dr. Matt Shaw, and Dr. Justin Schneiderman at the Jet Propulsion Lab. They provided us the rf-SET devices and gave priceless advice on measurements.

I am also grateful to folks in the superconducting phase qubit group for useful discussions: Prof. Chris Lobb, Prof. Bob Anderson, Dr. Rupert Lewis, Dr. Sudeep Dutta, Dr. Tauno Palomaki, Ben Cooper, Hyeokshin Kwon, and Tony Przybysz. Hyeokshin and I shared the hotel room at many conferences and talked about physics.

I must thank Dr. Jonghee Lee, who taught me how to use programs (Pro Engineering and Latex) for this thesis. Especially, Jonghee took care of my personal issues and gave me good advice for living. I must thank Dr. Dong Hun Park, who welcomed me and my wife to the United States and helped me get an apartment to settle down quickly. He also drove the U-haul truck when I moved to another apartment. Much appreciation goes to my relative Byeongchun Kim and his friend Hong Y. Lee. Byeongchun Kim drove from Ohio to see me with a TV when I just arrived in the United States. Hong Y. Lee took care of my first car, a Civic, car insurance, and paper work at the MVA.

I am also grateful to fellows at the LPS: Dr. Junghwan Kim, Dr. Hanhee Paik, Dr. Michael Dreyer, Dr. Dan Sullivan, Dr. Sang Hwui Lee, Dr. Hui Wang, Moe Khalil, Dr. Jookyoung Lee, Dr. Sergiy Gladchenko, Dr. Micah Stoutimore, Bahman Sarabi, Dr. Seok-Hwan Chung, Jin Seock Ma, Dr. Luyan Sun, Dr. Robert McFarland, Tomasz Kott, Paval Nagornykh, Konrad Aschenbach, Mark Gubrud, Anita Roychowdhury, Paul Hannah, Greg Latini, Lisa Lucas, Nolan Ballew, John Sugrue, Peter Krusen, Victor Yun, and Toby Olver. Hanhee taught me how to fit the resonance curve using her Matlab codes and she was willing to become my co-signer for my apartment.

I am also grateful to Korean fellows at the campus: Prof. Young Suh Kim, Prof. Ho Jung Paik, Prof. Eun-Suk Seo, Dr. Euyheon Hwang, Prof. Ki-Yong Kim, Kwan Lee, Chaun Jang, Young Soo Yoon, Young-Noh Yoon, Hana Hwang, Dr. Juhee Park and Jae Kwang Jeong. Young-Noh taught me how to measure the CPB states using the rf-SET. Then he left the group and became a theorist in the chaos group.

Most of all, I would like to thank my wife Kyoungmi, who has always been supportive and patient. I cannot imagine my Ph.D. without her. I must add my heartfelt appreciation for my parents, who gave endless love and support to my family. Finally, I acknowledge financial support from Korea Science and Engineering Foundation for two years.

Table of Contents

List of Tables

List of Figures

List of Abbreviations

Fundamental constants

h	Planck's constant (6.626×10^{-34} J $\cdot$ s)
$\hbar$	reduced Planck's constant (1.054×10^{-34} J$\cdot$ s)
k_B	Boltzmann's constant (1.381×10^{-23} J/K)
e	1.602×10^{-19} C
$\Phi_\circ$	magnetic flux quantum ($h/2e = 2.068 \times 10^{-15}$ T$\cdot$m^2)

Junction parameters

I_0	critical current
I_J	current through a junction
V_J	voltage across a junction
γ	gauge-invariant phase difference across a junction
L_J	Josephson inductance
E_J	Josephson energy
R_J	tunneling resistance of a junction
C_J	capacitance of a junction
Δ_g	superconducting energy gap
Δ_{Al}	superconducting energy gap of aluminum

SET parameters

rf-SET	radio frequency single electron transistor
n_e	number of excess electrons in the SET island
$C_{g,e}$	gate capacitance
$V_{g,e}$	gate voltage of SET
$n_{g,e}$	reduced gate voltage, $C_g V_{g,e}/e$
V_{DS}	drain-source voltage
$C_{\Sigma,e}$	total capacitance of the island
$E_{C.e}$	charging energy of SET,, $e^2/2C_{\Sigma,e}$
κ_i	fraction of the drain-source voltage across a junction
α_i	attenuation factor
S_I	noise power spectral density of current fluctuations
R_{SET}	tunneling resistance of the SET junctions
η	Fano factor
Z_{tank}	impedance at the input of the tank circuit
P_N	average noise power from the SET
G	gain of the system
T_N	noise temperature of the system

Qubit parameters

CPB	Cooper Pair Box
n	number of excess Cooper pairs on the island
n_g	reduced gate voltage, $C_g V_g/e$
C_g	gate capacitance
V_g	gate voltage of CPB
C_Σ	total capacitance of the island
E_C	charging energy of CPB, $e^2/2C_\Sigma$
E_{el}	electrostatic energy of CPB
Φ_a	applied magnetic flux
U_R	rotational matrix
T_1	energy relaxation time of a CPB in the excited state
T'	decay time constant of a Rabi oscillation
T_φ	dephasing time
T_2	coherence time
T_2^*	spectroscopic coherence time
$T_2^\dagger$	inhomogeneous broadening time
κ_c	coupling constant, C_g/C_Σ
$S_{cl}(f)$	classical spectral density of noise
$S_V(f)$	spectral density of voltage noise
$S_q(f)$	spectral density of charge noise
$\varphi_n(t)$	random phase noise in a CPB
$f_\varphi(t)$	dephasing factor
Ω	2π times the Rabi flopping frequency
Ω_R	2π times the bare Rabi flopping frequency
P_e	excited state population of qubit

Two level fluctuator parameters

ε_a	energy of the fluctuator at position x_a
ε_b	energy of the fluctuator at position x_b
T_{ab}	tunneling matrix element between the two sites
Q_{TLF}	charge of the fluctuator
Q_{pi}	induced polarization charge on the island of the CPB
η	angle of displacement relative to the electric field in the junction

Resonator parameters

Q_i	internal quality factor of the resonator
Q_e	external quality factor of the resonator
Q_L	total or loaded quality factor of the resonator
S_{21}	transmission of the resonator from port 1 to port 2
T_c	transition temperature of the superconductor
α_k	fractional kinetic inductance
f_0	resonator resonant frequency

CQED parameters

$a^\dagger a$	number operator for photons stored in the resonator
ω_r	resonator resonant angular frequency
ω_a	CPB transition angular frequency
κ_r	decay rate of resonator, ω_r/Q_L
Δ	detuning between ω_a and ω_r, $\omega_a - \omega_r$
g	coupling strength between the CPB and resonator
χ	dispersive angular frequency shift, g^2/Δ
$C_{g,r}$	coupling capacitance between the CPB and resonator
n_r	number of photons stored in the resonator

Chapter 1

Introduction

1.1 Motivation

After Richard Feynman proposed in 1982 that a quantum computer could simulate a quantum system more efficiently than a classical computer [1], many theorists began working on understanding what a quantum computer might be capable of doing. A decade later David Deutsch and Richard Jozsa noticed that a quantum algorithm could be exponentially faster than a classical algorithm and proposed the Deutsch−Jozsa algorithm as an example [2]. In the algorithm, a black box computes a function $f(x_1, x_2, ..., x_n)$ with n inputs $x_1, x_2, ..., x_n$. The input x_n is either 0 or 1. If the black box maps all its inputs to the same number, 0 or 1, the function f is defined to be *constant*. If the black box maps 50 % of inputs to 0 and the other 50 % to 1, the function f is defined to be *balanced*. The task is to determine whether f is *constant* or *balanced* with a minimum number of queries. For example, suppose we query the black box for inputs of 0 and 1. If the black box outputs $f(0) = f(1) = 0$ or $f(0) = f(1) = 1$, then we can say the black box is *constant*. If it outputs $f(0) \neq f(1)$, the black box is *balanced*. In this classical example, to figure the task out, we queried the black box twice. For n inputs, we need to query the black box $2^{n-1} + 1$ times in the worst case. What is remarkable is that if the Deutsch−Jozsa quantum algorithm is used, we can get the answer after querying

the black box only one time if we input the superposition of the n possible inputs.

A monumental step forward in quantum computing occurred in 1994 when Peter Shor discovered a quantum algorithm (Shor's algorithm [3]) that could factor numbers exponentially faster than any known classical algorithm. Subsequently, Lov Grover developed another quantum algorithm that could search an unsorted database with quadratic speedup over classical computers [4].

In conventional computing, information is stored as 0's and 1's, or "bits". In a quantum computer, quantum two-level systems (*i.e.* a physical system with two distinct energies) or "qubits", are used to store information. Because a qubit is a quantum mechanical system, it can not only be in $|0\rangle$ or $|1\rangle$, but it can exist in an infinite number of possible superposition states $\alpha|0\rangle + \beta|1\rangle$. These superposition states give a quantum computer a significantly greater number of resources for tackling certain types of problems.

It was soon recognized that it would not be easy to build a quantum computer. In particular, quantum superposition states can be destroyed by interaction with the environment. In a classical digital computer, one can preserve bit information by making multiple copies and using error correction techniques. However, in a quantum system, an unknown quantum state cannot be copied since the quantum system would collapse to an eigenstate once it is measured; this is called the no-cloning theorem [5]. Remarkably, Shor found a way to perform error correction on qubits by copying and correcting a quantum system in which the information was spread among highly entangled qubits [6]. Raymond Laflamme was subsequently able to establish key results on compact quantum error correcting codes and showed

that the codes would work if the error rate is below a certain tolerance limit [7]. Experimentalists were inspired by this theoretical progress, and many groups began working towards constructing an actual quantum computer. As a result, many potential qubits have been proposed and tested, though none have yet moved beyond the laboratory.

In principle, any quantum two level system could be used as a qubit. Many physically different approaches have been proposed: nuclear spins (NMR), trapped ions, semiconductor quantum dots, and various superconducting devices. They all have advantages and disadvantages. For example, NMR and trapped ions have demonstrated long coherence times and entanglement of many qubits (up to 8 so far). But it is generally believed that scaling to many more qubits will be difficult for these systems. In contrast semiconductor and superconductor approaches appear to have good scalability; they can take advantage of very large scale integration (VLSI) using conventional fabrication technology. However, the general problems with superconducting qubits are that coherence times have been fairly short (typically microseconds or less) and the devices are sensitive to defects in the material from which they are made. My work has been on one particular type of superconducting qubit, the Cooper Pair Box.

1.2 Superconducting Qubits

Unlike a qubit formed from a single trapped ion [8], quantum superconducting circuits typically involve billions of atoms and electrons. Such a many-particle

system can still act like a qubit (two-level system) because in a superconductor the wave function describing the electrons condenses to one state. One consequence of the condensation of the wave function is that when a superconducting loop is cooled down below its transition temperature T_c, one finds the magnetic flux in the loop is quantized in units of $\Phi_\circ = h/2e = 2.068 \times 10^{-15}$ T·m^2. Another consequence of the condensation to the ground state is that the electrons form Cooper pairs with charge $-2e$, where $e = 1.602 \times 10^{-19}$ C.

The key circuit component in all superconducting qubits is the Josephson junction [9]. An ideal Josephson tunnel junction consists of two superconducting electrodes separated by a thin insulating tunnel barrier (see Fig. 1.1). The dc Josephson relation [10] says that the supercurrent I_J through the junction depends on the phase difference γ across the tunnel barrier by the following relation:

$$I_J = I_0 \sin \gamma, \tag{1.1}$$

where I_0 is the critical current of the tunnel junction. The ac Josephson relation says that γ will change with time if a voltage (V_J) is placed across the junction:

$$\frac{d\gamma}{dt} = \frac{2e}{\hbar} V_J \equiv \frac{2\pi}{\Phi_0} V_J, \tag{1.2}$$

where Φ_0 is the flux quantum.

The effective inductance of a tunnel junction can be obtained by taking the time derivative of Eq. 1.1:

$$\frac{dI_J}{dt} = I_0 \cos \gamma \frac{d\gamma}{dt}. \tag{1.3}$$

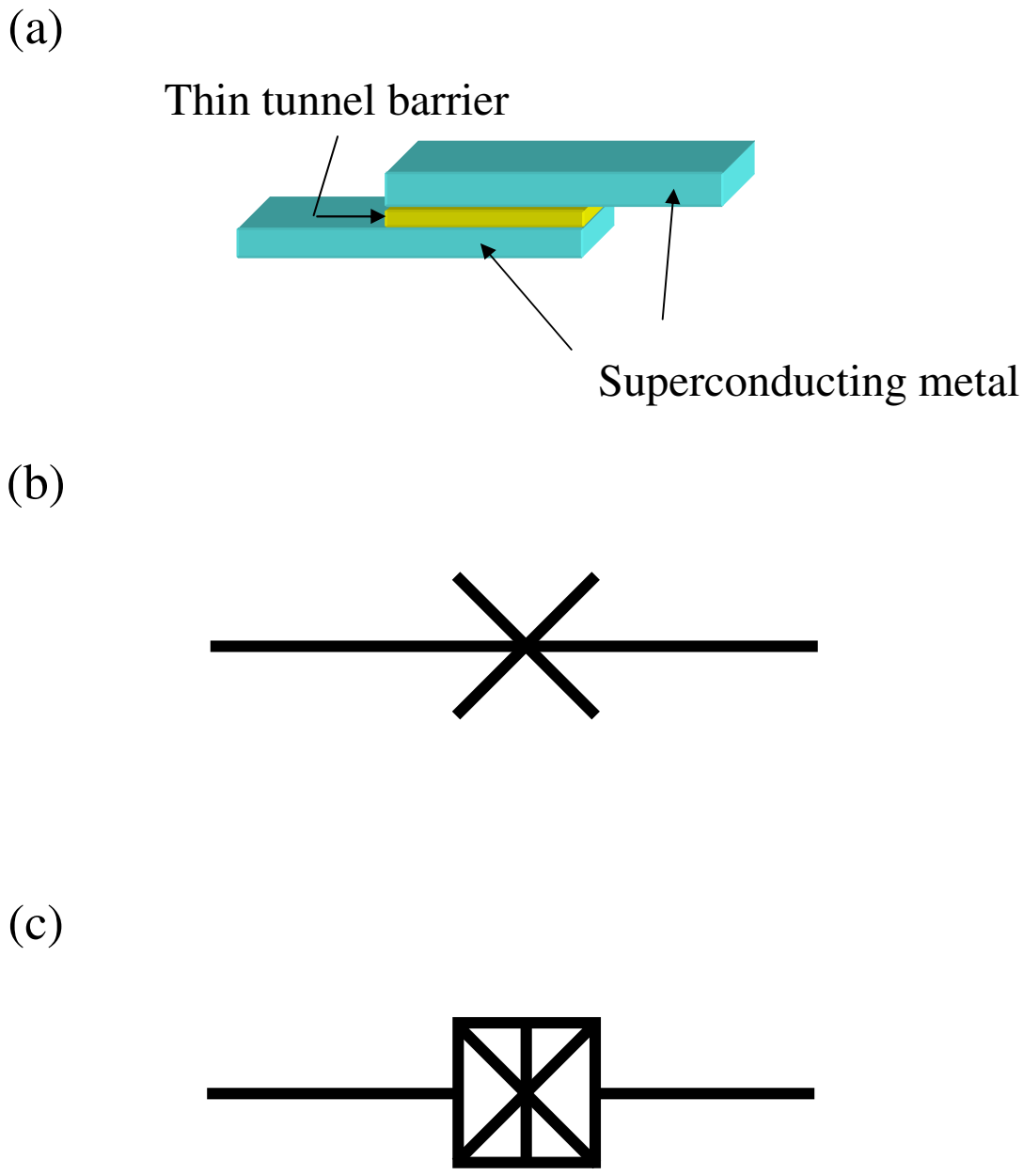

Figure 1.1: (a) Schematic of a Josephson junction. (b) Circuit symbol for a big Josephson junction and (c) circuit symbol for an ultra-small Josephson junction.

Combining Eq. 1.2 and Eq. 1.3 leads to

$$V_J = \frac{\Phi_0}{2\pi I_0 \cos\gamma} \frac{dI_J}{dt}. \tag{1.4}$$

Equation 1.1 can now be used to write $\cos\gamma$ in the form

$$\cos\gamma = \sqrt{1 - \left(\frac{I_J}{I_0}\right)^2}. \tag{1.5}$$

We note that for an inductor, $V = LdI/dt$. Comparing this with Eq. 1.4, we can now define the Josephson inductance as

$$L_J = \frac{\Phi_0}{2\pi\sqrt{I_0^2 - I_J^2}}. \tag{1.6}$$

L_J clearly depends on the current and hence a junction acts as a non-linear inductor. With the sandwich geometry used in typical junctions (see Fig. 1.1), one also gets a capacitance that shunts across the junction and causes the junction to act as a non-linear LC resonator. Because of the non-linearity associated with the inductor, the energy levels are anharmonic. This is critical for being able to treat the junction as a qubit (two-level system).

Roughly speaking, there are three broad classes of superconducting qubits [11]: phase qubits, charge qubits, and flux qubits. The basic circuit schematics of the qubits are illustrated in Fig. 1.2.

The prototypical phase qubit consists of a single Josephson junction biased by a dc current. This device can be understood from the resistively and capacitively shunted junction (RCSJ) model [12]. The current through the junction is the control parameter; it controls the tilt of the washboard [see Fig. 1.2 (b)]. The potential has

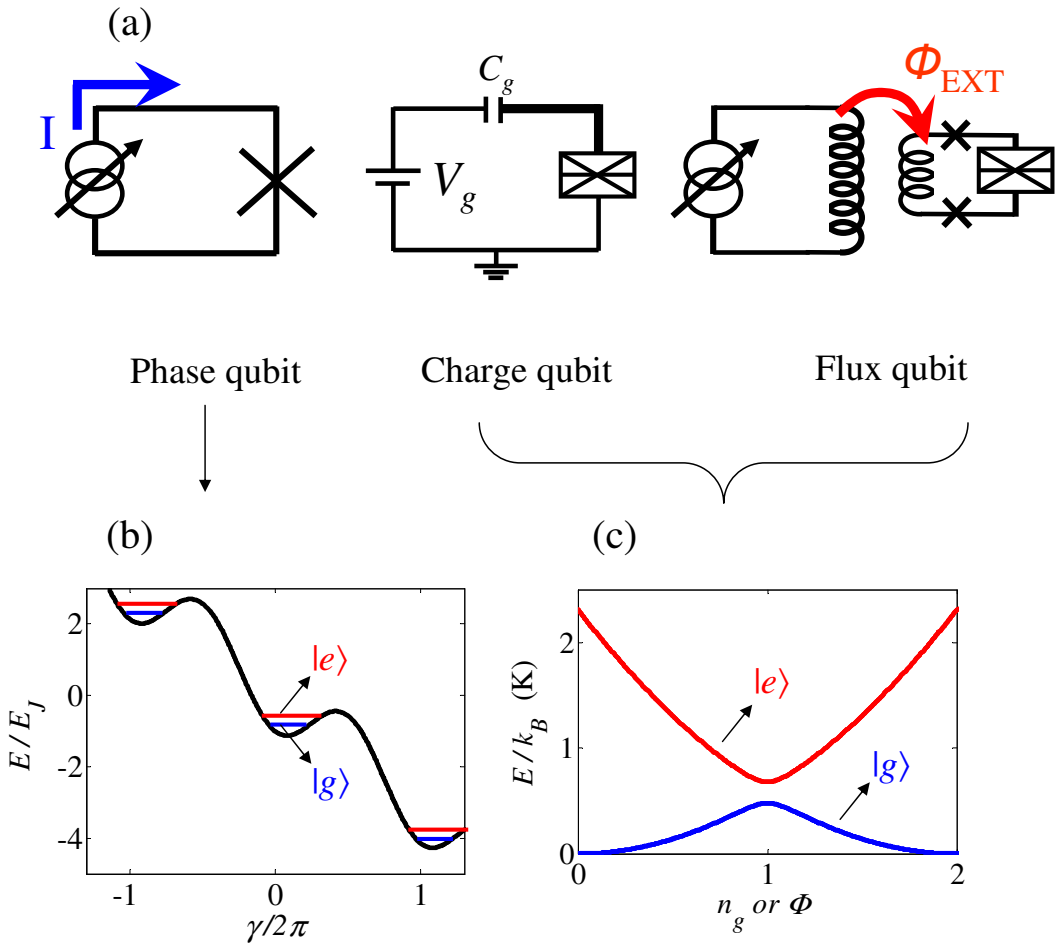

Figure 1.2: Various superconducting qubits. (a) Schematic of phase qubit, charge qubit, and flux qubit. (b) Energy levels of the phase qubit, and (c) Energy levels of the charge qubit or flux qubit. Horizontal axis is n_g for the charge qubit and Φ for the flux qubit.

wells with a potential barrier height that is adjustable by the bias current. Discrete meta stable quantum states form in each well. The two lowest energy levels in a well can be used as the ground state and the first excited state of the qubit. Quantum mechanically, the system can tunnel out through the potential barrier with a finite probability and begin running down the tilted washboard. This will lead to a dc voltage across the junction. The tunneling escape rate depends on the qubit state; higher states have a larger escape rate, since the barrier is smaller. Thus, by measuring the escape rate and the bias current when a voltage appears across the junction, one can infer the quantum state of the qubit. This also means the phase qubit itself behaves as a read-out.

A charge qubit consists of an ultra-small Josephson junction that is connected to a superconducting island, which has a small capacitance. In this qubit, the number of excess Cooper-pairs on the island is typically quantized and can be controlled by an external gate voltage. The charge qubit has energy levels that are very anharmonic and the two lowest energy levels can be chosen as the qubit states [see Fig. 1.2 (c)]. The energy spacing between qubit levels is tunable by a gate voltage V_g, which is capacitively coupled to the island with capacitance C_g (or the reduced gate voltage $n_g = C_g V_g/e$), which is the control parameter. I discuss the theory of charge qubits in chapter 2.

A flux qubit has one or more Josephson junctions in a small superconducting loop. Typically, one junction is smaller than the other junctions and this effectively increases the inductance of the loop. The direction of the supercurrent in the loop can be either clockwise or counterclockwise, or a superposition of both directions,

and is controlled by an external magnetic flux. Qubit states that have opposite directions of magnetic moment in the loop can be measured using a dc SQUID (Superconducting Quantum Interference Device), which is very sensitive to magnetic flux.

1.3 History of the Cooper Pair Box

The Cooper Pair Box (CPB) was invented by the Saclay group in 1997 [13]. To measure the excess charge, they used a dc-single electron transistor (SET) coupled to the CPB island. The following year Rob Schoelkopf's group at Yale developed a radio frequency SET and was able to read out the CPB states quickly, *i.e.* with a much larger bandwidth than was previously possible [14]. Then in 1999, Nakamura *et al.* at NEC demonstrated the ability to coherently manipulate and measure the quantum states of a CPB [15]. This was the first true superconducting qubit.

Unfortunately, the SET read-out turned out to be inherently dissipative and too strongly coupled to the CPB, so that the CPB suffered from measurement back-action [16]. Also, the SET cannot measure the CPB states at the charge degeneracy point, where the CPB level spacing is insensitive to charge. To get around these problems, in 2002 the Saclay group demonstrated a charge qubit with a new read-out scheme, which they called Quantronium [17]. In this qubit a large shunting capacitor made of a Josephson junction is weakly coupled to the CPB. This was the first step towards a dispersive read-out scheme for the CPB and eventually evolved into the Josephson bifurcation amplifier [18]. In 2004, the Yale group finally devised

a true dispersive read-out "circuit Quantum electrodynamics (QED)" scheme [19] in analogy with cavity QED in quantum optics [20] (see Fig. 1.3 and section 1.3.2).

1.3.1 Dissipative Read-Out

To measure the quantum states of our CPB qubit, I initially used a radio-frequency single electron transistor (SET or Coulomb-blockade electrometer). A radio-frequency single electron transistor is a very sensitive charge detection device, with demonstrated charge sensitivities down to 6 $\mu e/\sqrt{Hz}$ [22]. By capacitively coupling an SET to the island of our CPB qubit, I was able to measure excess charge on the CPB island and infer the state of the CPB.

While this scheme worked very well, there were two problems. First, I was not able to measure the qubit at the charge degeneracy point (the so called "sweet spot") where the coherence times are longest. Second, the static dissipated power was quite large ($\sim$pW) and we believed this could create a fundamental source of dissipation for our qubit.

1.3.2 Dispersive Read-Out

A dispersive read-out involves measuring a change in a reactance by observing the shift in the resonance frequency of an LC circuit. In my work, the LC circuit was a superconducting resonator with a resonant frequency of 5.4 GHz.

In the Yale group's cavity quantum electrodynamics (QED) technique, one measures the change of the electric susceptibility of a qubit by observing the res-

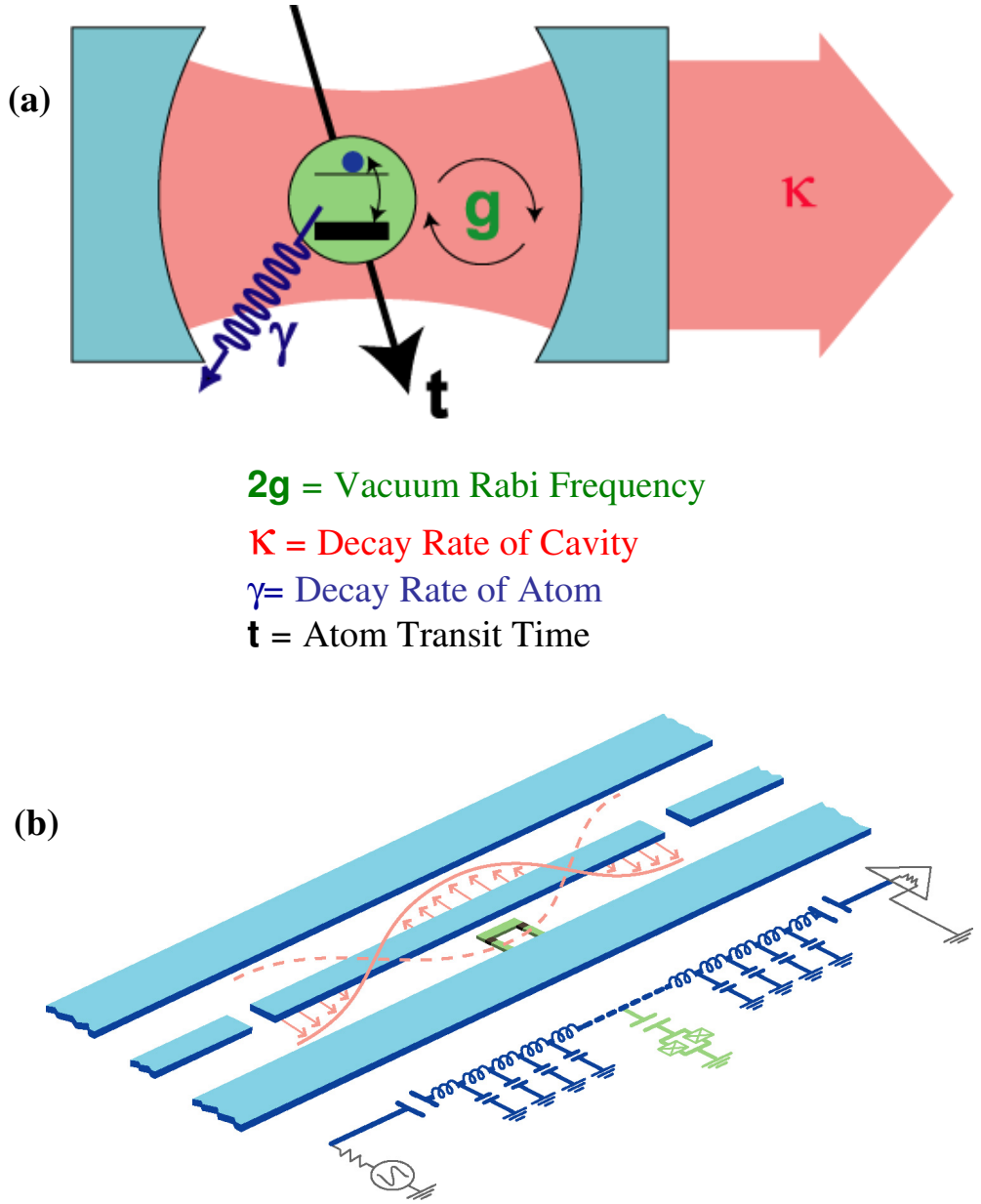

Figure 1.3: Schematic of cavity quantum electrodynamics (QED). (a) Schematic of optical cavity QED (picture from Jeff Kimble's quantum optics group at Caltech) and (b) schematic of superconducting circuit QED [21] (picture from Schoelkopf's group at Yale University).

onance frequency change (Δf_r) of a linear resonator coupled to a CPB. When a resonator is capacitively coupled to a CPB, the resonance frequency depends on the state of the CPB. This read-out is also called a dispersive read-out. If this read-out is implemented properly, there can be very little power dissipated in the device and very little back-action on the qubit.

For the circuit QED technique, many research groups have used a thin-film half-wavelength resonator. A half-wavelength resonator is basically a length (L) of metal that is capacitively connected to both the input and output transmission lines. Since the ends are "open" at resonance, a current node and voltage anti-node are formed at each end and there will be a lowest frequency mode and higher harmonics. These higher harmonics can have a dramatic effect on T_1 when operating the qubit above the fundamental resonance [24].

To minimize the detrimental effect of harmonics on our qubit, I designed a lumped element resonator with $f_0 = 5.4$ GHz, and no harmonics up to $f = 20$ GHz. When I coupled this resonator to a qubit, I observed the CPB spectrum, measured T_1 up to 200 μs, and observed Rabi oscillations. This work is described in Chapters 5-6.

1.4 Overview of the Thesis

Although many qubits will be needed to build a useful quantum computer, research on single qubits is important for understanding qubit manipulation, read-out, and decoherence mechanisms. To quantify decoherence, I measured the energy

spectrum, energy relaxation times (T_1), and Rabi decay times (T') of a CPB. Another decoherence source is the back-action from the qubit read-out. By testing different read-out schemes (dissipative and non-dissipative), I was able to see some back-action effects.

In this thesis, I begin in Chapter 2 by discussing the CPB Hamiltonian, eigenstates, and sources of decoherence. I next discuss my use of an SET to make measurements of a CPB in Chapter 3. In Chapter 4, I present my detailed spectroscopic measurements of anomalous avoided level crossings. I also compare these measurements with a model for a charge fluctuator coupled to a CPB and examine the effect of these charge fluctuators on the relaxation time T_1 of the qubit. In Chapter 5, I discuss the lumped-element microwave resonator that I designed, built, and measured. In Chapter 6, I then describe coupling the resonator to a CPB and discuss my measurements on the coupled system. Finally, in Chapter 7, I finish with a discussion of possible future work and some concluding and summary remarks.

Chapter 2

Theory of the Cooper Pair Box (CPB)

2.1 Overview

In this chapter, I discuss the basic physics of a CPB, including the Hamiltonian, energy levels, states, and factors that contribute to decoherence.

2.2 CPB Hamiltonian

Figure 2.1 (b) shows an SEM image of a typical CPB and Fig. 2.1 (a) shows the circuit schematic. The CPB has a small superconducting island (100 nm wide by 500nm long by 30 nm thick) connected to Cooper pair reservoirs or a superconducting ground through two small Josephson junctions in parallel. Due to the small island capacitance and high impedance of the tunnel barrier, the electrostatic energy it takes to add a single Cooper-pair is dominant in a CPB.

A Josephson junction also stores Josephson energy that depends on the phase difference across the junction. The charging energy and the Josephson energy are added together to get the CPB Hamiltonian. The energy levels and the relative strengths of the charging versus Josephson energy can be tuned by an external magnetic flux and an applied gate voltage, which are controllable variables or experimental knobs. The tuning of the Josephson energy is basically related to the

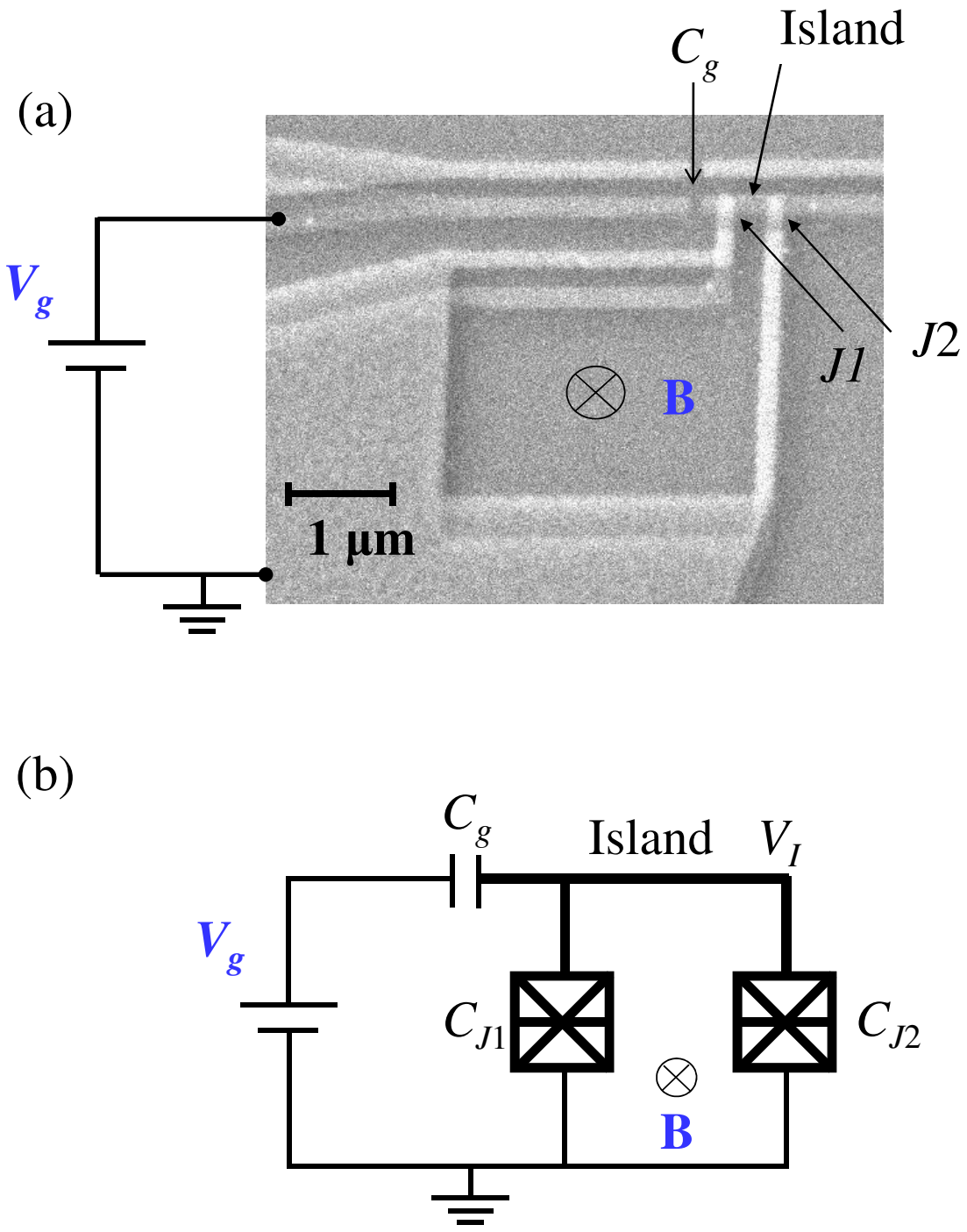

Figure 2.1: Schematic of a CPB. (a) SEM image of a CPB. The picture was taken by Dr. Pierre Echternach at the Jet Propulsion Laboratory (JPL). (b) Circuit schematic of a CPB. Island is shown as bold lines.

quantization of the magnetic flux in the CPB loop. The tuning of the charging energy is related to the quantization of the charge in the CPB island.

2.2.1 Josephson Energy

The Josephson energy E_J can be derived from the Josephson relations (Eqs. 1.1 and 1.2). The work done on the junction can be found by integrating the "power" $W = \int dt I_J V_J$. Using the Josephson relations, one finds

$$W = c_0 - E_J \cos\gamma, \tag{2.1}$$

where $E_J = I_0\Phi_0/2\pi$ and c_0 is a constant that can be neglected. We see that the only experimental parameter in E_J is the critical current I_0 of the junction. To modulate the critical current and hence the Josephson energy, we can place two nominally identical junctions in parallel and apply an external magnetic flux Φ_a to the resulting loop (see Fig. 2.1). In this situation, $I_0 = I_0^{max}|\cos(\pi\Phi_a/\Phi_0)|$, where I_0^{max} is the sum of the critical currents of the two junctions. Thus E_J can be tuned according to $E_J = E_J^{Max}|\cos(\pi\Phi_a/\Phi_\circ)|$ where $E_J^{Max} = \hbar I_0^{max}/2e$. Hence by changing the magnetic field we can effectively modulate or change the effective Josephson energy.

2.2.2 Charging Energy

By applying voltage V_g to a gate electrode, which is capacitively coupled to the CPB island with capacitance C_g, we can control the discrete number n of excess Cooper pairs on the island with respect to the neutral charge state on the island

[see bold lines in Fig. 2.1 (b)]. The voltage affects the energy of Cooper pairs on the island and the rate at which they can tunnel from the ground to the island.

The electrostatic potential of the island V_I is determined by the gate voltage V_g and the number n of excess Cooper pairs on the island. If there are no excess charges on the island, then $n = 0$. The circuit in Fig. 2.1 (b) can be treated as a voltage divider, and then the island potential is given by

$$V_I = \frac{\frac{1}{C_J}}{\frac{1}{C_J} + \frac{1}{C_g}} V_g = \frac{C_g V_g}{C_\Sigma}, \tag{2.2}$$

where $C_J = C_{J1} + C_{J2}$ and $C_\Sigma = C_g + C_J$ is the total capacitance of the CPB island. One can also consider the situation in which the gate voltage is zero and there are n excess Cooper pairs on the island. For this case, the gate capacitor and junctions are effectively connected to the island in parallel and the resulting island voltage is:

$$V_I = -\frac{2ne}{C_\Sigma}. \tag{2.3}$$

When both excess Cooper pairs and positive gate voltage are both present, the island potential is found by combining Eqs. 2.2 and 2.3:

$$V_I = \frac{e}{C_\Sigma}(n_g - 2n), \tag{2.4}$$

where $n_g = C_g V_g / e$ is the reduced gate voltage and $e = 1.602 \times 10^{-19}$ C. The electrostatic energy of the CPB island is given by

$$U = \frac{1}{2} C_g (V_I - V_g)^2 + \frac{1}{2} C_J (V_I - 0)^2. \tag{2.5}$$

In this circuit the gate voltage source does work to transfer excess charges onto the island through the tunneling junction. Suppose there are n excess Cooper pairs on the island and then another Cooper pair with charge $-2e$ is delivered to the island by the gate voltage source. Then, the new voltage on the island is given by

$$V_I' = \frac{e}{C_\Sigma}[n_g - 2(n+1)]. \tag{2.6}$$

Thus, the voltage difference for the tunneling is equal to $-2e/C_\Sigma$, so the charge on the gate capacitor changes by $-2eC_g/C_\Sigma$. The work W done by the gate voltage source for an excess Cooper pair is $(2eC_g/C_\Sigma)V_g$, and for n excess Cooper pairs, $W = 2neC_g/C_\Sigma V_g = 2nn_g e^2/C_\Sigma$ [12].

Inserting Eq. 2.4 into U and subtracting W from U, we can get the electrostatic free energy E of the system:

$$E = \frac{1}{2}\frac{e^2}{C_\Sigma}(2n - n_g)^2 + const., \tag{2.7}$$

where the $const = \frac{e^2}{2C_\Sigma}(\frac{C_J}{C_g} - 1)n_g^2$ can be dropped since it does not depend on n and thus has no effect on the charge transfer [12]. Hence, by changing the gate voltage, our other experimental knob, we can control the number of excess Cooper pairs on the island and also the detuning of CPB energy level.

Combining the Josephson energy and the electrostatic term discussed so far, the Hamiltonian of a CPB is

$$H = E_C(2n - n_g)^2 - E_J \cos\gamma, \tag{2.8}$$

where $E_C = e^2/2C_\Sigma$ and $E_J = E_J^{Max}|\cos(\pi\Phi_a/\Phi_\circ)|$.

We can also write $\cos\gamma = (e^{i\gamma} + e^{-i\gamma})/2$; the Josephson term corresponds to a change of $+/-$ one Cooper pair, and the $e^{+i\gamma}$ and $e^{-i\gamma}$ correspond to raising and lowering operators [12]. The Hamiltonian describing the CPB in the number representation is then given by [13, 25]

$$\hat{H}_{CPB} = E_C \sum_n (2n - n_g)^2 \left|n\right\rangle \left\langle n\right| - \frac{E_J}{2} \sum_n (\left|n+1\right\rangle \left\langle n\right| + \left|n\right\rangle \left\langle n+1\right|), \tag{2.9}$$

where the summation is over all possible numbers of excess Cooper pairs and $|n\rangle$ is the number state of excess Cooper pairs on the island. The quasiparticle states [26, 27] were neglected in this calculation. For a numerical calculation, we truncate the sum. For example, for four charge states n=-1, 0, 1, and 2, the Hamiltonian becomes:

$$\hat{H}_{CPB} = \begin{pmatrix} E_C(-2\times 1 - n_g)^2 & -E_J/2 & 0 & 0 \\ -E_J/2 & E_C(2\times 0 - n_g)^2 & -E_J/2 & 0 \\ 0 & -E_J/2 & E_C(2\times 1 - n_g)^2 & -E_J/2 \\ 0 & 0 & -E_J/2 & E_C(2\times 2 - n_g)^2 \end{pmatrix}. \tag{2.10}$$

We can numerically solve the truncated CPB Hamiltonian and get the eigenvalues, which correspond to the energy levels of a CPB. Figure 2.2 shows the three lowest levels (red, blue, and green curves) of the 4-level Hamiltonian. The dashed curves correspond to the energy associated with the electrostatic charging energy for n=-1, 0, 1, and 2. Note that the n=0 and n=1 dashed curves are degenerate at n_g=1 and the effect of E_J is to break that degeneracy by approximately E_J. At $n_g = 1$, the degenerate energy levels split into two energy levels: the ground state (red curve in Fig. 2.2) and the first excited state (blue curve in Fig. 2.2). The first and second excited state have a minimum splitting of approximately $E_J^2/16E_C$ and

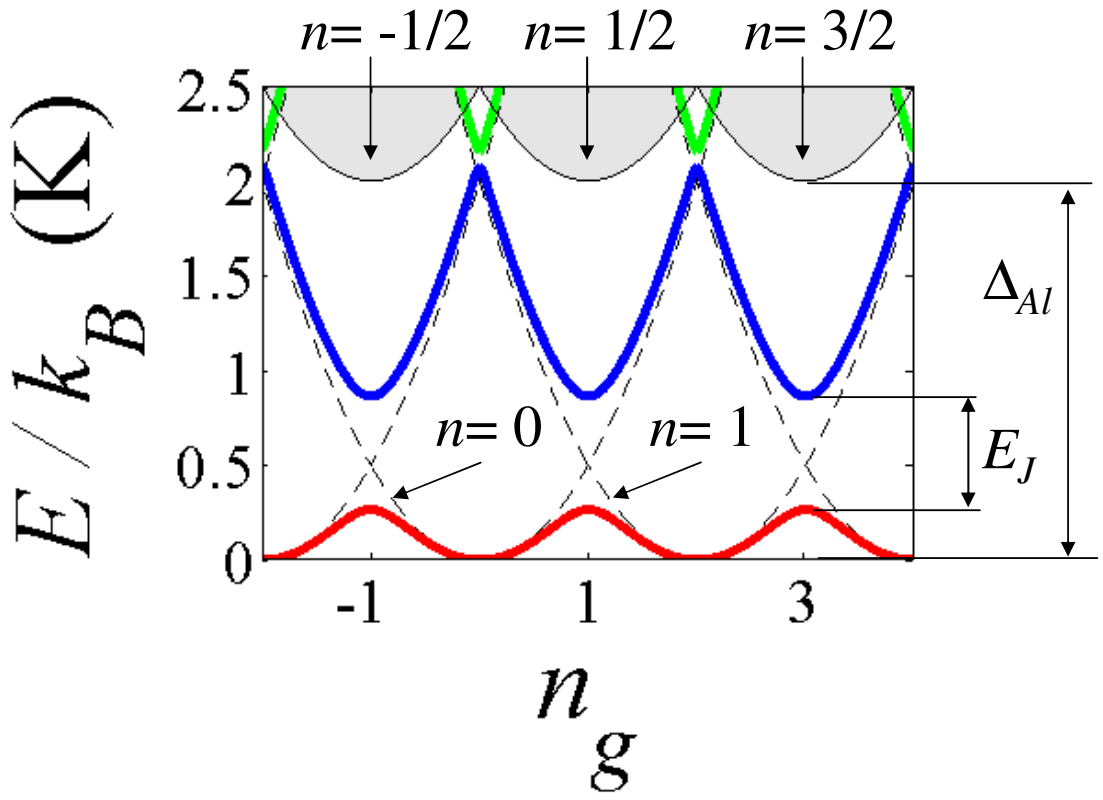

Figure 2.2: CPB energy levels. Dashed curves are the electrostatic energy of a CPB with E_C/k_B=0.5 K and different number n of excess pairs. Red and blue curves are energy eigenvalues from the CPB Hamiltonian with E_J/k_B=0.6 K. The energy of states with a quasiparticle are plotted as gray with the superconducting energy gap Δ_{Al}/k_B of 2 K.

this minimum occurs at even values of n_g. Finally, the grey region above the first excited state, with minimum at odd n_g values, corresponds to a continuum of states of the system in which a quasiparticle is present; they have been drawn schematically in Fig. 2.2.

The operator n for the excess number of Cooper pairs is diagonal in the charge basis and is given by

$$\hat{n} = \sum_n n \left|n\right\rangle \left\langle n\right| . \tag{2.11}$$

In thermal equilibrium the average number $\langle n \rangle$ of excess Cooper pairs on the island of a CPB is:

$$\langle n \rangle = \sum_i \left\langle i\right| \hat{n} \left|i\right\rangle P_i, \tag{2.12}$$

where $P_i = \exp(-E_i/k_BT)/\sum_i \exp(-E_i/k_BT)$ is the probability of finding n excess Cooper pairs on the island at a temperature T, $\sum_i P_i = 1$, and $|i\rangle$ is the i-th energy eigenvector of the system.

2.3 Two-Level Approximation

For much of my work, I will be working in the limit $E_J < E_C$ with the device biased near the charge degeneracy point. In this case, just two states $n = 0$ and $n = 1$ play a role and all other states can be ignored because they have a much higher energy. Hence, in this limit I can approximate the Hamiltonian as a two-level system [28], specifically I will take the summation in Eq. 2.9 over just $n = 0$ and $n = 1$.

2.3.1 Energy Levels

The 2-level CPB Hamiltonian in matrix form is

$$\hat{H}_{CPB} = \begin{pmatrix} E_C(2\times 0 - n_g)^2 & -E_J/2 \\ -E_J/2 & E_C(2\times 1 - n_g)^2 \end{pmatrix}. \tag{2.13}$$

Eq. 2.13 can be divided into two terms:

$$\hat{H}_{CPB} = \begin{pmatrix} -2E_C(1-n_g) & -E_J/2 \\ -E_J/2 & 2E_C(1-n_g) \end{pmatrix} + E_C[(1-n_g)^2+1] \begin{pmatrix} 1 & 0 \\ 0 & 1 \end{pmatrix}. \tag{2.14}$$

Note that the first matrix can be rewritten as

$$\hat{H} = -\frac{E_{el}}{2}\sigma_z - \frac{E_J}{2}\sigma_x, \tag{2.15}$$

where $E_{el} = 4E_C(1-n_g)$ and σ_z and σ_x are Pauli spin matrices. This Hamiltonian shows the CPB behaves as a fictitious spin-1/2 particle under a pseudo-magnetic field with components $B_z = E_{el}$ and $B_x = E_J$. Thus, E_{el} points in the $+z$ direction on the Bloch sphere [see Fig. 2.3 (a)] in the charge basis and the north pole corresponds to $|0\rangle$. Equation 2.15 also implies that E_J points in the $+x$ direction on the Bloch sphere. Hence, the eigenstates of the CPB will lie on the XZ plane aligned with the sum of two pseudo-magnetic fields. One can also see that a fluctuation in n_g will perturb E_{el} by $\delta E_{el} = -4E_C\delta n_g$ [see Fig. 2.3 (c)].

The second matrix in Eq. 2.14 is diagonal and just a multiple of the identity matrix, and hence it does not play a role in the difference of the energy eigenvalues.

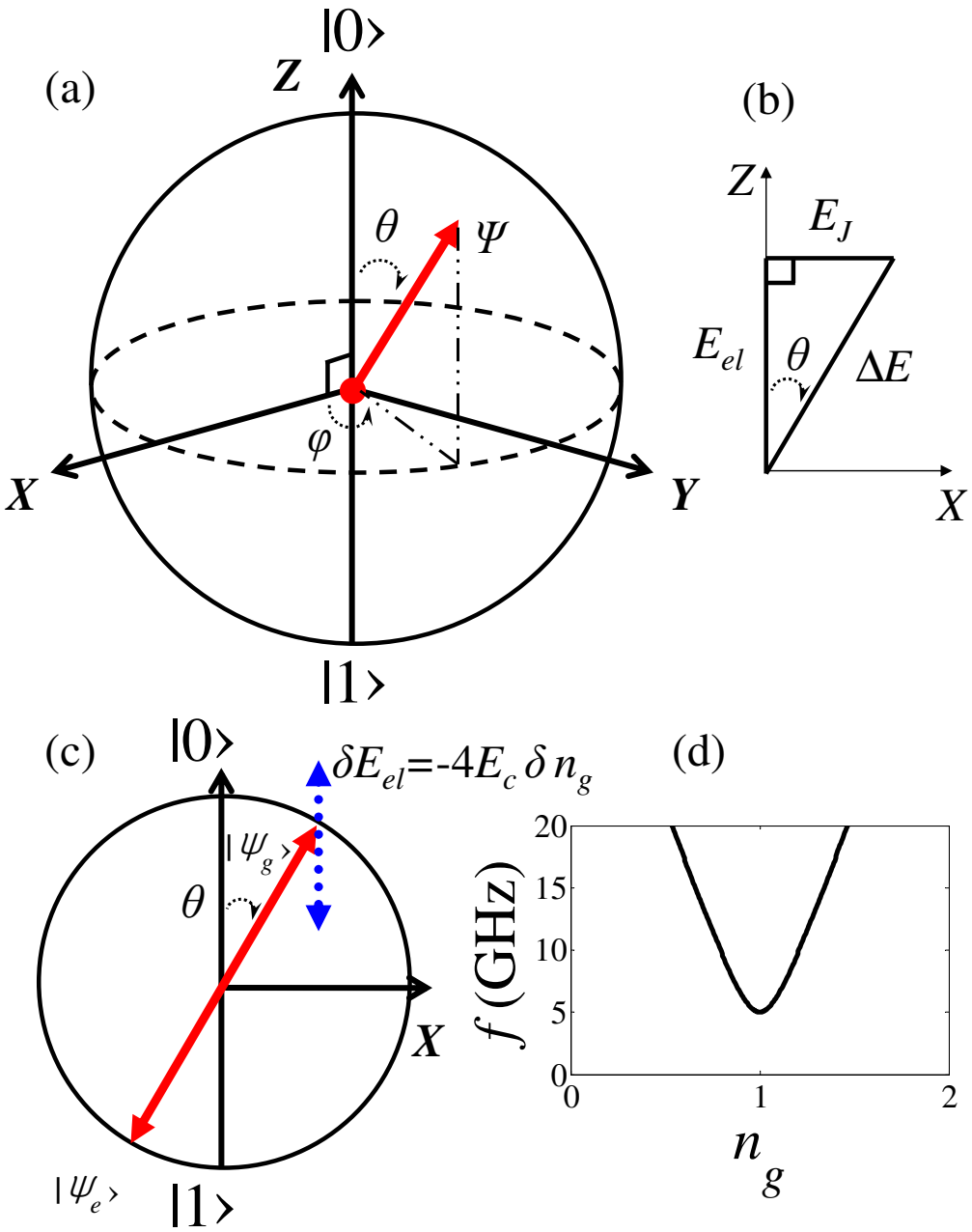

Figure 2.3: (a) Bloch sphere of a CPB in the charge basis and (b) the triangular relationship of θ. (c) A voltage fluctuation (blue dashed line) leads to a fluctuation of the electrostatic energy. (d) The energy difference ($\Delta E = hf$) between the ground state and the first excited state of a CPB near $n_g = 1$.

Neglecting the second term, the energy eigenvalues are

$$E_g = -\frac{1}{2}\sqrt{[4E_C(1-n_g)]^2 + E_J^2} \tag{2.16}$$

and

$$E_e = +\frac{1}{2}\sqrt{[4E_C(1-n_g)]^2 + E_J^2}, \tag{2.17}$$

where the subscript g represents the ground state and the subscript e represents the first excited state of the system. These eigenvalues are plotted in Fig. 2.4 (a) as a function of n_g. The energy difference between E_e and E_g is

$$\Delta E = \sqrt{[4E_C(1-n_g)]^2 + E_J^2}. \tag{2.18}$$

Note that $\Delta E = E_J$ at n_g=1 and $\Delta E \simeq 4E_C$ at n_g=2 if $E_C \gg E_J/4$. For example, when E_C/h is 10.4 GHz and E_J/h is 5 GHz, one can get the CPB spectrum as in Fig. 2.3 (d).

2.3.2 States

The eigenstates in terms of the excess charge states $|0\rangle$ and $|1\rangle$ are

$$|\Psi_g\rangle = \cos(\theta/2)\,|0\rangle + \sin(\theta/2)\,|1\rangle \tag{2.19}$$

and

$$|\Psi_e\rangle = -\sin(\theta/2)\,|0\rangle + \cos(\theta/2)\,|1\rangle\,, \tag{2.20}$$

where $\theta = \arctan[E_J/4E_C(1-n_g)]$ is a function of n_g and essentially the angle that rotates the charge basis to the energy eigen basis [see Figs. 2.3 (b) and (c)]. If the coherence time T_2 (see section 2.5) is long enough, then we can create an arbitrary

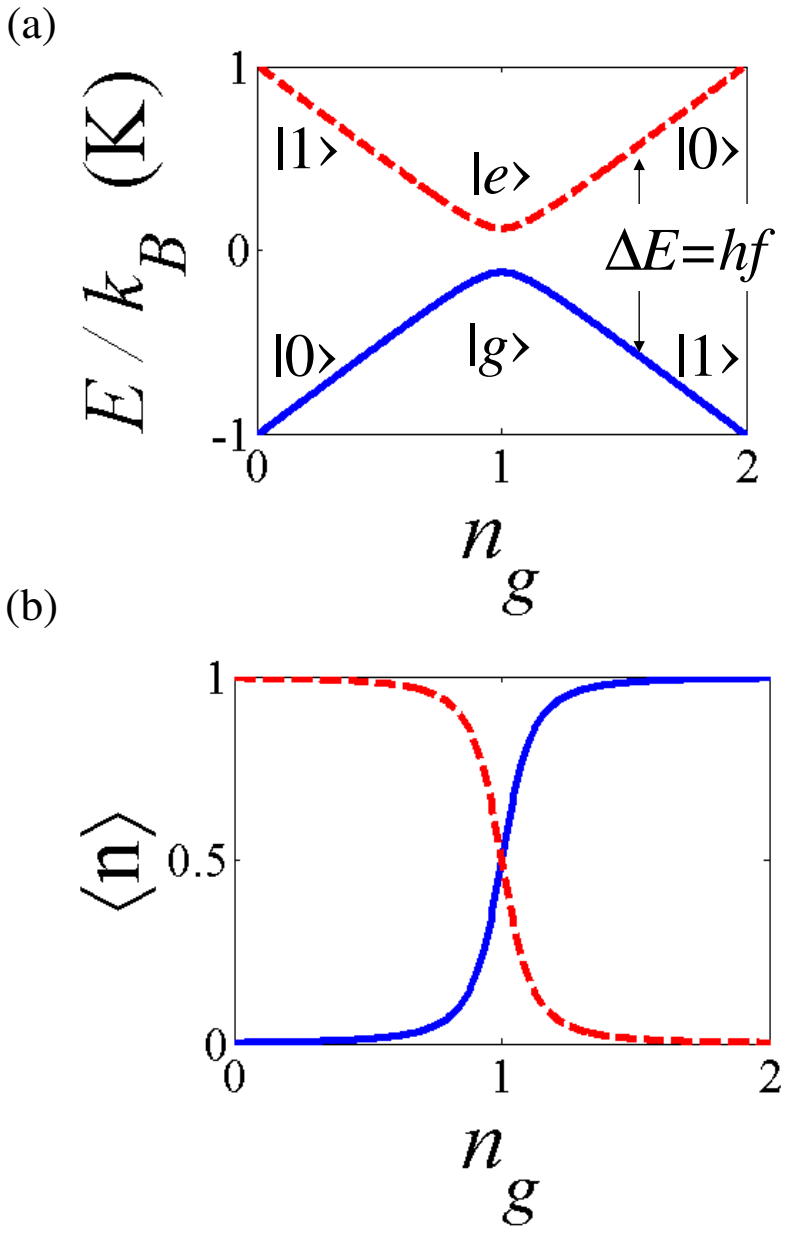

Figure 2.4: The two lowest levels of a CPB. (a) The energy levels in the first excited state (red dashed curve) and the ground state (blue curve), and (b) The pair number expectation values $\langle n \rangle$ in the first excited state (red dashed curve) and the ground state (blue curve).

state on the Bloch sphere [see Fig. 2.3 (a)] with a phase factor φ by exciting the qubit at ΔE. At the charge degeneracy point of $n_g = 1$, or $\theta = \pi/2$, the ground and excited states are in a superposition state of charge [see Fig. 2.4 (a)] as:

$$|\Psi_g(n_g = 1)\rangle = \frac{1}{\sqrt{2}}(|0\rangle + |1\rangle) \tag{2.21}$$

and

$$|\Psi_e(n_g = 1)\rangle = \frac{1}{\sqrt{2}}(-|0\rangle + |1\rangle). \tag{2.22}$$

2.3.3 Charge

We can also calculate the average number of excess Cooper pairs in the ground state by $\langle\Psi_g|\,\hat{n}\,|\Psi_g\rangle = \sin^2(\theta/2)$, plotted as the blue curve in Fig. 2.4 (b). The average charge in the excited state $\langle\Psi_e|\,\hat{n}\,|\Psi_e\rangle$ is $1 - \sin^2(\theta/2)$, shown as the red-dashed curve in Fig. 2.4 (b). The staircase-like charge response to the gate voltage is due to Coulomb blockade and is typically referred to as the Coulomb staircase. For $0 < n_g < 1$, the average charge $\langle n\rangle \simeq 0$ in the ground state. When the qubit is excited by resonant microwaves, the average excess charge $\langle n\rangle$ will increase towards 1 for this range of n_g. In contrast, for $1 < n_g < 2$, the average charge $\langle n\rangle \simeq 1$ in the ground state while the average charge $\langle n\rangle$ will decrease close to 0 when the qubit is excited.

If E_J is made smaller, the curvature of the E or $\langle n\rangle$ versus n_g plot at n_g=1 becomes larger, representing the fact that the charge state becomes a better quantum state of the system. It is also worth pointing out that if quasiparticles are present in the system, then a step at n_g=1 with $\langle n\rangle$ ~1/2 will be present (see [30] for example).

2.4 Energy Relaxation

With suitable choices for E_C and E_J, the difference in energy between the first excited state and the ground state can be reached with a standard microwave source.

To excite our qubit, we typically introduce a microwave voltage perturbation to the gate of the qubit: $\delta V_g(t)$. With the perturbation, the Hamiltonian in the charge basis becomes

$$\hat{H}_{CPB} = \begin{pmatrix} -2E_C(1-n_g) & -E_J/2 \\ -E_J/2 & 2E_C(1-n_g) \end{pmatrix} + 2E_C\delta n_g(t) \begin{pmatrix} 1 & 0 \\ 0 & -1 \end{pmatrix}, \quad (2.23)$$

where $\delta n_g(t) = C_g \delta V_g(t)/e$. Here the first matrix is the unperturbed Hamiltonian and the second matrix is a perturbation. One can see that the σ_z term in the charge basis, which arises from the electrostatic energy E_{el}, is perturbed by $\delta n_g(t)$ [see Fig. 2.3 (b) and (c)]. After rotating to the energy basis, such a perturbation will couple the eigenstates $|\Psi_e\rangle$ and $|\Psi_g\rangle$, and can be decomposed into longitudinal and transverse components with respect to the direction of eigenstates. To better understand the effect of a fluctuation in n_g, we can rotate the perturbed term in Eq. 2.23 into the Ψ_e and Ψ_g basis using the rotational matrix

$$U_R = \begin{pmatrix} \cos(\theta/2) & -\sin(\theta/2) \\ \sin(\theta/2) & \cos(\theta/2) \end{pmatrix}. \quad (2.24)$$

The rotated perturbation Hamiltonian is given by

$$\hat{H'} = 2E_C\delta n_g(t)U_R^T \begin{pmatrix} 1 & 0 \\ 0 & -1 \end{pmatrix} U_R, \tag{2.25}$$

or

$$\hat{H'} = 2E_C\delta n_g(t) \begin{pmatrix} \cos\theta & -\sin\theta \\ -\sin\theta & -\cos\theta \end{pmatrix}. \tag{2.26}$$

Using the triangular relationship for θ, $E_C = e^2/2C_\Sigma$, and $\delta n_g(t) = C_g\delta V_g(t)/e$, we can rewrite the perturbation Hamiltonian as

$$\hat{H'} = \delta V_g(t)e\kappa_c \begin{pmatrix} \cos\theta & -\sin\theta \\ -\sin\theta & -\cos\theta \end{pmatrix}, \tag{2.27}$$

or

$$\hat{H'} = \frac{e\kappa_c\delta V_g(t)}{\Delta E} \begin{pmatrix} 4E_C(1-n_g) & -E_J \\ -E_J & -4E_C(1-n_g) \end{pmatrix}, \tag{2.28}$$

where $\Delta E = \sqrt{[4E_C(1-n_g)]^2 + E_J^2}$ and $\kappa_c \equiv C_g/C_\Sigma$ is the coupling constant.

The off-diagonal terms in the perturbation Hamiltonian couple the ground state to the excited state and vice versa and scales as $E_J/\Delta E$. If $E_J/\Delta E$ is small in the experiment, then I will need to increase the driving amplitude to see the same population in the excited state because off-diagonal terms correspond to transitions between the ground and excited state. The off-diagonal terms are also relevant to energy relaxation from charge noise. As I will show in Chapter 3, I was able to increase the lifetime of the qubit (off the charge degeneracy point) by decreasing E_J. Thus, one can effectively decouple a CPB from relaxation due to voltage noise or charge noise and increase the energy relaxation time T_1.

The energy relaxation time T_1 can be derived from Fermi's golden rule [29]. One finds:

$$\frac{1}{T_1} = \frac{A^2}{\hbar^2} S_V(\triangle E/h), \tag{2.29}$$

where A is a coupling factor for voltage fluctuations and $S_V(\triangle E/h)$ is the spectral density of voltage noise. I will discuss the spectral density of voltage noise in section 2.7. The coupling strength $A = e\kappa_c \sin\theta$ can be found from the off-diagonal terms in Eq. 2.27. Note that a voltage fluctuation leads to a fluctuation in the electrostatic energy, which can be divided into two components: $\delta E_{el} \sin\theta$ and $\delta E_{el} \cos\theta$. $\delta E_{el} \sin\theta$ is the component perpendicular to the direction of the eigenstates [See Figs. 2.3 (b) and (c)]. This perturbation will cause mixing between states if the frequency is equal to the energy level spacing ΔE. For voltage noise applied to the gate, Eq. 2.29 can be rewritten explicitly as

$$\frac{1}{T_1} = \left(\frac{e\kappa_c}{\hbar}\right)^2 \frac{E_J^2}{[4E_C(1-n_g)]^2 + E_J^2} S_V(\triangle E/h). \tag{2.30}$$

In general, to extract the spectral density of voltage noise, one needs to know the source of noise and the CPB's coupling to that noise source. For charge fluctuations, a better figure of merit is the spectral density of charge noise, which is related to the effective gate voltage power spectral density by $S_q = C_g^2 S_V$. The spectral density of charge noise S_q can be extracted from

$$\frac{1}{T_1} = \left(\frac{2E_C}{e\hbar}\right)^2 \frac{E_J^2}{[4E_C(1-n_g)]^2 + E_J^2} S_q(\triangle E/h). \tag{2.31}$$

2.5 Dephasing

The coherence of the qubit is fragile and can be destroyed by interaction with degrees of freedom of the environment. Such interactions affect the dynamics of a qubit, causing energy relaxation and dephasing. Energy relaxation produces "population" decay, which is quantified by T_1, while a pure dephasing process is quantified by T_φ. A pure dephasing process conserves the population but destroys the phase coherence of superposition states. In general, decoherence sources include energy relaxation and pure dephasing, and can be quantified by the coherence time T_2 [33, 34]

$$\frac{1}{T_2} = \frac{1}{2T_1} + \frac{1}{T_\varphi}. \tag{2.32}$$

To better understand dephasing, suppose the qubit is in an arbitrary state at $t = 0$

$$|\psi(t=0)\rangle = \alpha\,|g\rangle + \beta e^{i\varphi_0}\,|e\rangle\,, \tag{2.33}$$

where $\sqrt{|\alpha|^2 + |\beta|^2} = 1$ and φ_0 is the phase at $t = 0$. The state will evolve with time as

$$|\psi(t)\rangle = \alpha\,|g\rangle + \beta e^{i\varphi_{01}(t)}\,|e\rangle\,, \tag{2.34}$$

where $\varphi_{01}(t) = (\Delta E/\hbar)t$. Suppose a random phase $\varphi_n(t)$ is added due to perturbation of the system so

$$|\psi(t)\rangle = \alpha\,|g\rangle + \beta e^{i[\varphi_0+\varphi_{01}(t)]}e^{i\varphi_n(t)}(t)\,|e\rangle\,. \tag{2.35}$$

For measurements, a statistical ensemble of pure states should be considered. So one can introduce the dephasing factor $f_\varphi(t) = \langle e^{i\varphi_n(t)}\rangle$, which becomes $e^{-\langle\varphi_n^2(t)\rangle/2}$

when $\varphi_n(t)$ is chosen from a Gaussian distribution [35]. The calculation of the mean-squared phase noise is given in references [35, 36, 37] as

$$\langle \varphi_n^2(t) \rangle = \frac{1}{\hbar^2 e^2} \left(\frac{\partial \Delta E}{\partial n_g} \right)^2 \int_{-\infty}^{+\infty} df S_\lambda(f) \frac{\sin^2(\pi f t)}{(\pi f)^2}, \tag{2.36}$$

where $\Delta E = \sqrt{[4E_C(1-n_g)]^2 + E_J^2}$ and $S_\lambda(f)$ is the spectral density of λ.

Here I will consider two kinds of classical charge noise $S_{cl}(f)$ as $S_\lambda(f)$: white noise and $1/f$ noise. Yoshihara *et al.* observed both types of noise in their flux qubit [38]. In the case of white noise, $S_{cl}(f)$ is constant over the whole frequency range and the integral in Eq. 2.36 is given by

$$\frac{S_{cl}(f=0)t}{\pi} \int_{-\infty}^{+\infty} d(\pi f t) \frac{\sin^2(\pi f t)}{(\pi f t)^2} \quad = \quad S_{cl}(f=0)t. \tag{2.37}$$

Then, the mean-squared phase noise becomes

$$\langle \varphi_n^2(t) \rangle = \frac{t}{\hbar^2 e^2} \left(\frac{\partial \Delta E}{\partial n_g} \right)^2 S_{cl}(f=0). \tag{2.38}$$

This leads to an exponential decay of the dephasing factor

$$f_\varphi(t) = e^{-t/T_\varphi}, \tag{2.39}$$

where

$$\frac{1}{T_\varphi} = \frac{1}{2\hbar^2 e^2} \left(\frac{\partial \Delta E}{\partial n_g} \right)^2 S_{cl}(f=0) \tag{2.40}$$

Using Eq. 2.18 for ΔE versus n_g, we get for the CPB in the presence of white noise,

$$\frac{1}{T_\varphi} = \frac{1}{2\hbar^2 e^2} \frac{(4E_C)^4 (1-n_g)^2}{[4E_C(1-n_g)]^2 + E_J^2} S_{cl}(f=0). \tag{2.41}$$

This result is what happens for diagonal terms in the perturbed Hamiltonian

(Eq. 2.26), which cause changes in the energy levels (*i.e.* ac Stark effect). Thus a charge or voltage fluctuation along the radial direction of the eigenstates can cause dephasing of a qubit and yields the dephasing time [39]

$$\frac{1}{T_\varphi} = \frac{B^2}{\hbar^2} S_V(f=0), \tag{2.42}$$

or

$$\frac{1}{T_\varphi} = \left(\frac{2E_C}{e\hbar}\right)^2 \frac{[4E_C(1-n_g)]^2}{[4E_C(1-n_g)]^2 + E_J^2} S_q(f=0), \tag{2.43}$$

where $B = e\kappa_c \cos\theta$ is the coupling strength of the fluctuation in Eq. 2.27. Equation 2.43 predicts that the dephasing time is maximum at $n_g = 1$ and decreases quickly away from $n_g = 1$. This is the origin of the charge noise "sweep spot" at $n_g = 1$.

The second type of classical noise is low frequency charge noise (*i.e.* $1/f$ noise). The calculation of the mean-squared phase noise can be found in references [35, 36, 37], which give:

$$\langle \varphi_n^2(t) \rangle = \frac{1}{\hbar^2 e^2} \left(\frac{\partial \Delta E}{\partial n_g}\right)^2 \int_{-\infty}^{+\infty} df \frac{\alpha}{|f|} \frac{\sin^2(\pi f t)}{(\pi f)^2}, \tag{2.44}$$

where typically the amplitude of charge noise $\sqrt{\alpha} \approx 10^{-3} - 10^{-4}\ e$. Within the maximum experimental measurement time t_e and the minimum time t_m, one can approximate Eq. 2.44 as [30, 37]

$$\langle \varphi_n^2(t) \rangle \simeq \frac{1}{\hbar^2 e^2} \left(\frac{\partial \Delta E}{\partial n_g}\right)^2 \int_{1/t_e}^{1/t_m} df \frac{\alpha t^2}{f}, \tag{2.45}$$

or

$$\langle \varphi_n^2(t) \rangle \simeq \frac{\alpha t^2}{\hbar^2 e^2} \left(\frac{\partial \Delta E}{\partial n_g}\right)^2 \ln\left(\frac{t_e}{t_m}\right), \tag{2.46}$$

which leads to the Gaussian dephasing factor

$$f_\varphi(t) = e^{-(t/T_\varphi)^2}. \tag{2.47}$$

Hence, the dephasing time T_φ is given by

$$\frac{1}{T_\varphi} = \sqrt{\frac{\alpha}{2\hbar^2 e^2} \ln\left(\frac{t_e}{t_m}\right)} \left|\frac{\partial \Delta E}{\partial n_g}\right|, \tag{2.48}$$

or

$$\frac{1}{T_\varphi} = \sqrt{\frac{\alpha}{2\hbar^2 e^2} \ln\left(\frac{t_e}{t_m}\right)} \frac{(4E_C)^2|1-n_g|}{\sqrt{[4E_C(1-n_g)]^2 + E_J^2}}. \tag{2.49}$$

For the dephasing at $n_g = 1$, one has to consider the second order fluctuation in energy ΔE [30]:

$$\delta(\Delta E) = \frac{1}{2}\frac{\partial^2 \Delta E}{\partial n_g^2}(\delta n_g)^2, \tag{2.50}$$

where

$$\frac{\partial^2 \Delta E}{\partial n_g^2} = \frac{(4E_C)^2}{\sqrt{[4E_C(1-n_g)]^2 + E_J^2}} - \frac{2(4E_C)^4(1-n_g)^2}{(\sqrt{[4E_C(1-n_g)]^2 + E_J^2})^3}. \tag{2.51}$$

At $n_g = 1$, this second order fluctuation is equal to $(4E_C)^2/E_J$. The rms deviation in n_g for $1/f$ charge noise is, [103]:

$$\begin{aligned} (\delta n_g)^2 &\approx \frac{1}{e^2}\int_{1/t_e}^{1/t_m} df \frac{\alpha}{f} \\ &= \frac{\alpha}{e^2}\ln\left(\frac{t_e}{t_m}\right). \end{aligned} \tag{2.52}$$

The corresponding rms phase noise [30] is then given by

$$\begin{aligned} \delta\varphi(t) &\approx \frac{1}{\hbar}\int_0^t \delta(\Delta E)\, dt \\ &= \frac{\alpha}{2e^2\hbar}\ln\left(\frac{t_e}{t_m}\right)\frac{(4E_C)^2}{E_J}\, t \end{aligned} \tag{2.53}$$

For $\delta\varphi(t) = 1$, the dephasing time T_φ at $n_g = 1$ is given by

$$\frac{1}{T_\varphi} = \frac{\alpha}{2e^2\hbar} \ln\left(\frac{t_e}{t_m}\right) \frac{(4E_C)^2}{E_J}. \tag{2.54}$$

If I assume a measurement bandwidth of 0.3 MHz or $t_e = (1/0.3)$ μs and $E_J/h = 6$ GHz or $t_m = (1/6)$ ns, then $\ln(t_e/t_m) \simeq 9.9$. Assuming the amplitude of charge noise $\sqrt{\alpha} \approx 10^{-3}$ e and $E_C/k_B = 0.3$ K, one expects a dephasing time $T_\varphi \simeq 310$ ns at $n_g = 1$.

2.6 Rabi Oscillations

In order to understand the dynamics of the qubit, the states of the qubit when it is driven sinusoidally should be examined through the time-dependent Schrödinger equation:

$$\hat{H} \left|\Psi\right\rangle = i\hbar \frac{\partial \left|\Psi\right\rangle}{\partial t}. \tag{2.55}$$

The qubit states can be written as

$$\left|\Psi(t)\right\rangle = c_g(t) e^{-iE_g t/\hbar} \left|g\right\rangle + c_e(t) e^{-iE_e t/\hbar} \left|e\right\rangle. \tag{2.56}$$

I will assume the driving harmonic wave has angular frequency ω, which is detuned from the qubit transition angular frequency ω_{01} by $\delta\omega$, so that

$$\omega = \omega_{01} + \delta\omega, \tag{2.57}$$

where $\omega_{01} = (E_e - E_g)/\hbar$. This harmonic wave causes a perturbation $\hat{V}(t)$ to the qubit Hamiltonian. Hence, the system Hamiltonian is given by

$$\hat{H} = \hat{H}_0 + \hat{V}(t), \tag{2.58}$$

where $\hat{H}_0$ is the unperturbed, or time-independent Hamiltonian.

The system Hamiltonian (Eq. 2.58) and states (Eq. 2.56) should satisfy the time-dependent Schrödinger equation, yielding two equations:

$$\dot{c_g}(t) = -\frac{i}{\hbar}\left(c_g(t)\left\langle g\right|\hat{V}(t)\left|g\right\rangle + c_e(t)\left\langle g\right|\hat{V}\left|e\right\rangle e^{-i\omega_{01}t}\right) \tag{2.59}$$

$$\dot{c_e}(t) = -\frac{i}{\hbar}\left(c_g(t)\left\langle e\right|\hat{V}\left|g\right\rangle e^{i\omega_{01}t} + c_e(t)\left\langle e\right|\hat{V}(t)\left|e\right\rangle\right). \tag{2.60}$$

To better understand the explicit form of $\hat{V}(t)$, we first consider a semi-classical situation in which the interaction between the harmonic wave and a qubit is due to an effective dipole interaction to the electric field [32]:

$$\hat{V}(t) = exE_x\cos\omega t, \tag{2.61}$$

where ex is the effective dipole moment of the qubit, which is aligned with the x-axis and E_x is the amplitude of the polarized electric field $\mathbf{E}(t) \equiv E_x\hat{x}\cos\omega t$. In this case, the perturbation matrix elements are given by

$$V_{ij}(t) \equiv \left\langle i\right|\hat{V}(t)\left|j\right\rangle = eE_x\cos\omega t\int \Psi_i^* x\Psi_j d^3x. \tag{2.62}$$

Due to the odd parity of x, $V_{g,g} = V_{e,e} = 0$. Therefore, the perturbation Hamiltonian is

$$\hat{V}(t) \;=\; \begin{pmatrix} 0 & eE_x\cos\omega t \\ eE_x\cos\omega t & 0 \end{pmatrix}, \tag{2.63}$$

where the dipole matrix elements $\left\langle g\right|\hat{V}(t)\left|e\right\rangle = \left\langle e\right|\hat{V}(t)\left|g\right\rangle = eE_x(e^{i\omega t} + e^{-i\omega t})/2$.

With these dipole matrix elements, Eqs. 2.59 and 2.60 can be re-expressed as

$$\dot{c_g}(t) = -\frac{i}{\hbar}\frac{eE_x}{2}\left(e^{i(\omega-\omega_{01})t} + e^{-i(\omega+\omega_{01})t}\right)c_e(t) \tag{2.64}$$

$$\dot{c_e}(t) = -\frac{i}{\hbar}\frac{eE_x}{2}\left(e^{-i(\omega-\omega_{01})t} + e^{i(\omega+\omega_{01})t}\right)c_g(t). \tag{2.65}$$

If we make the rotating wave approximation, we can neglect fast oscillating terms such as $\pm(\omega+\omega_{01})$. The time derivative of Eq. 2.65 then leads to

$$\ddot{c_e}(t) + i(\omega-\omega_{01})\dot{c_e}(t) + \left(\frac{eE_x}{2\hbar}\right)^2 c_e(t) = 0. \tag{2.66}$$

A trial solution of the form $e^{\xi t}$ yields the quadratic equation

$$\xi^2 + i(\omega-\omega_{01})\xi + \left(\frac{eE_x}{2\hbar}\right)^2 = 0. \tag{2.67}$$

And the solution to the equation is

$$\xi = -i\frac{\omega-\omega_{01}}{2} \pm i\frac{\Omega}{2}, \tag{2.68}$$

where

$$\Omega \equiv \sqrt{(\omega-\omega_{01})^2 + 4\left(\frac{eE_x}{2\hbar}\right)^2} \tag{2.69}$$

is the Rabi flopping angular frequency. On resonance, $\omega-\omega_{01}=0$ and Ω becomes $\Omega_R \equiv |eE_x|/\hbar$, which is called the bare Rabi flopping angular frequency.

The initial conditions of $c_g(0)=1$ and $c_e(0)=0$ lead to

$$|c_e|^2 = \left(\frac{\Omega_R}{\Omega}\right)^2 \sin^2(\Omega t/2) \tag{2.70}$$

In reality, the Rabi oscillation will be damped with a time constant T' [33, 34] that

is related to T_1 and T_2 by

$$\frac{1}{T'} = \frac{1}{2T_1} + \frac{1}{2T_2}. \tag{2.71}$$

We now consider explicitly the perturbation Hamiltonian of the CPB qubit (see Eq. 2.26). Instead of voltage noise $\delta n_g(t)$, one can apply the harmonic perturbation $n_g^{rf}\cos(\omega t)$, where n_g^{rf} is the driving amplitude for the qubit. Hence, the CPB Hamiltonian becomes:

$$\hat{H} = \frac{\Delta E}{2}\begin{pmatrix} -1 & 0 \\ 0 & 1 \end{pmatrix} + \frac{2E_C n_g^{rf}\cos(\omega t)}{\Delta E}\begin{pmatrix} 4E_C(1-n_g) & -E_J \\ -E_J & -4E_C(1-n_g) \end{pmatrix}. \tag{2.72}$$

At $n_g = 1$, the perturbation Hamiltonian reduces to

$$2E_C n_g^{rf}\cos(\omega t)\begin{pmatrix} 0 & -1 \\ -1 & 0 \end{pmatrix}. \tag{2.73}$$

Comparing Eq. 2.73 with Eq. 2.63 yields the bare Rabi angular frequency of the CPB qubit:

$$\Omega_R = \frac{2E_C|n_g^{rf}|}{\hbar}. \tag{2.74}$$

2.7 Spectral Density of Voltage Noise

Thermally driven electrical noise is common in low temperature experiments. Such noise can be quantified by the power spectral density. The spectral density of noise [29, 30] is defined as

$$S_f(\omega) = \frac{1}{2\pi}\int_{-\infty}^{\infty} d\tau e^{i\omega\tau}\langle f(\tau)f(0)\rangle, \tag{2.75}$$

where f can represent the current, charge, or voltage depending on the type of the noise source and τ is time. The spectrum is symmetric for classical noise; $S_f(-\omega) = S_f(+\omega)$ since there's no distinction between negative and positive frequency. In quantum mechanics, $f(\tau)$ and $f(0)$ are operators and do not commute necessarily [29]. Therefore, $S_f(-\omega) \neq S_f(+\omega)$. Negative frequency noise transfers energy from the noise source to the two-level system (exciting the two-level system), and positive frequency noise does the opposite (relaxing the two-level system) [29].

The spectral density of voltage noise from a resistor R at frequency f in thermal equilibrium at a temperature T is given by [29]

$$S_V(f) = \frac{2R\hbar\omega}{1 - e^{-\hbar\omega/k_BT}} \tag{2.76}$$

$S_V(f)$ from a 50 Ω resistor is plotted in Fig. 2.5 at temperatures of 0.1 K, 1 K, and 4K. Note that Eq. 2.76 is the "double-sided" power spectral density, which means $-\infty < \omega < \infty$. Much more commonly used is the single-sided spectrum with $\omega \geq 0$, which I am here calling the classical spectrum. For example, for $\hbar\omega \ll k_BT$, Eq. 2.76 reduces to $S_V = 2k_BTR$, whereas the conventional single-sided expression for Johnson noise is $S_V = 4k_BTR$.

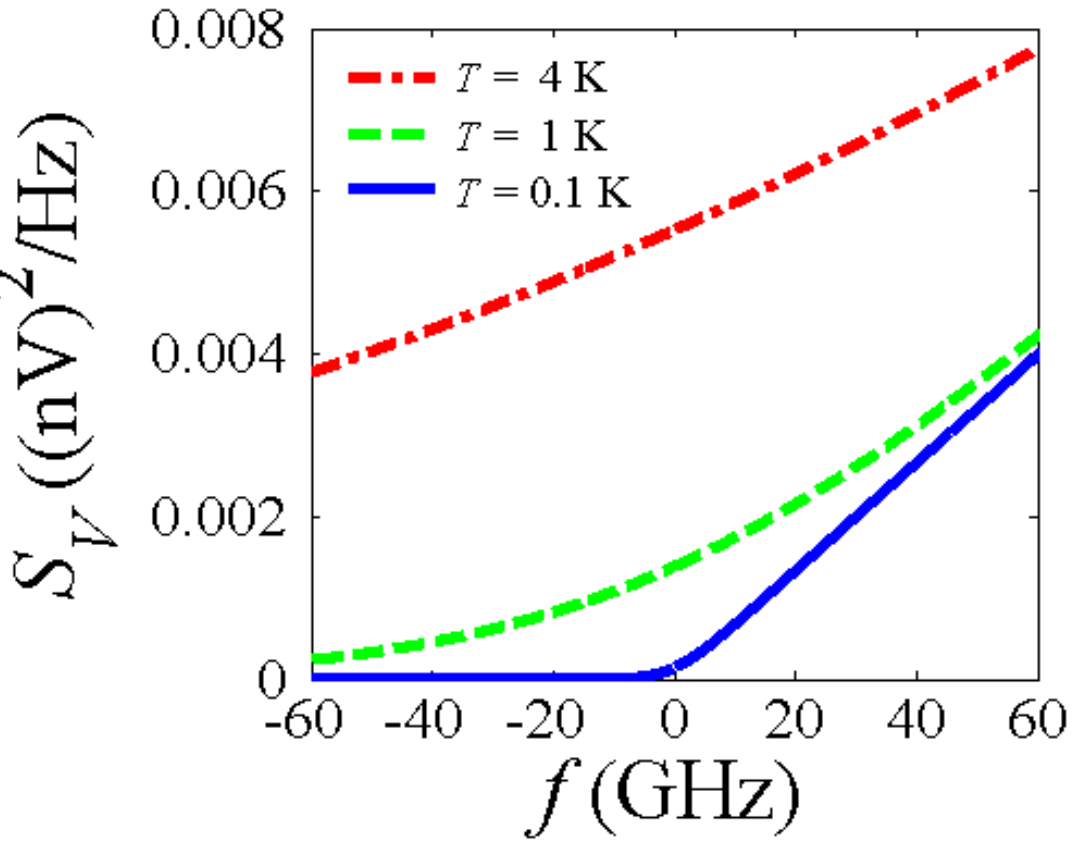

Figure 2.5: Spectral density of voltage noise. $S_V(f)$ at T=0.1 K (blue solid), 1 K (green dashed), and 4 K (red dashed) for a 50 Ω resistor.

Chapter 3

Dissipative Read-out Using a Superconducting Single Electron Transistor

3.1 Overview

In this chapter, I describe the basic physics of the superconducting single electron transistor (SET) and explain how I used a SET to read out the state of a CPB. Similar to a CPB, the SET has a small superconducting island that is coupled to two superconducting leads by two ultra-small tunnel junctions and the number of excess Cooper pairs or electrons is controlled by a gate voltage V_g, which is capacitively coupled to the island of the SET (see Fig. 3.1). Unlike the Cooper Pair Box, we apply a bias voltage V_{DS} across the two leads of the SET (the drain and source) and measure the tunneling current through the device.

There are a few general conditions for tunneling processes to occur in SETs; if these conditions are not met, an average tunneling current will not occur. First, the process must be energetically favorable. Second, the total process must conserve charge; *i.e.* when the cycle is complete the charge on the island must be the same as when it began. This second condition is not too difficult to satisfy for single electron tunneling but can be difficult to satisfy for Cooper-pair tunneling in superconducting SETs. The interplay of Cooper-pair and quasiparticle tunneling produces a very

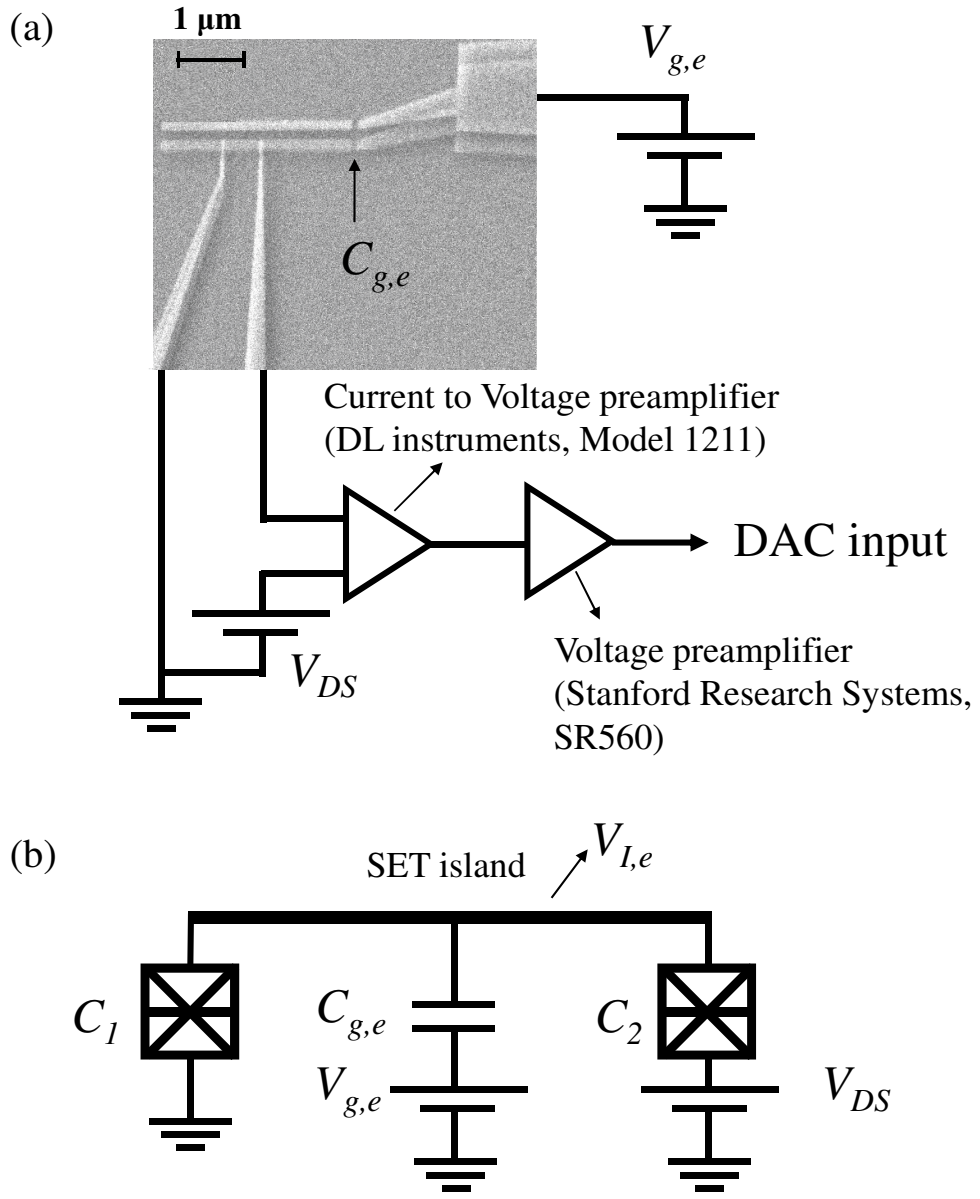

Figure 3.1: dc SET. (a) Schematic set up for dc SET. (b) Circuit schematic of a SET. C_1 and C_2 are the ultra-small junction capacitances. $C_{g,e}$ is the gate capacitance, $V_{g,e}$ is the gate voltage, and $V_{I,e}$ is the voltage on the island of the SET ("e" represents the electrometer). V_{DS} is the bias voltage applied to the junction C_2.

rich structure in a measurement of the tunneling current versus V_{DS} and V_g. I will not write down a master equation and work out the tunneling rates of these different processes in this thesis [30]. Instead, I will explain where we observe specific resonances in SETs, describe how we use these resonances during charge measurements, and finally show how we can perform fast measurements using an rf-SET.

3.2 dc SET

3.2.1 SET in the Normal State

To describe the general properties of tunneling in an SET, I begin by examining an SET in the normal state. Assume that initially there are n_e excess electrons on the island of the SET and a voltage V_{DS} is across one junction (C_2) [see Fig. 3.1 (b)]. The electrostatic energy of the SET island can be calculated using an approach that is similar to what was used for the CPB (see the section 2.2.2). One finds [12]

$$U = \frac{1}{2}C_{g,e}(V_{I,e} - V_{g,e})^2 + \frac{1}{2}C_1(V_{I,e} - 0)^2 + \frac{1}{2}C_2(V_{I,e} - V_{DS})^2, \tag{3.1}$$

where the parameters are explained in Fig. 3.1 (b) and $C_{g,e}V_{g,e} = n_e e$. With finite V_{DS}, electrons can tunnel through the junctions. When electrons tunnel and n_e goes to $n_e \pm 1$ through a junction, the change in the electrostatic energy is $(1/2 \pm n_e)e^2/C_{\sum,e}$, where $C_{\sum,e} = C_{g,e} + C_1 + C_2$ is the total capacitance of the SET island.

To find the free energy of the system, one needs to calculate the work done by the two voltage sources. When an electron tunnels through the junction C_j, the

work done by the voltage sources [12] is given by

$$W_j = -e\sum_i (V_j - V_i)\frac{C_i}{C_\Sigma}. \tag{3.2}$$

Therefore, the work done for an electron tunneling through the junction C_1 is $W_1 = e(C_{g,e}V_{g,e} + C_2V_{DS})/C_\Sigma$. And the work done for an electron tunneling through the junction C_2 is $W_2 = n_e e(C_{g,e}V_{g,e} - C_1V_{DS})/C_{\sum,e}$.

Then, the change in the free energy by an electron tunneling from n_e to $n_e \pm 1$ through the junction C_1 is given by

$$\Delta E_1^{\pm} = E_1(n_e \pm 1) - E_1(n_e), \tag{3.3}$$

where $E_1(n_e \pm 1) = U(n_e \pm 1) - (n_e \pm 1)\cdot W_1$ and $E_1(n_e) = U(n_e) - n_eW_1$. And one finds [12]

$$\Delta E_1^{\pm} = \frac{e^2}{C_{\sum,e}}\left[\left(\frac{1}{2} \pm n_e\right) \mp \frac{C_{g,e}V_{g,e} + C_2V_{DS}}{e}\right]. \tag{3.4}$$

In a similar way, one can find the change in the free energy due to an electron tunneling from n_e to $n_e \pm 1$ through the junction C_2 [12]:

$$\Delta E_2^{\pm} = \frac{e^2}{C_{\sum,e}}\left[\left(\frac{1}{2} \pm n_e\right) \mp \frac{C_{g,e}V_{g,e} - C_1V_{DS}}{e}\right]. \tag{3.5}$$

For such a tunneling process to be energetically favorable, the energy change should be less than zero. If the energy change is positive, then an average current will not flow and this is called "the Coulomb blockade effect".

For $\Delta E_1^{\pm} > 0$, one finds

$$e(n_e - 1/2) < C_2V_{DS} + en_{g,e} < e(n_e + 1/2), \tag{3.6}$$

and for $\Delta E_2^{\pm} > 0$,

$$e(n_e - 1/2) < -C_1 V_{DS} + e n_{g,e} < e(n_e + 1/2). \tag{3.7}$$

The corresponding Coulomb blockade regimes are plotted as gray boxes in Fig. 3.2 (a). If the two junctions have different capacitances, the shape of the area becomes asymmetric [see Fig. 3.2 (b)]. This kind of plot is generally called a "diamond map". Diamonds (gray areas) repeat by when $\Delta n_e = 1$ along $n_{g,e}$ and are degenerate at $n_{g,e} = \pm 1/2, \ \pm 3/2$, etc. Outside these diamonds, there is a higher current flow by single electron tunneling. One can also show that the current through the device is modulated along $n_{g,e}$ at a fixed V_{DS} with a periodicity of 1.

3.2.2 SET in the Superconducting State

The last section described single-electron tunneling in normal metal SET's. Tunneling in superconducting devices is profoundly changed because of Cooper-pair tunneling and quasiparticle-quasiparticle tunneling. Quasiparticle tunneling events in the superconducting SET can be understood by the "semiconductor model" [12], where tunneling transitions are all horizontal; *i.e.* they occur at constant energy after adjusting the relative levels of the Fermi energy μ in the two superconductors to account for the applied potential difference eV (see Fig. 3.3). For quasiparticle tunneling through one of the tunnel junctions at $T = 0$, the applied energy eV should be equal to or bigger than $2\Delta_g$, where Δ_g is the superconducting energy gap [see Fig. 3.3 (a)]. We can estimate the energy available during tunneling from the drain-source voltage across the SET junction capacitance. The portion of the total

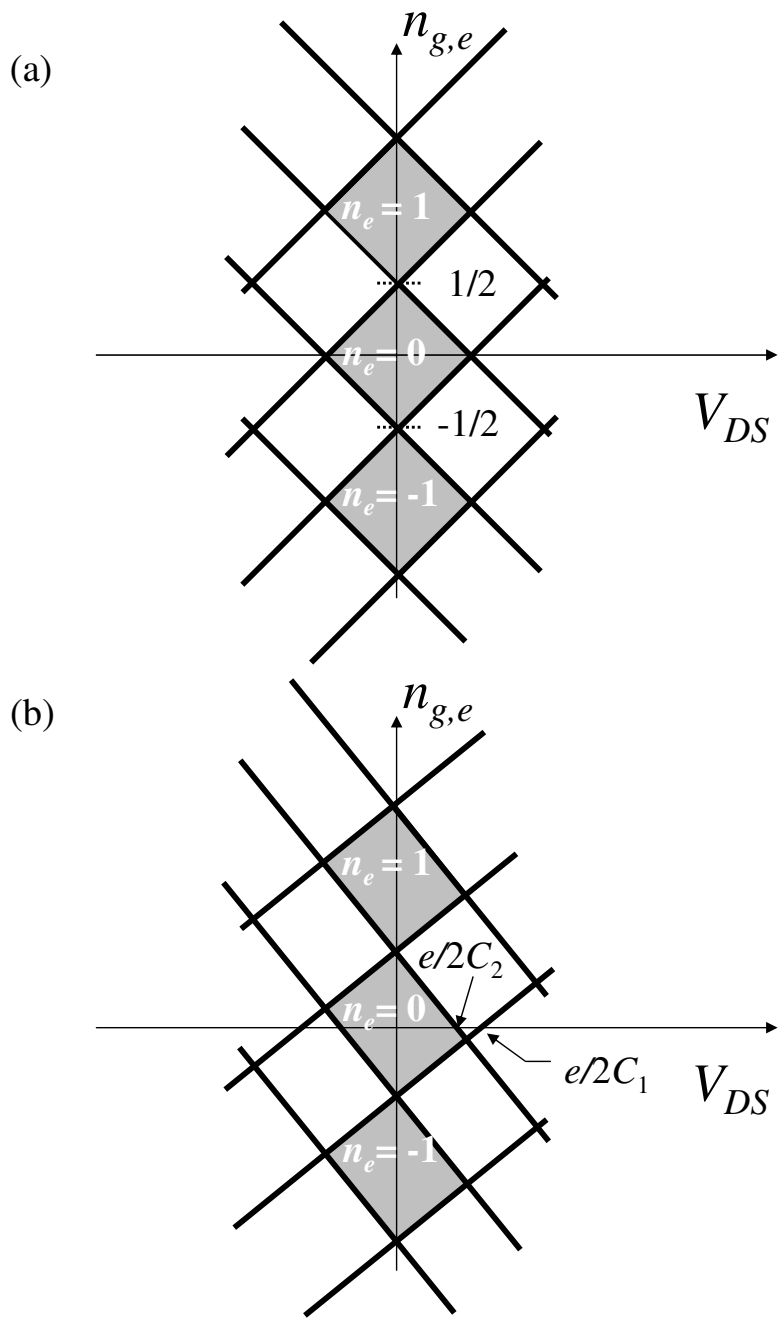

Figure 3.2: The Coulomb blockade area in a normal state SET. (a) The Coulomb blockade area is shown as gray boxes when $C_1 = C_2$. (b) The Coulomb blockade area becomes asymmetric when $C_1 \neq C_2$.

bias energy across each junction is $\kappa_1 eV_{DS}$ or $\kappa_2 eV_{DS}$ due to the voltage divider formed by the three capacitances, C_1, C_2, and $C_{g,e}$ (see Fig. 3.1), where

$$\kappa_1 = \frac{C_2}{C_{\sum,e}} \tag{3.8}$$

$$\kappa_2 = \frac{C_1 + C_{g,e}}{C_{\sum,e}}. \tag{3.9}$$

κ_i tells us the asymmetry between the two tunnel junctions in the SET; note that $\kappa_1 + \kappa_2$ is equal to 1.

For quasiparticle tunneling at $T = 0$, the available energy must be enough to break a Cooper pair into quasiparticles:

$$\kappa_i eV_{DS} \geq \Delta E_{n_e \to n_e+1} + 2\Delta_g, \tag{3.10}$$

where $\Delta E_{n_e \to n_e+1} = E_{n_e+1} - E_{n_e}$ is the change in the electrostatic energy due to a single quasiparticle tunneling on to the island of the SET and $E_{n_e} = E_{C.e}(n_{g,e} - n_e)^2$. We can rewrite Eq. 3.10 as

$$\kappa_i eV_{DS} \geq E_{C,e}(2n_e - 2n_{g,e} + 1) + 2\Delta_g. \tag{3.11}$$

In this range of V_{DS}, quasiparticle tunneling is energetically favorable. Eq. 3.11 is plotted as red lines in Fig. 3.4 (b).

For resonant tunneling of Cooper pairs through the SET, the free energy difference across two junctions should be zero [see Fig. 3.3 (b)]. Thus, the applied energy must match the change in the electrostatic energy due to a Cooper pair tunneling. Thus

$$2\kappa_i eV_{DS} = \Delta E_{n_e \to n_e+2}, \tag{3.12}$$

(a)

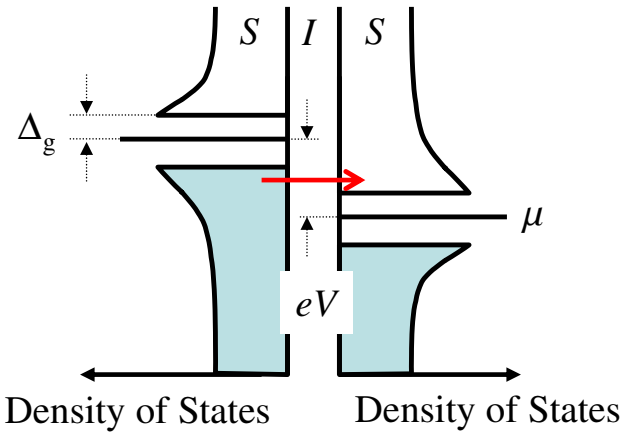

(b)

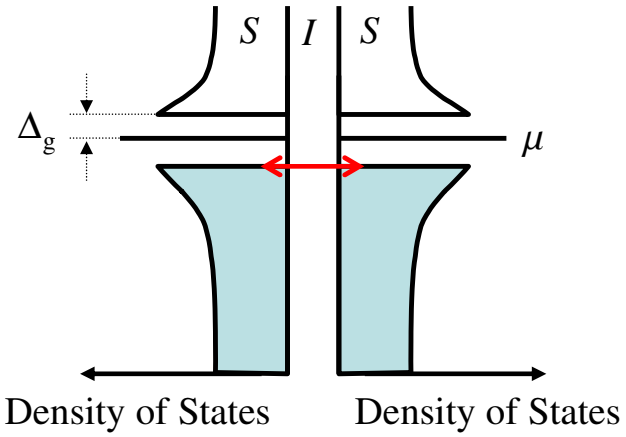

Figure 3.3: Semiconductor model for SIS tunneling at $T = 0$. Density of states vs. energy level of a superconducting/insulating/superconducting (SIS) tunnel junction. (a) quasiparticle tunneling (b) Cooper pair tunneling. Blue area is occupied by quasiparticles.

where $\Delta E_{n_e \to n_e+2} = E_{n_e+2} - E_{n_e}$. We can rewrite this as

$$\kappa_i e V_{DS} = E_{C,e}(2n_e - 2n_g + 2). \tag{3.13}$$

Note this is a resonant process and hence Eq. 3.13 is an equality, unlike the threshold process associated with quasiparticle tunneling (Eq. 3.11). Quasiparticles can carry extra energy as kinetic energy but a Cooper-pair cannot. Eq. 3.13 is plotted as white lines in Fig. 3.4 (b).

Figure 3.4 (a) shows a false color plot of the measured current through a superconducting SET versus V_{DS} and $n_{g,e}$. The schematic of the setup used for measurement is shown in Fig. 3.1 (a). The current through the device "SET1" was measured using a current-to-voltage preamplifier (DL instruments, Model 1211) in battery mode. This voltage was in turn amplified by a low-noise voltage preamplifier (Stanford Research Systems, Model SR560) in battery mode. These amplifiers were set up close together inside the shielded room. A DAC (Data Acquisition Card, National Instruments, PCI-6259) was used to adjust V_{DS} and $V_{g,e}$. I stepped V_{DS} typically from -1 mV to 1 mV while monitoring the amplified voltage at each V_{DS} through the DAC. Then, I stepped $V_{g,e}$, repeating the same procedure.

From the map of the SET current versus V_{DS} and $n_{g,e}$, one can extract the superconducting energy gap Δ_g, the SET charging energy $E_{C,e}$, and the junction resistance in the normal state [see Fig. 3.5 (a)]. When V_{DS} goes above $4\Delta_g/e$ or below $-4\Delta_g/e$, quasiparticle current starts to flow. One can determine the superconducting energy gap Δ_g from these V_{DS}. Once V_{DS} is large enough for quasiparticle-quasiparticle tunneling, the current becomes proportional to V_{DS}. One can also

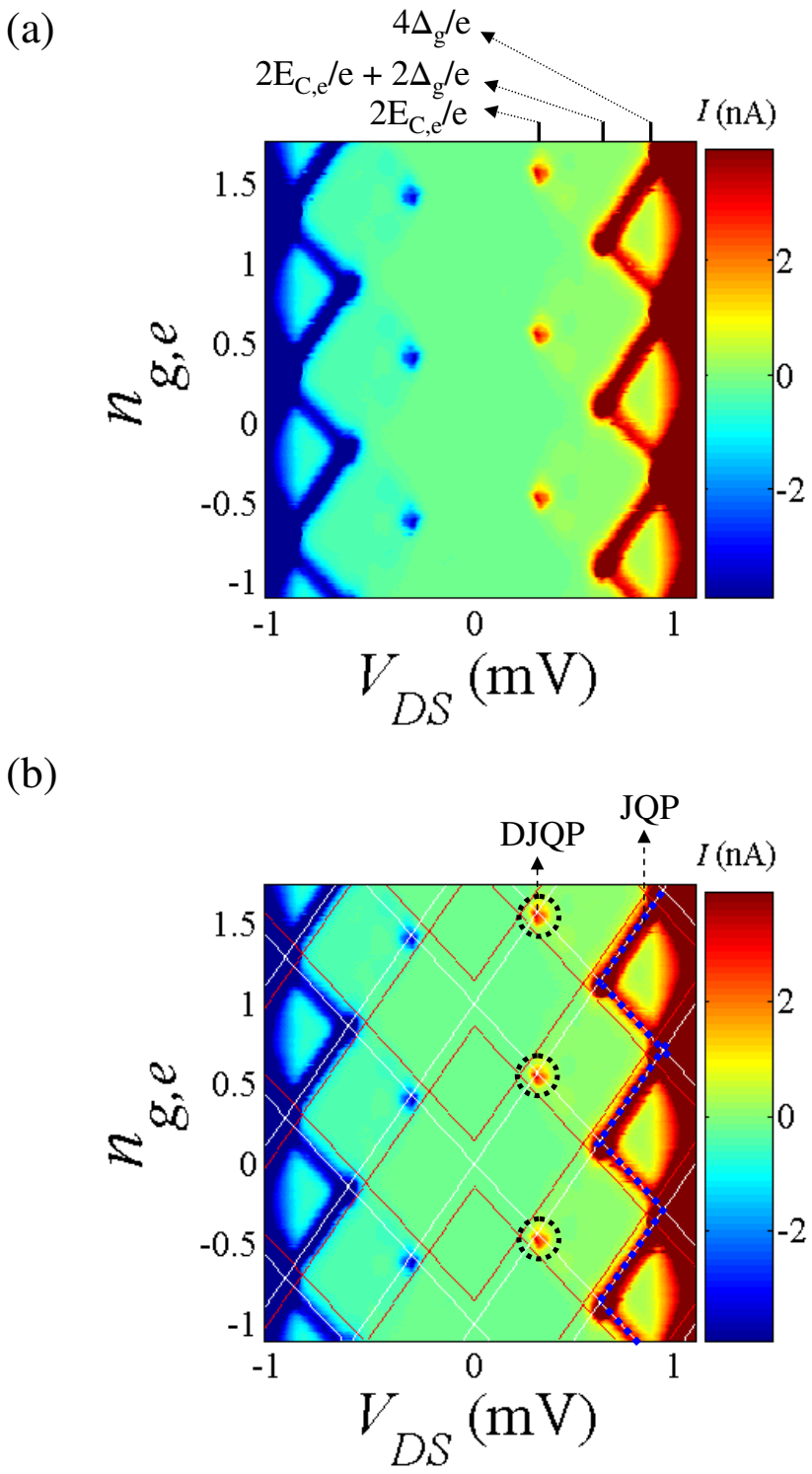

Figure 3.4: dc-SET diamond map of device "SET1". (a) Measured current through a superconducting SET versus V_{DS} and $n_{g,e}$, and (b) same as (a) with predicted tunneling process: quasiparticle tunneling (red lines) from Eq. 3.11 and Cooper pair tunneling (white lines) from Eq. 3.13.

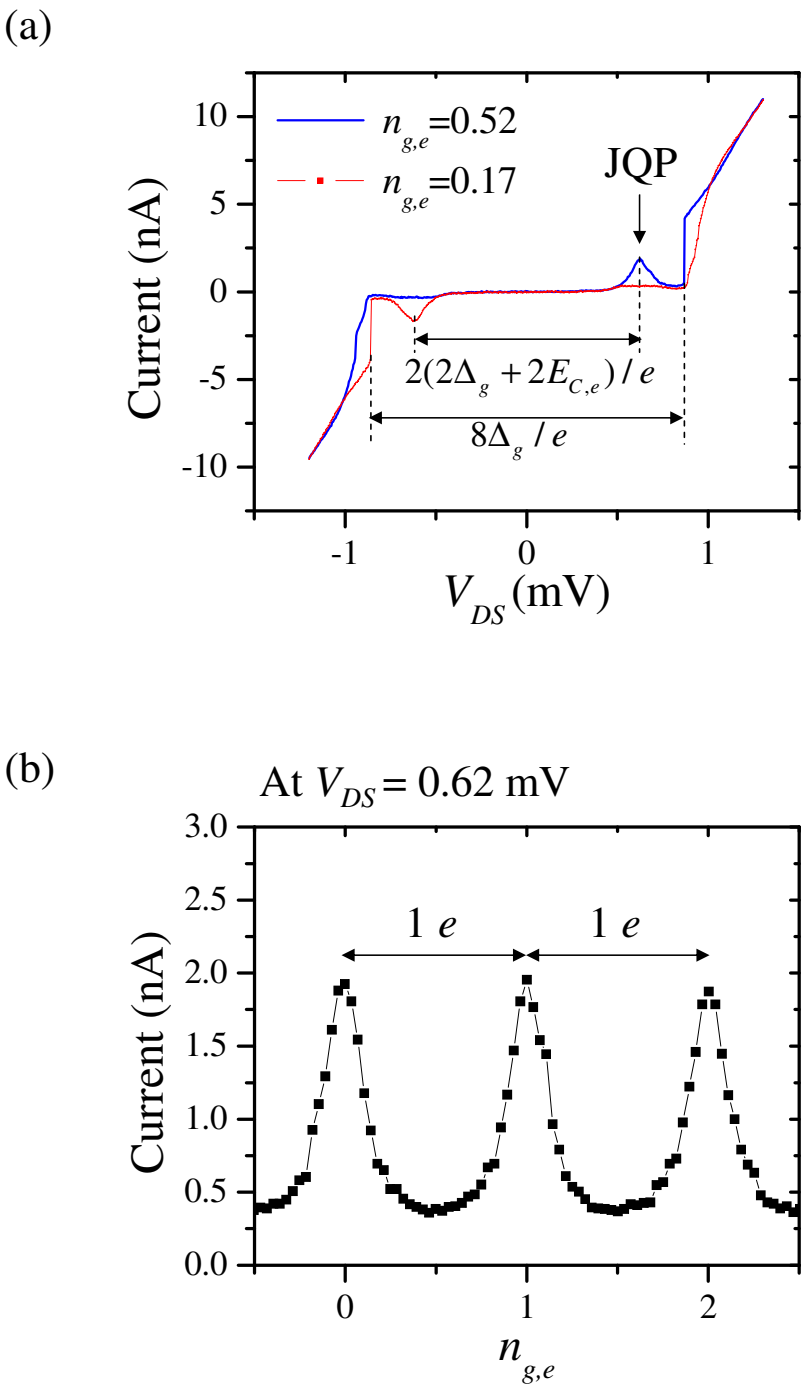

Figure 3.5: Line cuts of SET diamond map of device "SET2". (a) Line cut at gate voltages of $n_{g,e} = 0.17$ and $n_{g,e} = 0.52$ showing JQP peak. (b) Line cut at drain-source voltage $V_{DS} = 0.62$ mV showing JQP peak. This is also called the "transfer function" of the dc SET.

extract the tunneling resistance R_{SET} of the two junctions in series from the slope of the current versus V_{DS} characteristic [see Fig. 3.5 (a)]. Table 3.1 shows the parameters I extracted from the diamond map of two devices.

Some of the tunneling events in the diamond maps of the superconducting SET involve sequential events composed of quasiparticle and Cooper pair tunneling through the SET junctions. Noticeable currents within $\pm 4\Delta_g$ are results of cycles, such as the Josephson quasiparticle (JQP) process and the double Josephson quasiparticle (DJQP) process [72].

The JQP process shown in Fig. 3.6 (a) involves a Cooper-pair tunneling first onto the SET island through one junction (e.g. junction 2). Then, two quasiparticle tunneling events follow in sequence, with the quasiparticles tunneling off the SET island through the other junction (e.g. junction 1). Since quasiparticle tunneling is a threshold process and pair tunneling is a resonant process, the JQP cycle will appear along white lines between $eV_{DS} = 2E_{C,e} + 2\Delta_g$ and $eV_{DS} = 4\Delta_g$, and is highlighted with a blue dashed line in Fig. 3.4 (b).

The DJQP process shown in Fig. 3.6 (b) involves a Cooper pair tunneling first onto the SET island through one junction (e.g. junction 2). Then, one quasiparticle tunnels off of the SET island through the other junction (e.g. junction 1). Next, a Cooper pair tunnels off of the SET island through junction 1. Finally, one quasiparticle tunnels onto the SET island through junction 2 to return the charge to its initial state. For this process, two Cooper pair tunneling events occur at the intersection of two white lines; e.g. $eV_{DS} = 2E_{C,e}$ and $n_{g,e} = 1/2$, which can be found using Eq. 3.12 when $\Delta E_{n_e=-1\rightarrow+1}$ and $\Delta E_{n_e=+2\rightarrow 0}$. Also, two quasiparticle tunnel-

Table 3.1: Parameters of two SET devices measured at 40 mK as extracted from measurements. A subscript "e" and "b" represent the electrometer and CPB, respectively (see Fig. 3.15).

Parameters	device "SET1"	device "SET2"
Δ_g	214 μeV	214 μeV
κ_1	0.57	0.58
κ_2	0.43	0.42
R_{SET}	195 kΩ	64 kΩ
$E_{C,e}$	156 μeV	103 μeV
$C_{\Sigma,e}$	0.5 fF	0.76 fF
$C_{g,e}$	7.6 aF	17.7 aF
$C_{g,eb}$	1.21 aF	3.92 aF
$C_{C,be}$	10 aF	8.5 aF
$C_{g,be}$	3.1 aF	2.45 aF
E_C/k_B	0.77 K	0.58 K
C_Σ	1.2 fF	1.57 fF
C_g	10.6 aF	6.5 aF

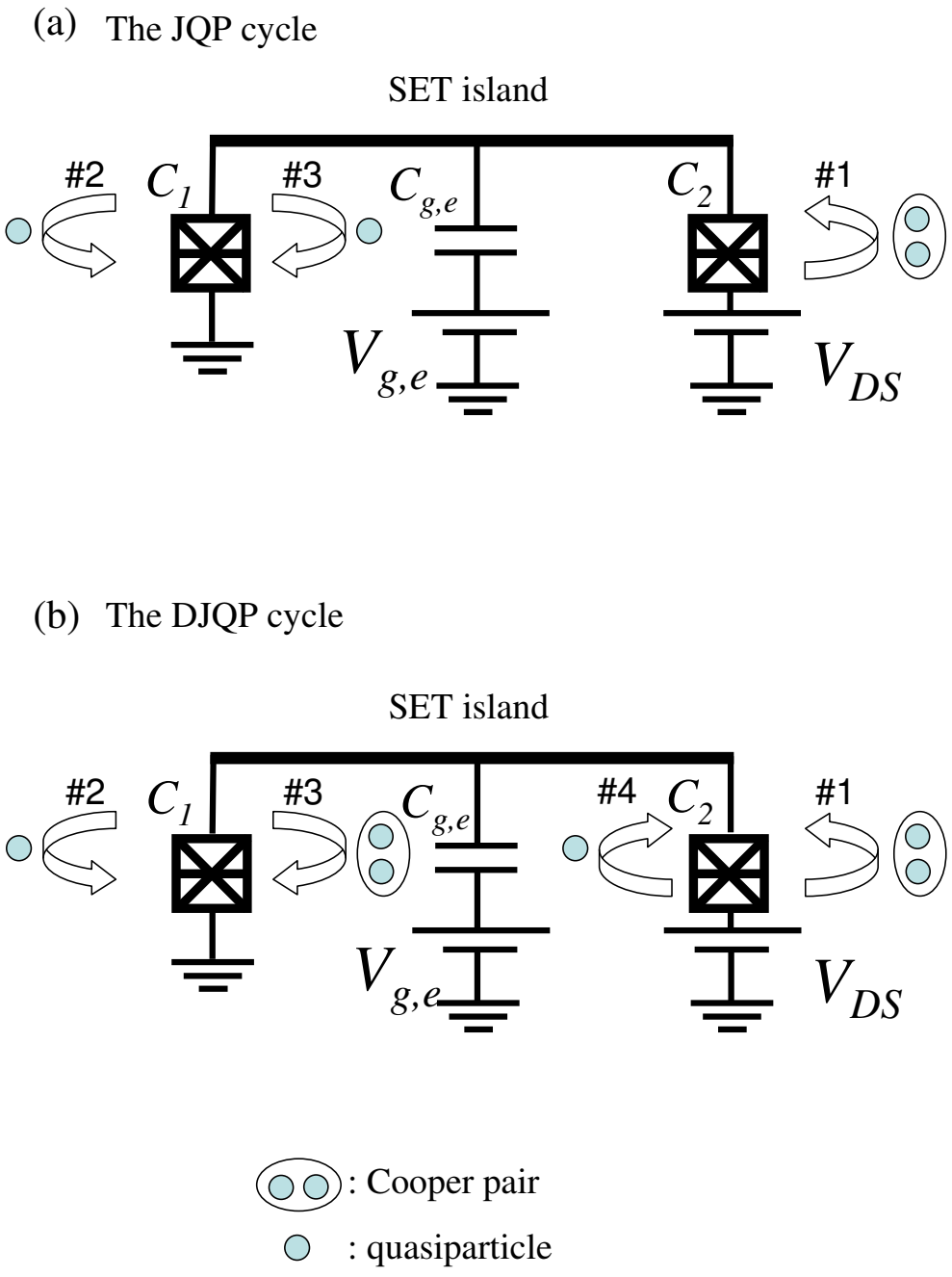

Figure 3.6: Schematics of tunneling processes in a superconducting SET. (a) The JQP cycle. The sequence of the process is #1 → #2 → #3 → #1 → ..... (b) The DJQP cycle.

ing events occur at the intersection of two red lines; e.g. $eV_{DS} = -4E_{C,e} + 4\Delta_g$ and $n_{g,e} = 1/2$, which can be found from two equations using Eq. 3.10 when $\Delta E_{n_e=+1\rightarrow+2}$ and $\Delta E_{n_e=0\rightarrow-1}$. Since quasiparticle tunneling is a threshold process and Cooper pair tunneling is a resonant process, the DJQP cycle will occur at $eV_{DS} = 2E_{C,e}$ above $eV_{DS} = -4E_{C,e} + 4\Delta_g$ [see Fig. 3.4 (b)]. This suggests that the DJQP is observable when $E_{C,e} > 2\Delta_g/3$. For example, device "SET2" had a charging energy of $E_{C,e} = 103$ μeV, which is smaller than $2\Delta_g/3$ and it did not show a DJQP peak (see Table 3.1). Note that all of the processes I have described involve some quasiparticle tunneling and so the current is periodic in $n_{g,e}$ with a period of one [see Fig. 3.5 (b)].

As figures 3.4 and 3.5 show, the current through my SETs is only a few nA for the DJQP and JQP process. On the other hand, these processes are relatively sharp in $n_{g,e}$ and hence very sensitive to changes in the electrostatic environment. Thus these bias points are a good place to use the superconducting SET as a sensitive electrometer.

3.3 rf-SET

One disadvantage of using a dc SET is that it has a small bandwidth when connected to a 50 Ω cable; the capacitance from a typical length of cable is on the order of 1 nF. Assuming the SET has a junction resistance of 100 kΩ, the measurement bandwidth would be $\Delta f = 1/2\pi RC \approx 1.5$ kHz. Such a small bandwidth will prevent fast measurements required for qubits. To overcome this limitation,

Schoelkopf *et al.* developed the rf-SET [14] and achieved bandwidths on the order of 100 MHz.

The basic idea of the rf-SET is to transform the high impedance of the SET to 50 Ω at a particular frequency (f_0) using an LC tank circuit. The resonance is then measured via the reflectance from the circuit at f_0 (see Fig. 3.7). If the effective impedance of the SET changes, this will change the impedance of the total circuit, hence changing the reflectance of the circuit.

In designing the rf-SET, specifically the capacitance and inductance of the tank circuit, there are two criteria we want to achieve:

1. we want to specify the resonant frequency.

2. we want the impedance to be 50 Ω on resonance.

For this calculation, we will assume the SET is simply a resistor R_{SET}. The impedance of the rf-SET circuit (see Fig. 3.7) is then given by

$$Z(\omega) = i\omega L_{tank} + \frac{1}{i\omega C_{tank} + \dfrac{1}{R_{SET}}}. \tag{3.14}$$

If $R_{SET} \to \infty$, the resonance frequency ω_0 can be approximated as

$$\omega_0 \simeq \frac{1}{\sqrt{L_{tank} C_{tank}}}. \tag{3.15}$$

The impedance at the input of the tank circuit at the resonance frequency is given by

$$Z(\omega_0) = \frac{R_{SET}}{1 + (\omega_0 R_{SET} C_{tank})^2}. \tag{3.16}$$

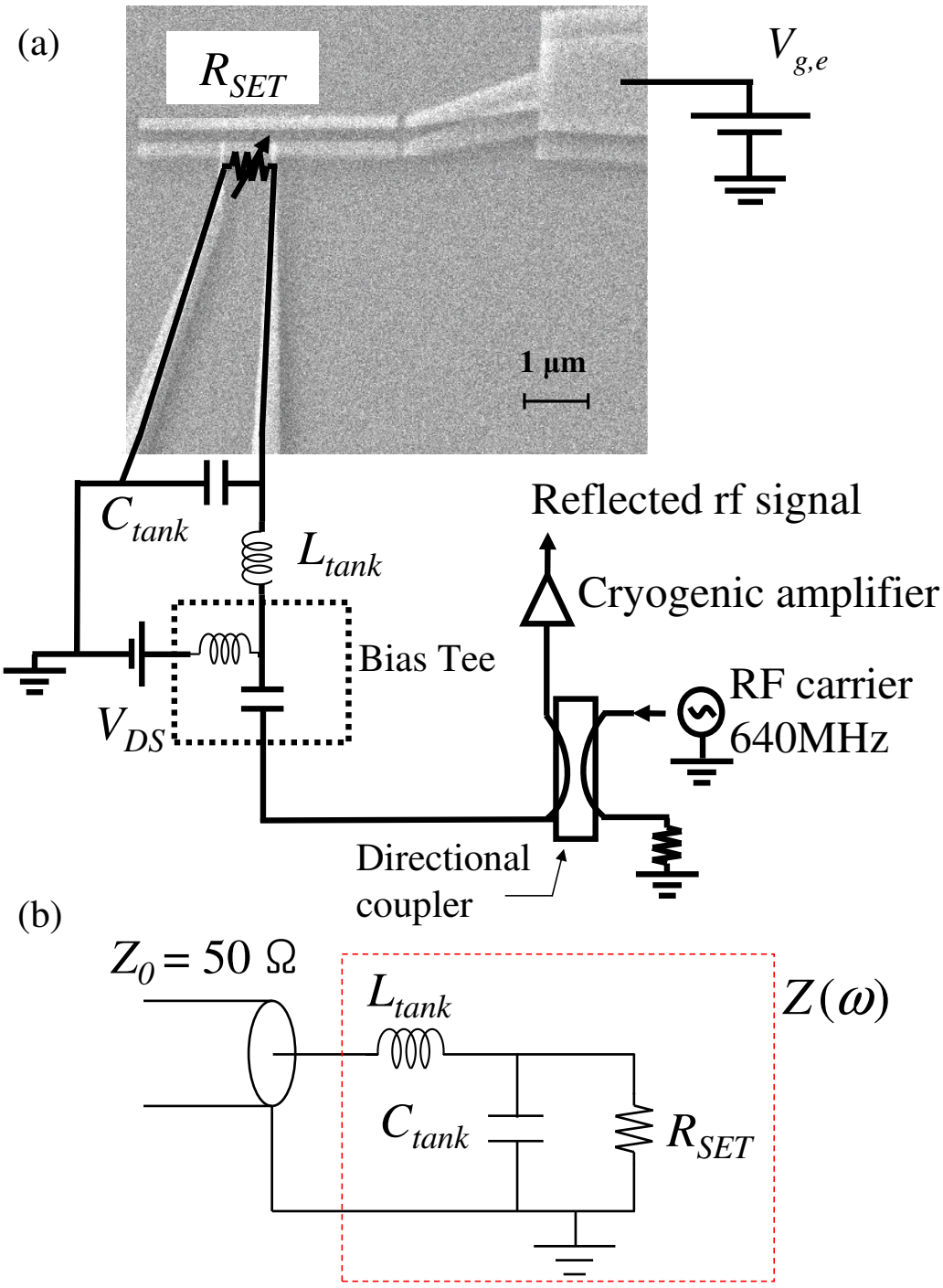

Figure 3.7: Schematic of the rf-SET. (a) Schematic of rf-SET with SEM image of SET. (b) Schematic of rf-SET tank circuit. R_{SET} is the resistance of the two junctions of the SET. $Z(\omega)$ represents the impedance of the rf-SET.

For $Q = \omega_0 RC \gg 1$, one finds Eq. 3.16 reduces to

$$Z(\omega_0) \simeq \frac{1}{R_{SET}(\omega_0 C_{tank})^2}. \tag{3.17}$$

If we set $Z(\omega_0) = Z_0 = 50\ \Omega$, then

$$C_{tank} = \frac{1}{\omega_0 \sqrt{R_{SET} Z_0}}. \tag{3.18}$$

For a resonance frequency of 640 MHz and $R_{SET} = 50\ \mathrm{k}\Omega$ to be matched to $Z_0 = 50\ \Omega$, one needs $C_{tank} = 157$ fF from Eq. 3.18, and $L_{tank} = 394$ nH from Eq. 3.15.

For my rf-SET, an rf signal (640 MHz from Agilent E4426B) was sent down to a directional coupler mounted on the mixing chamber of a dilution refrigerator (see section 3.5 and Fig. 3.12). To provide both a dc bias (V_{DS}) and the rf bias to the SET, I used a bias-T [Minicircuit, see Figs. 3.7 (a) and 3.12]. The LC tank circuit, which consists of a spiral inductor and an interdigitated capacitor, is shown in Figs. 3.7 (b) and 3.9. The rf reflectance from the SET island was measured at the resonance frequency (640 MHz) while the SET was dc biased at the JQP or DJQP resonance with the gate of the electrometer tuned to maximize the sensitivity to charge changes [72]. The resonance frequency can also be measured by looking at the shot noise from the SET as it is filtered through the tank circuit. The rf signal from the rf-SET was reflected back to the directional coupler and amplified by a cryogenic amplifier at 4 K. After another rf-amplifier at room temperature, the reflected signal was combined with a local oscillator signal at a mixer for a homodyne measurement. The mixer output was amplified by a low-noise voltage preamplifier and recorded.

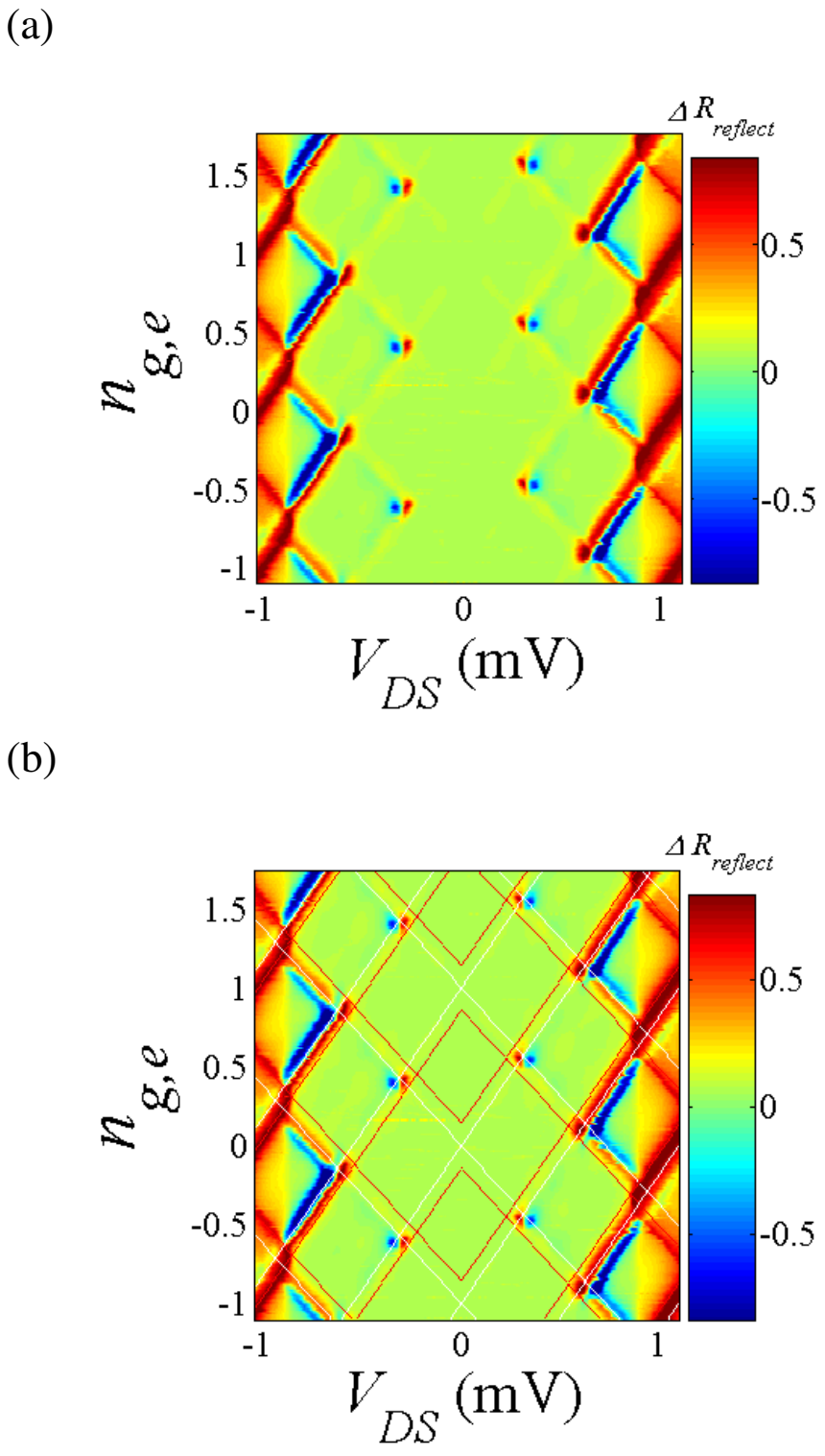

Figure 3.8: rf-SET diamond map of device "SET1". (a) Measured rf-reflectance through a superconducting SET versus V_{DS} and $n_{g,e}$. (b) Same as (a) with predicted tunneling process: quasiparticle tunneling (red lines) from Eq. 3.11 and Cooper pair tunneling (white lines) from Eq. 3.13. Compare with Fig. 3.4 for corresponding dc maps.

Figure 3.8 shows the rf reflectance as a function of V_{DS} and gate voltage for device "SET1". A DAC (Data Acquisition Card, National Instruments, PCI-6259) was used to sweep V_{DS} and $V_{g,e}$. I stepped V_{DS} from -1 mV to 1 mV while monitoring the amplified mixer output at each V_{DS} with the DAC. Then, I stepped $V_{g,e}$, repeating the same procedure. Since there was a small rf signal on top of V_{DS}, the measured rf reflectance was the dithered current signal, or the derivative of the I-V curve. We could also sweep $V_{g,e}$ up to a few kHz by using a digital oscilloscope (Tektronix, TDS 3014B) instead of the DAC to take the data.

3.4 Device Fabrication

The SETs I used were fabricated at the Jet Propulsion Laboratory (JPL) by Matt Shaw and Justin Schneiderman in Pierre Echternach's group [42, 43]. They patterned the tank circuit and the coplanar wave guide (see Fig. 3.9) using standard lift-off photolithography on a single-crystal quartz substrate. They used a superconducting Al/Ti/Au trilayer deposited in an electron-beam evaporator for the superconducting films of the tank circuit. The SET and the CPB were formed together on top of the trilayer. They used electron beam lithography and standard double-angle evaporation of Al with an oxidation step to form an AlO_X tunnel barrier between the two Al layers [71]. A bilayer of MAA-MMA copolymer and ZEP520 was used as the electron beam resist. I present a detailed description of the fabrication in Chapter 5.

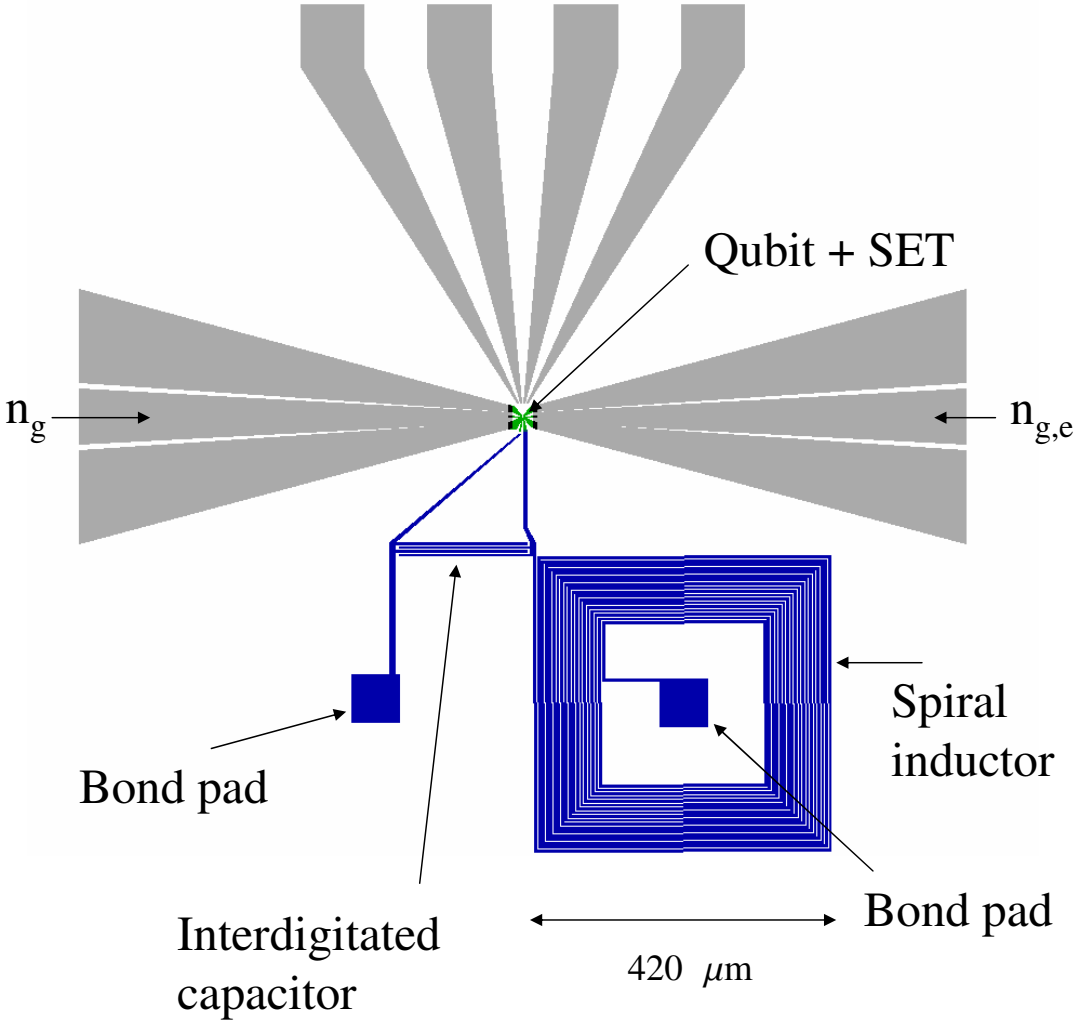

Figure 3.9: L-edit image of the tank circuit. Gray color represents the coplanar waveguide. Green area is for the e-beam fabrication. Blue colored area shows the interdigitated capacitor and the spiral inductor for the tank circuit.

3.5 Dilution Refrigerator Setup

A dilution refrigerator uses a mixture of He-3 and He-4 to reach mK temperatures. Our Oxford Instruments model 100 dilution refrigerator has a cooling power of 100 μW at 100 mK (see Fig. 3.11). I achieved a typical base temperature of 40 mK for the rf-SET measurements of the CPB. The refrigerator has different temperature stages: 300 K, 4 K, 1.5 K, 0.6 K, and 40 mK from the top of the fridge to the cold stage. Since we were performing high frequency spectroscopy (up to 50 GHz) on the qubit, we used coaxial cables that were not lossy. If we just ran a microwave cable from room temperature to the mixing chamber, black body noise from room temperature would create a number of deleterious effects, including exciting the qubit.

To reduce or remove black body radiation, we used power attenuators at various temperatures in the refrigerator, with the goal of reducing the spectral density of noise to that corresponding to the base temperature of the refrigerator. For this work, we had a 10 dB attenuator at 4 K, 20 dB on the still at 0.6 K, and another 10 dB on the mixing chamber [see Figs. 3.10 (b) and 3.12]. In this case, the power spectral density of the voltage noise at the cold end of the transmission line will be

$$S_V(f, T_3 = 0.03K) + \alpha_3 S_V(f, T_2 = 0.6K) + \alpha_3\alpha_2 S_V(f, T_1 = 4K) + \alpha_3\alpha_2\alpha_1 S_V(f, T_0 = 300K), \tag{3.19}$$

where

$$S_V(f) = \frac{2R\hbar\omega}{1 - e^{-\hbar\omega/k_B T}}. \tag{3.20}$$

Here $R = 50\ \Omega$ and α_i is the attenuation of the attenuator at temperature T_i. Eq. 3.19 is plotted in Fig. 3.10 (a) as a black dotted curve with $\alpha_1 = \alpha_3 = 10^{-1}$ for

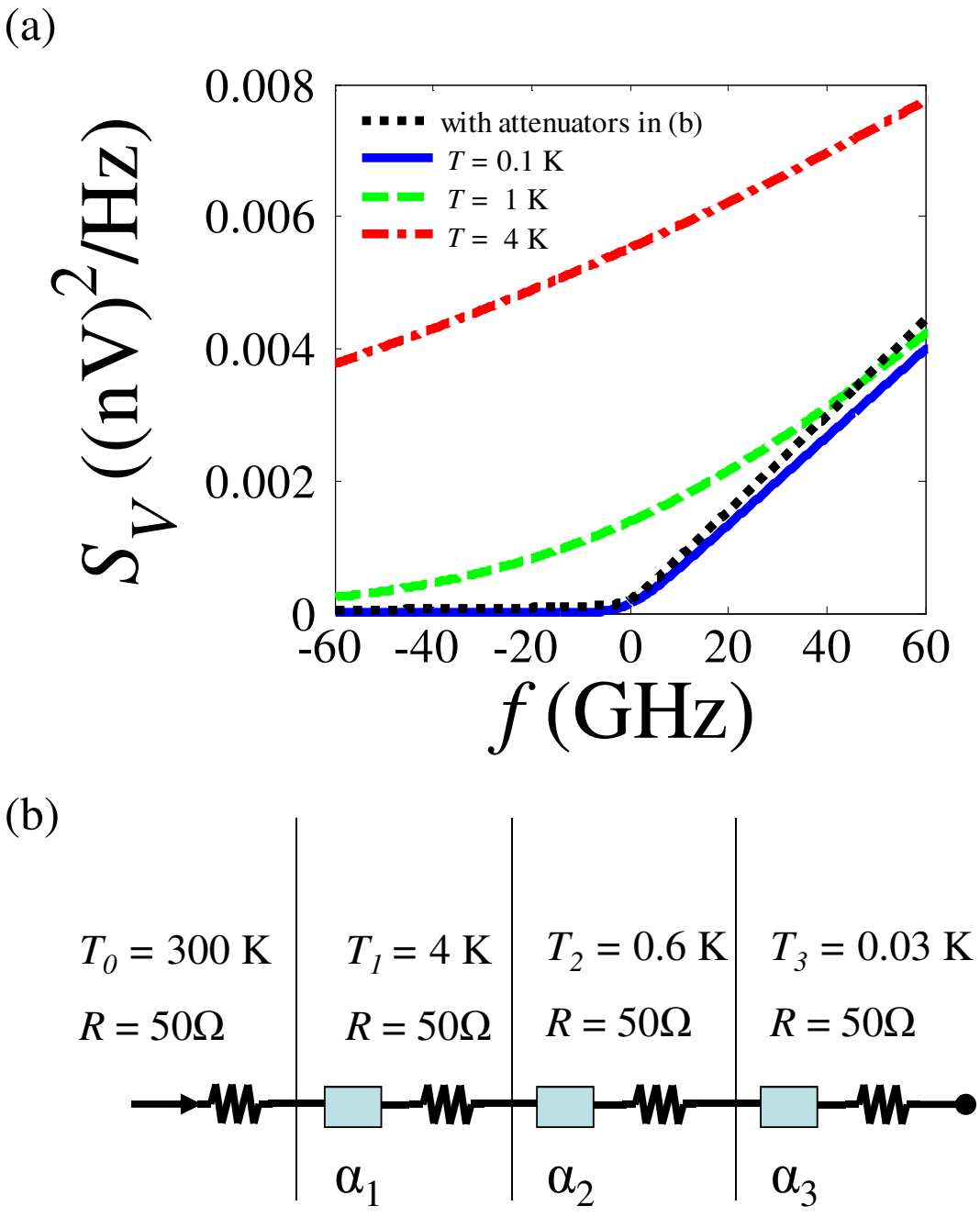

Figure 3.10: Power spectral density of voltage noise. (a) $S_V(f)$ at T=0.1 K (blue solid), 1 K (green dashed), and 4 K (red dashed) for a 50 Ω resistor. The total $S_V(f)$ with attenuators from room temperature to the base temperature is shown as black dotted curve. (b) Coax cables with 50 Ω impedance attenuators at different temperature stages. For a black dotted curve in (a), $\alpha_1 = \alpha_3 = 10^{-1}$ for the 10 dB attenuators and $\alpha_2 = 10^{-2}$ for the 20 dB attenuator.

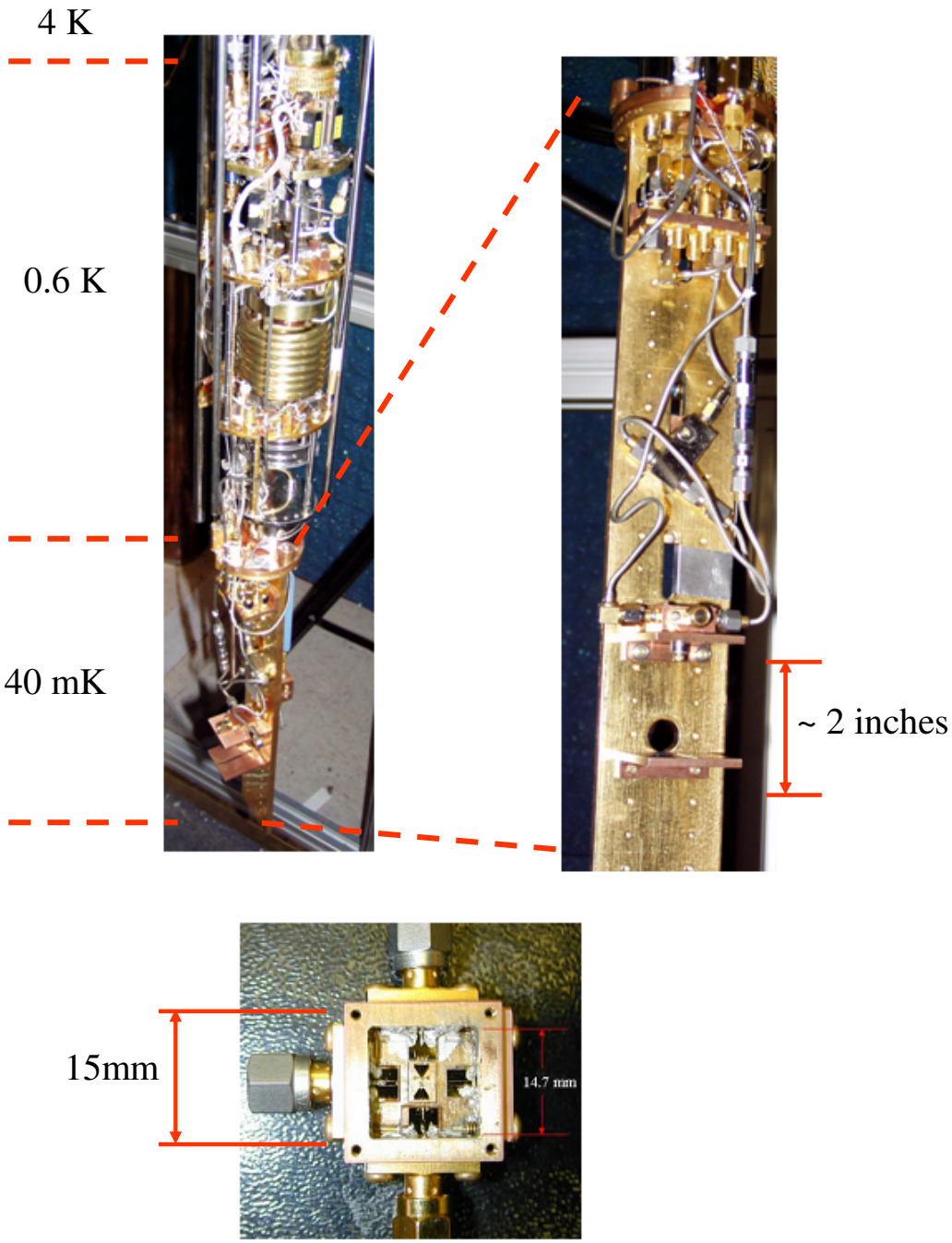

Figure 3.11: Images of the dilution refrigerator and sample holder.

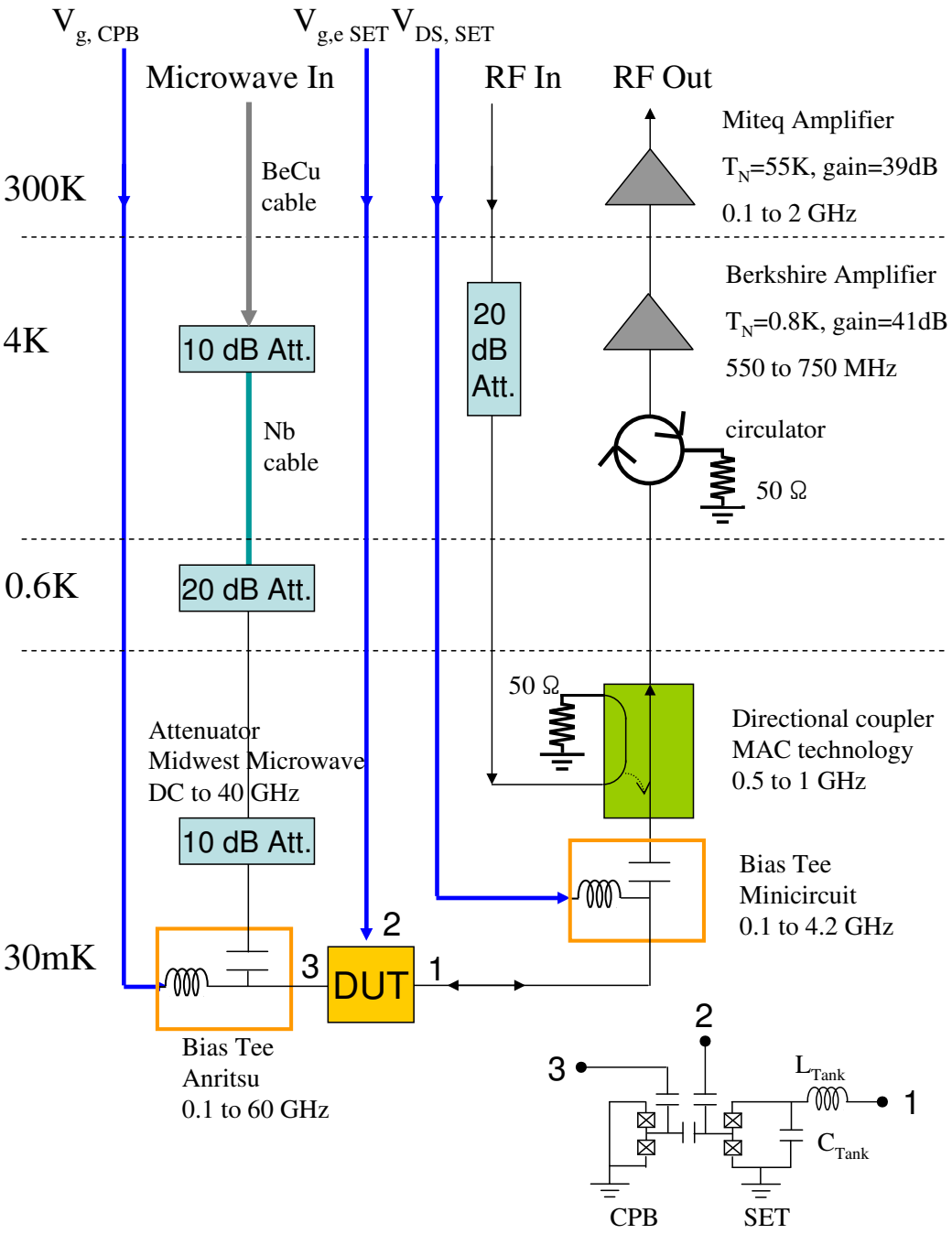

Figure 3.12: Schematic diagram of the wiring setup inside the refrigerator for rf-SET measurement of a CPB. dc cables are shown in blue. DUT means Device Under Test and its schematic is in the lower right-hand corner.

the 10 dB attenuators and $\alpha_2 = 10^{-2}$ for the 20 dB attenuator. Although the cable is connected to room temperature, Fig. 3.10 shows that the spectral density in this set-up reaches the spectral density of noise at about 0.1 K and is compared with the spectral density of noise at 1 K (dashed green curve) and 4 K (dashed red curve).

3.6 Shot Noise from the SET

One way that I characterized our rf-SET and the measurement set-up was by measuring the shot noise in the SET. This allows us to find the resonance frequency and measure the gain and noise temperature of our system. The idea is that the SET produces classical shot noise $S_I = 2e\eta I$, where I is a current through the SET and η is 0.5 for large drain-source voltages [44]. This noise is white up to the bandwidth of the SET.

The impedance $Z_{tank}(\omega)$ at the input of the tank circuit was given by Eq. 3.14. Given a current I_{DC} through the tank circuit [see Fig 3.13 (a)], the voltage V_{tank} at the input of the tank circuit is

$$V_{tank} = I_{DC} Z_{tank}. \tag{3.21}$$

The impedance of the SET junctions R_{SET} and the capacitance C_{tank} is given by

$$Z_{RC} = \frac{1}{\frac{1}{R_{SET}} + i\omega C_{tank}}. \tag{3.22}$$

The voltage drop V_{RC} across R_{SET} and C_{tank} is given by

$$V_{RC} = \frac{V_{tank}}{Z_{tank}} Z_{RC}. \tag{3.23}$$

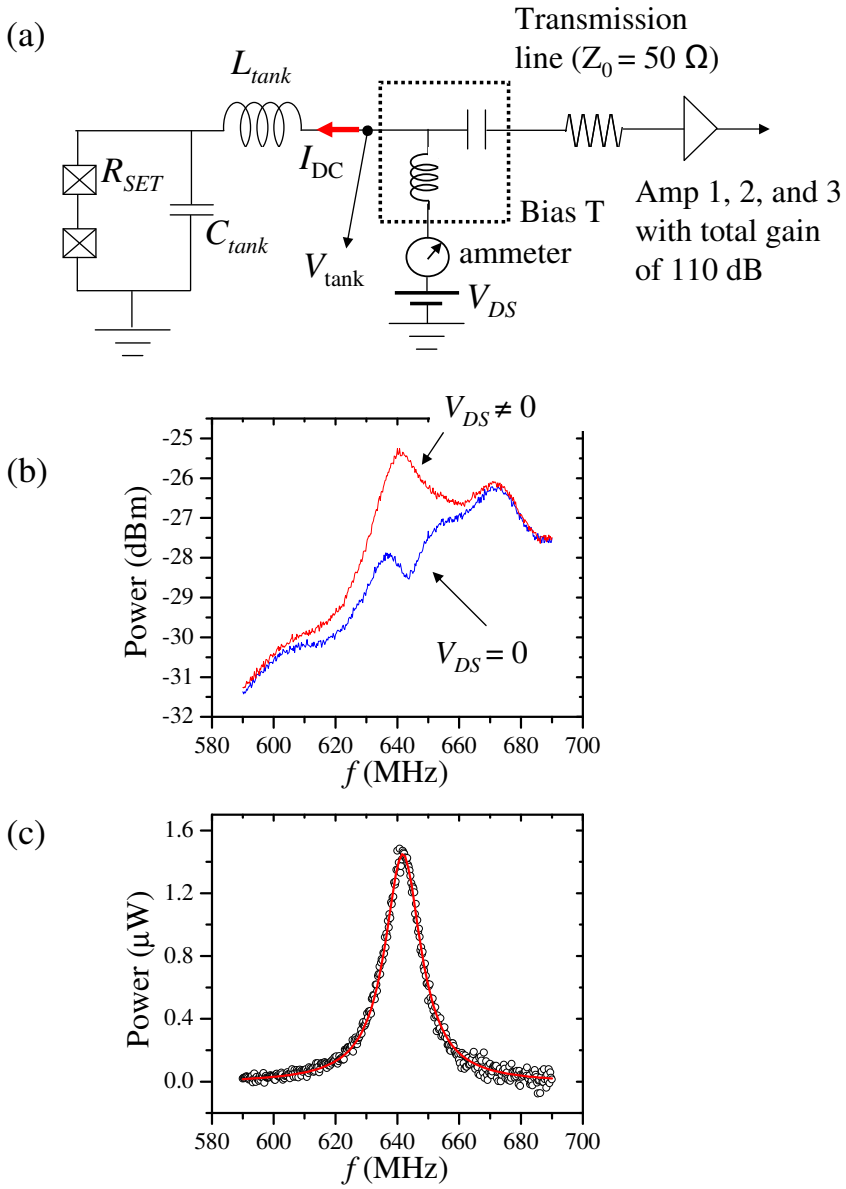

Figure 3.13: Set up for shot noise measurement. (a) Amp1 from Berkshire is at 4 K and has a gain of 41 dB. Amp2 from Miteq is at room temperature and has a gain of 39 dB. Amp3 is from Minicircuit, at room temperature, with a gain of 30 dB. (b) Shot noise in "SET1". The blue curve is with V_{ds}=0. The red curve is with V_{ds}=4.33 mV and the measured current I_n=20 nA. (c) The noise power after subtracting the blue curve from the red curve in (b). From the Lorentzian fit (red curve), the extracted resonance frequency (f_0) is 642 MHz and the bandwidth (Δf) is 14.2 MHz. The loaded $Q_L = f_0/\Delta f = 45$. The resolution bandwidth (B) and video bandwidth of the spectrum analyzer (Agilent E4407B) were both 1 MHz.

Hence, fluctuations in V_{RC} and V_{tank} are related by

$$\delta V_{RC} = \frac{\delta V_{tank}}{Z_{tank}} Z_{RC}. \tag{3.24}$$

For shot noise, the rms current fluctuation is

$$\delta I = \sqrt{2e\eta B I_{DC}}, \tag{3.25}$$

where B is the measurement bandwidth. The resulting rms voltage fluctuation across the SET junctions R_{SET} is then given by

$$\delta V = \delta I R_{SET} = \sqrt{2e\eta B I_{DC}} R_{SET}. \tag{3.26}$$

This voltage fluctuation δV is the same as δV_{RC} since R_{SET} and C_{tank} are connected in parallel. Thus, the rms voltage fluctuation across the tank circuit is:

$$\delta V_{tank} = \frac{\delta V Z_{tank}}{Z_{RC}} = \frac{\sqrt{2e\eta B I_{DC}} R_{SET} Z_{tank}}{Z_{RC}}. \tag{3.27}$$

Finally, the average noise power at the input of the tank circuit is given by

$$P = \frac{|\delta V_{tank}|^2}{Re[Z_{tank}]} = \frac{2e\eta B I_{DC} R_{SET}^2}{Re[Z_{tank}]} \left| \frac{Z_{tank}}{Z_{RC}} \right|^2. \tag{3.28}$$

Assuming $Z_{tank} = Z_0 = 50\ \Omega$ on resonance, one can approximate $Z_{RC} \simeq 1/i\omega C_{tank}$ since $R_{SET} \gg 1/\omega C_{tank}$, where $C_{tank} \simeq 1/(\omega_0 \sqrt{Z_0 R_{SET}})$. Then, $Z_{RC} \simeq -i\sqrt{R_0 R_{SET}}$. The approximate noise power on resonance is then

$$P = 2e\eta B I_{DC} R_{SET}. \tag{3.29}$$

Including the total gain G and the noise temperature T_N of the system, the measured

noise power is given by

$$P_N = GB(k_B T_N + 2e\eta I_{DC} R_{SET}). \tag{3.30}$$

3.7 Noise Temperature of the System

I measured the noise power output [40] of the rf-SET (device "SET1") as a function of frequency near the tank circuit resonance when applying a relatively large dc current through the SET (see Fig. 3.13). The dc current through the SET produced shot noise, which excited the tank circuit. This noise was sent through the three amplifiers to the spectrum analyzer [see Fig. 3.13 (b)]. The noise power at non-zero V_{DS} could be obtained by subtracting the zero V_{DS} data from the non-zero V_{DS} data [see Fig. 3.13 (c)]. The current I_{DC} through the tank circuit due to V_{DS} was measured by an ammeter [see Figs. 3.1 (a) and 3.13 (a)]. Figure 3.14 shows the noise powers at the peak plotted as a function of I_{DC}. By linearly fitting the peak noise power versus I_{DC}, I could determine the gain and the noise temperature of the system using Eq. 3.30, where R_{SET} was 195 kΩ. The extracted power gain was 3.04×10^9 or 95 dB, which was 15 dB lower than the expected gain of 110 dB. The noise temperature was 23 K. These results implied that there was additional loss in the system (e.g. lossy cables between the device and the cryogenic amplifier).

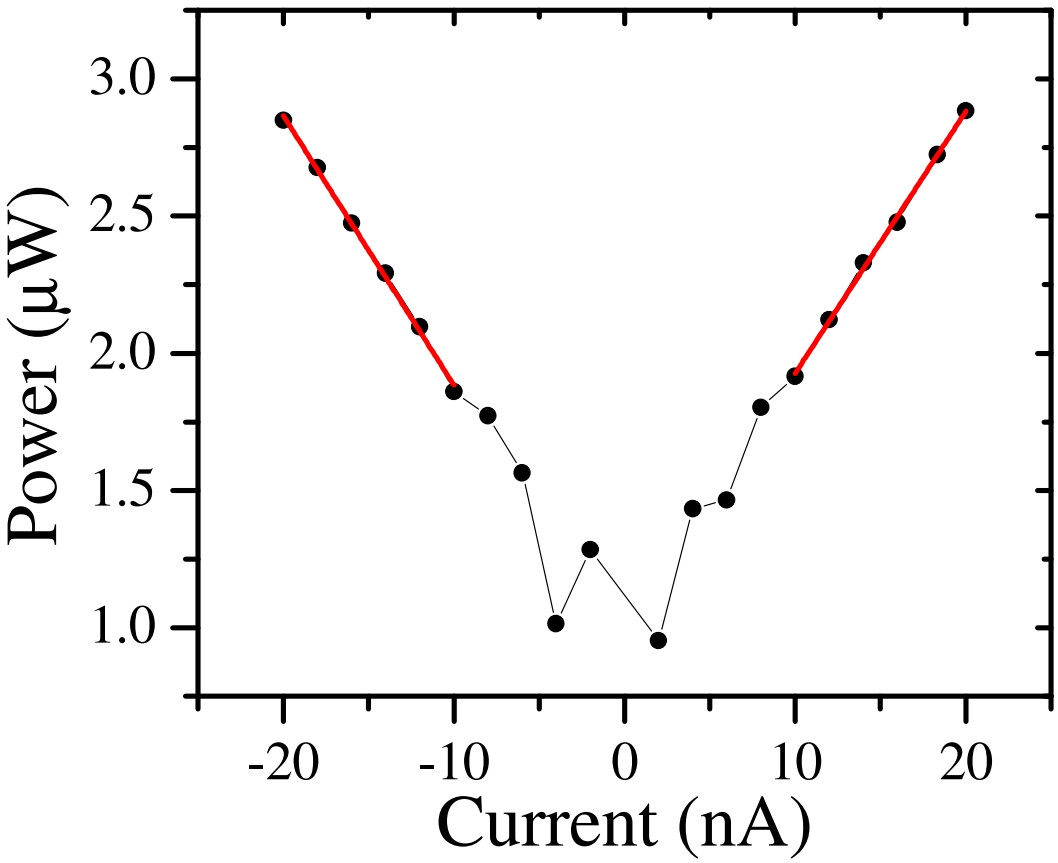

Figure 3.14: Peak power reflected from "SET1" at 30 mK as a function of applied current. The red curves are the linear fits.

3.8 Measurements of Charge Staircase and CPB parameters

Up to now I have described the individual elements of my system. For example in Chapter 2, I described how the CPB works and at the beginning of this chapter I described how the SET works. Here I put it all together and describe the total system and how we measure the excess charge on the CPB.

Figure 3.15 (a) shows an SEM image of the total device with the CPB and SET labeled. As one can see in this image, the distance between the two islands of the CPB and SET is small and the overlap length is large. This implies the capacitance between the two islands is non-negligible.

The circuit schematic of the coupled system is shown in Fig. 3.15 (b). The islands of the CPB and the rf-SET are capacitively coupled to the gate voltage V_g and $V_{g,e}$, respectively. The SET and CPB are capacitively coupled to each other with coupling capacitance $C_{C,be}$. When an electron tunnels onto the CPB island, the electrostatic potential of the CPB island changes by an amount $\Delta V = e/C_\Sigma$, where C_Σ is the total capacitance of the CPB island. This change in the electrostatic potential of the CPB island is analogous to changing the gate voltage of the SET ($n_{g,e}$) by an amount $\Delta n_{g,e} = C_{C,be}\Delta V/e = C_{C,be}/C_\Sigma$.

For all of the measurements in this dissertation, the rf-SET was biased at a DJQP or JQP point. This is because the SET has a lot of gain at these biases and there is also not a lot of current flowing through the SET. Figure 3.16 (a) shows the change in reflectance as a function of V_{DS} and $n_{g,e}$ near the DJQP peak for device "SET1". The transfer function [the line cut of the red line in Fig. 3.16 (a)] is plotted

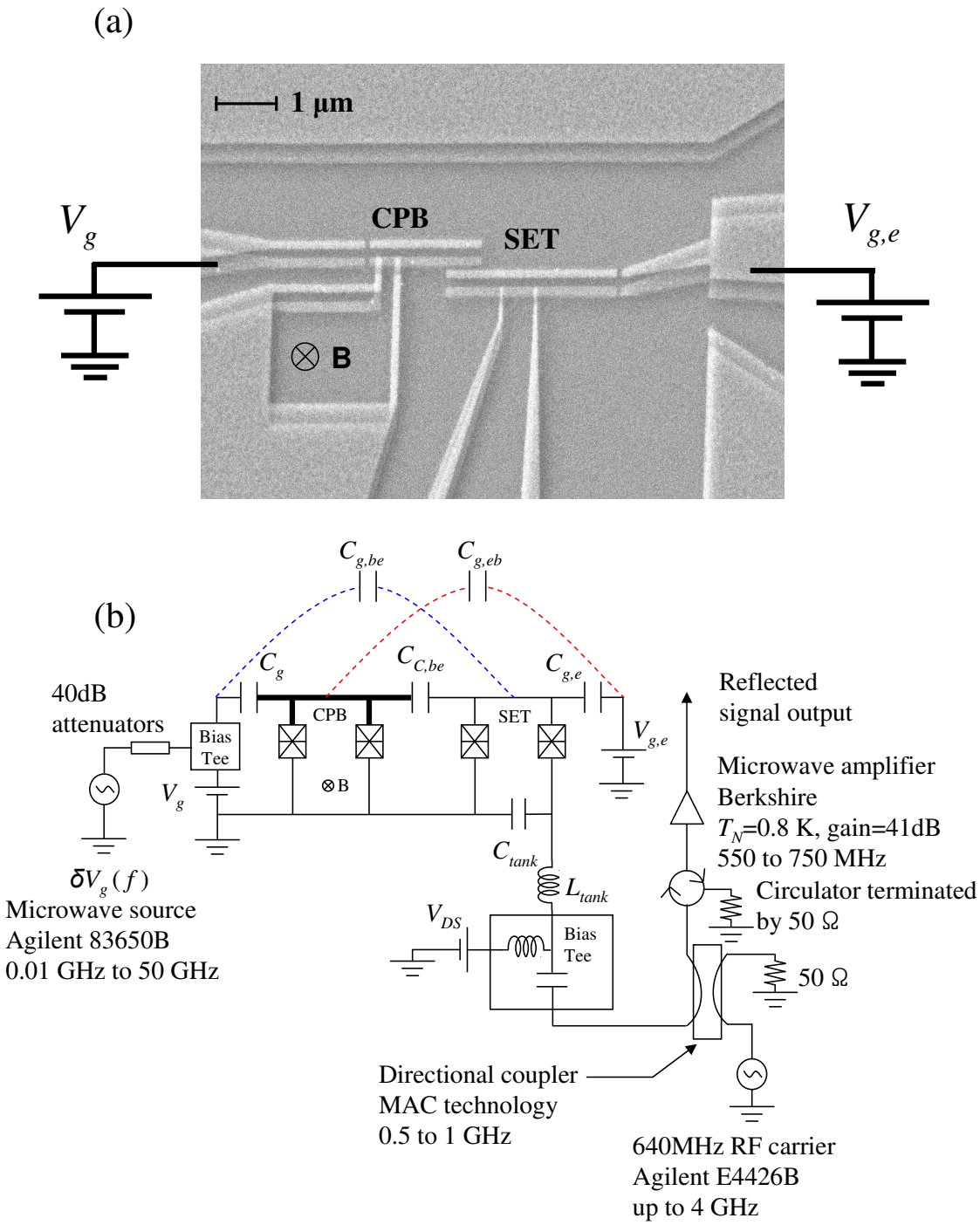

Figure 3.15: Schematic of rf-SET coupled to a CPB. (a) Scanning electron micrograph of the devices. (b) Schematic of experimental setup. The island of the rf-SET is coupled to the island of the CPB (bold line) through the coupling capacitance of $C_{C,be}$. The cross talk between gate leads and islands is plotted as the dotted line. The parameters are listed in Table 3.1. One can operate the SET in a dc mode by measuring the current through V_{DS}.

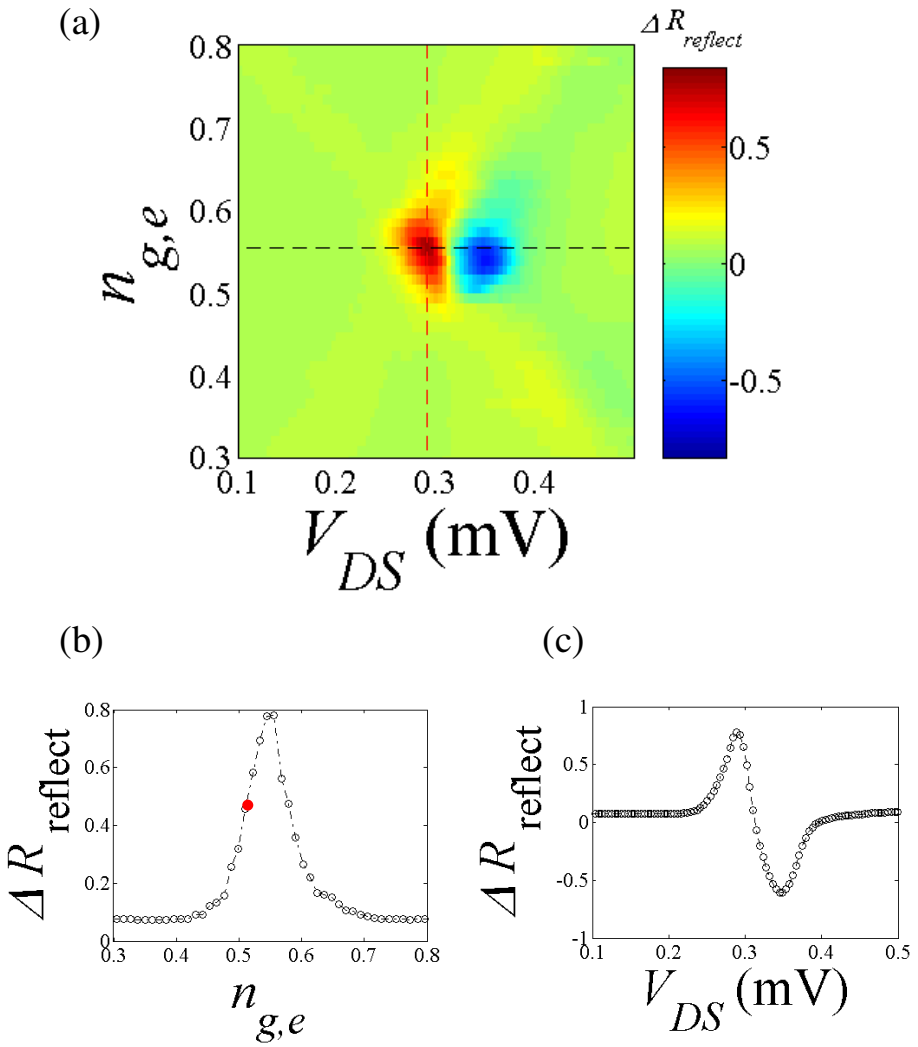

Figure 3.16: Transfer function of the rf-SET. (a) The reflected rf power as a function of V_{DS} and $V_{g,e}$ in the diamond map of device "SET1". (b) ΔR along the line cut of the red line in (a) along $n_{g,e}$ at a fixed V_{DS}. This curve is called the transfer function. (c) The line cut along the black line in (a), *i.e.* along V_{DS} at a fixed $n_{g,e}$.

in Fig. 3.16 (b). The gain or sensitivity of the transfer function was maximum when the SET was biased at $n_{g,e} \approx 0.52$ [see the red dot in Fig. 3.16 (b)]. An rf generator (Agilent E4426B) was used to apply the rf signal. To take this data, a reflected rf-signal was combined with a local oscillator signal (Agilent 83732B) at a single port mixer for a homodyne measurement. It was the same method explained in section 3.3.

There is unwanted cross talk between the gate voltage leads to the CPB and SET, which is labeled as $C_{g,be}$ and $C_{g,eb}$ in Fig. 3.15 (b) (also see Table 3.1) . This means that if I start to change V_g it will also cause $n_{g,e}$ to change. Thus, the SET gate lead coupled to the CPB and the CPB gate lead coupled to the SET. One way to compensate this cross talk is to ramp the SET and CPB gate voltages in opposite directions. I used two arbitrary waveform generators (Agilent 33250A) to provide the gate voltages. These were phase-locked together. I typically swept the gate voltage linearly using a ramp at a frequency of 2 kHz. By compensating the SET gate voltage with the CPB gate voltage, we could measure the CPB charge staircase [see Fig. 3.17 (a)] at the operating point of the SET [see the red dot in Fig. 3.16 (b)]. Without exciting the CPB, one can observe the charge staircase [see blue curve in Fig. 3.17 (a)], which is calibrated to the number of electrons on the CPB island. The small step around n_g=1 is due to non-equilibrium quasiparticles [26].

By measuring the staircase and applying a continuous microwave drive, I could also excite the CPB when the microwaves were resonant with a CPB transition to the excited state [see Fig. 2.4 (b)]. For example, when the CPB was resonant with the microwave frequency $f = 30$ GHz, spectroscopic resonances of the CPB

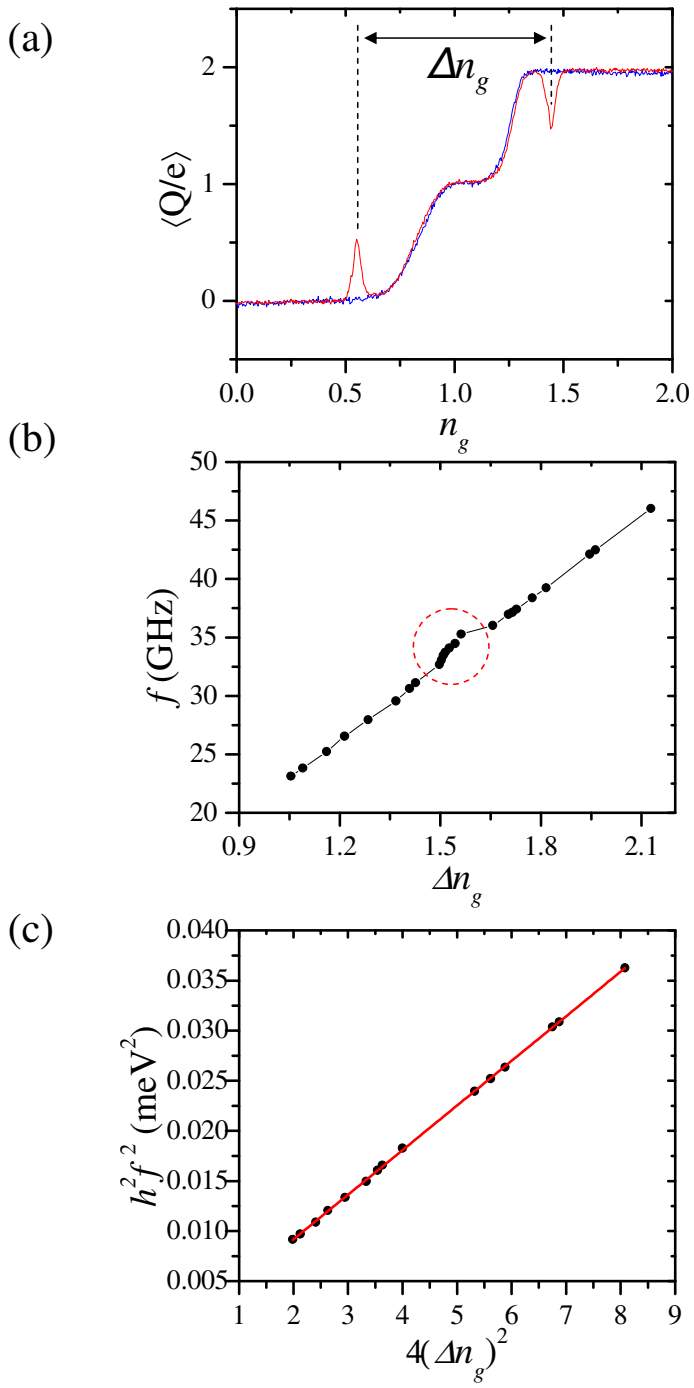

Figure 3.17: (a) Charge staircase of CPB qubit "SET1". The blue curve is when the CPB is in the ground state. The red curve is when the CPB is excited at $f =$ 30 GHz. (b) Microwave frequency vs. Δn_g. The rf-SET was biased at the DJQP peak. (c) Extraction of E_J from the linear fit (red line) without points inside the red-dashed circle in (b).

appeared at an n_g of 0.55 and 1.45 [red curve in Fig. 3.17 (a)]. In order to extract E_J and E_C of the CPB, I took the staircases at different microwave frequencies with a constant magnetic field from the superconducting magnet. In the first device "SET1" I measured, I was not able to perform a continuous frequency sweep; instead I found a few frequencies where I was able to excite the CPB. This problem was due to a poorly matched microwave line (see Fig. 3.12). For this measurement, we used an Agilent 83650B microwave source that allowed us to excite the CPB up to 50 GHz.

Figure 3.17 (b) shows the microwave frequency f versus the observed Δn_g between two resonances of the CPB. The plot shows a distortion at Δn_g= 1.5 for f between 33 and 37 GHz (the red dashed circle), which will be discussed in Chapter 4. For now, I will not include the data points in the red dashed circle when doing fits. Using the two level approximation in Eq. 2.18, I extracted $E_C/k_B = (0.774 \pm 0.0012)$ K and $E_J/k_B = (0.195 \pm 0.0225)$ K by fitting to the remaining points [see Fig. 3.17 (c)]. This implies the minimum transition frequency E_J/h = 4.06 GHz, which is outside the range of data shown due to the non-equilibrium quasiparticle step.

3.9 Measurements of Energy Relaxation Time T_1

In order to measure the energy relaxation time T_1 of the first excited state of the CPB "SET1", I used an rf-SET instead of a dc-SET so that I could make fast measurements. The measurement bandwidth was determined by the tank circuit in the rf-SET. To find the resonance frequency of the CPB for a particular n_g, I

measured the CPB charge staircase by ramping the gate voltage n_g while applying a continuous microwave frequency; e.g. I found $n_g = 0.55$ and 1.45 were resonant to the CPB at $f = 30$ GHz [see Fig. 3.17 (a)]. I then biased the CPB with a fixed n_g (either 0.55 or 1.45) and turned the microwaves on for 100 μs to put the CPB in an incoherent mixed state. The microwaves were then turned off and the decay from the excited state was monitored as a function of time using the digital oscilloscope (Agilent 54855A Infiniium). By averaging 500,000 individual time traces, an exponential decay from a mixed state to the ground state was measured; this decay was fit to extract T_1 (see Fig. 3.18).

By varying n_g and the frequency, I was able to measure T_1 as a function of frequency. I performed these measurements from 23 GHz to 50 GHz; the lower limit was determined by non-equilibrium quasiparticles populating the CPB and the higher limit was fixed by our synthesized signal generator (Agilent 83650B). Figure 3.19 (a) shows measurements of T_1 at different Josephson energies E_J of the CPB.

If I assume that voltage noise is the dominant noise source [45], then the energy relaxation time T_1 from the excited state to the ground state is given by Eq. 2.30:

$$\frac{1}{T_1} = \left(\frac{e\kappa_c}{\hbar}\right)^2 \frac{E_J^2}{[4E_C(1-n_g)]^2 + E_J^2} S_V(\triangle E/h). \tag{3.31}$$

My T_1 measurements confirmed that T_1 was enhanced by decreasing E_J, which is consistent with Eq. 2.30 and with voltage or charge noise being the dominant T_1 mechanism (also see the perturbed Hamiltonian of the CPB in Eq. 2.28).

From a theoretical analysis of the spectral density of voltage noise using the

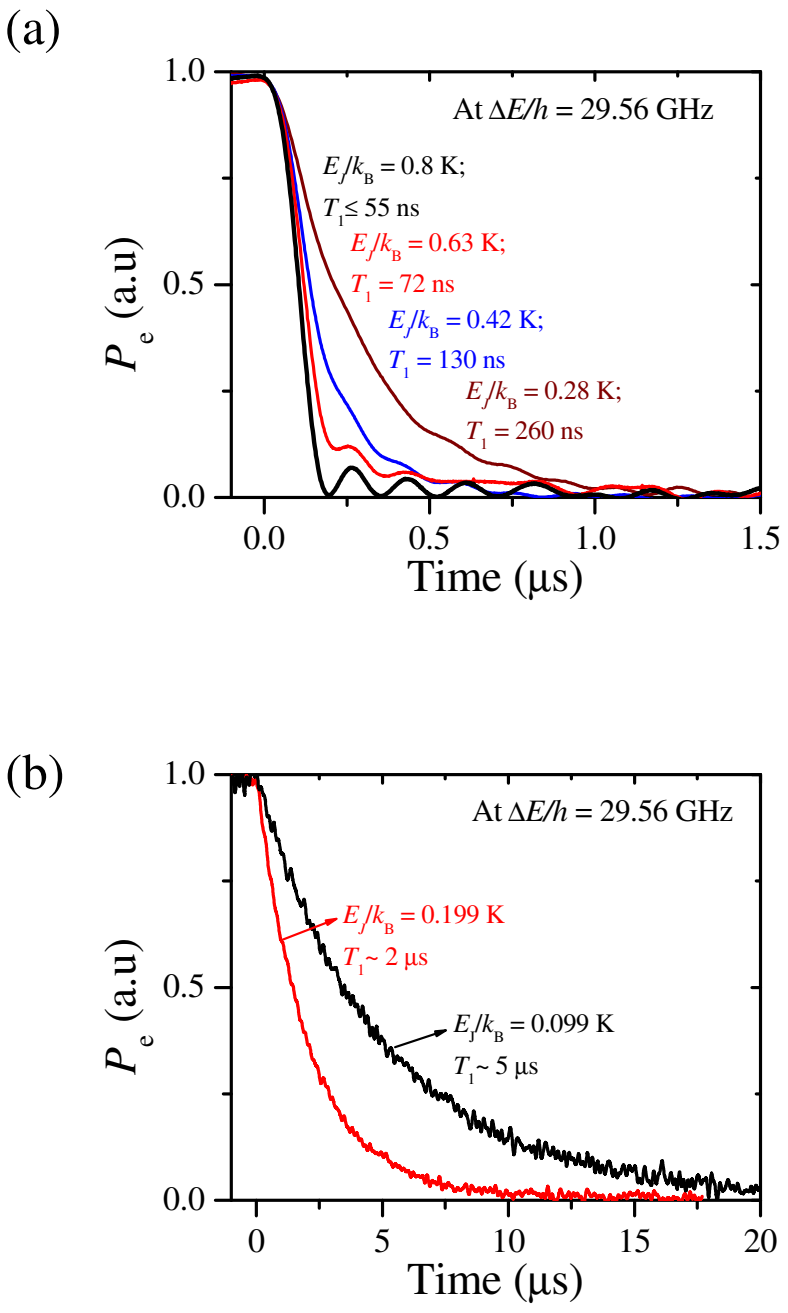

Figure 3.18: T_1 versus E_J at $\Delta E/h$ =29.56 GHz for CPB "SET1".

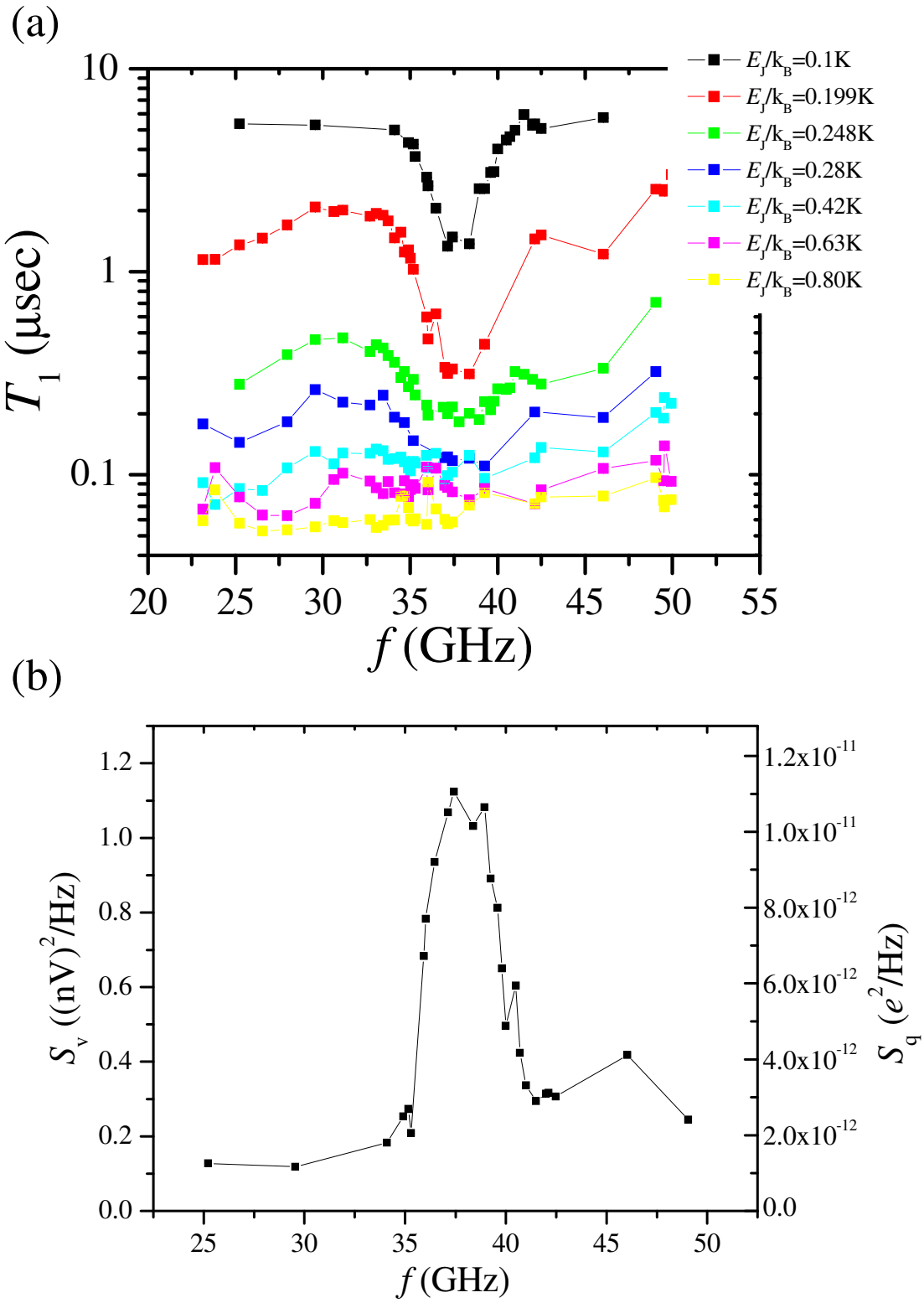

Figure 3.19: T_1 versus E_J and $\Delta E/h$ of "SET1". (a) T_1 versus $f = \Delta E/h$ for different E_J. (b) Voltage noise found from T_1 data at E_J/k_B =0.199 K shown in (a).

gate capacitance of the CPB [45] and the SET [46], I extracted a spectral density of voltage noise on the order of 0.1 nV^2/Hz from the SET to be the dominant noise source. The effective coupling between the CPB and the SET was $\kappa_{eff} = C_{C,be}/C_\Sigma \sim 0.01$ where $C_{C,be}$ is the coupling capacitance between the island of the CPB and the island of the SET and C_Σ is the total capacitance of the CPB island.

The effective charge noise S_q using Eq. 2.31 was also from the T_1 data [see Fig. 3.19 (b)]. S_V is the power spectral density of voltage noise and S_q charge noise that the qubit sees. The spectral density of noise from T_1 data shown in Fig. 3.19 (b) had a peak around 37 GHz. Later, I found that such a peak in the spectral density of noise could be linked to anomalous energy level seen in Fig. 3.17 (b), although this was not clear at the time.

3.10 CPB Spectrum

Before I moved on to the second device (CPB "SET2"), we upgraded the microwave cable (the original was replaced with a BeCu cable with K connectors) inside the refrigerator (see Fig. 3.12). This allowed measurements with bandwidth up to 50 GHz and I was able to take continuous spectroscopy of the CPB (see Fig. 3.20).

If E_C of the CPB is known, one can fit the CPB spectrum as a function of E_J. An easy way to fit the CPB spectrum is to take the staircase of the CPB as a function of microwave frequency and overlay the theory plot on top of the data. In Fig. 3.20, the color represents the average charge $\langle Q/e \rangle$ on the CPB island. When

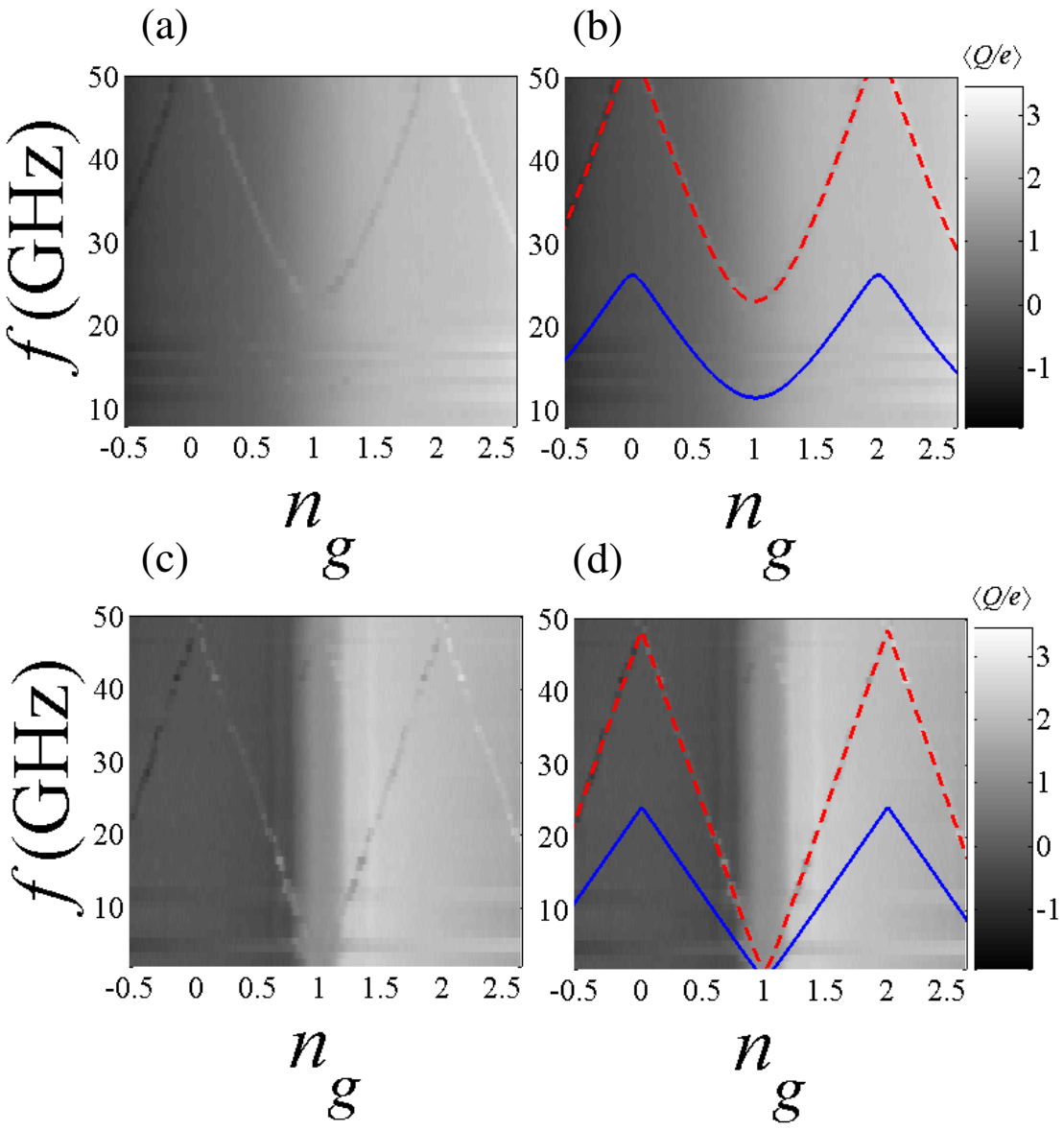

Figure 3.20: Transition spectrum of device CPB "SET2" at different E_J. (a) The CPB spectrum at zero magnetic field. The step size in frequency was 1 GHz. (b) Same as (a) with the predicted spectrum from our system Hamiltonian (red dashed curve) using the parameters E_J/k_B= 1.1 K and E_C/k_B= 0.58 K. Blue curve is due to two photon absorption. (c) The CPB spectrum at 6.45 Gauss. (d) Same as (c) except for the predicted spectrum with E_J/k_B= 0.1 K.

the applied microwave frequency is resonant with a level splitting of the CPB, the CPB state changes, causing a change in the charge on the island, which causes a change in the reflectance of the rf-SET. For $0 < n_g < 1$, $\langle Q/e \rangle \approx 0$ and the plot shows darker gray when the CPB is in the ground state. In this region when the CPB is excited by resonant microwaves, $\langle Q/e \rangle$ increases towards 2 (brighter gray). For $1 < n_g < 2$, $\langle Q/e \rangle = 2$ (brighter gray) when the CPB is in the ground state. When the CPB is excited by microwaves, $\langle Q/e \rangle$ decreases toward zero (dark gray). Regions where the color changes comprise the CPB spectrum.

For fitting the data in Fig. 3.20, I used more than four n states since the two-level approximation breaks down when E_J becomes larger [red dashed curve in Fig. 3.20 (a)]. When E_J/k_B was about 1.1 K, I was able to see the minimum of the CPB spectrum at around 25 GHz (which corresponds to 1.1 K). When E_J/k_B was very small, it was hard to see the minimum of the CPB spectrum since there were non-equilibrium quasiparticles at odd n_g [26]. Also note that in Fig. 3.20 (c) around $f = 47$ GHz the first excited state has a close avoided crossing with the second excited state. I also found that when I applied relatively high power microwaves to the CPB, two photon absorption was observed [blue curve in Fig. 3.20 (b) and (d)] and this part of the spectrum also fit well to the theory. Table 3.1 summarizes the parameters that I extracted for "SET1", "SET2", and their CPBs.

Chapter 4

Anomalous Avoided Level Crossings in a CPB

4.1 Overview

In superconducting devices based on the dc and ac Josephson effects, impurities and defect states have long been linked to critical current fluctuators [49-53] and charge noise [56-59]. Understanding this noise is interesting from a microscopic point of view and is a key issue for certain applications, such as quantum computing, where noise can severely limit the coherent manipulation of the quantum states. Recently, several groups have reported the observation of discrete "two-level systems" coupled to superconducting qubits [61-65]. Coupling between a superconducting device and anomalous two-level systems (TLS) creates avoided level crossings in the transition spectrum of the device. Such coupling is important because it causes energy dissipation, dephasing, and loss of measurement fidelity. These new observations are also interesting because they represent a new approach to studying fluctuators that allows the extraction of microscopic information about individual microstates.

Initially, Ray Simmonds *et al.* observed many avoided level crossings in the spectrum of a phase qubit [61] and argued that discrete TLSs were responsible. Subsequently B. Plourde *et al.* observed them in the flux qubit [64], G. Ithier *et al.* found them in the quantronium [65], and J. Schreier *et al.* observed them in the transmon [67]. In this chapter, I describe my results on the first reported

observations of avoided level crossings in a CPB [68, 69].

While it was initially proposed that the anomalous avoided level crossings in phase qubits were due to critical current fluctuators [61], a later comparison of the extracted hopping distance (from an analysis of an ensemble of avoided level crossings) to atomic distances suggested that charge fluctuators were the source of the avoided level crossings [62]. In contrast to a phase qubit, a Cooper Pair Box is directly sensitive to charge. Thus we should expect to gain more information about discrete charge fluctuators if they can be observed in the CPB spectrum.

As noted in Chapter 3, measurements of T_1 as a function of frequency in CPB "SET1" showed a large dip around 37 GHz. Our original hypothesis was that the dip was happening at the charging energy of the SET, as predicted by theory [70]. To test this hypothesis we decided to measure a second device: "SET2".

During preliminary measurements on "SET2", I noticed two interesting things about T_1 and the energy levels. Figure 4.1 (a) shows a plot of the energy relaxation rate Γ_1 $(= 1/T_1)$ versus f at a small E_J. As one can see, there were a few notable peaks in the decay rate, specifically at $f = 19$ GHz and $f = 34$ GHz. As Fig. 4.1 (a) shows, when I plotted Δn_g versus f from the CPB staircase, I also found a few distortions in the energy level, as I observed in "SET1" [see Fig. 3.17 (b)]. Comparing the energy relaxation rate (red squares) and the Δn_g (blue dots) showed a correlation between them, which seemed to have nothing to do with the charging energy of the SET, $E_{C,e}/h = 24.9$ GHz. That raised the question of what was causing T_1 to decrease at these specific frequencies.

To try to answer that question, I decided to take some detailed spectroscopic

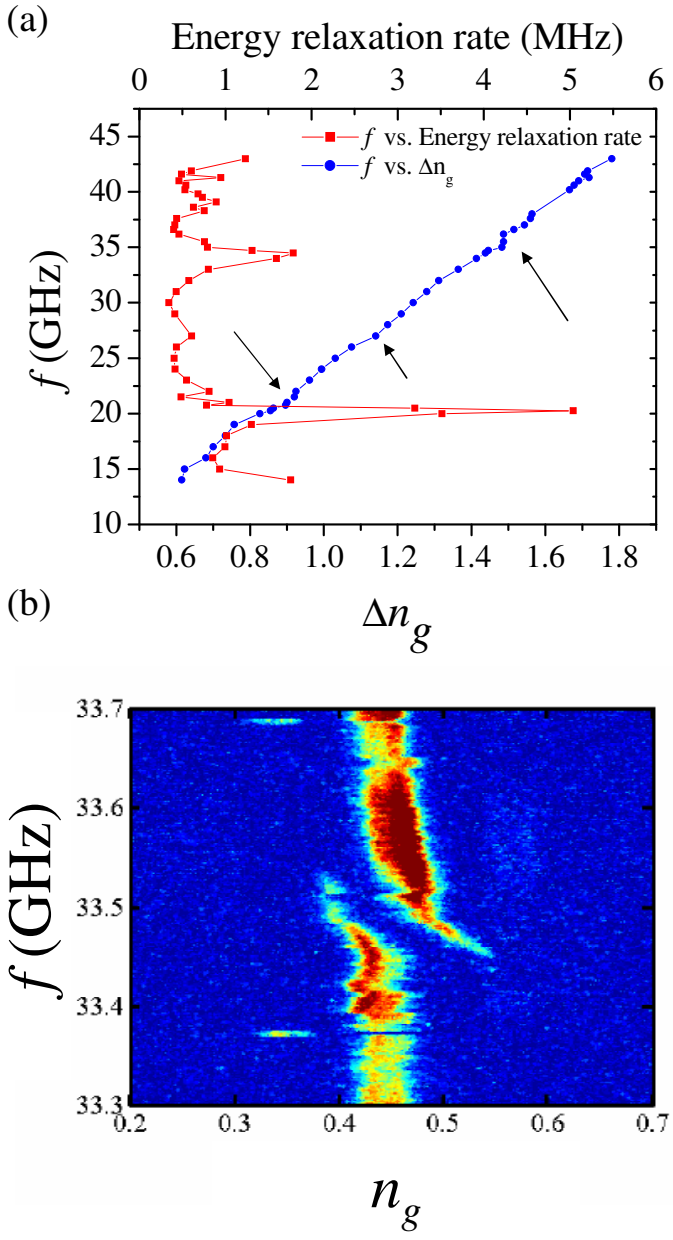

Figure 4.1: (a) Plot of $1/T_1$ and energy levels of the CPB "SET2". The energy relaxation rate ($1/T_1$) of the CPB as a function of microwave frequency (red squares) and Δn_g [defined in Fig. 3.17 (a)] versus microwave frequency (blue circles). The decay rate increased when there were distortions in the plot of Δn_g versus f [see the black arrows]. (b) Detailed view of one prominent avoided level crossing around 33.5 GHz in the spectrum of the CPB "SET2". The red and blue colors represent a high probability to be in the excited and ground states of the CPB, respectively.

measurements of the qubit. Remarkably, I observed a few anomalous avoided level crossings in the CPB spectrum in the 20 to 50 GHz frequency range [68]. For example, Fig. 4.1 (b) shows one avoided level crossing in the measured CPB spectrum near 33 GHz. Even more remarkably, it turned out that these anomalous avoided level transitions were voltage dependent, just as you would expect if they were due to charge fluctuators that were located in the Josephson tunnel junctions of the CPB. From fitting our spectrum using a model of a charge fluctuator coupled to a CPB Hamiltonian [69], I was able to extract microscopic parameters for each fluctuator, such as the hopping distance, asymmetry of the well, and the tunneling rate. From plots such as Fig. 4.1 (a), I was also able to show that these TLFs cause dissipation in the CPB and found that by measuring T_1 as a function of frequency I was able to locate individual charge fluctuators. In the rest of this chapter, I describe in detail the data and my analysis of the avoided level crossings.

4.2 E_J and Gate Voltage dependence of Crossings

Figure 4.2 shows a plot of the measured excess charge spectrum as a function of n_g and f for CPB "SET2". The color scale represents the measured change in the rf reflectance of the rf-SET, which is related to the induced charge on the CPB. The measurement set-up was described in section 3.9 of the previous chapter (see Fig. 3.15). For Fig. 4.2, I swept the gate voltage from $n_g = -0.5$ to $n_g = 2.5$ and stepped the applied microwave frequency from 24 to 50 GHz in steps of 30 MHz. For Fig. 3.20 the step size was 1 GHz. The white parabolic-like band for $0 < n_g < 1$

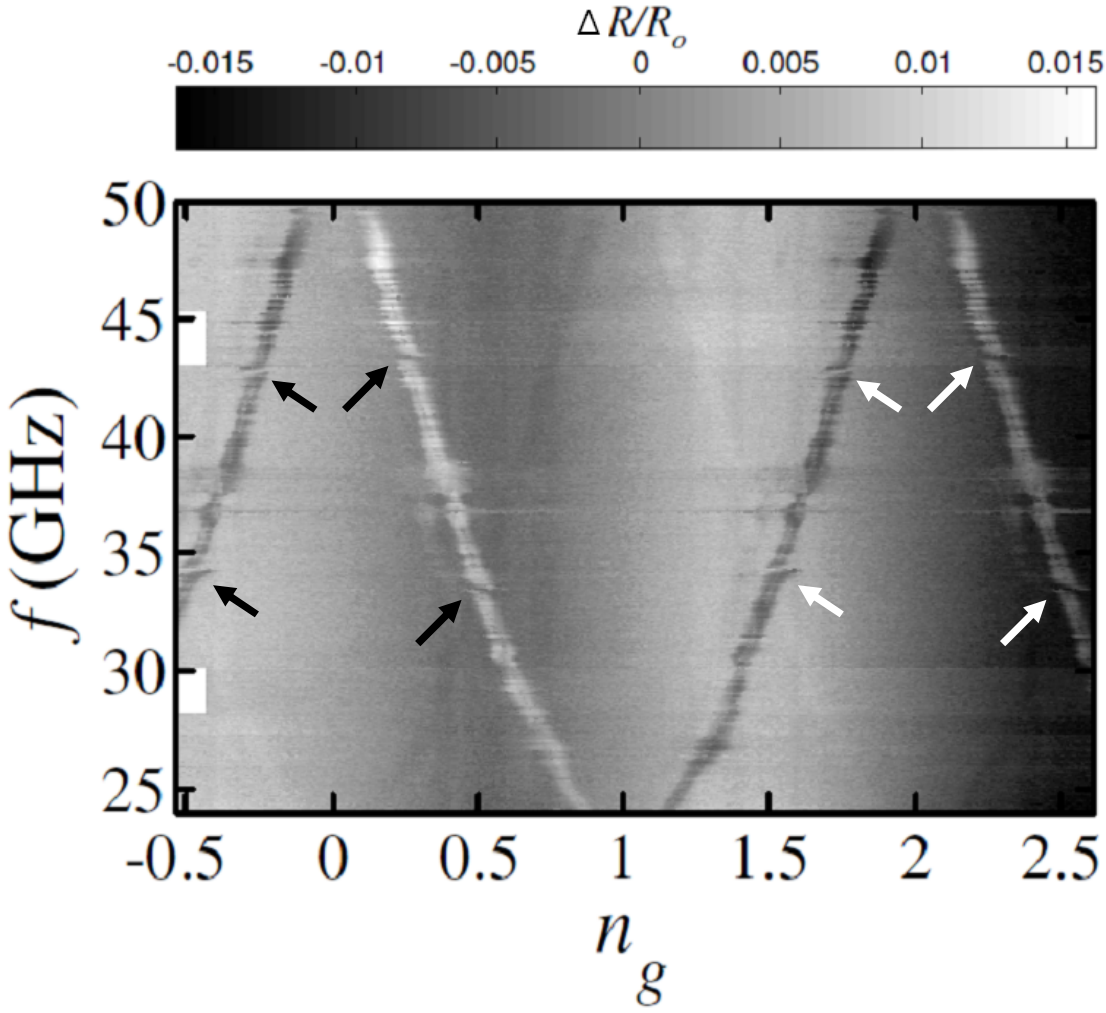

Figure 4.2: Measured spectrum of CPB "SET2" when the applied microwave frequency f was adjusted from 24 GHz to 50 GHz with E_J/k_B= 1.12 K. The step size of the frequency was 30 MHz. The white parabolic like band between $0 < n_g < 1$ corresponds to a measured change of $\approx 1e$ on the island of the CPB while the black parabola between $1 < n_g < 2$ corresponds to a measured change of $\approx -1e$ on the island of the CPB. The black and white arrows point to prominent avoided level crossings.

in Fig. 4.2 corresponds to a measured change of $\approx 1e$ on the island of the CPB while the black parabola for $1 < n_g < 2$ corresponds to a measured change of $\approx -1e$ on the island of the CPB. This is what one would expect if the CPB is being saturated by resonant microwave power.

There are a number of things about this plot that I should comment on. First, it is very challenging to design a microwave system that works at cryogenic temperatures with a 50 GHz bandwidth. In particular not all of the connectors were made to work up to 40 GHz and our sample packaging was not designed for such high frequencies. This can lead to standing waves and places where very little power or a lot of power gets to the device. For example, around 37 GHz the transfer function of the rf-SET changed because there was a large amount of power reaching it. Similarly, there are features around 40 GHz that we attribute to standing waves.

Despite these problems, there are a few things that can be observed in this spectrum. For example, if one looks at the spectrum around 34 GHz and 43 GHz, one finds there are discontinuities or avoided level crossings. These avoided level crossings are not predicted by our Hamiltonian for the CPB (Eq. 2.9). Anomalous avoided level crossings indicate that the qubit is coupled to additional quantum systems. From my data we determined that these additional quantum systems are charge fluctuators.

Figures 4.3 (a-d) show the spectrum around 34 GHz for E_J/k_B=1.0 K, 0.87 K, 0.55 K, and 0.1 K. There are a few observations that I can make about this data. First, the avoided level crossings at $n_g = -0.43$ occurs at $f = 34.3$ GHz while for $n_g = 0.48$ it occurs at $f = 33.5$ GHz. This suggests that the anomalous system that

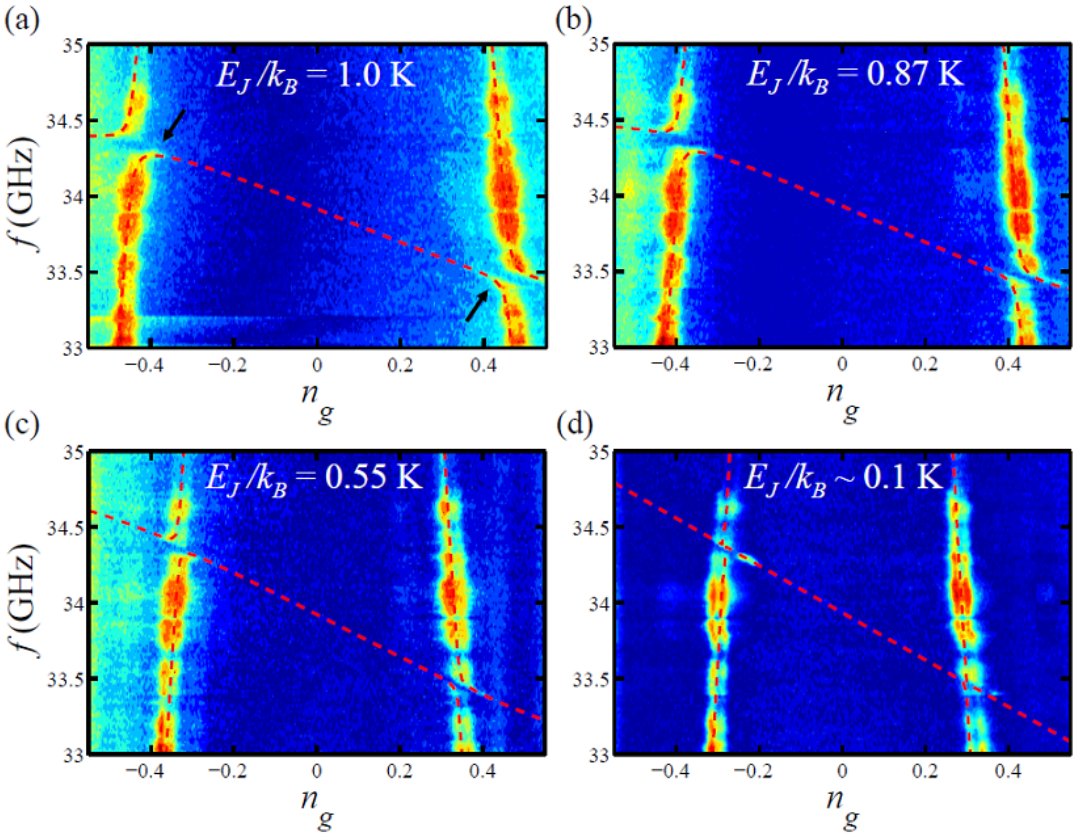

Figure 4.3: Measured spectrum of CPB "SET2" around 34 GHz at different Josephson energies, as specified in the plots. The red and blue colors represent the charge on the island corresponding to a high probability of being in the excited and ground state of the system, respectively. The arrows in (a) indicate small projections of the avoided level spectrum that appear to point toward one another. The red dashed curve is the predicted spectrum using a Hamiltonian consisting of a charged two level fluctuator (see Table 4.1 for the microscopic parameters of the TLF) coupled to a CPB.

the qubit is coupled to is voltage sensitive, *i.e.* it has a charge. Second, the splitting is largest at the largest value of E_J and decreases as E_J decreases; in particular at the largest value of E_J the splitting size was 150 MHz while at the smallest E_J I was not able to discern the splitting size. All of the anomalous avoided crossings we observed showed this general E_J and n_g dependence except for a possible splitting at $f = 39$ GHz, which had a splitting size too small to measure at even the largest E_J. This dependence of the crossings on gate voltage and Josephson energy is consistent with the CPB being coupled to a charged fluctuator that is coupled to the charge degree of freedom of the CPB. Also, note that in Fig. 4.2 the avoided level crossings have a 2-e periodicity. This behavior suggests that the charge fluctuator resides in one of the two tunnel junctions that form the CPB; the electrostatic potential of the CPB island is given by $V_I = (n_g - 2n)e/C_\Sigma$ which has a periodicity of 2 in n_g for the different states of the CPB.

4.3 Model of a Charged TLS interacting with a CPB

In general, the Hamiltonian for a charged fluctuator would depend on the local environment including other charged defects in the system. To simplify the problem, we assume that the fluctuator takes the form of a point charge moving between two potential wells, which is asymmetric (see Fig. 4.4). In this approximation the Hamiltonian for the TLF is

$$\hat{H}_{TLF} = \varepsilon_a |x_a\rangle \langle x_a| + \varepsilon_b |x_b\rangle \langle x_b| + T_{ab}(|x_a\rangle \langle x_b| + |x_b\rangle \langle x_a|) \tag{4.1}$$

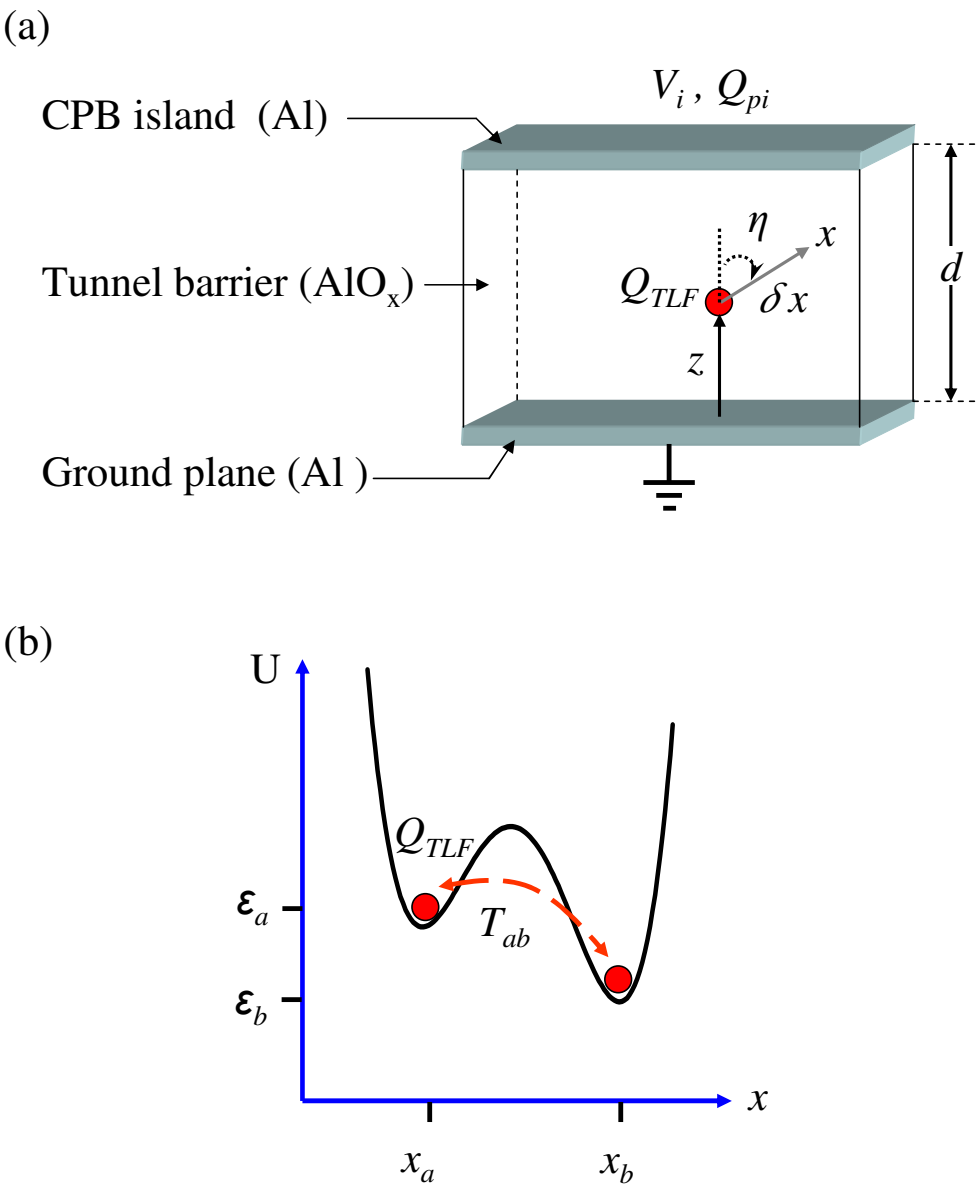

Figure 4.4: Schematic of TLF-CPB model. (a) Thin tunnel junction AlO_X layer with thickness "d" is sandwiched by Al ground plane and CPB island. The position of TLF charge can be denoted by "x". Red dot with black arrow represents hopping of a TLF. (b) Asymmetric potential well for a charged fluctuator Q_{TLF} hopping between two locations with tunneling rate T_{ab}.

or

$$\hat{H}_{TLF} = \begin{pmatrix} \varepsilon_a & T_{ab} \\ T_{ab} & \varepsilon_b \end{pmatrix}, \tag{4.2}$$

where ε_a is the energy of the fluctuator at position x_a, ε_b is the energy of the fluctuator at position x_b, and T_{ab} is the tunneling matrix element between the two sites. For an isolated fluctuator, the difference in energy between the two states of the TLF is given by $\sqrt{(\varepsilon_b - \varepsilon_a)^2 + 4T_{ab}^2}$.

In order to see how the charged fluctuator is coupled to the CPB, assume that the fluctuator is a point charge that resides in the tunnel junction with charge Q_{TLF} [see Fig. 4.4 (a)]. Then, the change in the induced polarization charge on the island of the CPB when the fluctuator tunnels from position x_a to x_b can be obtained by Green's reciprocity theorem, which relates electric potential and charge density. Green's reciprocity theorem [73] can be written as

$$\int_V \rho\Phi' d\tau + \int_S \sigma\Phi' da = \int_V \rho'\Phi d\tau + \int_S \sigma'\Phi da, \tag{4.3}$$

where Φ is the potential due to a volume-charge density ρ within a volume V and a surface-charge density σ on the conducting surface bounding the volume V, while Φ' is the potential due to another charge distribution ρ' and σ'. For the first charge distribution, one can set $\rho = Q_{TLF}\delta(x)\delta(y)\delta(z - z_0)$ for the charged fluctuator and $\Phi = 0$ with both conducting plates grounded. One can also assume those two plates [see Fig. 4.4 (a)] are infinitely big so that one can ignore the fringe effect of the E-field at the edge of plates. $\sigma = \sigma_1 + \sigma_2$ is the induced surface charge on both plates 1 and 2, which we are trying to find. For the second charge distribution, one

can set $\rho' = 0$ (no charge inside the volume) and $\Phi' = zV_1/d$ with plate 1 grounded and plate 2 (CPB island) at the voltage V_1, where d is the distance between two plates, or thickness of the tunnel junction. One also can set $\sigma' = \varepsilon_0 V_1/d$.

Now the first term in the left hand side of Eq. 4.3 yields $Q_{TLF}V_1 z_0/d$. And the second term becomes $V_1 \int_{S_2} \sigma_2 da = V_1 Q_2$ since $\Phi'(z=0) = 0$ and $\Phi'(z=d) = V_1$. The first term in the right hand side of Eq. 4.3 is zero since $\rho' = 0$ in the volume. The second term also becomes zero since $\Phi = 0$. Hence, the induced surface charge Q_2 on the CPB island is equal to $-Q_{TLF}z_0/d$. When the ion Q_{TLF} hops from z_a to z_b, the induced surface charge, or the polarization charge Q_{pi} would change from $-Q_{TLF}z_a/d$ to $-Q_{TLF}z_b/d$. Then, the difference is $\Delta Q_{pi} = Q_{TLF}(z_b - z_a)/d$. By defining the x-axis as in Fig. 4.4 (a), we can write $z_b - z_a = (x_b - x_a)\cos(\eta)$, where $x_b - x_a$ is the maximum displacement of the fluctuator and η is the angle of displacement relative to the electric field in the junction. Finally, $\Delta Q_{pi} = Q_{TLF}(x_b - x_a)\cos(\eta)/d$.

Assume that there is an excess charge $2ne$ on the island from an initially neutral condition and there is a charge fluctuator with Q_{TLF} at z in the tunnel barrier. The induced surface charge $Q_2 = -Q_{TLF}z/d$ is formed locally close to the charge fluctuator. Since the net charge on the island will be constant to maintain $2ne$, a charge $-Q_2$ will appear on the rest of the island. This charge is not a local charge and is distributed over the gate and the junction capacitance in proportion to their magnitude. The voltage at the island V_I using Eq. 2.4 is given by

$$V_I = \frac{1}{C_\Sigma}[(2ne - Q_2) - n_g e]. \tag{4.4}$$

Note one can replace $2ne$ by $(2ne - Q_2)$ when there is a charge fluctuator. With the existence of the charge fluctuator, the voltage difference is equal to $-Q_2/C_\Sigma$, leading to the charge on the gate voltage capacitor changing by $-Q_2 C_g/C_\Sigma$. The work W_{TLF} done by the gate voltage source for that charge is $(Q_2 C_g/C_\Sigma)V_g$, or

$$W_{TLF} = \frac{eQ_{TLF}}{C_\Sigma}\frac{z}{d}n_g. \tag{4.5}$$

Inserting Eq. 4.4 into U (Eq. 2.5) and subtracting W_{TLF} (Eq. 4.5) and W done for n excess Cooper pair from U, we can get the free energy E of the system, which is

$$E = \frac{1}{2}C_g(V_I - V_g)^2 + \frac{1}{2}C_J(V_I - 0)^2 - W - W_{TLF} \tag{4.6}$$

or

$$E = \frac{e^2}{2C_\Sigma}\left(2n + \frac{zQ_{TLF}}{ed} - n_g\right)^2 + \frac{e^2}{2C_\Sigma}\left(\frac{C_J}{C_g} - 1\right)n_g^2. \tag{4.7}$$

It can be reorganized as

$$E = \frac{e^2}{2C_\Sigma}(2n - n_g)^2 + \frac{e^2}{C_\Sigma}(2n - n_g)\frac{zQ_{TLF}}{ed} + U_{TLF}(z), \tag{4.8}$$

where $U_{TLF}(z)$ is given by

$$U_{TLF}(z) = \frac{Q_{TLF}^2}{2C_\Sigma}\left(\frac{z}{d}\right)^2 + const., \tag{4.9}$$

where the $const = \frac{e^2}{2C_\Sigma}(\frac{C_J}{C_g} - 1)n_g^2$ can be dropped since it does not depend on n and z. In Eq. 4.8, the first term only depends on n and n_g, thus it describes the charging energy of the CPB. By adding the Josephson energy term, one has the Hamiltonian of the CPB as Eq. 2.9. The second term shows the coupling between the CPB and the TLF. Here, one can use the x-axis, defined as in Fig. 4.4 (a), and

take $z = x\cos(\eta)$. This coupling Hamiltonian can be put in the form [69]:

$$\hat{H}_{CPB-TLF} = 2E_C \sum_{x=x_a,x_b} \sum_n (2n - n_g) \frac{Q_{TLF}}{e} \frac{x\cos(\eta)}{d} |n\rangle |x\rangle \langle x| \langle n| . \tag{4.10}$$

In Eq. 4.8, the last term $U_{TLF}(z)$ is the quadratic potential of the TLF. By adding the kinetic energy of the TLF, we can get the Hamiltonian of the TLF as

$$H_{TLF} = \frac{P_{TLF}^2}{2M_{TLF}} + U_{TLF}(z), \tag{4.11}$$

where P_{TLF} and M_{TLF} are the momentum and the mass of the TLF, respectively. Now we assume that the TLF experienced atomic scale interactions that give the potential $U_{TLF}(z)$ two wells that the TLF can tunnel between [see Fig. 4.4 (b)] and that allow us to reduce H_{TLF} to a 2 by 2 matrix as in Eq. 4.2.

The total Hamiltonian for a CPB coupled to a single charge fluctuator from Eqs. 2.9, 4.2, and 4.10 is thus given by

$$\hat{H}_{tot} = \hat{H}_{CPB} + \hat{H}_{TLF} + \hat{H}_{CPB-TLF}. \tag{4.12}$$

Now, let us consider a truncated Hamiltonian for the CPB with three charge states n=-1, 0 and 1 so that

$$\hat{H}_{CPB} = \begin{pmatrix} E_C(-2-n_g)^2 & -E_J/2 & 0 \\ -E_J/2 & E_C(0-n_g)^2 & -E_J/2 \\ 0 & -E_J/2 & E_C(2-n_g)^2 \end{pmatrix}. \tag{4.13}$$

The Hamiltonian without the coupling between the CPB and TLF is given by

$$
\begin{aligned}
&\hat{H}_o = \hat{H}_{TLF} + \hat{H}_{CPB} \\
&= \begin{pmatrix} \varepsilon_a & T_{ab} \\ T_{ab} & \varepsilon_b \end{pmatrix} \otimes I_3 + I_2 \otimes \begin{pmatrix} E_C(-2-n_g)^2 & -E_J/2 & 0 \\ -E_J/2 & E_C(0-n_g)^2 & -E_J/2 \\ 0 & -E_J/2 & E_C(2-n_g)^2 \end{pmatrix} \\
&= \begin{pmatrix} E_C(-2-n_g)^2+\varepsilon_a & -E_J/2 & 0 & T_{ab} & 0 & 0 \\ -E_J/2 & E_C(0-n_g)^2+\varepsilon_a & -E_J/2 & 0 & T_{ab} & 0 \\ 0 & -E_J/2 & E_C(2-n_g)^2+\varepsilon_a & 0 & 0 & T_{ab} \\ T_{ab} & 0 & 0 & E_C(-2-n_g)^2+\varepsilon_b & -E_J/2 & 0 \\ 0 & T_{ab} & 0 & -E_J/2 & E_C(0-n_g)^2+\varepsilon_b & -E_J/2 \\ 0 & 0 & T_{ab} & 0 & -E_J/2 & E_C(2-n_g)^2+\varepsilon_b \end{pmatrix},
\end{aligned}
\tag{4.14}
$$

where I_2 and I_3 are unit matrices. The coupling Hamiltonian between the CPB and TLF is given by

$$
\begin{aligned}
&\hat{H}_{TLF-CPB} \\
&= I_2 \otimes \begin{pmatrix} (-2-n_g) & 0 & 0 \\ 0 & (0-n_g) & 0 \\ 0 & 0 & (2-n_g) \end{pmatrix} \bullet \frac{2E_C Q_{TLF}}{ed} \cos(\eta) \begin{pmatrix} x_a & 0 \\ 0 & x_b \end{pmatrix} \bigotimes I_3 \\
&= \begin{pmatrix} E_a(-2-n_g) & 0 & 0 & 0 & 0 & 0 \\ 0 & E_a(0-n_g) & 0 & 0 & 0 & 0 \\ 0 & 0 & E_a(2-n_g) & 0 & 0 & 0 \\ 0 & 0 & 0 & E_b(-2-n_g) & 0 & 0 \\ 0 & 0 & 0 & 0 & E_b(0-n_g) & 0 \\ 0 & 0 & 0 & 0 & 0 & E_b(2-n_g) \end{pmatrix},
\end{aligned}
\tag{4.15}
$$

where $E_a = 2E_C Q_{TLF} x_a \cos(\eta)/ed$ and $E_b = 2E_C Q_{TLF} x_b \cos(\eta)/ed$. For convenience, I take $x_a = 0$, thus $E_a = 0$ and also $\varepsilon_b = 0$. This leaves five parameters:

E_C, E_J, E_b, ε_a, and T_{ab}, where E_C and E_J are determined by the CPB spectrum independently of the TLF. Hence, ε_a, T_{ab}, and E_b characterize the avoided level crossings, where ε_a sets the well asymmetry, T_{ab} sets the tunneling rate between the two wells, and E_b determines the magnitude of the charge and its hopping distance.

4.4 Extracting TLS Tunneling, Asymmetry, and Dipole Parameters

There are three conditions in the data that can be used to determine the three TLF parameters. The first condition is the excitation energy or the resonance frequency of the avoided crossings. The second condition is the splitting size of the avoided crossings. The last one is the "tilt" of the avoided crossings when the transition frequency of a TLF is plotted versus n_g.

Figures 4.5 and 4.6 show the energy eigenvalues and the transition frequencies from the ground state to the excited states of the system of the total Hamiltonian (Eq. 4.12) using $T_{ab}/k_B = 0.39$ K, $Q_{TLF}\delta x\cos(\eta)/ed = -0.074$, and $(\varepsilon_a - \varepsilon_b)/k_B = 1.43$ K (see parameters of $N = 2$ in Table 4.1). We note that in this model, an avoided crossing occurs when the first excited state of the TLF is resonant with the first excited state of the CPB. The change in the induced polarization charge on the CPB island due to the fluctuator being excited ultimately gives rise to the avoided level crossings at two different frequencies and two different reduced gate voltages (*i.e.* it breaks the symmetry of the CPB). One can see the small shift of the red curve (TLF energy band) horizontally by $\Delta Q_{pi}/e$ along n_g with respect to the black curve (the ground state of the system) [See Fig. 4.5 (a)].

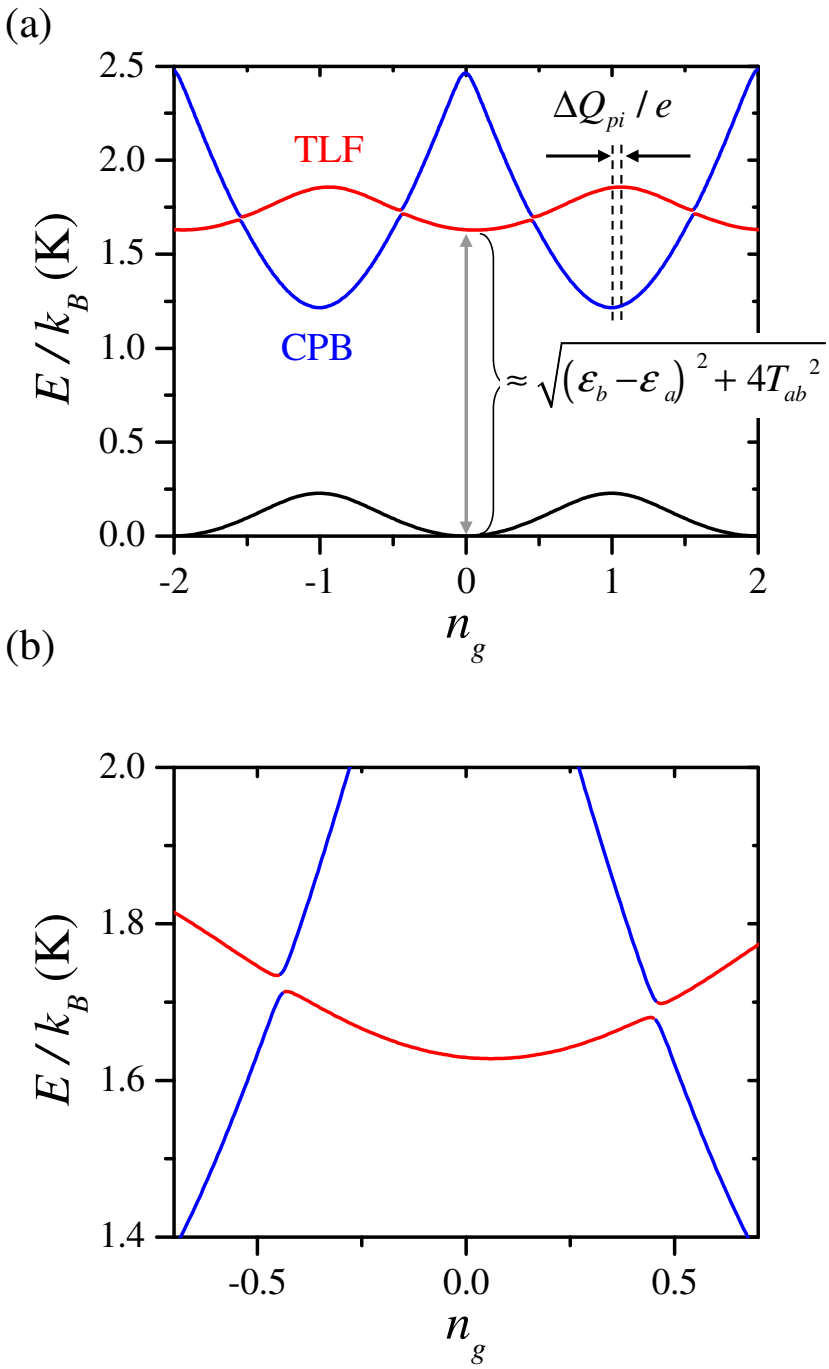

Figure 4.5: Theory plot of coupled TLF-CPB energy levels. (a) Energy levels of the coupled system. The parameters for this plot are given in $N = 2$ in Table 4.1. Black curve represents the system in the ground state. Blue curves are for the CPB in the excited state and the TLF in the ground state. Red curves are for the TLF in the excited state and the CPB in the ground state. (b) Zoom in around n_g=0 and E/k_B=1.7 K.

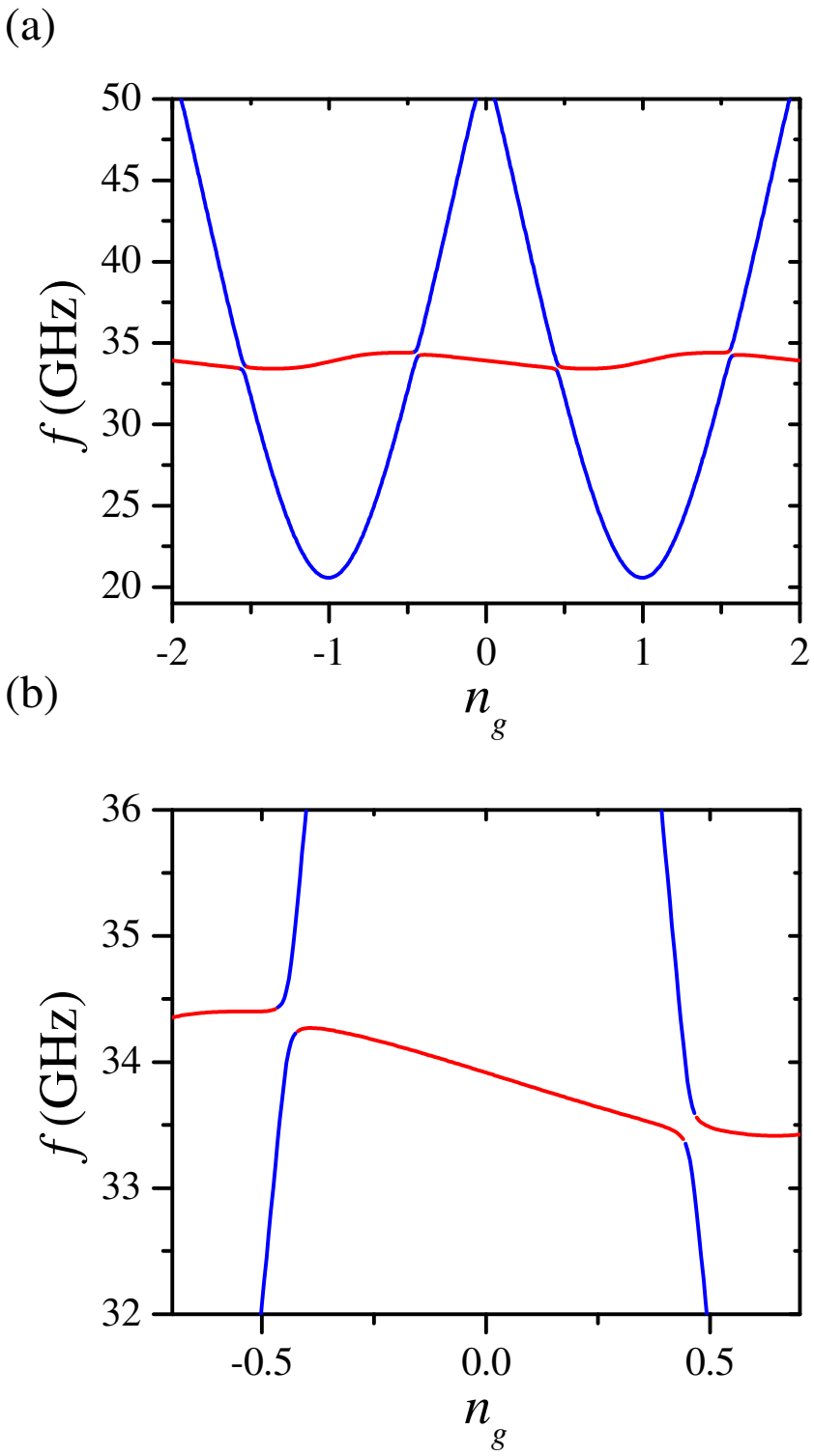

Figure 4.6: Theory plot of coupled TLF-CPB spectrum. (a) The transition spectrum from Fig. 4.5. Red and blue curves are for the TLF and the CPB spectrum, respectively. (b) Zoom in around n_g=0 and 34 GHz. One finds avoided level crossings between the TLF and CPB.

The splitting size in our model also depends on E_J because coupling the two excited states together is a second order process that involves both the tunneling of a Cooper-pair and the tunneling of the TLF. We also note that the splitting size depends on T_{ab} as well. The dashed red curve in Fig. 4.3 shows the predicted spectrum for the splitting we found near 34 GHz. Here we used fit parameters $(\varepsilon_b - \varepsilon_a)/k_B = 1.427$ K, $T_{ab}/k_B = 0.39$ K, and $Q_{TLF}\delta x \cos(\eta)/ed = -0.074$ where $\delta x = (x_b - x_a)$ is the maximum displacement of the fluctuator. We note that extracting these three parameters requires us to measure the splitting size and frequency of the avoided crossings at two different gate voltages and that these fit parameters can be varied by approximately 10 % while still yielding a good fit.

Table 4.1 summarizes the best fit results for all the avoided crossings I observed. The avoided crossing near 39 GHz had a splitting size too small to resolve, which places an upper bound on T_{ab} of the TLF [see Fig. 4.7 (b)]. Note the splittings around 43 and 43.5 GHz in Fig. 4.7 (a) cross the CPB spectrum in the opposite direction from other splittings and have the largest tunneling rate (0.65 K, or 13.5 GHz). Assuming a TLF charge of $Q_{TLF} = e$ and a tunnel barrier thickness of $d = 1.0$ nm, we extract minimum hopping distances for the fluctuators that range from 0.32 Å to 0.83 Å. It is worth noting that the crossings occur at different frequency and gate voltage; these "four" avoided levels can be attributed to different distinguishable charges, hopping with unique energy parameters.

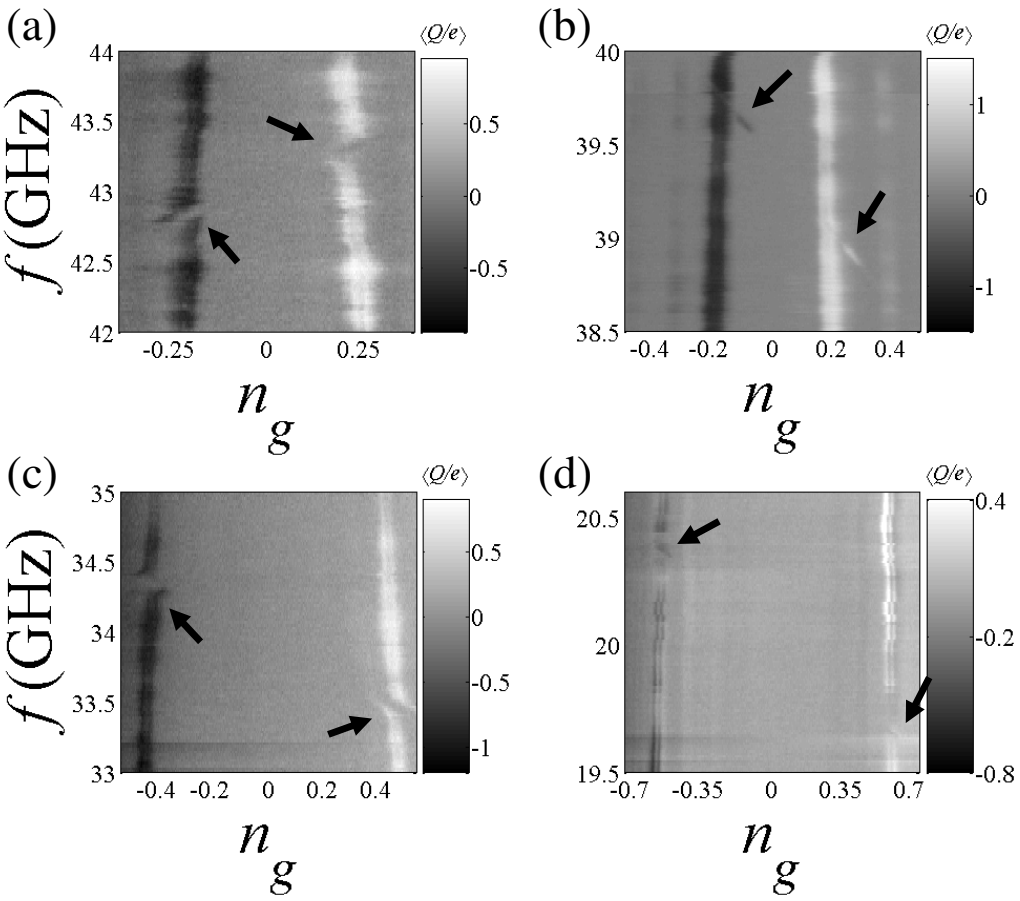

Figure 4.7: Four avoided level crossings. (a) Splittings around 43 GHz at E_J/k_B =0.95 K, (b) splitting features around 39 GHz at E_J/k_B =0.1 K, (c) splittings around 34 GHz at E_J/k_B =1 K, and (d) splittings around 20 GHz at E_J/k_B =0.1 K.

4.5 Excess Charge Spectroscopy

The model also predicts state transitions of the TLF at gate voltages away from the observed avoided crossings. Although these were not visible in Fig. 4.3, we found that weak transitions could be observed far from the avoided crossing when the microwave excitation power was increased by approximately a factor of ten to -48 dBm. Figure 4.8 (a) shows the measured excess charge spectrum between an applied frequency of 33 and 34.6 GHz; note the very faint transition due to the TLF between n_g = -1.25 and n_g = -0.75. In this region the measured excess charge on the CPB is approximately -0.03 e. I note that this is about an order of magnitude smaller than predicted from our simple theory [68, 69], which is given by

$$\frac{Q\delta x}{2d}\frac{1}{\sqrt{1+(\frac{2T_{ab}}{\varepsilon_b-\varepsilon_a})^2}}. \tag{4.16}$$

For comparison, Fig. 4.8 (b) overlays the predicted spectrum using the parameters found in Fig. 4.3 and we find good agreement with the theory.

Similarly, Fig. 4.8 (c) shows the measured excess charge spectrum from 41.5 to 44.5 GHz; a frequency range where another prominent avoided crossing was observed. Note that in Fig. 4.8 (c) we observe weak voltage-dependent transitions, due to the TLF, near $n_g = 0.8$ and $f = 44.25$ GHz; as well as between $n_g = -0.8$ and -0.4. Again the predicted spectrum [see Fig. 4.8 (d)] follows the measured spectrum accurately, strongly supporting the idea that the avoided level crossings are due to charged TLFs. In this spectrum, we observe additional features due to non-equilibrium quasiparticles, which create the apparent periodicity in n_g of

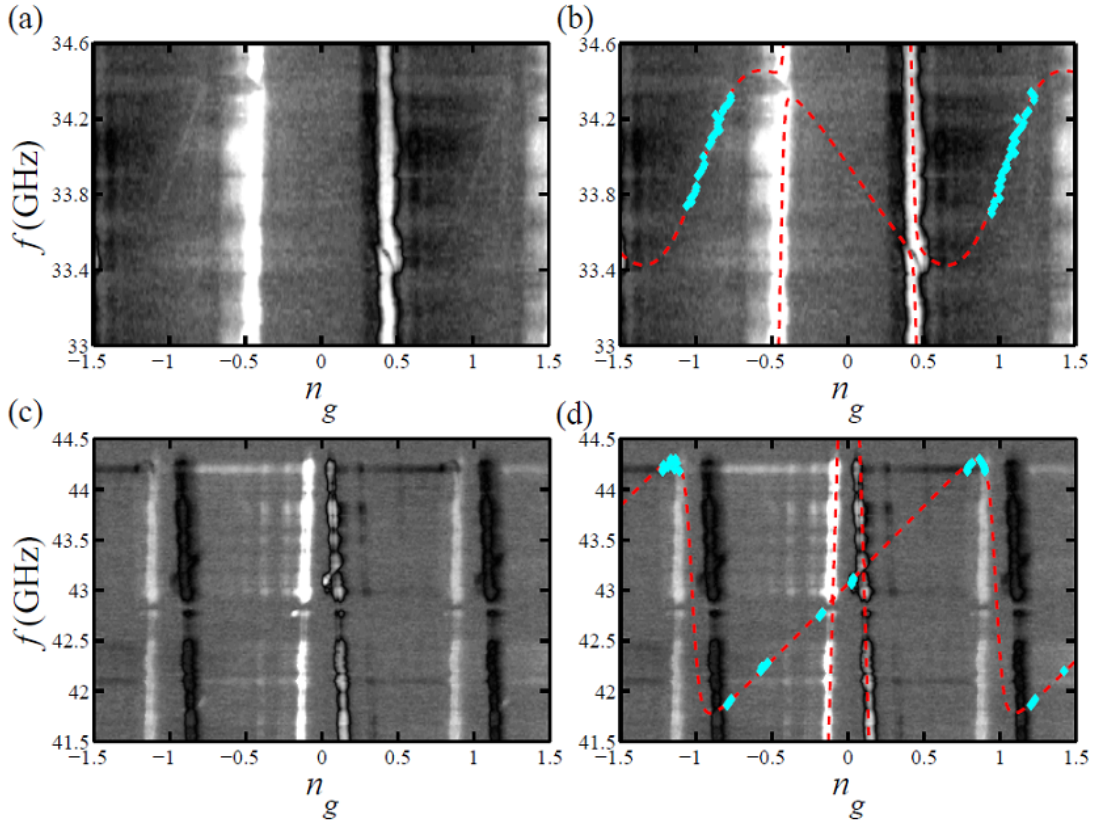

Figure 4.8: Excess charge spectrum in CPB "SET2" showing very weak TLF features. Measured excess charge spectrum at relatively large microwave drive amplitudes near two of the more prominent avoided level crossings. (a) Measured spectrum between 33 and 34.6 GHz with E_J/k_B= 0.95 K (same avoided level crossing as in Fig. 4.3). (b) Same as (a) with the predicted spectrum from our system Hamiltonian (red dashed curve) using the parameters in Fig. 4.3 and Table 4.1 and observed local peaks in the spectrum due to the TLF as the blue points. (c) Measured spectrum between 43 and 44.5 GHz at E_J/k_B= 0.1 K. (d) Same as (c) with predicted spectrum (red dashed curve) using the parameters in Table 4.1 and observed local peaks in the spectrum due to the TLF as the blue points.

1, [26, 27] multiple CPB spectra (*i.e.* spectra parallel to the CPB spectrum) due to low frequency charge fluctuators, and horizontal bands which are due to a change in the gain of the Coulomb-blockade electrometer.

4.6 T_1 Measurement

I also measured the lifetime (T_1) of CPB device "SET2" for the excited state of the CPB as a function of the transition frequency. For these measurements, the CPB was excited at its zero-to-one transition frequency, and the charge on the island was continuously monitored as a function of time using the rf-SET after the excitation source was turned off. The measurements were done at a small Josephson energy to decouple the CPB from charge perturbations in the system and hence increase the lifetime of the qubit to a maximum value [45, 46]. Figure 4.9 shows the measured decay rate ($\Gamma_1 = 1/T_1$) from 15 GHz to 45 GHz at $E_J/k_B = 0.1$ K. Several peaks in the decay rate are evident. These increases in Γ_1 occur when the CPB is in resonance with a TLF; the measured lifetime decreases from a few microseconds to 1 μs or less. This decrease in T_1 near a resonance was a useful tool for finding some of the avoided crossings. This behavior suggests that the lifetime of these TLFs is smaller than a few microseconds and that the interaction of the CPB with a charged TLF is a source of dissipation for the CPB [74].

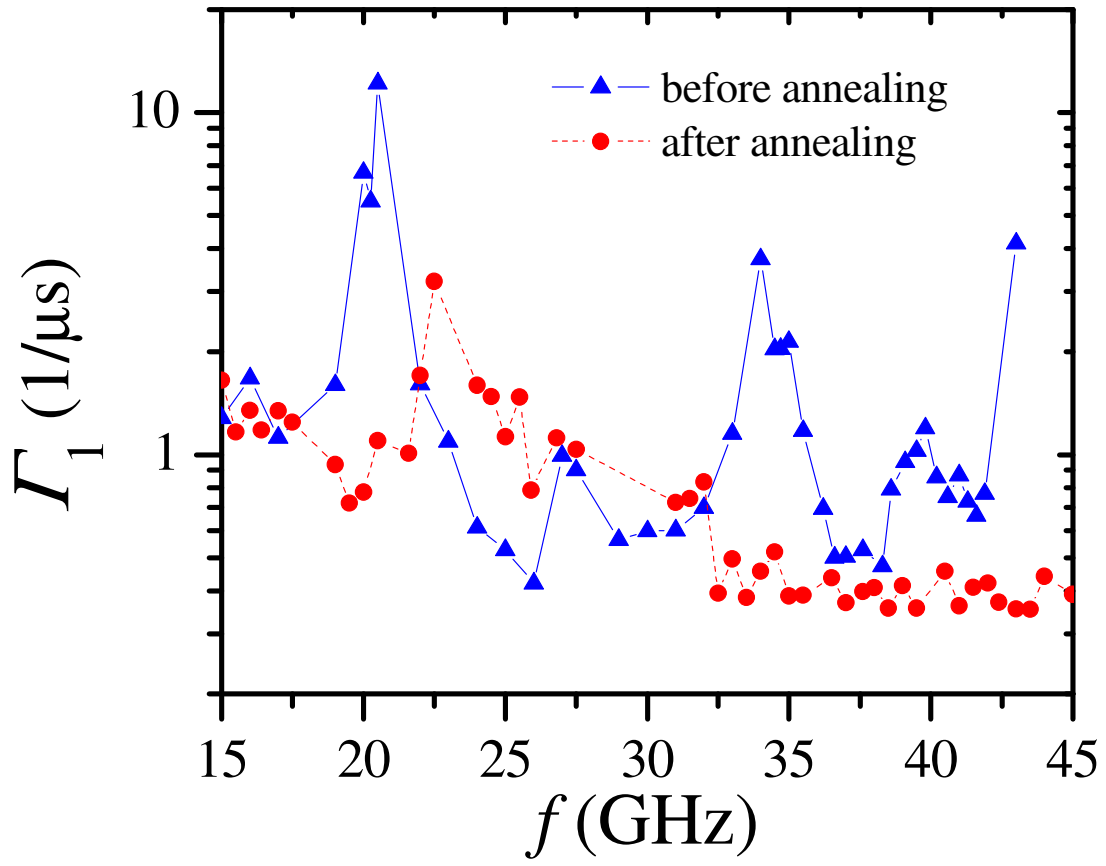

Figure 4.9: Measured decay rate (Γ_1) of excited state of a CPB "SET2" at $E_J/k_B = 0.1$ K as a function of energy level separation after first cooldown (blue triangles) and after the device was warmed up to room temperature and cooled back down to $T = 40$ mK (red circles). The observed peaks in Γ_1 before annealing (20, 34, 39, and 43 GHz) and after annealing (23 GHz) correlate with the location of observed avoided level crossings (see Table 4.1).

4.7 Room Temperature Anneal

In order to investigate the stability of the TLFs, the device was warmed up to room temperature. After "annealing" at room temperature for 14 days, the device was cooled again to 40 mK. I found an avoided crossing associated with one level in the 20 - 50 GHz range and one peak in the decay rate at the same frequency. The new crossings occurred around $f = 23$ GHz and fitting to the charge model gave: $(\varepsilon_b - \varepsilon_a)/k_B = 0.34$ K, $T_{ab}/k_B = 0.52$ K, and $Q_{TLF}\delta x \cos(\eta)/ed = 0.078$ (see Fig. 4.10). We also note that the fluctuators observed here were stable after annealing at 4 K for two days or after placing the device in the normal state by applying a 1 T magnetic field for one hour.

4.8 Conclusion

In conclusion, I observed unintended voltage-dependent transitions and avoided level crossings in the excited state spectrum of a CPB, consistent with charge fluctuators that can tunnel between two locations separated by atomic scale distances in the tunnel junction. The spectra allow us to extract key microscopic parameters of the TLF, such as the tunneling matrix element, and test some theories of fluctuators in these devices [49, 75, 76]. The best fit parameters for the 5 TLF's I observed are summarized in Table 4.1. I also emphasize these are the first measurements of the tunneling rates of TLFs in solid state qubits or other superconducting devices. The hopping distances are at the Angstrom scale, as expected, but the tunneling terms are surprisingly large.

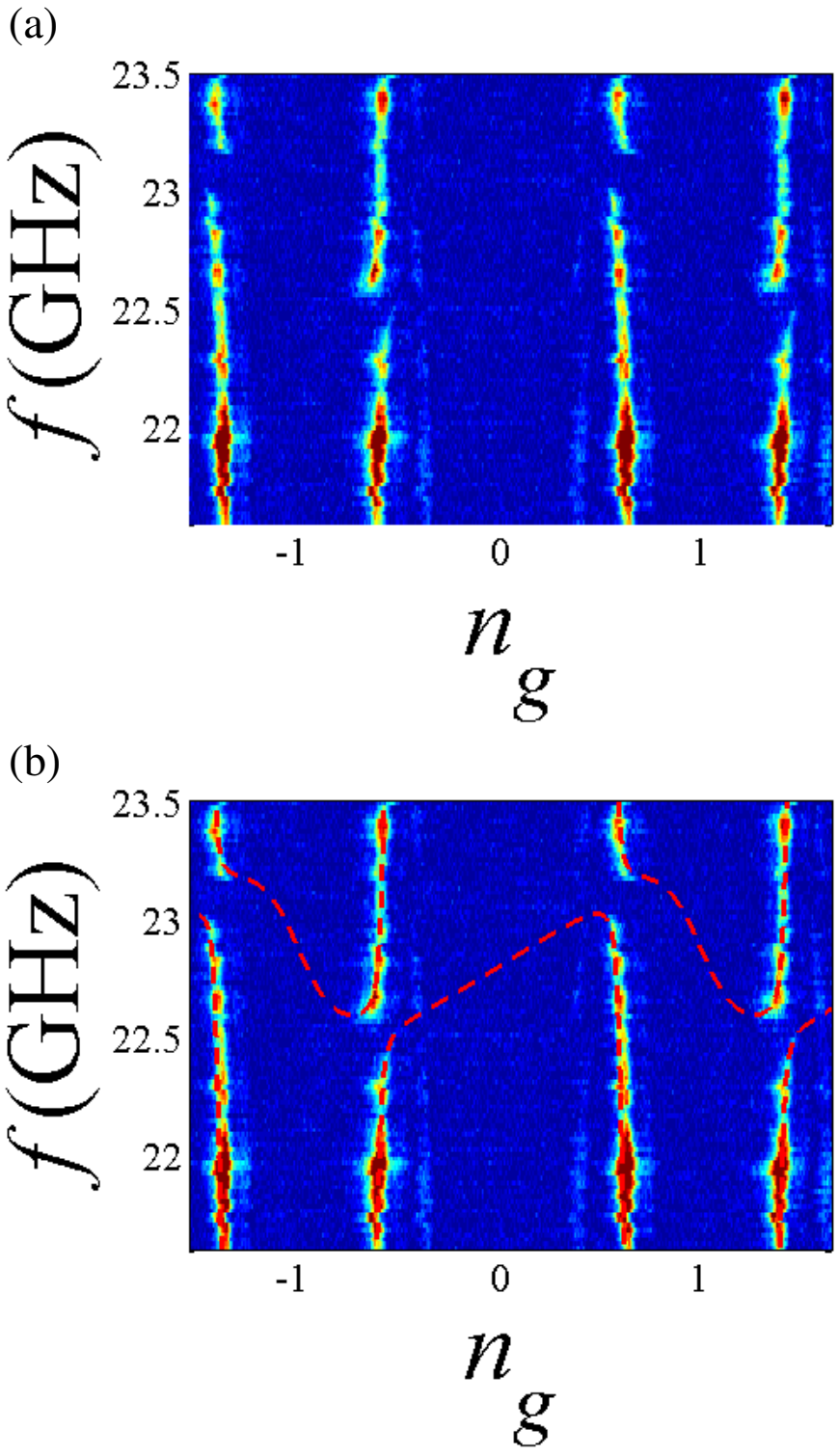

Figure 4.10: CPB spectrum after annealing to room temperature. (a) Avoided level crossings around 23 GHz after annealing to room temperature. Red color represents the excited state of the system with the maximum magnitude of $1e$. Blue color represents the ground state of the system. E_J/k_B=0.55 K. (b) Same as (a) with the predicted spectrum from our system Hamiltonian (red curve) using the parameters in Table 4.1.

Table 4.1: Parameters of observed two-level fluctuators in CPB "SET2". N is the TLF number, f is the frequency near where the avoided level crossing occurs, $n_g^{-/+}$ is the negative and positive reduced gate voltage location of each TLF and $\Delta^{-/+}$ represents the splitting size of the crossing at $n_g^{-/+}$ for the specified value E_J. $(\varepsilon_a - \varepsilon_b)$ is the asymmetry in the potential energy of the TLF in the two wells, $Q\delta x \cos(\eta)/ed$ is the coupling between the TLF and the CPB and T_{ab} is the tunneling term between the two potential wells. For the fluctuator of $N = 3$, the splitting size was too small to resolve. The $N = 5$ fluctuator was measured after annealing at $T = 300$ K for 14 days.

N	f (GHz)	n_g^-	Δ^- (MHz)	n_g^+	Δ^+ (MHz)	E_J/k_B (K)	$(\varepsilon_a - \varepsilon_b)/k_B$ (K)	$Q_{TLF}\delta x \cos(\eta)/ed$	T_{ab}/k_B (K)
1	20	-0.60	30	0.63	10	0.3	0.75	-0.032	0.3
2	34	-0.43	140	0.48	80	1.0	1.43	-0.074	0.39
3	39	-0.34	-	0.36	-	1.1	1.86 - 1.89	-0.083	< 0.17
4	43	-0.26	120	0.25	220	1.1	1.61	0.083	0.65
5	23	-0.57	90	0.58	140	0.55	0.34	0.078	0.52

Chapter 5

Dispersive Read-out: Superconducting Microwave Resonator

5.1 Overview

Compact thin-film superconducting (SC) microwave resonators can achieve very high quality factors due to extremely low loss in the superconductor and substrate. The resonance frequency will be perturbed by coupling to other systems, allowing them to be used as detectors at low temperature. In this chapter, I describe the basic physics of the SC microwave resonator that I used to measure CPB qubits.

The simplest component in a microwave network is a transmission line, which consists of a center line and a ground. Since the transmission line typically has a much longer length l than the wavelength λ of waves it carries, it can be treated as a distributed-parameter network, where voltages and currents vary along the line and in time [77]. If one takes an infinitesimal length Δz of the transmission line, it can be modeled as a lumped-element circuit [see Fig. 5.1 (b)]. The entire transmission line can then be modeled as an infinite series of lumped elements, so called the distributed element model.

For microwave integrated circuits, a planar transmission line is most convenient since it is two-dimensional, compact, low cost, and easily fabricated [77]. The coplanar wave guide (CPW) [78, 79] is commonly used as a transmission line but

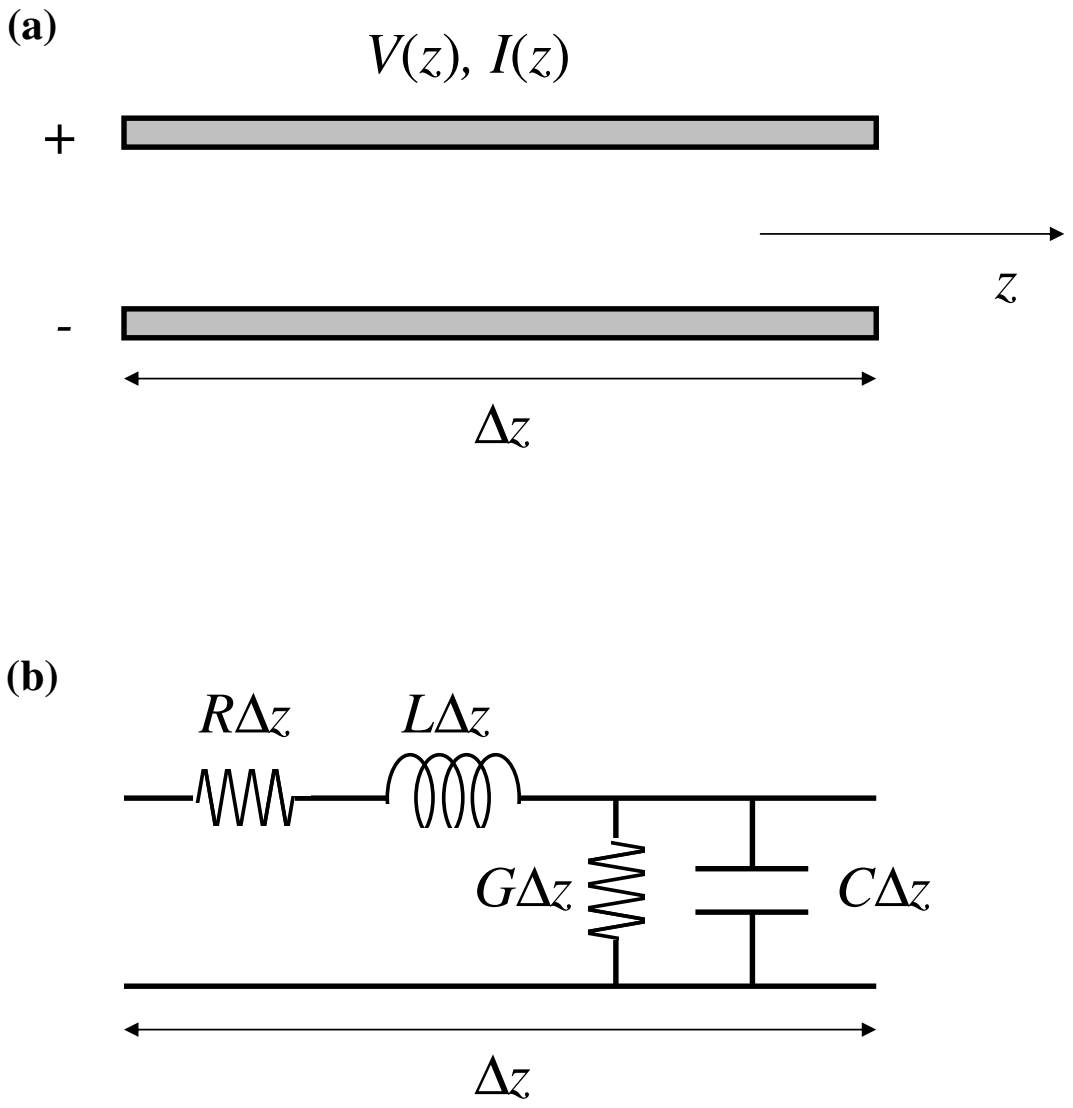

Figure 5.1: Lumped-element model of a transmission line. (a) Top view of two planar conducting wires forming a transmission line. Voltage $V(z)$ and current $I(z)$ from waves propagation in $+$ and $-$ z direction. (b) Lumped-element equivalent circuit of an infinitesimal length Δz of the transmission line [77]. The series resistance R per length is due to the finite conductivity of the conductor, the series inductance L per length is from the total self-inductance of the two conductors, the shunt conductance G per length is due to dielectric loss in the material between the two conductors, and the shunt capacitance C per length is from the close proximity of two conductors.

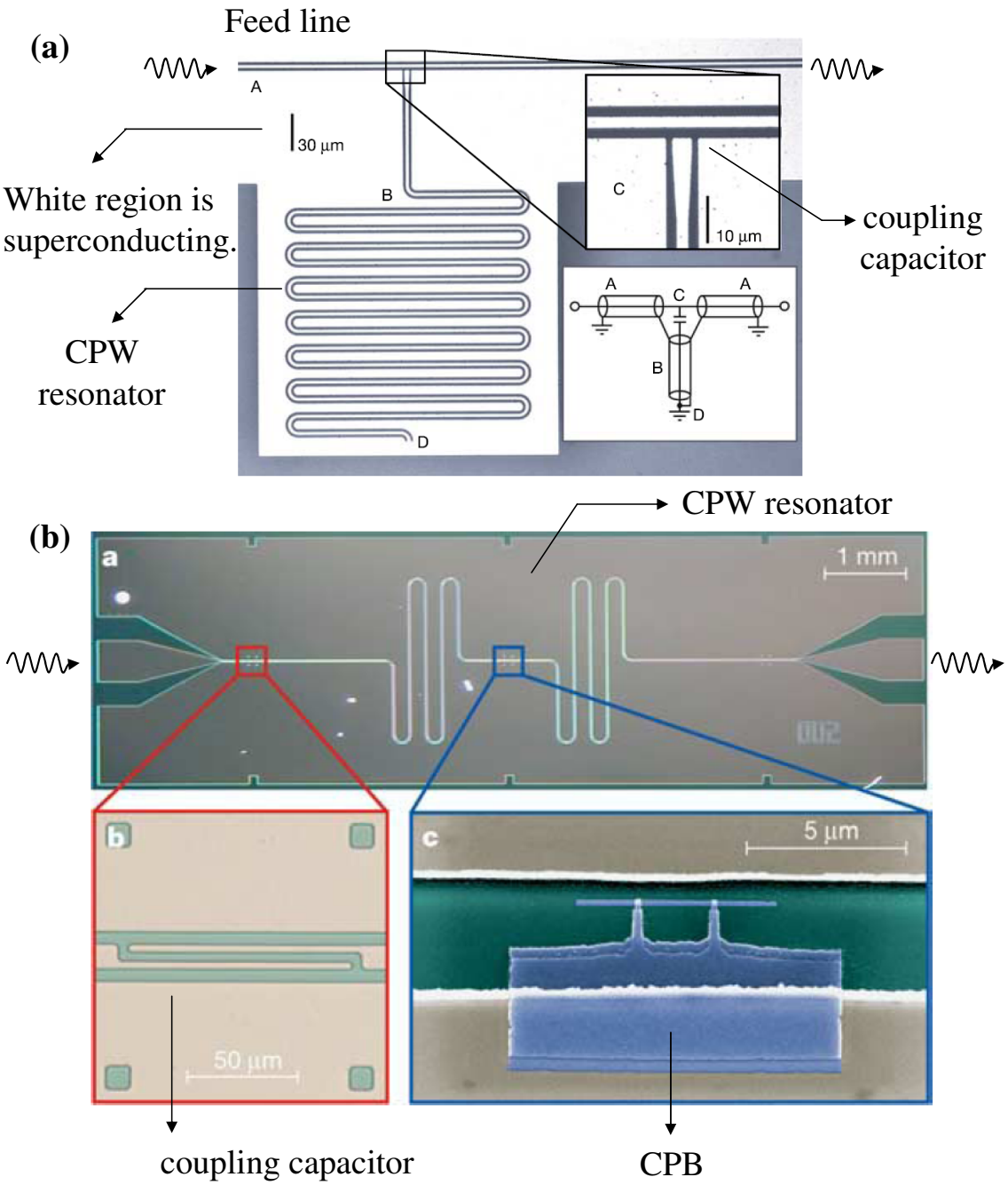

Figure 5.2: Coplanar waveguide (CPW) resonators. (a) A quarter-wavelength ($\lambda/4$) resonator from the Jet Propulsion Laboratory and CalTech [80] and (b) half-wavelength ($\lambda/2$) resonator from Schoelkopf's group at Yale University [19].

it also can be used to make a SC transmission line resonator. One way to make a resonator is to take a CPW transmission line, short one end, and capacitively couple the other end to another transmission line, or feed line [80] [see Fig. 5.2 (a)]. This "quarter-wavelength ($\lambda/4$) resonator" will have resonances when the wavelength is such that there is a current node on the open end and a voltage node at the shorted end, *i.e.* when the length of the resonator $l = (2n+1)\lambda_n/4$, where $n = 0, 1, 2, ...$ The fundamental resonance frequency f_0 is given by $c/4ln_{eff}$, where c is the speed of light in vacuum, $n_{eff} = \sqrt{(\epsilon+1)/2}$ is the effective index of refraction for a CPW, and ϵ is the dielectric constant of the substrate [81]. Another type of CPW resonator is the half-wavelength ($\lambda/2$) resonator [19, 82] [see Fig. 5.2 (b)]. In this case, both ends of the transmission line are open and capacitively coupled to the input and output transmission lines. Thus, resonances will occur whenever $l = n\lambda_n/2$.

Note that both the $\lambda/4$ and $\lambda/2$ resonators have higher harmonics. Houck *et al.* found these higher harmonics can significantly reduce the lifetime of the qubit [24] due to the Purcell effect [84], which enhances the spontaneous emission of the qubit.

To couple to a CPB qubit without these higher harmonics, I built a quasi-lumped element resonator [see Fig. 5.3 (b)]. This lumped-element resonator has physical dimensions that are smaller than the operating wavelength so that the variation of the voltage and current is minimized along the resonator. Ideally, this leads to a single resonance frequency and makes it possible to read far-detuned qubit states. Moreover, by minimizing the Purcell effect from higher harmonics, the coherence time of a qubit coupled to the resonator should increase.

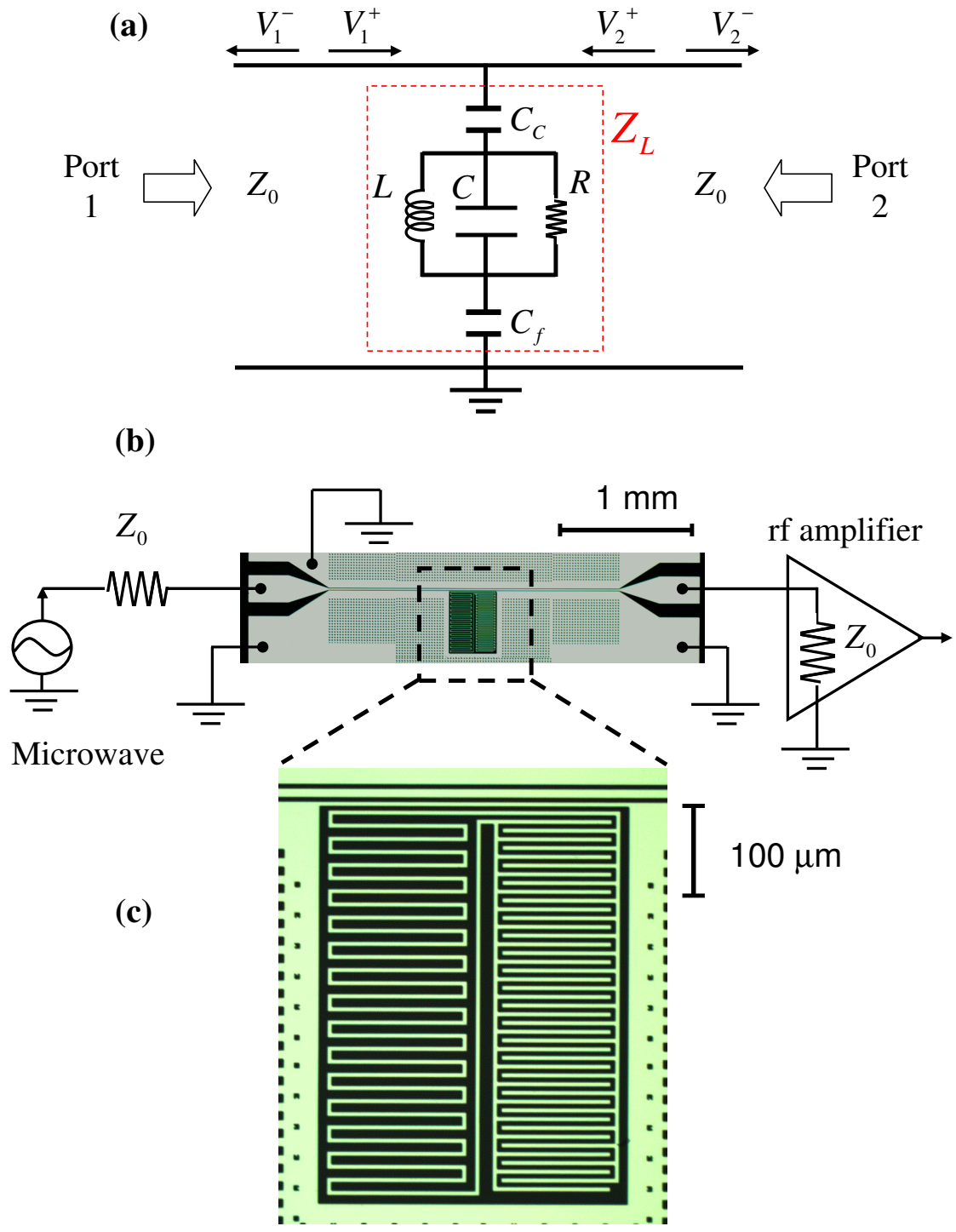

Figure 5.3: (a) Schematic of a lumped-element resonator coupled to a two-port network. The expected L and C from the geometry were 2 nH and 400 fF, respectively [30, 79]. (b) Schematic of the wiring and the device picture. The transmission line is connected to two matched loads Z_0 in the microwave source and the input of the rf amplifier. (c) Zoom-in of the resonator image. The green color is Al metal and black is the sapphire substrate.

5.2 Circuit Model of the Resonator and the S-Parameters

5.2.1 S-Parameters

The scattering matrix describes an N-port network and relates voltage waves incident on the ports to those reflected from the ports. The matrix elements of the scattering matrix are called S-parameters [77], which can be directly measured by a vector network analyzer.

Consider the two-port network shown in Fig. 5.3 (a), where port 1 is on the left side of the resonator and port 2 is on the right side of the resonator. The incident voltage waves towards the resonator are defined as V_1^+ and V_2^+ from the two ports and the reflected voltage waves from the resonator are defined as V_1^- and V_2^- for the two ports. Those waves are related by the scattering matrix $[S]$ as [77]

$$\begin{bmatrix} V_1^- \\ V_2^- \end{bmatrix} = \begin{bmatrix} S_{11} & S_{12} \\ S_{21} & S_{22} \end{bmatrix} \begin{bmatrix} V_1^+ \\ V_2^+ \end{bmatrix}, \tag{5.1}$$

where the matrix element S_{ij} is determined as

$$S_{ij} = \left[\frac{V_i^-}{V_j^+} \right]_{V_k^+=0 \ for \ k \neq j}. \tag{5.2}$$

Thus, S_{ij} is obtained by measuring V_i^- with the incident wave V_j^+ and all other incident waves zero, or terminated by matched loads Z_0 to avoid reflections. Hence, $S_{11} = V_1^-/V_1^+$ and $S_{21} = V_2^-/V_1^+$ with $V_2^+ = 0$. And $S_{12} = V_1^-/V_2^+$ and $S_{22} = V_2^-/V_2^+$ with $V_1^+ = 0$.

Another useful set of parameters in the two-port network are the ABCD pa-

rameters, which are the elements of the ABCD matrix [77]. The ABCD matrix is particularly useful when one has a cascade connection of two-port networks, because the response of a cascaded network can be found by multiplying the matrices of individual two-port networks. The ABCD matrix is defined by the total voltages and currents at the input and output ports and is given by

$$\begin{bmatrix} V_1 \\ I_1 \end{bmatrix} = \begin{bmatrix} A & B \\ C & D \end{bmatrix} \begin{bmatrix} V_2 \\ I_2 \end{bmatrix}, \tag{5.3}$$

where $V_n \equiv V_n^+ + V_n^-$ and $I_n \equiv I_n^+ - I_n^-$. The ABCD parameters are listed in Table 4.1 in the book by D. Pozar [77] for various two-port circuits. Pozar also gives the conversion between ABCD parameters and S-parameters (see table 4.2 ref [77]). For example, one finds that

$$S_{22} = \frac{-A + B/Z_0 - CZ_0 + D}{A + B/Z_0 + CZ_0 + D} \tag{5.4}$$

and

$$S_{21} = \frac{2}{A + B/Z_0 + CZ_0 + D}. \tag{5.5}$$

5.2.2 Loaded Parallel RLC Resonator

Our parallel RLC resonator is physically and galvanically floated from the surrounding ground plane [see Fig. 5.3 (c)]. This allows one to capacitively bias the resonator to a finite dc voltage, which is useful for biasing a CPB. The resonator is in turn coupled to a transmission line. Note that a narrow ground strip is physically located between the transmission line and resonator. The ground strip had a width

of 5 μm and its presence reduced the coupling between the resonator and transmission line by a factor of approximately 7. The coupling likely has both capacitive and inductive components, but in this thesis I assumed capacitive coupling to model the impedances and S-parameters. For this model, I included capacitances C_c and C_f from the resonator to the transmission line and to the ground plane, respectively [see Fig. 5.3 (a)].

The resonator has a quasi-lumped inductor (L) on the left side and a quasi-lumped capacitor (C) on the right side [see Fig. 5.3 (c)]. The capacitor has an interdigital structure and the inductor has a meander structure. Two closely spaced wires connect the two sides.

Our lumped-element resonator circuit has an impedance Z_L formed from a series connection of the parallel RLC resonator and the two capacitors C_c and C_f [see Fig. 5.3 (a)]. From Table 4.1 in Pozar [77], one finds the ABCD matrix:

$$\begin{bmatrix} A & B \\ C & D \end{bmatrix} = \begin{bmatrix} 1 & 0 \\ 1/Z_L & 0 \end{bmatrix}, \tag{5.6}$$

where Z_L is given by

$$Z_L = \frac{1}{i\omega C_c} + \frac{1}{i\omega C_f} + \frac{1}{\frac{1}{i\omega L} + i\omega C + \frac{1}{R}}. \tag{5.7}$$

We expect the impedance of C_f around the resonance frequency to be much smaller than the other impedances, so Z_L can be approximated as

$$Z_L \simeq \frac{1}{i\omega C_c} + \frac{1}{\frac{1}{i\omega L} + i\omega C + \frac{1}{R}}. \tag{5.8}$$

Given the ABCD parameters in Eq. 5.6, the S-parameters for our resonator can then be found from Eqs. 5.4 and 5.5:

$$S_{22} = -\frac{Z_0}{2Z_L + Z_0} \tag{5.9}$$

and

$$S_{21} = \frac{2Z_L}{2Z_L + Z_0}. \tag{5.10}$$

Note $S_{11} = S_{22}$ and $S_{12} = S_{21}$ based on the symmetry of the circuit. From Eqs. 5.9 and 5.10, one can also find that $S_{21} = 1 + S_{22}$.

Insertion of Z_L (Eq. 5.7) into S_{22} (Eq. 5.9) yields

$$S_{22} = -\frac{\zeta}{\frac{1}{i\omega L} + i\omega(C + C_c) + \frac{1}{R} + \zeta}, \tag{5.11}$$

where

$$\zeta = i\omega C_c \left(\frac{1}{i\omega L} + i\omega C + \frac{1}{R}\right)\frac{Z_0}{2}. \tag{5.12}$$

Note that the loaded resonance frequency is defined as $\omega_0^2 = 1/L(C + C_c)$ and I also define $\omega = \omega_0 + \Delta$, where Δ is the detuning. $i\omega(C + C_c)$ can be rewritten as $i(\omega_0 + \Delta)/\omega_0^2 L$. And $\omega^{-1} = \omega_0^{-1}(1 + \Delta/\omega_0)^{-1} \simeq \omega_0^{-1}(1 - \Delta/\omega_0)$ for $\Delta \ll \omega_0$. Then, $1/i\omega L$ in the denominator of Eq. 5.11 can be approximated as $1/i(\omega_0 + \Delta)L \simeq (1 - \Delta/\omega_0)/i\omega_0 L$, which leads to the following approximation

$$\frac{1}{i\omega L} + i\omega(C + C_c) \simeq i\frac{2\Delta}{\omega_0^2 L}. \tag{5.13}$$

If we assume the detuning is small and that $\omega \simeq 2\pi \times 5$ GHz and C_c =4 fF,

then $R \gg \omega C_c$ and ζ can be approximated as

$$\zeta \simeq \left(\frac{C_c}{L} - \omega^2 C_c C \right) \frac{Z_0}{2}. \tag{5.14}$$

One can also rewrite $C_c/L = C_c(C + C_c)/L(C + C_c) = \omega_0^2 C_c(C + C_c)$. Near the resonance, $\omega \simeq \omega_0$ so that $\zeta \simeq (\omega C_c)^2 Z_0/2$. I can now define the external impedance R_e as

$$\frac{1}{R_e} = \frac{(\omega C_c)^2 Z_0}{2}. \tag{5.15}$$

We can then rewrite S_{22} in Eq. 5.11 as

$$S_{22} \simeq -\frac{1/R_e}{i\dfrac{2\Delta}{\omega_0^2 L} + \dfrac{1}{R} + \dfrac{1}{R_e}}. \tag{5.16}$$

By defining $1/R_L = 1/R + 1/R_e$ and multiplying R_L in both the numerator and denominator of Eq. 5.16, S_{22} becomes

$$S_{22} \simeq -\frac{R_L/R_e}{1 + i\dfrac{R_L}{\omega_0 L}\dfrac{2\Delta}{\omega_0}}, \tag{5.17}$$

or

$$S_{22} \simeq -\frac{Q_L/Q_e}{1 + iQ_L\dfrac{2(\omega - \omega_0)}{\omega_0}}, \tag{5.18}$$

where $Q_L = R_L/\omega_0 L$ is the loaded or total Q and $Q_e = R_e/\omega_0 L$ is the external Q. The internal Q, $Q_i = R/\omega_0 L$, can be obtained from $1/Q_i = 1/Q_L - 1/Q_e$.

Since $S_{21} = 1 + S_{22}$, from Eqs. 5.9 and 5.10 we find

$$S_{21} = 1 - \frac{Q_L/Q_e}{1 + iQ_L\dfrac{2(\omega - \omega_0)}{\omega_0}}. \tag{5.19}$$

In our system $|S_{21}|$ is just the ratio of the "output voltage" to the "input voltage"

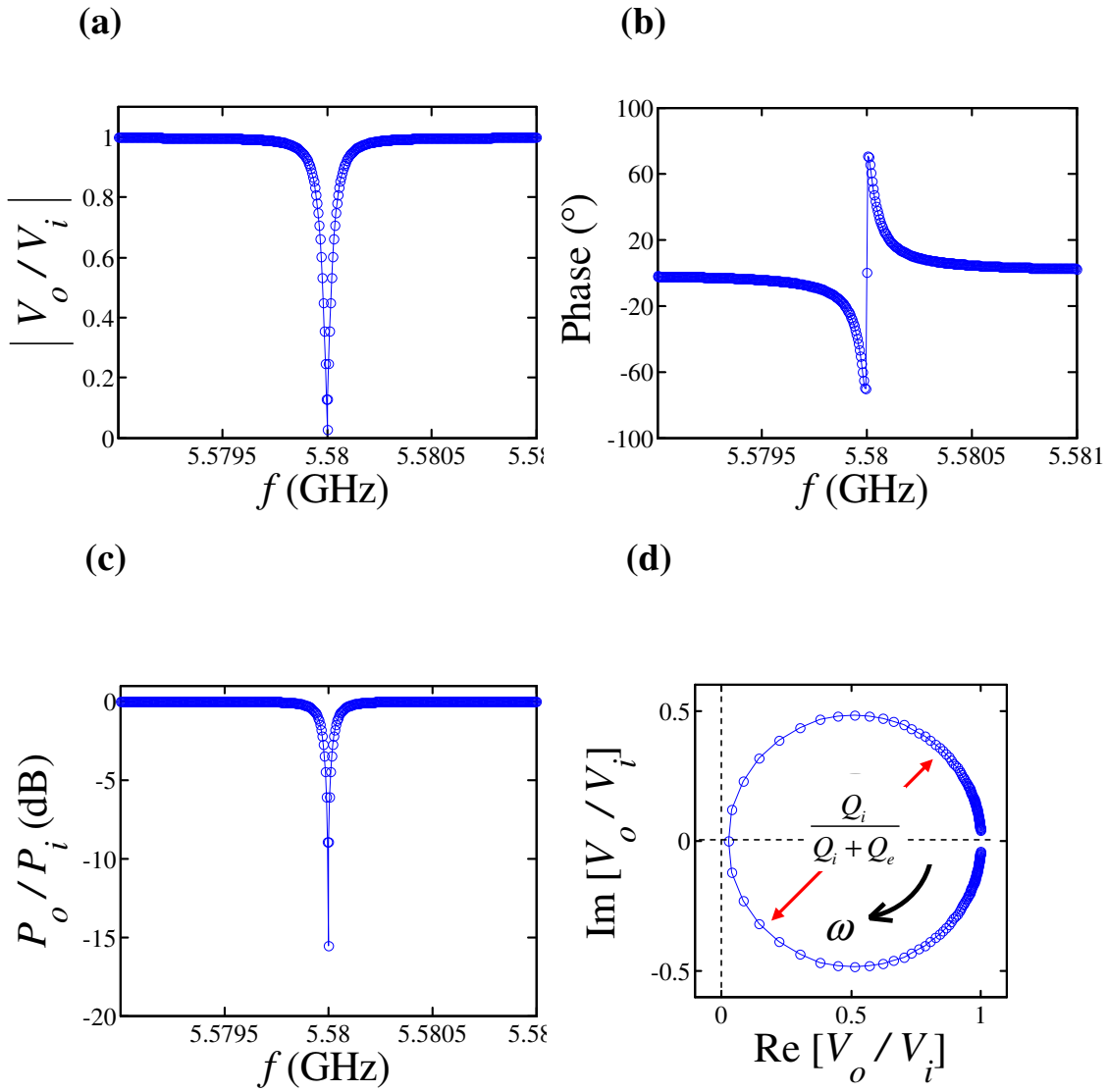

Figure 5.4: Theory plots of the resonator resonance. (a) $|S_{21}|$ from Eq. 5.19, (b) phase from Eq. 5.28, (c) P_o/P_i from Eq. 5.20, and (d) circle from Eq. 5.26 and 5.27. For the plots, I used following parameters: Q_L=70,000, Q_e=72,000, and $\omega_0/2\pi$=5.58 GHz. The resulting Q_i=2,520,000 from Q_L and Q_e.

$|S_{21}| = |V_0/V_i|$ [see Fig. 5.4 (a)]. The ratio of transmitted power to the input power through the resonator is $|S_{21}|^2$ [see Fig. 5.4 (c)] and is given by

$$\frac{P_o}{P_i} = \left| 1 - \frac{Q_L/Q_e}{1 + iQ_L \dfrac{2(\omega - \omega_0)}{\omega_0}} \right|^2 . \tag{5.20}$$

For additional discussion of Fig. 5.4, see section 5.4.3.

5.2.3 Microwave Office Simulation

A lumped-element resonator has a smaller size than the wavelength at the resonance frequency. This requires using a complex geometry compared to that of a typical CPW $\lambda/4$ or $\lambda/2$ resonator. Our resonator is surrounded by a ground plane and is coupled to the transmission line. Accurate physical simulations of the resonator are essential to understanding its behavior. This design is similar to another existing resonators designed by Kevin Osborn. This new design differs from those designs in that it is not connected to the ground plane.

To aid in the simulation and design of the resonator, I used Microwave Office (by AWR) [85]. Microwave Office is a planar-3D microwave simulator, which allows faster simulation times compared to a full 3D microwave simulator such as HFSS (High Frequency Structure Simulation) [86].

To simulate the Al films in the resonator, I used a "perfect metal" with thickness of 100 nm. For the sapphire substrate, I used an insulator with a dielectric constant of $\epsilon = 10.7$, loss tangent of 5×10^{-6}, and thickness of 500 μm. Above the metal surface I set the dielectric constant to its vacuum value $\epsilon = 1$. The simulation

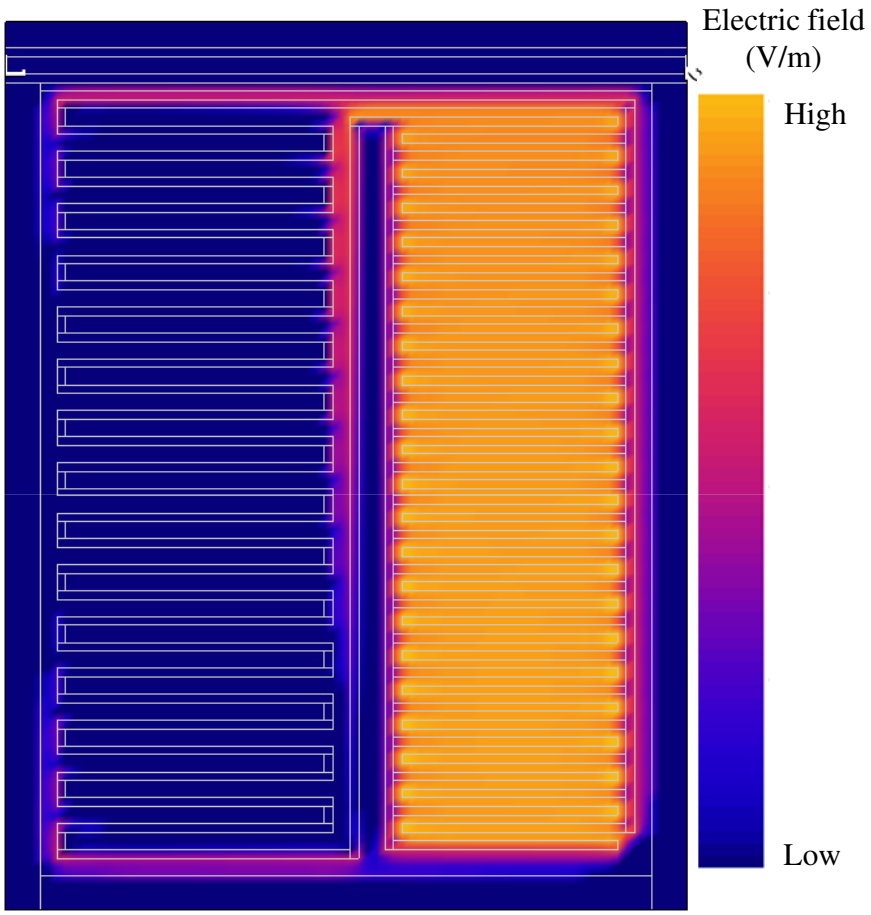

Figure 5.5: Electric field simulation by Microwave Office of a lumped-element resonator driven on resonance.

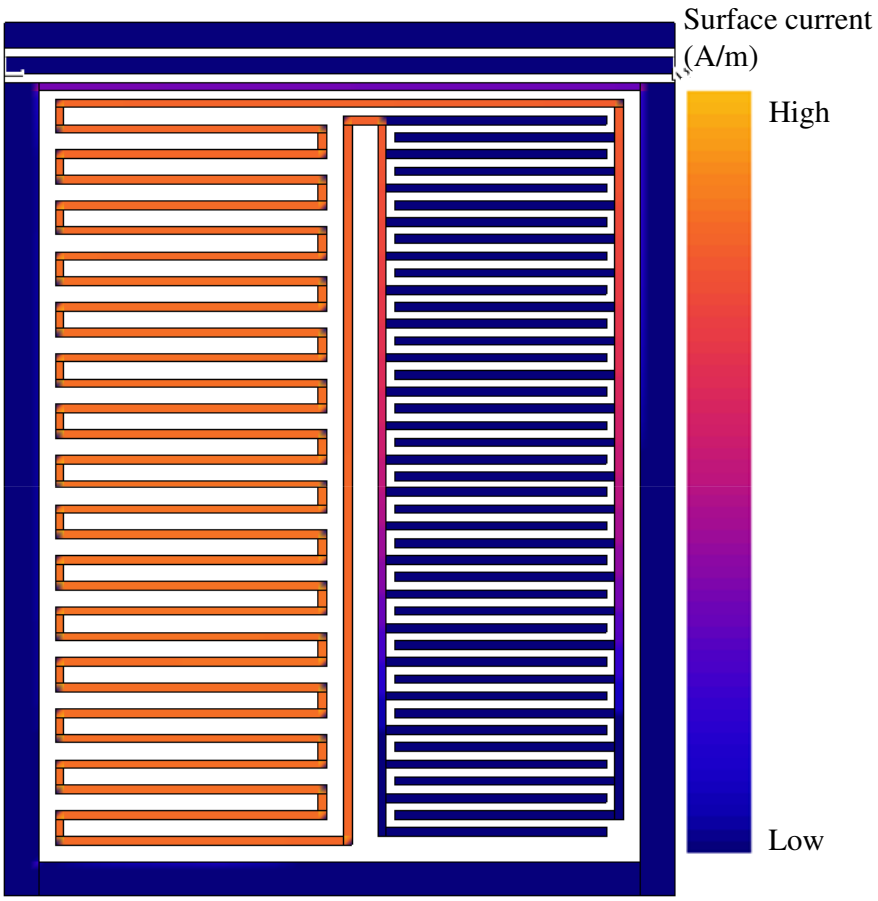

Figure 5.6: Current simulation by Microwave Office of a lumped-element resonator driven on resonance.

volume extended 500 μm above the Al metal layer and was defined by a perfect conductor. For fast simulations, I typically simulated the area just around the resonator (see the simulation area in Fig. 5.5). The cell size for the simulation was 5 μm by 5 μm, which was the minimum feature size in the resonator. This gave a typical simulation time of about 5 minutes. I also tried reducing the cell size to 1 μm by 1 μm and found no significant differences except a longer simulation time.

I used some measurements of quarter-wavelength resonators (on the same type of sapphire) to define the dielectric constant of $\epsilon = 10.7$. The simulated resonance frequency was approximately 5.555 GHz, which deviated 5 % from the measured resonance frequency. Since the dielectric loss determined the internal quality factor (Q_i) of the resonator in the simulation, I simulated the resonator with different dielectric losses of the substrate: $\tan\delta = 0$, 10^{-6}, 5×10^{-6}, 10^{-5}, and 10^{-4}. As expected, the dielectric loss did not affect the external quality factor (Q_e) of the resonator, which was approximately $Q_e \sim 45{,}000$. Using the single model of capacitive coupling between the resonator and transmission line (*i.e.* Eqs. 5.15 and 5.19) yielded $C_c = 3.42$ fF for the coupling capacitance.

Microwave Office also provides a 2D simulation of the electric fields in the dielectrics and currents in the metals. Figure 5.5 shows that the E-field is mainly concentrated in and distributed evenly over the capacitor on resonance. Figure 5.6 shows the corresponding even distribution of currents through the meandering inductor at $f = f_0$. These simulations confirmed that the design was acting as a quasi lumped-element resonator. Microwave simulations of this resonator show no other mode up to $f = 28.3$ GHz.

5.3 Fabrication

In this section, I describe the fabrication of the resonator and the CPB qubit. All processes were done at LPS.

After modeling the resonator in Microwave Office, the design was imported into a CAD program (L-Edit), which I used to design the mask pattern for individual cells and chips for a 3-inch wafer. Our standard cell or chip size was about 5 mm by 5 mm and I left about 250 μm between adjacent cells. One 3-inch wafer contained about 100 chips typically. Once the layout was finalized, I exported it into GDS format for an optical mask and submitted an order to Microtronics, Inc. [87]. The 4-inch by 4-inch soda-lime quartz mask had chrome features with the same scale as the final features.

Two optical lithography masks were ordered: one for an Al layer and another for a Ti/Au layer. The Al layer was for the resonator and the Ti/Au layer was for leads of a SET and alignment markers. The SET and CPB were made by e-beam lithography; I used the SET to estimate the junction resistances of the CPB (see section 5.3.6).

5.3.1 Optical Lithography for defining the resonator

The optical lithography was done by conventional techniques in the LPS clean room. I used a programmable spinner at 3000 RPM for 60 seconds in the fume hood in order to spin the photo resist on the wafer [see Fig. 5.7 (a)]. For both the Al and Ti/Au layers, I used a single layer resist (Futurrex, NR9-1000PY), which provides a

(a)

Spinner and hot plates

(b)

Contact aligner
(Karl Suss MJB3)

(c)

E-beam evaporator
(CHA : Mark – 40)

(d)

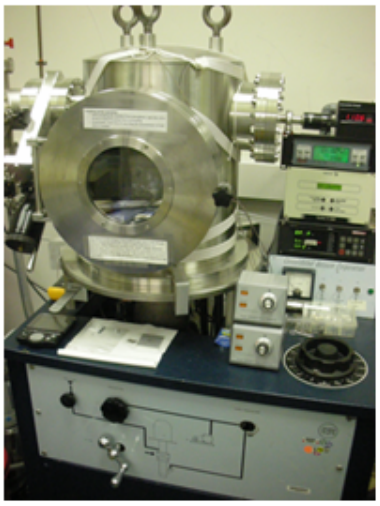

Thermal evaporator

Figure 5.7: Equipment for fabrication. (a) Spinner and hotplates in the clean room, (b) contact aligner in the clean room, (c) E-beam evaporator "CHA" in the clean room, and (d) thermal evaporator.

(a)

Dicing Saw
(Disco-DAD 321)

(b)

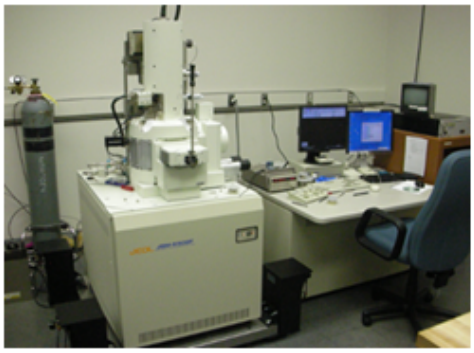

E-beam writing SEM
(JEOL-6500F)

(c)

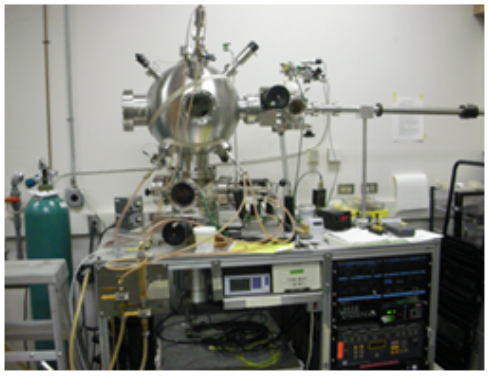

E-beam evaporator

(d)

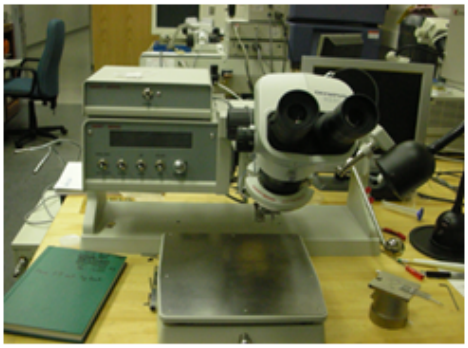

Wire bonder
(West-Bond)

Figure 5.8: Equipment for fabrication. (a) Dicing saw, (b) E-beam writing SEM, (c) E-beam evaporator "Sputnik", and (d) wire-bonder.

sufficient undercut for lifting off the deposited metal. After spinning the resist, the wafer was baked on a hot plate at 160°C for 3 minutes 30 seconds in a fume hood. Exposure of UV light through the optical mask was done on a Karl Suss contact aligner [see Fig. 5.7 (b)]. The wafer was then post-baked on a hot plate at 120°C for 3 minutes 30 sec, then developed in RD6 developer for 12 sec, rinsed with distilled water, and then dried with dry nitrogen. To deposit the Ti/Au layer, I used the CHA electron beam evaporator with metal pockets [see Fig. 5.7 (c)].

For the Al deposition, I used a thermal evaporator [see Fig. 5.7 (d)]. This thermal evaporator was mostly dedicated to aluminum and used a turbo molecular pump from Varian (Turbo-V550) and a scroll pump from Varian. The vacuum pressure in the main chamber reached 2×10^{-7} Torr measured by an ion gauge (Varian: SenTorr). The current through the tungsten e-beam filament was controlled manually to maintain a deposition rate of 5.5 Å/s at the deposition rate monitor (Sycon: STM-100). After depositing about 100 nm of Al from the tungsten boat, the chamber was vented, the boat was replaced, and two pure Al pellets (AL-0605, 99.9995 %, 4.74 mm diameter by 10 mm long, from Atomergic Chemetals Corp.) were added in preparation for another sample. Once the chamber was vented, it typically took a day to pump on the main chamber and reach base pressure. This thermal evaporator also supports double-angle evaporation; it has a load-lock chamber and rotatable feed-through.

Dielectric loss in the substrate can limit the internal quality factor of the resonator and could affect the qubit as well. Single crystal sapphire has very low dielectric loss at low drive voltages and low temperatures. With this in mind,

we used c-plane oriented single-side-polished sapphire wafers with a thickness of 0.43 mm (Kyocera Industrial Ceramics Co.). For the optical lithography, I used a negative lift-off resist (NR9-1000PY) (see detailed recipe in Appendix A). I had some trouble with adhesion of the Al and undercut with this resist and the sapphire wafers. With silicon wafers, I did not have these problems and we suspected that it was due to the transparency of the sapphire. One way to solve the issue is to deposit Al initially and then etch the Al layer. For etching the Al layer, I deposited Al on the substrate first by either the thermal evaporator or CHA system with a thickness of 100 nm. I checked the adhesion of the Al layer by using the wire-bonder to make sure the adhesion was good. I then spun positive photo resist (OiR 906-10) on the wafer and did photolithography (see the recipe in Appendix A). Another advantage of the etching method over lift-off techniques is that a smooth sidewall can be obtained.

5.3.2 Sample Preparation for Electron Beam Lithography

After depositing Al and Ti/Au, the wafer was ready for electron-beam (e-beam) lithography. The SEM is the most common method in research laboratories for fabricating sub-micron features [see Fig. 5.8 (b)]. I used two layers of E-beam resist: ZEP 520A DR2.3 on the top and MMA(8.5)MMA EL11 for the undercut on the bottom [see Fig. 5.10 (a)]. The thickness of ZEP and MMA was about 120 nm and 850 nm, respectively. They have different sensitivities to E-beam exposure and require different developers [42, 43]. To prevent charging by the electron

beam, which occurs with an insulating substrate, we deposit a 12.5 nm thick "anti-charging" layer of Al on top of the resist by thermal evaporation before E-beam writing. We do not use the E-beam evaporator for the anti-charging layer since the E-beam resist could be exposed to scattered electrons before e-beam writing.

After depositing the anti-charging layer, the wafer was diced. Before dicing the wafer, the resists and anti-charging layer was protected by a layer of "blue resist" (FSC-M) (see recipe in Appendix A). LPS has a dicing saw [see Fig. 5.8 (a)] and we used diamond blades (Dicing Blade Technology). The blade was a Hubbed Resinoid type, which was permanently bonded to the hub and does not need a flange. The choice of the blade depends on the material being cut. To dice single crystal quartz and sapphire, we used a CX-010-325-080-H blade. For silicon and fused quartz, we used a CX-010-600-080-H. The rotation speed of our blade was 22,000 rpm. The feed speed for dicing also depends on the material. For silicon and fused quartz, the feed speed was 3 mm/s. For single crystal quartz, the feed speed was 1.25 mm/s. For single crystal sapphire, the feed speed was 0.75 mm/s. When I used a feed speed of 3 mm/s for sapphire, I found many cracks on the wafer. One day, I found a lot of unknown material stuck to the wafer surface and suspected someone had used the saw to dice an inappropriate material, which covered the dicing saw. After that, I usually inspected the dicing saw (or sprayed water) around the blade chuck. The wafer was fastened to the sample chuck in the dicing saw using double-sided tape (ADWILLD-520T from ADWILL, Lintec). Any air bubbles should be removed between the wafer and tape, otherwise the tape may release chips during dicing. The dicing saw has a calibration process (Hairline alignment) in which the

machine calibrates the position of the wafer after a test cutting.

Once the wafer was diced, I removed the individual chips and cleaned them with Acetone, Methanol, and IPA for 1 minute each to remove the resist (FSC-M). Any insulating residue could cause charging in the SEM, hence this needs to be removed completely. I had the impression that when I stored the cleaned chip in the dry box in the lab (not clean room) for more than a month, the E-beam resist cracked after developing. I suspect the "blue resist" (FSC-M) protected the E-beam resist from air. So, I liked to keep the chip with blue resist in the clean room and I cleaned chips only when I was ready to perform e-beam lithography.

5.3.3 Electron Beam Writing

For E-beam writing, I used a JEOL 6500 SEM [see Fig. 5.8 (b)] with an acceleration voltage of 30 kV. Maximum magnification is 500,000 and I imaged a contamination spot to obtain a good focus. This SEM was also used to take device images. For E-beam writing, I used the program Nanometer Pattern Generation System (NPGS) [88], which controls the SEM. NPGS requires that the design be in DesignCAD format. I imported my CAD drawings into Design CAD using LinkCAD. NPGS supports two layouts: alignment and pattern. After importing my CAD drawing into DesignCAD, I created a Run file in NPGS, which contains the exposure parameters: magnification, beam current, line dose (nC/cm), and area dose (nC/cm^2). Typical parameters during e-beam lithography were a magnification for the writing equal to 900, beam current of 17 pA, and line dose of 8 nC/cm for

the CPB and SET. The Run file executes an alignment layout first and then the pattern layout. Using the alignment layout, one can adjust the position of the beam relative to my Ti/Au alignment markers [see squares with size of 4μm by 4μm in Fig. 5.9 (b) and (c)]. Then, NPGS processes the pattern layout to write the E-Beam pattern based on the position of the alignment markers. One thing to be careful about is to place the alignment markers away from the patterns by more than 30 μm, since the beam also exposes the resist during the alignment and the exposed area is large compared with the size of the alignment markers [see the white area (Al) around the alignment makers in Fig. 5.9 (c)].

Initially, I used Al for the resonator and alignment markers. I found that it was really hard to see a thin Al layer on the sapphire wafer using the SEM and this made it hard to even find the alignment markers. This happens because Al is a low Z material and does not produce many secondary electrons that the SEM detects for imaging. I also tried a low acceleration voltage and the backscattering detector instead of the secondary electron detector, and tried using the coordinates of the resonator to find the alignment markers. I also tried using a very sharp tip to make a mark on the alignment markers. These methods did not help very much and eventually I settled on using Ti/Au marks. This meant I had to use two masks and two depositions; one for the Al resonator and another for the Ti/Au alignment marks.

Once I finished the E-beam writing, I went to the clean room to develop the two E-beam resists (see recipe in Appendix A). The develop time for ZEP was fixed at 3 minutes, while the develop time for MMA could be varied depending on the

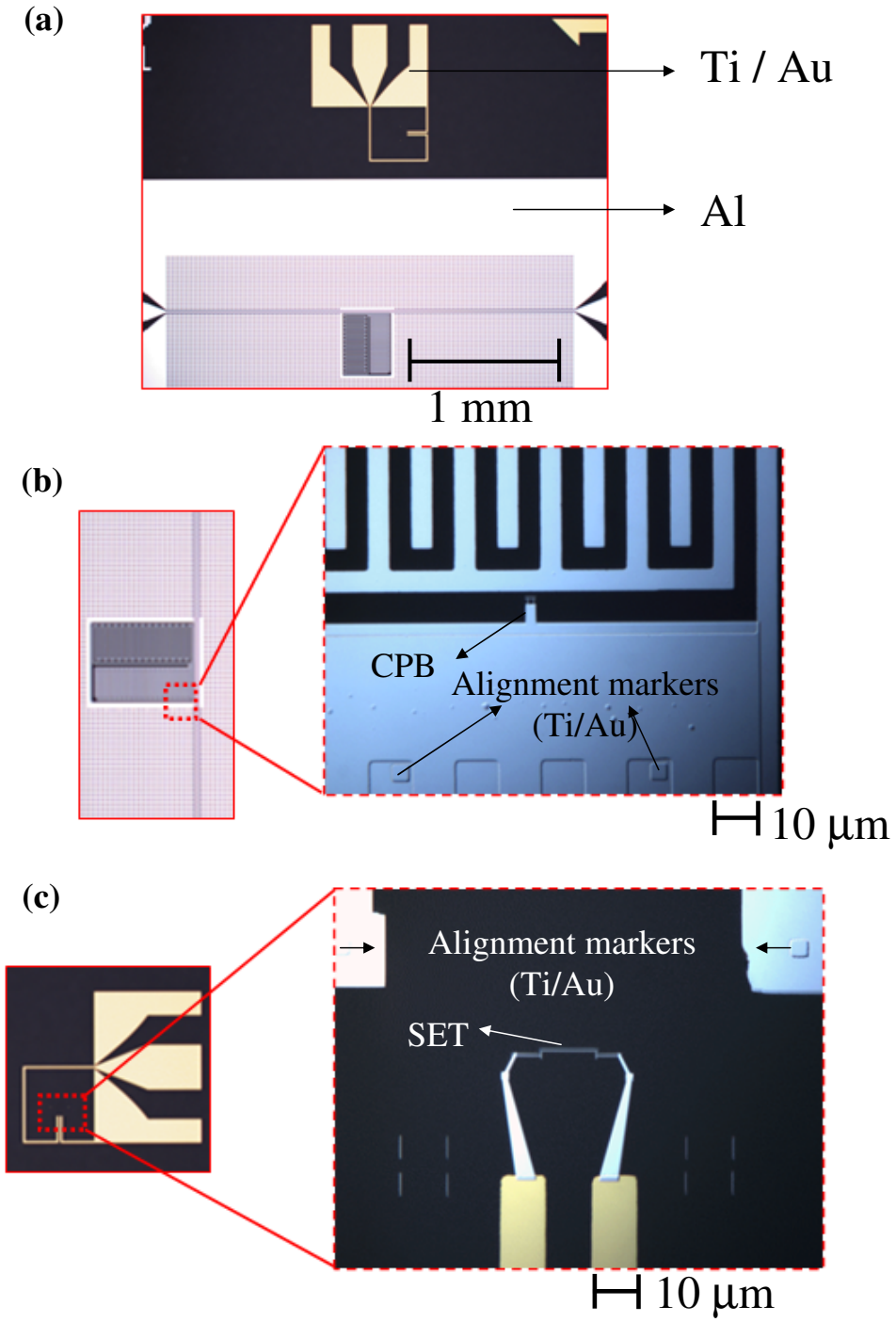

Figure 5.9: Device images. (a) Chip image showing the CPW for SET and the resonator, (b) CPB by E-beam lithography, and (c) SET by E-beam lithography.

desired undercut.

5.3.4 Double-Angle Evaporation

I used standard double-angle evaporation of Al with an intervening oxidation step to form an AlO_X tunnel barrier between the two Al depositions [71] (see the sequence of process steps in Fig. 5.10). Our E-beam evaporator, which we have nicknamed "Sputnik" to distinguish from the CHA system, was used for my devices. It has a turbo pump (Varian: Turbo-V1000HT), one scroll pump (Varian: SH-110) to back up the turbo molecular pump, and another scroll pump to evacuate the load-lock chamber. Sputnik consists of two chambers: a main chamber (for crucible stages and a hemispherical cage) and a load-lock chamber. The base pressure of the main chamber can reach 8×10^{-8} Torr. There are four crucibles for different materials, but I only used an Al crucible. I put two pellets, which are the same type of pellets I used for the thermal evaporator, in an intermetallic crucible, which is reachable by long tweezers from the nearest small window.

The electron beams ejected from a tungsten filament were deflected by a magnet toward the center of the crucible. The E-beam power supply (e-Vap: CVS-3 (3kW)) was set to 5.36 kV, which was the optimum accelerating voltage to center the beam on the crucible. Heated Al atoms evaporate toward the hemispherical cage. The temperature of the crucible is high enough to melt Al (the melting point of Al$\simeq 660°$C), so it needs to be water-cooled. There's a shutter to block unwanted Al right above the crucible. The deposition rate monitor (Inficon XTM/2) measures

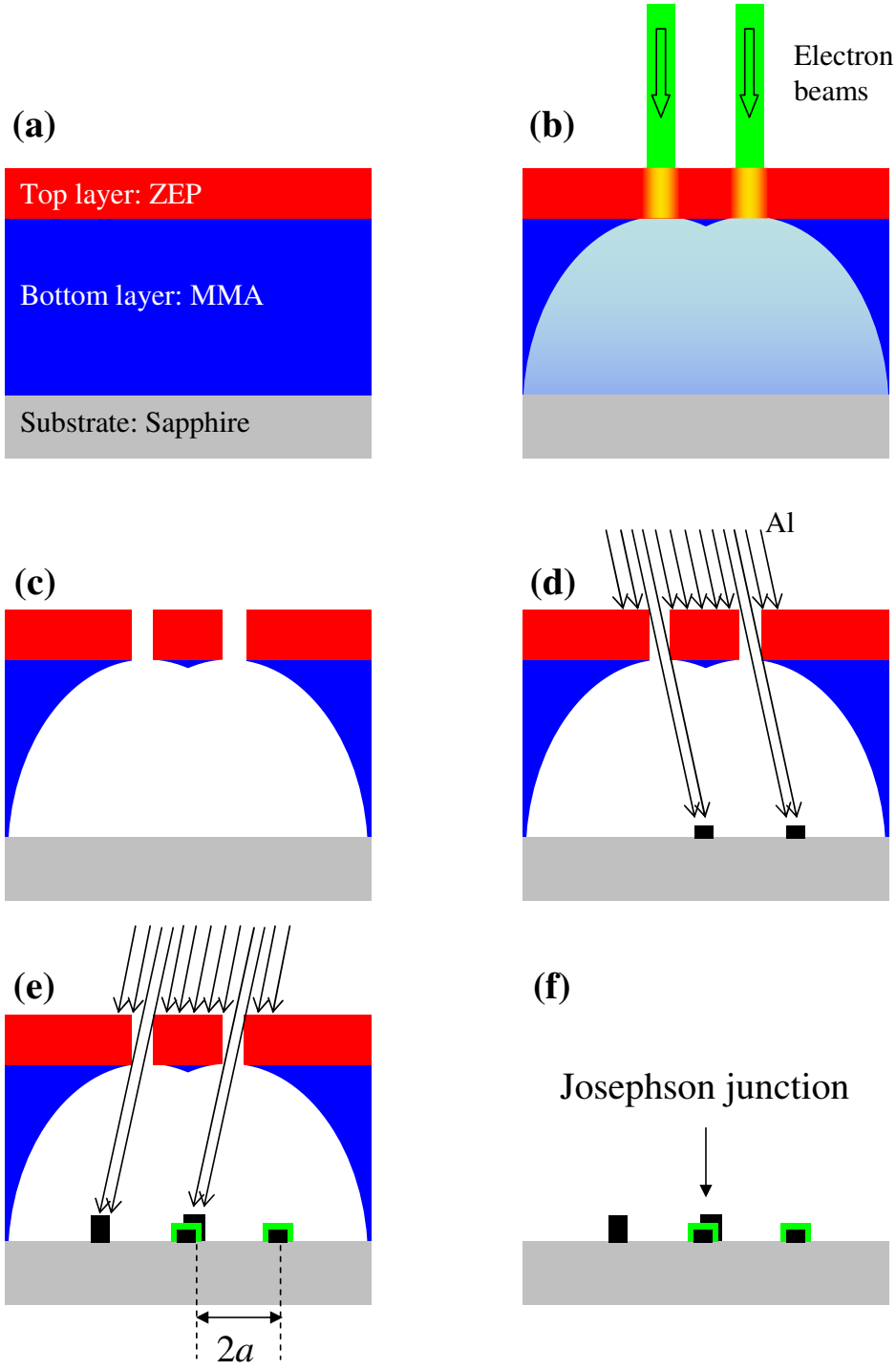

Figure 5.10: Schematic of E-beam lithography. (a) Profile of resists on a chip. The top layer is ZEP, the bottom layer is MMA, and the substrate or wafer is sapphire. The picture is not to scale and the color is false. (b) Irradiate resist with focused electron beam. (c) Develop resists, selectively. (d) First evaporation of Al at angle θ_1. (e) Oxidization of the first Al layer, followed by the second evaporation of Al at angle θ_2. Green color represents AlO_X. (f) After lift-off of MMA.

the resonance frequency (6 MHz) of a quartz crystal, which shifts due to the additional mass as material is deposited on the crystal. Since the crystal was located on the hemispherical cage, we had to open the shutter to see the deposition rate. When there is too much material on the crystal, the resonance shifts by several percent, and the crystal needs to be replaced.

Once the deposition rate was stabilized to about 6 Å/s, I closed the shutter and moved the sample from the load-lock chamber to the main chamber. The first deposition angle (-15°) was set on the transfer rod, then I opened the shutter and monitored the deposition rate and accumulated thickness [see Fig. 5.10 (d)]. The first deposition was set to a thickness of 30 nm. Then, I moved the device back to the load-lock chamber, turned off the E-beam, and isolated the two chambers by closing the gate valve. Before applying oxygen (ultra pure grade, UN1072) to the device in the load-lock chamber, I measured the oxygen pressure in the small volume of the pipe connected to a vacuum gauge. The ratio of the pressure in the small pipe to that in the load-lock chamber was roughly 200. The device was oxidized for 2 minutes with an oxygen pressure of 757 mTorr in the load-lock chamber. After that, the load-lock chamber was quickly pumped out using the scroll pump and then I opened the gate valve to connect the two chambers. The second deposition was done at an opposite angle (+15°) with a film thickness of 50 nm. The lift-off process of MMA [see Fig. 5.10 (f)] can be found in Appendix A.

The proper overlapping of the two Al layers in the double-angle evaporation is essential to form a Josephson junction. Figure 5.11 (a) shows a side profile of the developed E-beam resists [see also Fig 5.10 (a)]. The thickness of the resist top

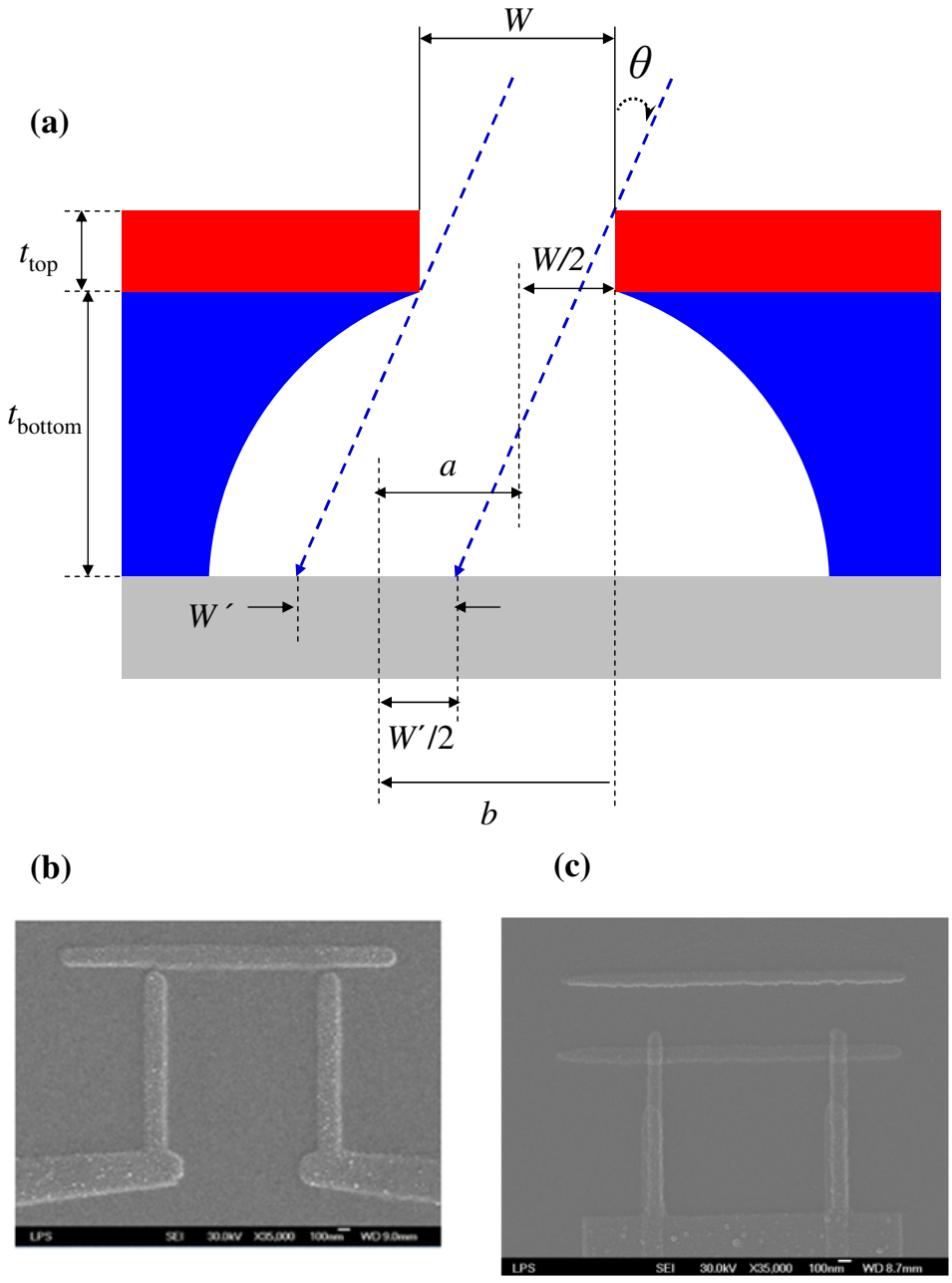

Figure 5.11: (a) Geometric dimensions of resist pattern, (b) example of a zero-angle evaporation, and (c) example of double-angle evaporation.

layer and bottom layer is given by $t_{top} = 120$ nm and $t_{bottom} = 850$ nm, respectively. The width of the opening in the developed top layer is defined as W. If the device is rotated by an angle θ with respect to the incident Al being evaporated, then the width of the deposited Al film, $W^{'}$, is equal to $W - t_{top} \tan\theta$. The distance from the right edge of the top hole to the center of the deposited film, b, is given by $W^{'}/2 + (t_{top} + t_{bottom}) \tan\theta$. Then, the distance between two centers of top hole and film, a, is given by $b - W/2$, or $W^{'}/2 + (t_{top} + t_{bottom}) \tan\theta - W/2$, which $2a$ corresponds to the distance between the centers of the two films after double-angle evaporation [see Fig. 5.10 (e)]. Therefore, one can estimate how far two films formed by double-angle evaporation will overlap, given t_{top}, t_{bottom}, W, and θ. For comparison, Fig. 5.11 (b) shows a pattern deposited with direct deposition, or zero-angle, without a second deposition, and Fig. 5.11 (c) shows two films deposited by double-angle evaporation with $\theta = 15°$.

5.3.5 Packaging

I used two different types of sample packaging; a Cu box and a PC board that was mounted in a sample box [see Fig. 5.12]. For the Cu box, we adhered two Ti/Au coplanar wave guides (CPW) to the Cu box; these wave guides were used for transition of the rf from the SMA connector to the device. An SMA connector was then soldered to the CPW. A device chip was inserted between the two CPWs and glued to the Cu box by Silver paste. The PC board [see Fig. 5.12 (b)] was designed by Ben Palmer and has a built-in CPW. The nice thing about the PC board is

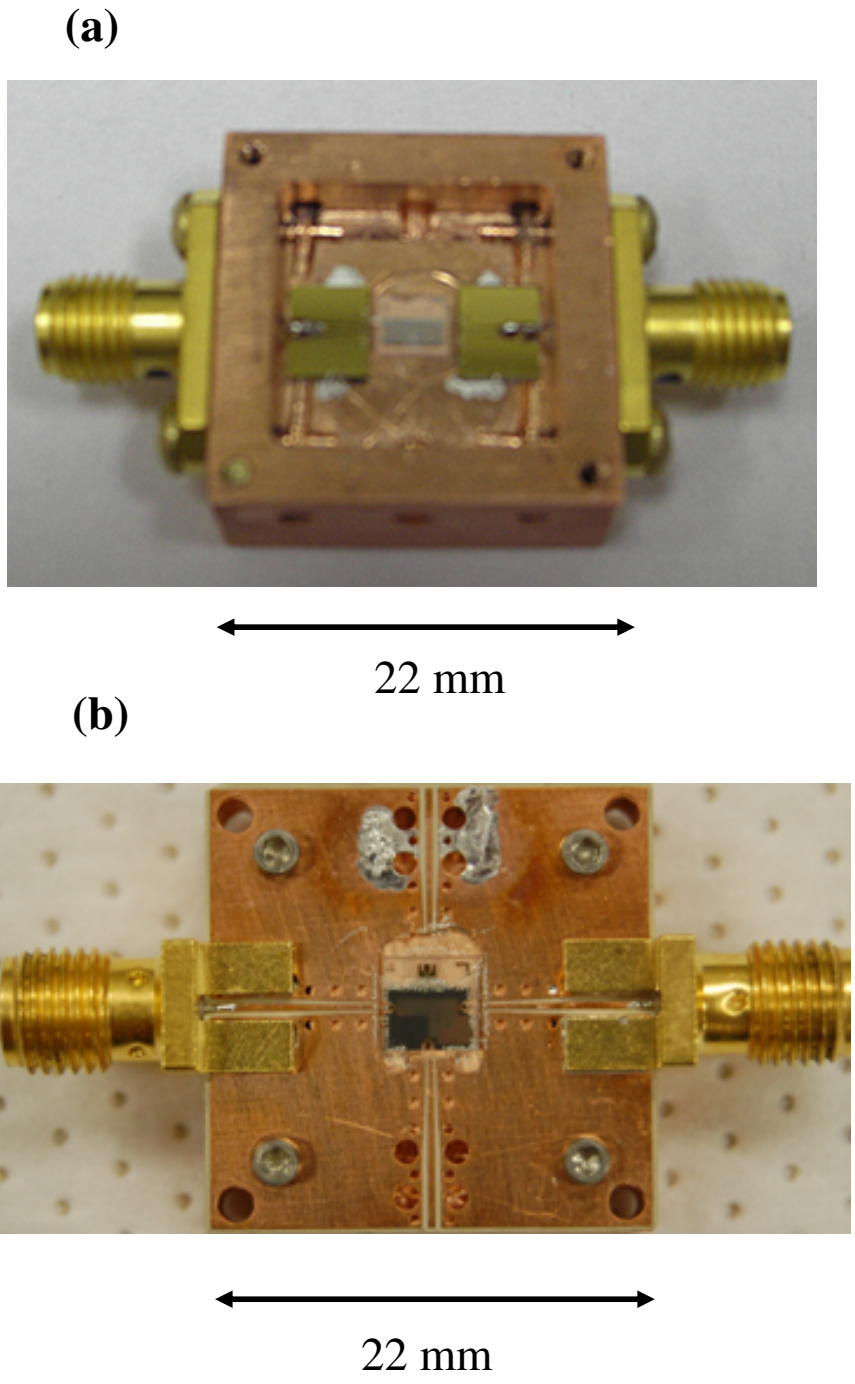

Figure 5.12: Sample holders. (a) Cu box and (b) PC Board with chip and connections.

that the ground connections were done better than the first sample box since the grounds were soldered in place and vias were also used to tie the upper ground plane to ground plane on the back side. The PC board is enclosed by two Cu plates that form the closed sample box.

After the device was mounted, wires need to be attached from the package to the device. LPS has two wire-bonders: one is for Al and the other is for Au. I used Al wires bonds to connect the device chip to the Ti/Au CPWs or the Cu on the PC board. Au wires were used to bond the CPWs to the Cu box for grounding. For the SET, I used Au wire-bonders since the SET was deposited on Ti/Au leads, which were connected to the CPW launcher. Before bonding the SET CPW launcher to the Ti/Au CPW, I shorted the CPW by putting a short to the SMA connector to prevent electrostatic discharge from destroying the tunnel junctions of the SET.

5.3.6 Estimation of E_J

The maximum E_J of the CPB can be estimated from the tunnel junction resistance and the superconducting gap using the Ambegaokar-Baratoff formula [89, 90]:

$$E_{J,max} = \frac{R_Q}{R_{CPB}} \frac{\Delta_{Al}}{8}, \tag{5.21}$$

where $R_Q \equiv h/e^2$ =25.9 kΩ is the resistance quantum, Δ_{Al}=2.5 K is the superconducting energy gap of Al, and R_{CPB} is the total resistance of the two CPB junctions in parallel. Since our CPB has two nominally identical junctions in parallel with junction resistance of R_1, we have $R_{CPB} = R_1/2$. Then, one can rewrite Eq. 5.21

as

$$E_{J,max} = \frac{2R_Q}{R_1}\frac{\Delta_{Al}}{8}. \tag{5.22}$$

By fabricating an SET with a CPB at the same time on the same chip with the same junction sizes, I could estimate the resistance of a CPB and E_J by measuring the SET resistance at room temperature. Of course the SET has two junctions in series. Hence, the total resistance R_{SET} of the SET is equal to $2R_1$, yielding the following relation between R_{SET} and $E_{J,max}$ of the CPB:

$$E_{J,max} = \frac{4R_Q}{R_{SET}}\frac{\Delta_{Al}}{8}. \tag{5.23}$$

Eq. 5.23 is plotted as a function of R_{SET} in Fig. 5.13.

I measured the SET resistance at room temperature with a multimeter that was set to a fixed 40 kΩ resistance range; if the multi meter is set to "Auto", a high current can go through the junctions and destroy them. Since static discharge can damage the SET junctions, we also need to ground ourselves carefully.

5.4 Transmission Measurement and Analysis

5.4.1 He-3 Refrigerator

I used a He-3 Refrigerator to cool resonators for transmission measurements [see the picture in Fig. 5.14 (a)]. The base temperature of the He-3 fridge is 350 mK, which is about a factor of ten higher than the base temperature of the He-3/He-4 dilution refrigerator. Since a temperature of 350 mK is below the transition temperature of aluminum ($T_c \simeq 1.2$ K), I was able to observe the resonance of the

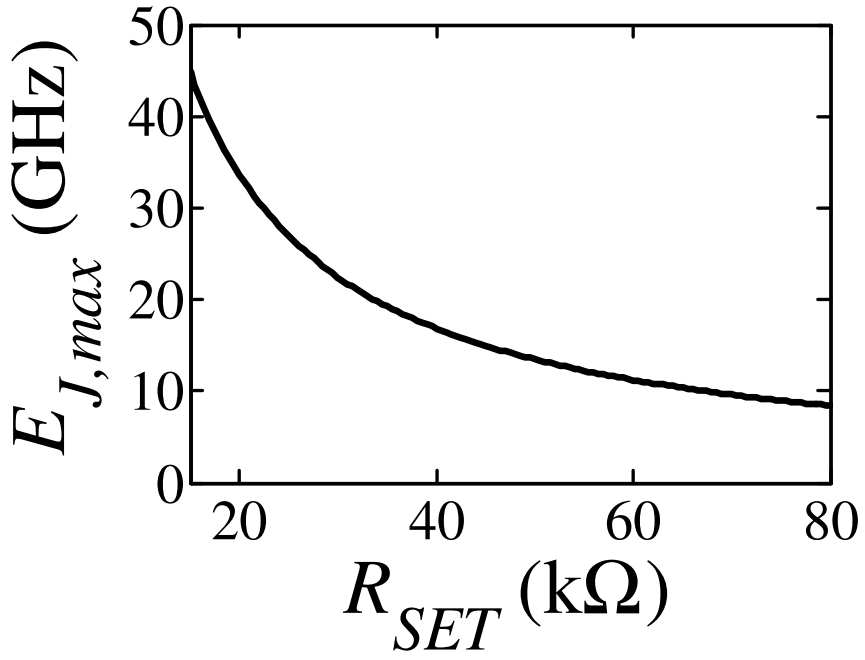

Figure 5.13: Expected $E_{J,max}$ of the CPB versus the resistance of a test SET prepared on the same chip. R_{SET} is the total resistance of two SET junctions in series.

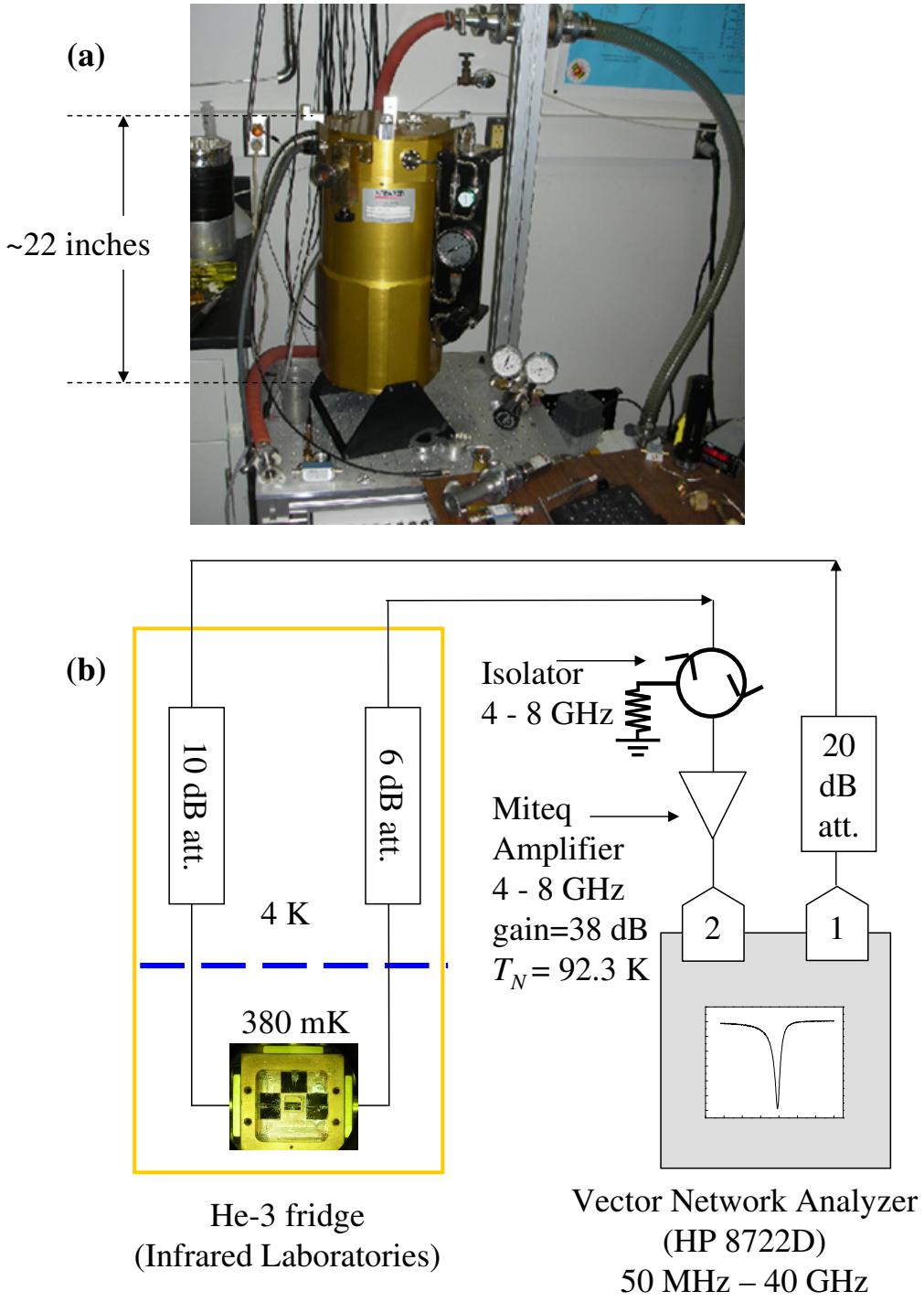

Figure 5.14: He-3 refrigerator. (a) Photograph of He-3 refrigerator, and (b) schematic of the He-3 system with the measurement setup. The input cables attached to the device have about 10 dB loss. The isolator was a PAMTECH circulator (CTH1409KS) terminated by 50 Ω.

Al resonator. The main advantage of using a He-3 fridge is that the operation is easier than the operation of a dilution refrigerator, the thermal cycling is quicker than the dilution refrigerator, and the He-3 fridge consumes less liquid helium. It is very useful when one needs to measure just the resonance frequency and quality factors of many devices.

There are two temperature stages in the He-3 fridge: 4 K and 380 mK [see Fig. 5.14 (b)]. The sample box was mounted on the cold stage, which is thermally anchored to the liquid He-3 container. There are two attenuators at 4 K to attenuate thermal noise from higher temperatures. An HP 8722D vector network analyzer was used to measure the magnitude and phase of S_{21}. For small applied powers, I used a low noise amplifier before the network analyzer.

I measured S_{21} up to 20 GHz in order to check for higher harmonics of the resonance. Fig. 5.15 (a) shows S_{21} up to 16 GHz. For this measurement, I used a wide bandwidth amplifier, which had relatively flat gain up to 20 GHz. The isolator was also removed. Though there were a lot of standing waves at high frequencies, we only see one sharp resonance. This gives supporting evidence that our resonator behaves as a lumped-element resonator.

One also sees a relatively slowly varying frequency-dependent background in S_{21} [see Fig. 5.15 (b)] due to standing waves in the system. We noticed this background was still present at 4.6 K, when the resonator was in the normal state. The 2 dB offset is most likely associated with the phase of the Al changing from a superconductor to a normal metal. By subtracting the S_{21} data at 4.6 K from the S_{21} at 380 mK, we were able to get a quasi-calibrated S_{21} measurement of the resonator

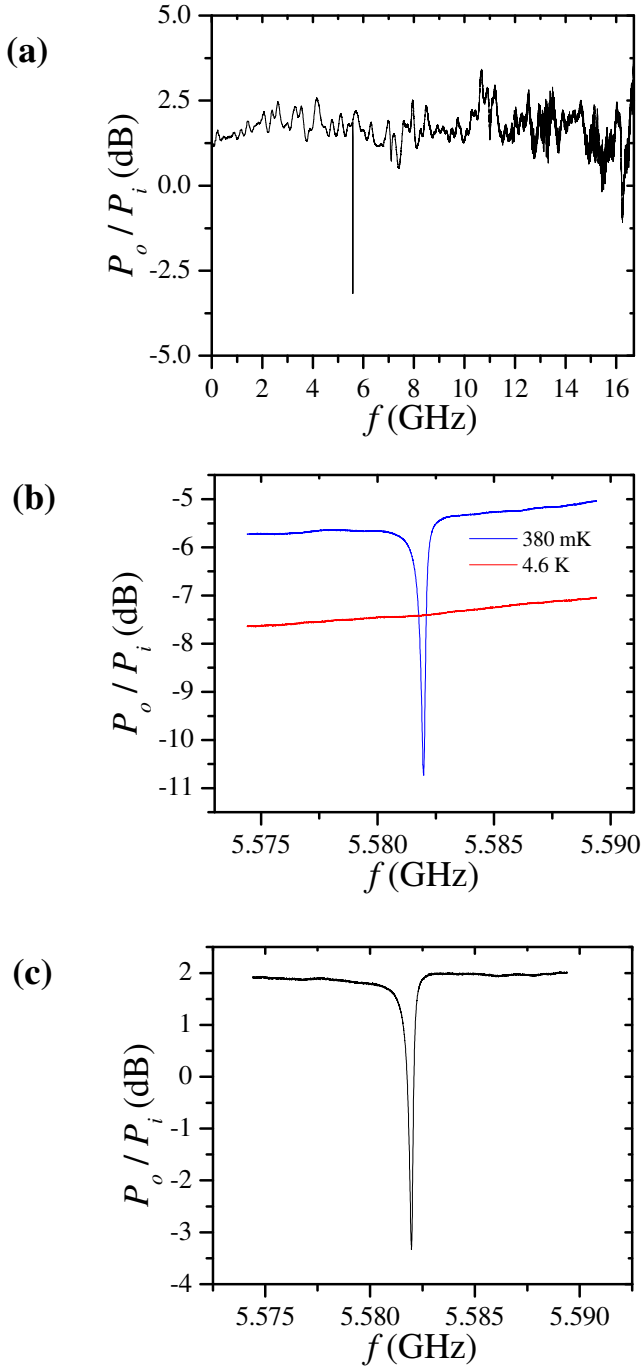

Figure 5.15: (a) S_{21} up to 16 GHz for "Resonator4" (see Table 5.1). S_{21} at 380 mK was calibrated by comparing S_{21} measured at 4.6 K, where the resonator was normal and the resonance disappeared. (b) S_{21} around the resonance measured at 380 mK and 4.6 K. (c) Calibrated S_{21} after subtraction of the two S_{21} in (b).

[see Fig. 5.15 (c)].

From the vector network analyzer, the magnitude and phase of S_{21} can be found from the magnitude of P_o/P_i and the phase θ [see Fig. 5.16 (a)]. The magnitude P_o/P_i is measured in units of dB for convenience and it can be converted to a linear scale. By taking the square root of P_o/P_i (in the linear scale), one can get the ratio of transmitted voltage and input voltage, V_o/V_i. The real part of the voltage ratio is then $(V_o/V_i)\cos\theta$ and the imaginary part is $(V_o/V_i)\sin\theta$, and these comprise a circle in the complex plane if Q_i and Q_e are independent of frequency.

5.4.2 He-3/He-4 Dilution Refrigerator

With the He-3 fridge, I noticed that the quality factor of the Al resonator kept increasing as the temperature decreased down to the base temperature of 350 mK. This suggested that the quality factor might go up more if the temperature dropped below 350 mK. To see if this would happen, we used the He-3/He-4 dilution refrigerator and measured the Al resonator at the base temperature of 30 mK. For the initial measurement in the dilution refrigerator, we did not have a cryogenic amplifier and cryogenic isolators. We added only one 20 dB attenuator after the device at the still stage, where the temperature is 0.6 K. The isolator and low noise amplifier used in the He-3 fridge were used again and connected to the vector network analyzer to measure S_{21} [see Fig. 5.16 (b)].

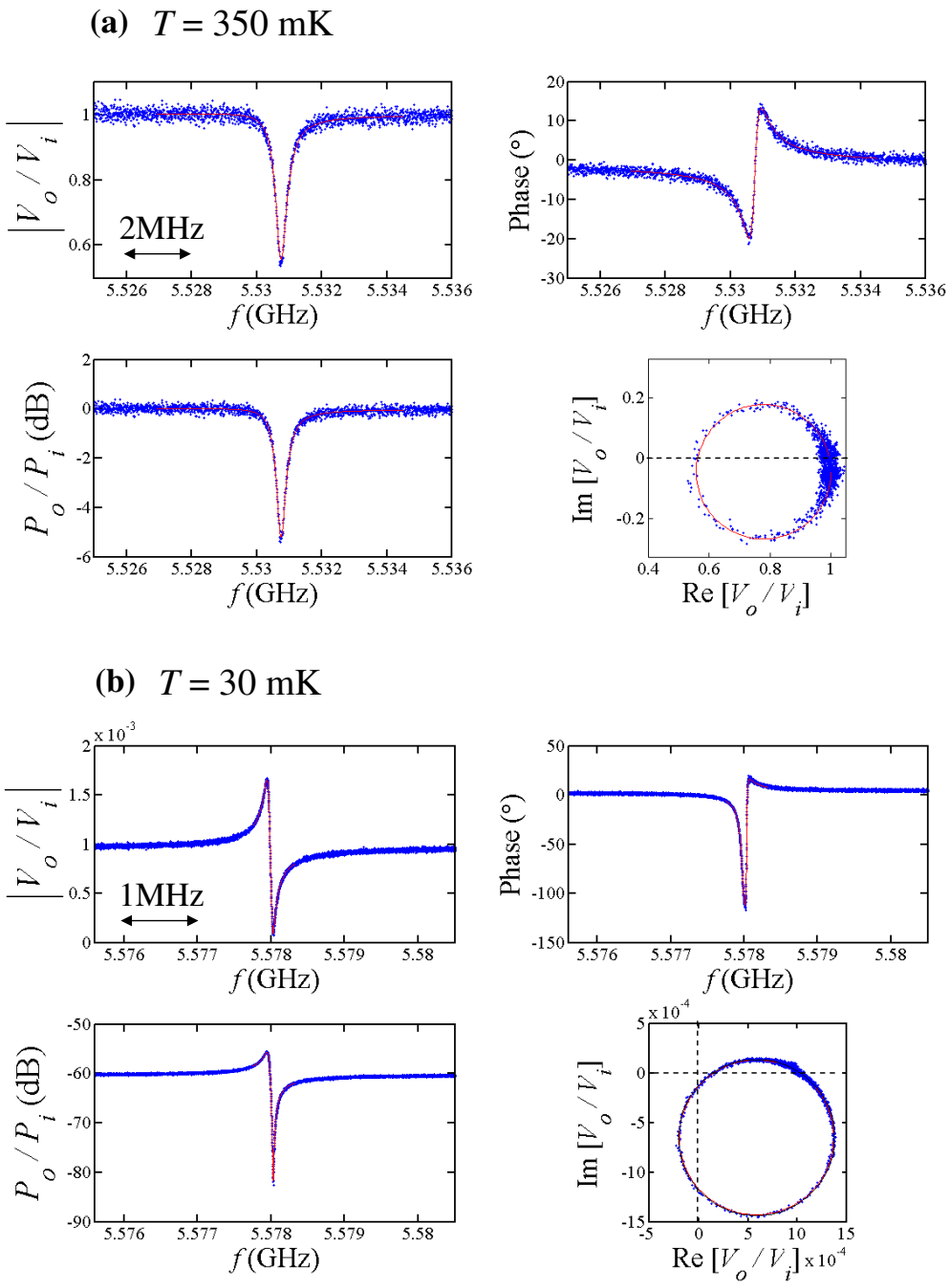

Figure 5.16: Measured resonance of "Resonator3" at 350 mK and "Resonator1" at 30 mK (see Table 5.1). (a) Resonance measured in the He-3 refrigerator at 350 mK. This data was calibrated by the data taken at 4 K, and the background S_{21} was normalized to 0 dB or 100 % transmission. (b) Resonance measured in the dilution refrigerator at 30 mK. This data was not calibrated and the background for S_{21} was not normalized.

5.4.3 Fitting the resonance

In my measurements, I typically found that the resonance was not symmetric, but could be fit [91, 92, 93], to a modified version of Eq. 5.20

$$\frac{P_o}{P_i} = \left| 1 - \frac{Q_L/Q_e e^{i\phi}}{1 + iQ_L \dfrac{2(\omega - \omega_0)}{\omega_0}} \right|^2 , \tag{5.24}$$

where ϕ is an additional fit parameter. Since $e^{i\phi} = \cos\phi + i\sin\phi$, we can rewrite this as

$$\frac{P_o}{P_i} = 1 - \frac{2Q_L}{Q_e} \frac{\cos\phi + Q_L \dfrac{2(\omega - \omega_0)}{\omega_0} \sin\phi - \dfrac{Q_L}{2Q_e}}{1 + \left[Q_L \dfrac{2(\omega - \omega_0)}{\omega_0} \right]^2}. \tag{5.25}$$

This is basically an ad hoc modified Lorentzian curve.

To get the phase function, one needs to decompose V_o/V_i into real and imaginary parts. The real part is given by

$$Re\left[\frac{V_o}{V_i}\right] = 1 - \frac{Q_L}{Q_e} \frac{\cos\phi + Q_L \dfrac{2(\omega - \omega_0)}{\omega_0} \sin\phi}{1 + \left[Q_L \dfrac{2(\omega - \omega_0)}{\omega_0} \right]^2}. \tag{5.26}$$

The imaginary part is given by

$$Im\left[\frac{V_o}{V_i}\right] = -\frac{Q_L}{Q_e} \frac{\sin\phi - Q_L \dfrac{2(\omega - \omega_0)}{\omega_0} \cos\phi}{1 + \left[Q_L \dfrac{2(\omega - \omega_0)}{\omega_0} \right]^2}. \tag{5.27}$$

The phase [see Fig. 5.4 (b)] is then given by

$$\theta = \theta_0 + \arctan\left(Im\left[\frac{V_o}{V_i}\right] / Re\left[\frac{V_o}{V_i}\right] \right). \tag{5.28}$$

One can also plot the complex voltage by plotting the imaginary part versus real part [see Fig. 5.4 (d)]. In the complex plot, the vector starts from (1,0) and

rotates clockwise as the frequency increases from zero. On resonance in the limit of zero damping, $V_o/V_i = 0$ and the vector is at the origin, (0,0). In general the vector comes close to the origin; the diameter of the circle corresponds to Q_L/Q_e. From $1/Q_L = 1/Q_i + 1/Q_e$, the diameter of the circle is also $Q_i/(Q_i + Q_e)$. Hence, this is another way to extract the Q_e while Q_L is determined by the width of the resonance curve. If there is non-zero ϕ, then the circle will pivot by ϕ around (1,1) and make the resonance curve asymmetric. This behavior is clearly evident in Fig. 5.16 (b). This behavior can happen if the input and output lines have standing wave resonances.

5.5 Power Dependence

The contribution of dielectric loss to the internal quality factor in the substrate increases significantly at low temperatures and low drive voltages or power [62, 94]. This behavior is consistent with two-level systems (TLSs) in the substrate or dielectric surface layers. In the low temperature and low voltage limit, TLSs are not saturated, and so they can absorb energy, producing loss. Such dielectric loss can be probed by measuring the quality factor of a superconducting high Q resonator which is deposited on top of the dielectric material.

The power dependence of "Resonator2" is shown in Fig. 5.17. As I increased the power, the line width of resonance curve decreased and the resonance frequency increased, implying lower loss in the system, consistent with TLS behavior. Unlike other resonators [94] on silicon wafers, our resonator on sapphire shows a relatively

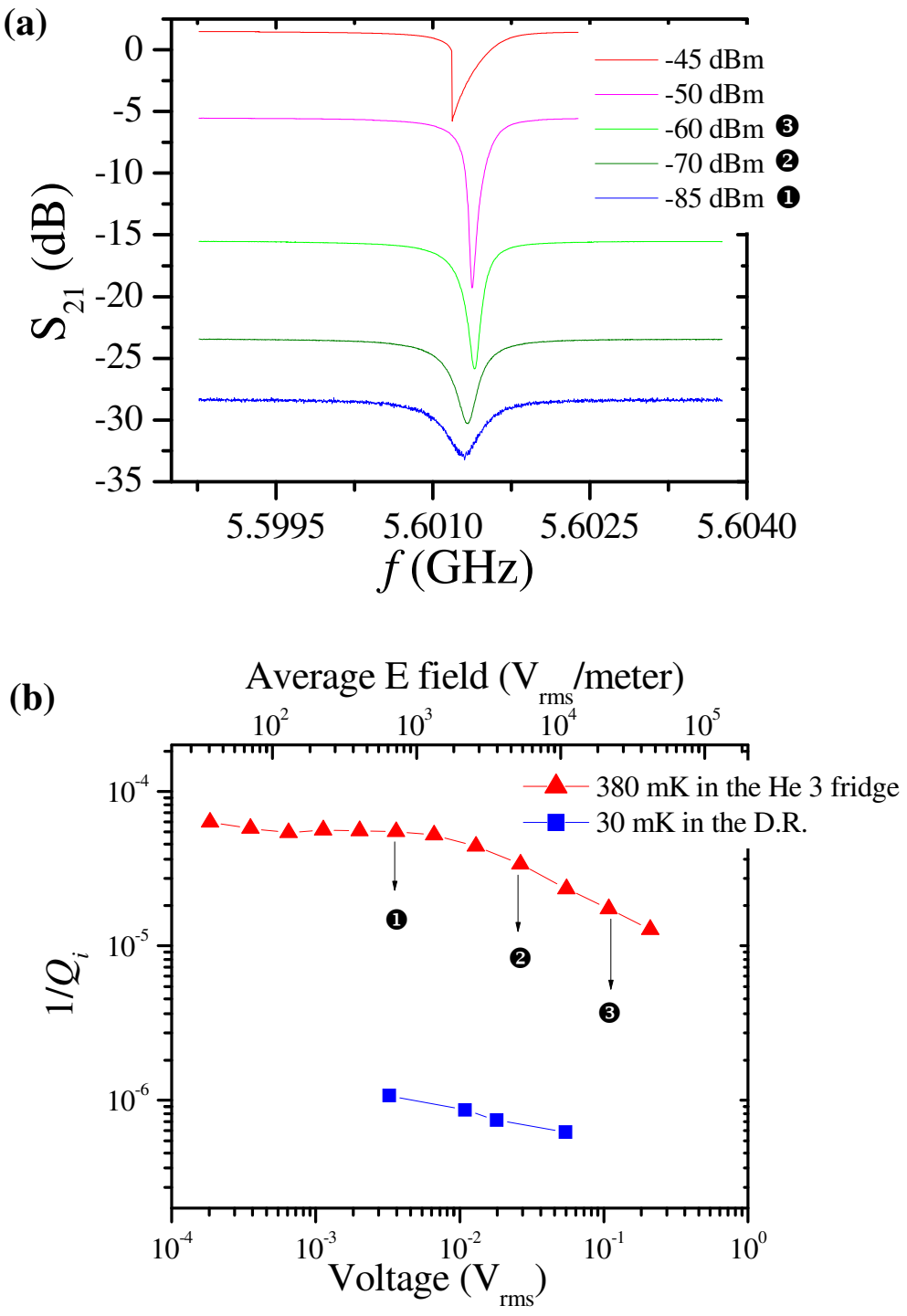

Figure 5.17: Power dependence of "Resonator2" (see Table 5.1). (a) S_{21} as a function of input power to the resonator at 380 mK, and (b) $1/Q_i$ as a function of the rms voltage on the resonator. Average electric field is also scaled on the top axis considering the gap of 5 μm between the fingers of the capacitor.

monotonic variation of $1/Q_i$ versus the applied voltage (power).

5.6 Temperature Dependence

In addition to the power, the temperature is also a good parameter to vary to probe the loss mechanism of the superconducting resonator. With the resonator in the He-3/He-4 dilution refrigerator, I observed a temperature dependence of the Al resonator from 30 mK to 500 mK. From 30 mK to 200 mK, the resonance curve for "Resonator1" did not change [see Fig. 5.18 (a)]. As the temperature was raised above 200 mK, the resonance shifted to lower frequency and the width of the resonance also got wider [see Fig. 5.18 (a)]. In the complex plot [see Fig. 5.18 (b)], the biggest circle corresponds to the sharpest resonance in S_{21}. The circles looked the same up to 200 mK. At 250 mK, the circle became slightly smaller and the diameter of the circle became smaller and smaller as the temperature increased above this, indicating that Q_i was decreasing.

Examination of Fig. 5.18 (a) reveals that the resonance is very asymmetric and the internal quality factor Q_i is large compared to Q_e at 30 mK. In fact the Q_L I extracted from the resonance curve fit at 30 mK was bigger than Q_e, which resulted in a negative Q_i. Instead, by fitting the diameter of the measured circle in the complex plot, I was able to extract maximum $Q_L = 70,000$ and $Q_i = 1,000,000$ and found they did not change significantly from 30 mK to 200 mK (see blue squares and red circles in Fig. 5.19). Since we did not have a cryogenic amplifier at that time, I had to apply a relatively high power to the device and this saturated the

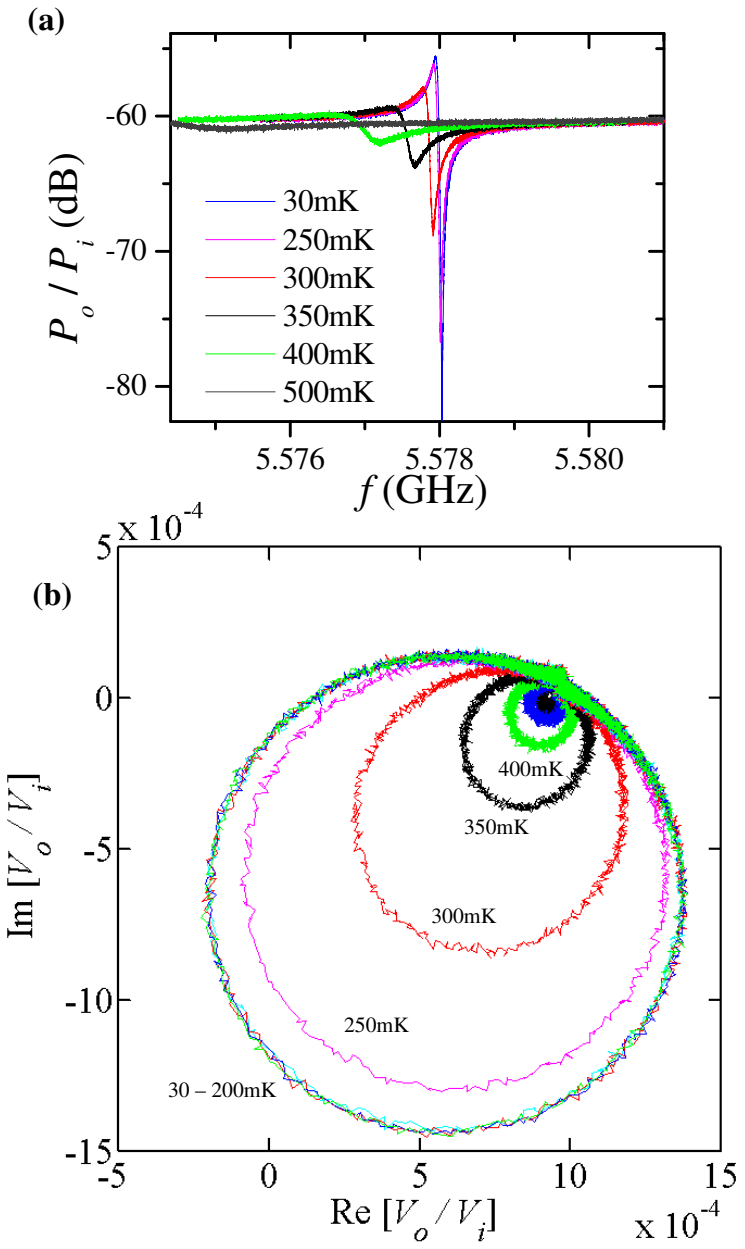

Figure 5.18: Temperature dependence of "Resonator1". (a) The transmitted power versus frequency for different temperatures. (b) Extracted circles from the transmitted power and phase for different temperatures.

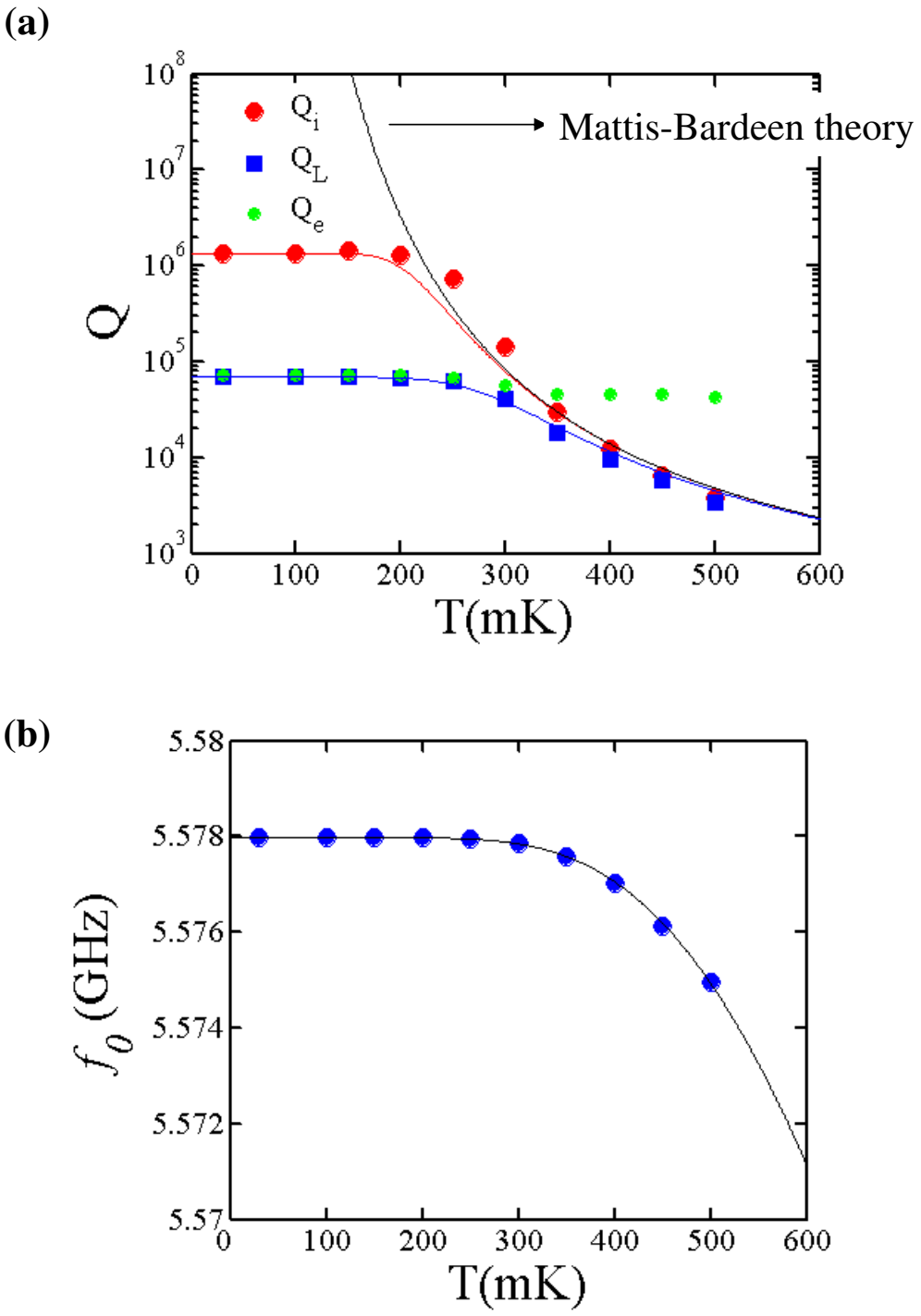

Figure 5.19: Temperature dependence of Q and resonance frequency of "Resonator1". (a) Extracted Q (Q_L, Q_e, and Q_i) from data in Fig. 5.18 as a function of temperatures. Solid curves are the fit from the Mattis-Bardeen theory, which is discussed in section 5.6.2. (b) The resonance frequency (f_0) from data in Fig. 5.18 as a function of temperatures. Solid curve is the fit from the Mattis-Bardeen theory.

TLSs in the sapphire wafer. This is why I got Q_i's up to a million.

By varying the temperature, I found Q_L started to decrease quickly above 200 mK, reaching 40,000 when the temperature increased to 300 mK (see Fig. 5.19). The minimum Q_L observed was about 3,000 at 550 mK. Q_e changed relatively little with temperature, as expected. Above 600 mK, it was hard to see a clear resonance. The resonance frequency also shifted lower as the temperature increased. The maximum shift of the resonance frequency from 5.578 GHz was -3 MHz as the temperature increased from 30 mK to 550 mK.

5.6.1 Two Fluid Model

To understand why the resonator behaves the way it does, I need to discuss some of the basic physics of superconductivity. Superconductivity occurs below the transition temperature $T_c \simeq 1.2$ K in aluminum. But superconductivity does not produce 100 % perfect loss-less conductivity at non-zero temperatures. This phenomenon can be explained by the Gorter-Casimir two-fluid model [12], which was a classical model that was established before the BCS theory. The two-fluid model assumes that a superconductor consists of a portion of superfluid (due to paired electrons) and a portion of normal fluid (from unpaired electrons). The density of paired electrons n_s is given by

$$\frac{n_s(T)}{n_{tot}} \cong 1 - \left(\frac{T}{T_c}\right)^4, \tag{5.29}$$

where $n_{tot} = n_s + n_n$ is the total density of electrons and n_n is the density of unpaired electrons [see Fig. 5.20 (a)]. At $T = 0$ K, this model has all of the electrons in the

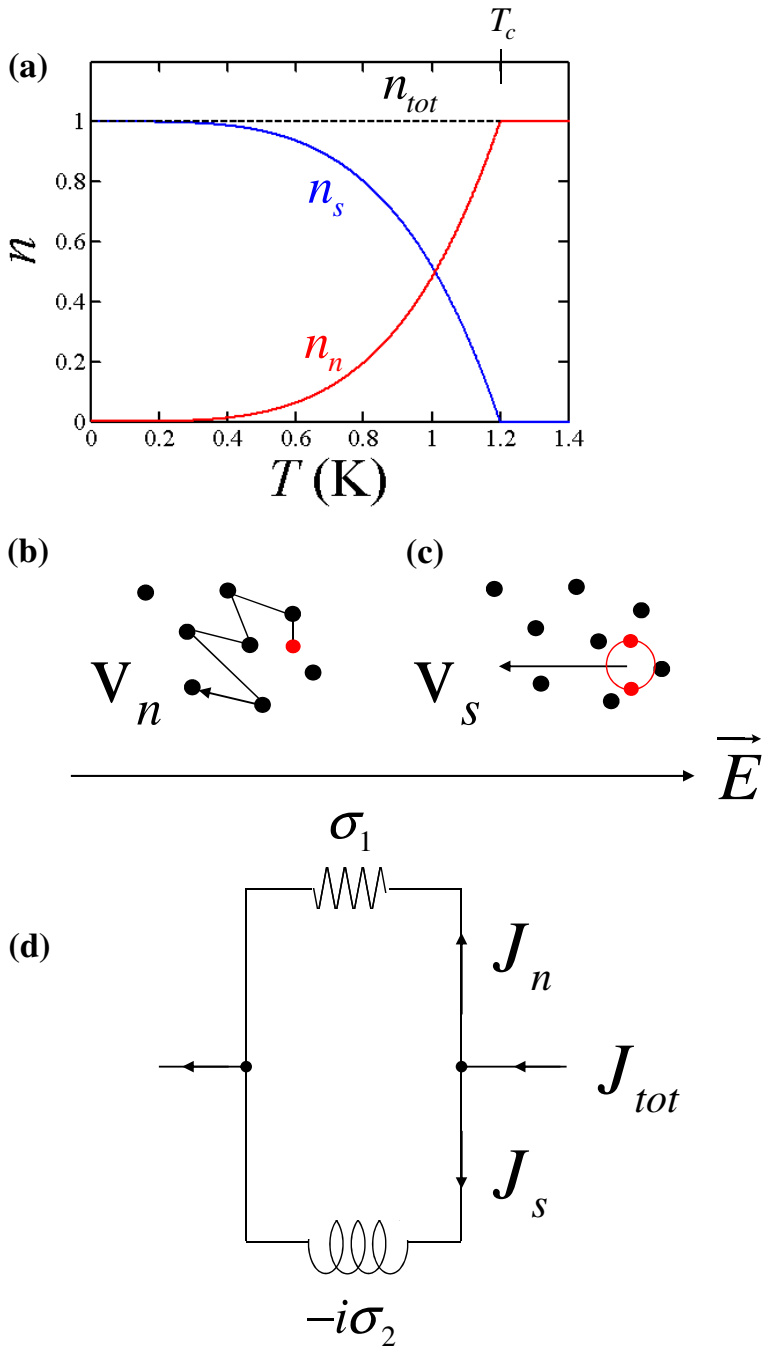

Figure 5.20: Two fluid model. (a) n_s and n_n as a function of temperature from two-fluid model. (b) Illustration of the flow of an unpaired electron (red dot) in the crystal ions (black dots). (c) Illustration of the flow of paired electrons (red dots). (d) Equivalent circuit of a superconductor in the two-fluid model.

superconductor paired. As temperature increases, the density of paired electrons decreases and the density of unpaired electrons increases. When the temperature approaches the transition temperature T_c, unpaired electrons become dominant. This model has been well supported by experiment. For example, Schawlow and Devlin [95] measured the penetration depth λ_L as a function of the temperature and found

$$\lambda_L(T) = \lambda_L(0)\left[1 - \left(\frac{T}{T_c}\right)^4\right]^{-1/2}, \tag{5.30}$$

where $\lambda_L^2 = m/\mu_0 n_s e^2$.

By combining the two-fluid model with the Drude model, one can understand the transport mechanism of electrons and pairs under an applied electric field $\mathbf{E}$ [see Figs. 5.20 (b) and (c)]. Using Newton's second law, the equation of motion of an electron can be written as

$$m\frac{d\mathbf{v}}{dt} = e\mathbf{E} - m\frac{\mathbf{v}}{\tau}, \tag{5.31}$$

where $\mathbf{v}$ is the velocity of the electron and τ is the relaxation time or mean free time between electron collisions. Writing the oscillating electric field as $Ee^{i\omega t}$, the velocity is

$$\mathbf{v} = \frac{e\tau}{m}\frac{1}{1+i\omega\tau}\mathbf{E}. \tag{5.32}$$

or

$$\frac{|\mathbf{v}|}{|\mathbf{E}|} = \frac{e\tau}{m}\frac{1}{1+(\omega\tau)^2} - i\frac{e}{m\omega}\frac{(\omega\tau)^2}{1+(\omega\tau)^2}. \tag{5.33}$$

Under the electric field, an unpaired electron would be scattered with a mean free time between collisions on the order of ps. Thus at microwave frequencies, well below the energy gap, $\omega\tau_n \ll 1$. In this limit, the imaginary term in Eq. 5.33 goes

to zero and $|\mathbf{v}_n|/|\mathbf{E}|$ is given by

$$\frac{|\mathbf{v}_n|}{|\mathbf{E}|} = \frac{e\tau_n}{m}. \tag{5.34}$$

In contrast, the paired electrons have a much longer mean free time. Then, $\omega\tau_s \gg 1$, which makes the real term in Eq. 5.33 go to zero and $|\mathbf{v}_s|/|\mathbf{E}|$ is given by

$$\frac{|\mathbf{v}_s|}{|\mathbf{E}|} = -i\frac{e}{m\omega}. \tag{5.35}$$

The total current density is made up of two current densities, or $\mathbf{J} = \mathbf{J}_n + \mathbf{J}_s$, where $\mathbf{J}_n = n_n e\mathbf{v}_n$ and $\mathbf{J}_s = n_s e\mathbf{v}_s$. This can be modeled as Ohmic and reactive channels in parallel [12] (see the equivalent circuit model in Fig. 5.20).

From the Ohm's Law relation $\mathbf{J} = \sigma\mathbf{E}$, one can get the complex conductivity for the two-fluid model

$$\sigma(\omega) = \frac{n_n e^2\tau_n}{m} - i\frac{n_s e^2}{m\omega}. \tag{5.36}$$

However, one needs to be careful in taking the limit $\omega \to 0$, and a full analysis reveals the conductivity is infinite at dc and $\sigma(\omega)$ is [12]

$$\sigma(\omega) = \frac{\pi n_s e^2}{2m}\delta(\omega) + \frac{n_n e^2\tau_n}{m} - i\frac{n_s e^2}{m\omega}. \tag{5.37}$$

Tinkham [12] defines the complex conductivity as

$$\sigma = \sigma_1 - i\sigma_2, \tag{5.38}$$

where σ_1 and σ_2 are

$$\sigma_1(\omega) = \frac{\pi n_s e^2}{2m}\delta(\omega) + \frac{n_n e^2\tau_n}{m} \tag{5.39}$$

and

$$\sigma_2(\omega) = \frac{n_s e^2}{m\omega}. \tag{5.40}$$

For nonzero frequencies, σ_1 is proportional to the density of unpaired electrons, which contributes to the Ohmic loss of the conductor. σ_2 is inversely proportional to frequency but proportional to the density of paired electrons, which contributes to the reactance of the conductor. One can also say that the paired electrons only contribute to the inductance of the conductor. In the two-fluid model, the temperature dependence of the conductivity is given by

$$\frac{\sigma_1(T)}{\sigma_n} = \left(\frac{T}{T_c}\right)^4 \tag{5.41}$$

and

$$\frac{\sigma_2(T)}{\sigma_n} = \frac{1}{\omega\tau}\left[1 - \left(\frac{T}{T_c}\right)^4\right], \tag{5.42}$$

where $\sigma_n = n_{tot}e^2\tau/m$ is the conductivity in the normal state. Figure 5.21 (a) shows the conductivity as a function of temperature when $T_c = 1.2$ K, $\omega/2\pi = 5.5$ GHz, and $\tau = 1$ ps.

5.6.2 Complex Conductivity from the Mattis-Bardeen Theory

Mattis and Bardeen applied and extended the BCS theory to describe local and nonlocal electrodynamics in superconductors, including effects of the energy gap. From the Mattis-Bardeen theory [96], σ_1 [97] in the limit $k_BT \ll \Delta_0$ and $\hbar\omega \ll \Delta_0$ can be approximated as

$$\frac{\sigma_1}{\sigma_n} \approx \frac{4\Delta_0}{\hbar\omega} e^{-\frac{\Delta_0}{k_BT}} \sinh(\xi) K_0(\xi), \tag{5.43}$$

where K_0 is the 0-th order modified Bessel function of the second kind, $\xi = \hbar\omega/2k_BT$, and $\Delta_0 = 1.6\ k_BT_c$ is the superconducting energy gap [98]. In the same limit, σ_2 [97] can be approximated as

$$\frac{\sigma_2}{\sigma_n} \approx \frac{\pi\Delta_0}{\hbar\omega}\left[1 - \sqrt{\frac{2\pi k_BT}{\Delta_0}}e^{-\frac{\Delta_0}{k_BT}} - 2e^{-\frac{\Delta_0}{k_BT}}e^{-\xi}I_0(\xi)\right], \tag{5.44}$$

where I_0 is the 0-th order modified Bessel function of the first kind. For comparison, Figure 5.21 shows the complex conductivity from the Mattis-Bardeen theory and that from the two-fluid model.

5.6.3 Complex Power and Surface Impedance

Consider a plane wave that is normally incident on the surface of a conductor [see Fig. 5.22 (a)]. I will assume that the conductor has a closed surface S and the plane wave enters the surface S_0, which is the front surface of the conductor. From Poynting's theorem, the complex power [77] into a closed surface S is

$$P = \frac{1}{2}\oint_S \mathbf{S}\cdot d\mathbf{s}, \tag{5.45}$$

where $\mathbf{S} = \mathbf{E}\times\mathbf{H}^*$ is the complex Poynting vector and $d\mathbf{s}$ points inward to the surface in the normal direction with respect to the surface S. $\mathbf{E}$ and $\mathbf{H}$ are orthogonal to each other and also to the direction of propagation. In Fig. 5.22 (a), $\mathbf{S}$ is parallel with $d\mathbf{s}$ at the front surface S_0 and the back surface of S. On the other sides, $\mathbf{S}$ is orthogonal to $d\mathbf{s}$, so $\mathbf{S}\cdot d\mathbf{s}$=0 there. I will assume the contribution from the back side of the surface is negligible because $\mathbf{S}$ decays rapidly in the conductor. Then,

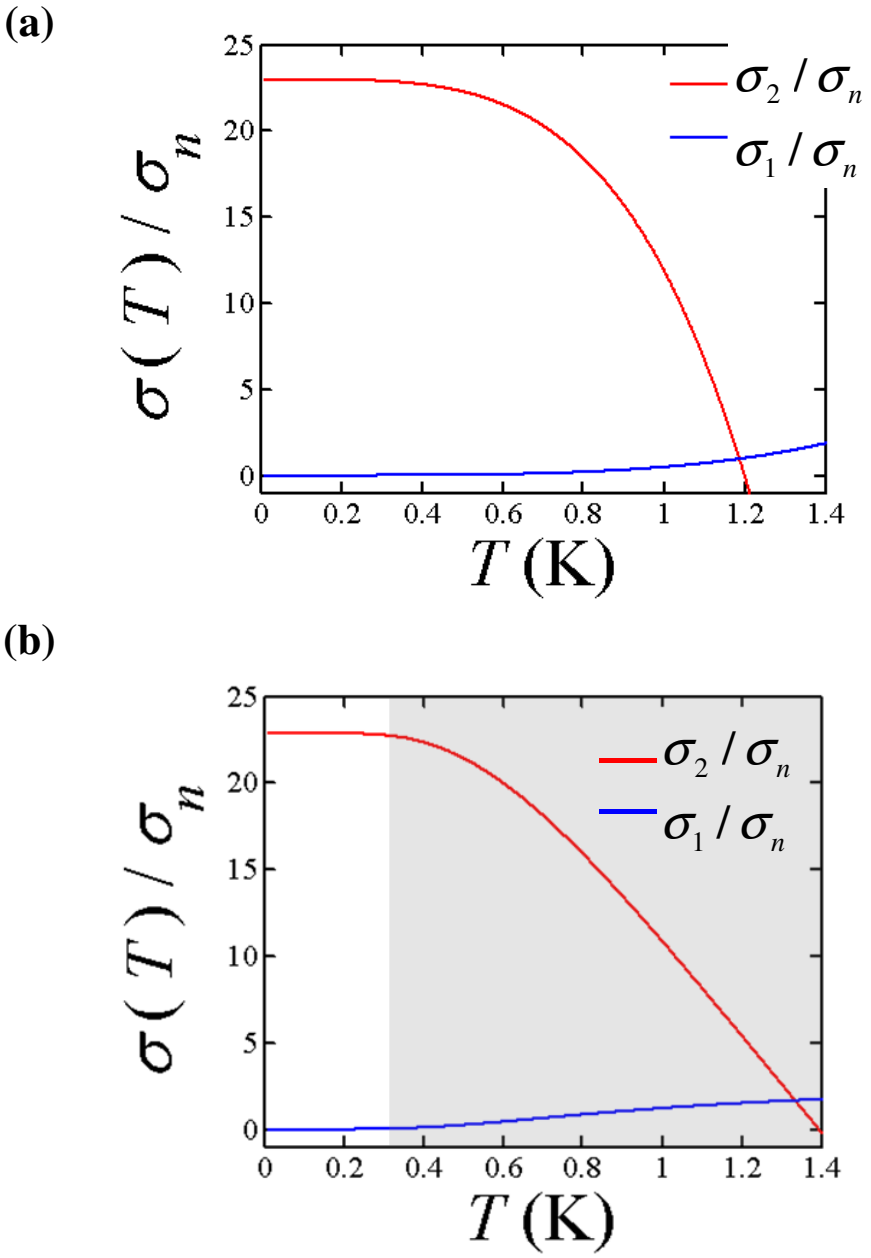

Figure 5.21: Complex conductivity of Al versus temperature. (a) Complex conductivity from the two-fluid model with $T_c = 1.2$ K, $\omega/2\pi = 5.5$ GHz, and $\tau = 1$ ps. (b) complex conductivity from the Mattis-Bardeen theory with $\Delta_0 = 1.6\ k_B T_c$, $T_c = 1.2$ K, and $\omega/2\pi = 5.5$ GHz. The solution in the gray region is not evaluated.

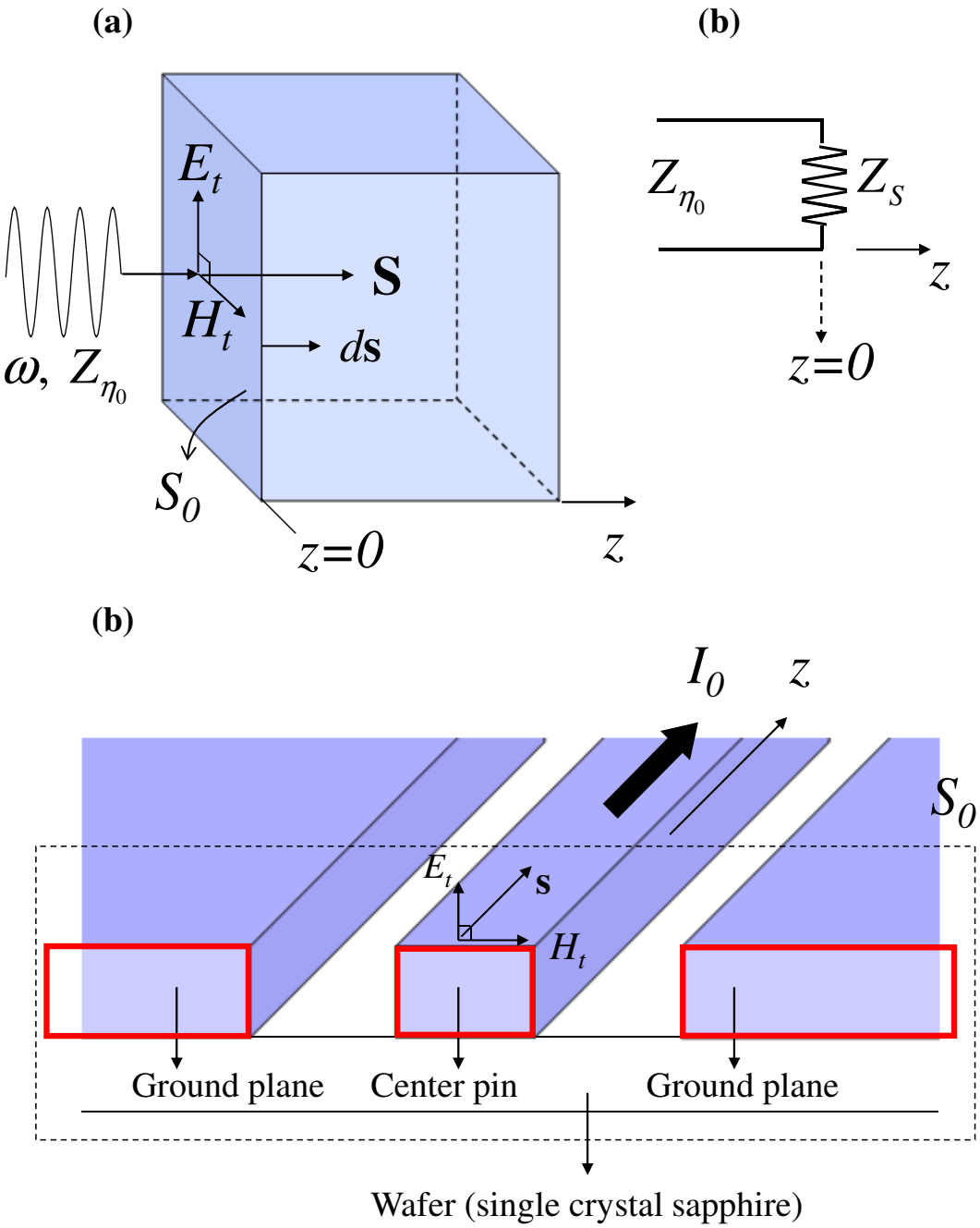

Figure 5.22: A wave incident on a superconducting thin film. (a) Illustration of an incident plane wave into the surface of a superconducting thin film, (b) equivalent circuit with (a), and (c) illustration of a current flow along a superconducting thin film CPW transmission line.

the complex power can be written as

$$P = \frac{1}{2}\int_{S_0} \mathbf{E} \times \mathbf{H}^* \cdot \hat{z} ds, \tag{5.46}$$

where $\mathbf{E}\times\mathbf{H}^*\cdot\hat{z} = (\hat{z}\times\mathbf{E})\cdot\mathbf{H}^* = Z_\eta \mathbf{H}\cdot\mathbf{H}^* = Z_\eta|\mathbf{H}_t|^2$ and where $\mathbf{H}_t$ is the component of the field tangential to the surface S_0. Z_η is the intrinsic wave impedance of the plane wave in the conductor, which is defined as the ratio of the E field and H field and can be found from [77]

$$\mathbf{H}(z) = \frac{\hat{z} \times \mathbf{E}(z)}{Z_\eta} \tag{5.47}$$

The intrinsic wave impedance of a plane wave in free space is $Z_{\eta_0} = \sqrt{\mu_0/\varepsilon_0} = 377\ \Omega$. At the surface S_0 or $z = 0$, one can define Z_η as the surface impedance

$$Z_s = \frac{E_t}{H_t}|_{z=0}. \tag{5.48}$$

Then, the complex power at the surface S_0 is given by

$$P = \frac{1}{2}\int_{S_0} Z_s|\mathbf{H}_t|^2 ds. \tag{5.49}$$

The surface impedance Z_s can be decomposed into real and imaginary parts:

$$Z_s = R_s + i\omega L_s, \tag{5.50}$$

where R_s, and L_s are the surface resistance and surface inductance, respectively. One can also obtain the real part and imaginary part of the complex power at the surface S_0 [see the circuit schematic in Fig. 5.22 (b)]. The real part corresponds to

power loss (P_l) at the surface S_0 due to the surface resistance and is

$$P_l = \frac{1}{2}\int_{S_0} R_s |\mathbf{H}_t|^2 ds. \tag{5.51}$$

The imaginary part represents the power (P_k) stored at the surface S_0 in the form of the kinetic energy of the charge carriers and is given by

$$P_k = \frac{1}{2}\int_{S_0} \omega L_s |\mathbf{H}_t|^2 ds. \tag{5.52}$$

5.6.4 Quality Factor of a Transmission Line Resonator

I now consider a situation that is more realistic for my experiments: a coplanar waveguide (CPW) which can support quasi-TEM (Transverse Electromagnetic) waves [see Fig. 5.22 (c)]. In an ideal TEM mode, **E** and **H** are orthogonal to the direction of the wave propagation. Also, **E** and **H** decay very quickly inside the conductor, so to first order, a good assumption is that there is no field inside the conductor. In a quasi-TEM mode, there could be a very small **E** field along the propagation direction. In this thesis for simplicity, I will assume the CPW guides an ideal TEM wave.

We can think of the TEM wave as propagating along the CPW in the $\hat{z}$ direction so that $\mathbf{E} \times \mathbf{H}$ is tangential to the surface S_0, which can be set at z=0. Since we assume that there is no field inside the conductor, we only need to calculate the complex power around the contour of the conductor surface [see red contours in Fig. 5.22 (c)]. Then, the power loss (P_l) per length at the surface S_0 due to the

surface resistance and is

$$P_l = \frac{1}{2}\oint_C R_s |\mathbf{H}_t|^2 dl, \tag{5.53}$$

where C includes three red contours in Figure 5.22 (c).

When there is a current flow I_0 in the transmission line through a series resistance R per length [see Fig. 5.1 (b)], the power dissipation per length is just $P_l = R|I_0|^2/2$. We then find

$$R = \frac{R_s}{|I_0|^2}\oint_C |\mathbf{H}_t|^2 dl. \tag{5.54}$$

The kinetic power (P_k) per length of the charge carrier is given by

$$P_k = \frac{1}{2}\int_C \omega L_s |\mathbf{H}_t|^2 dl. \tag{5.55}$$

Here we can define the kinetic inductance L_k per length, which is due to the inertia of the charge carriers and the fact that they do not scatter. From circuit theory with L_k and I_0 in the transmission line, the kinetic power per unit length is just $P_k = \omega L_k |I_0|^2/2$. Then, the kinetic inductance L_k per unit length is given by

$$L_k = \frac{L_s}{|I_0|^2}\oint_C |\mathbf{H}_t|^2 dl. \tag{5.56}$$

The $\mathbf{H}$ and $\mathbf{E}$ fields fill the space around the conductors. The time-average stored magnetic energy (W_m) and electric energy (W_e) per length is:

$$W_m = \frac{L_m |I_0|^2}{4} \tag{5.57}$$

and

$$W_e = \frac{C|V_0|^2}{4}, \tag{5.58}$$

where L_m is the self-inductance per unit length and C is the capacitance per unit length, which are both determined by the geometry of the CPW. The total inductance per unit length in the system is the sum of L_k and L_m. Then, the total magnetic energy stored in the system per length is given by

$$W_{m,tot} = \frac{(L_m + L_k)|I_0|^2}{4}. \tag{5.59}$$

The internal quality factor of the circuit is defined as [77]

$$Q_i = \omega \frac{\texttt{average energy stored}}{\texttt{power loss}}. \tag{5.60}$$

When the circuit is driven on resonance, $W_{m,tot} = W_e$. Therefore, the average energy stored is $2W_{m,tot}$ and the power loss is P_l. Then, we have

$$\begin{aligned} Q_i &= \omega \frac{(L_m + L_k)|I_0|^2/2}{R|I_0|^2/2} \\ &= \omega \frac{(L_m + L_k)}{R}. \end{aligned} \tag{5.61}$$

Here we can introduce the kinetic inductance fraction α_k [81, 92], which is the ratio of the kinetic inductance L_k to the total inductance $L_k + L_m$:

$$\alpha_k = \frac{L_k}{L_k + L_m}, \tag{5.62}$$

and we can write the quality factor as

$$Q_i = \frac{\omega}{\alpha_k} \frac{L_k}{R}. \tag{5.63}$$

Finally from Eqs. 5.54 and 5.56, one can express the quality factor in terms of the

surface inductance and surface resistance:

$$Q_i = \frac{\omega}{\alpha_k}\frac{L_s}{R_s}. \tag{5.64}$$

5.6.5 Relation between the Complex Conductivity and the Surface Impedance

In a superconductor, both local and non-local transport of current can be observed. In particular, when the mean free path of the paired electrons becomes very large in a "clean" superconductor, a non-local relationship is needed to explain the electrodynamics.

The electrodynamic behavior of superconductors can be classified into three regimes: (i) the extreme anomalous (non-local) limit in a thick film, (ii) the dirty (local) limit in a thick film, and (iii) the dirty limit in a thin film. One can extract information about which limit a film is in from measurements of the surface impedance, which can be related to the complex conductivity using the Mattis-Bardeen theory [96, 81, 92].

For a thick film in the extreme anomalous limit [92],

$$Z_s \sim (\sigma_2 + i\sigma_1)^{-1/3}. \tag{5.65}$$

For a thick film in the local limit [92],

$$Z_s \sim (\sigma_1 - i\sigma_2)^{-1/2}. \tag{5.66}$$

and for a thin film in the local limit [92],

$$\begin{aligned} Z_s &\sim (\sigma_1 - i\sigma_2)^{-1} \\ &\sim (\sigma_1 + i\sigma_2)/(\sigma_1^2 + \sigma_2^2). \end{aligned} \tag{5.67}$$

Comparing Eq. 5.50 with Eq. 5.67 for a thin film in the limit $\sigma_1 \ll \sigma_2$, we find that

$$R_s \sim \sigma_1/(\sigma_2)^2 \tag{5.68}$$

and

$$L_s \sim 1/(\omega\sigma_2). \tag{5.69}$$

Using log differentiation, we can relate Z_s and σ for the three limits [92] by

$$\frac{\delta Z_s}{Z_s} = \gamma \frac{\delta\sigma}{\sigma} \tag{5.70}$$

where $\gamma = -1/3$ for a thick film in the extreme anomalous limit, -1/2 for a thick film in the local limit, and -1 for a thin film in the local limit. These relations are useful for understanding how a superconducting resonator behaves as the temperature changes, as described in the next section.

5.6.6 Resonance Frequency and the Quality factor

The resonance frequency of a superconducting resonator will depend on temperature due to the changes in the surface inductance. Applying log differentiation to $f_0 = 1/2\pi\sqrt{LC}$, the fractional frequency change of the resonator due to changes in the inductance is

$$\frac{\delta f_0}{f_0} = -\frac{\delta L}{2L}, \tag{5.71}$$

where the total inductance is $L = L_k + L_m$. Assuming $L \gg \delta L_m$, one can approximate Eq. 5.71 as

$$\frac{\delta f_0}{f_0} = -\alpha_k \frac{\delta L_k}{2L_k}, \tag{5.72}$$

where $\alpha_k = L_k/L$ is the fractional kinetic inductance. Using Eqs. 5.56 and 5.72, one can express this fractional frequency change in terms of the surface inductance:

$$\frac{\delta f_0}{f_0} = -\alpha_k \frac{\delta L_s}{2L_s}. \tag{5.73}$$

For the thin films we are interested in, $L_s \sim 1/(\omega\sigma_2)$ from Eq. 5.69. Then, one can re-express Eq. 5.73 in terms of the conductivity as

$$\frac{\delta f_0}{f_0} = \alpha_k \frac{\delta \sigma_2}{2\sigma_2}. \tag{5.74}$$

Integrating both sides, one has

$$\begin{aligned} \frac{f_0(T)}{f_0(0)} &= \left[\frac{\sigma_2(T)}{\sigma_2(0)}\right]^{\frac{\alpha_k}{2}} \\ &= \left[1 - \frac{\sigma_2(0) - \sigma_2(T)}{\sigma_2(0)}\right]^{\frac{\alpha_k}{2}} \end{aligned} \tag{5.75}$$

Using a Taylor's series expansion in the limit $[\sigma_2(0) - \sigma_2(T)]/\sigma_2(0) \ll 1$, to a first order, one has

$$\frac{f_0(T)}{f_0(0)} \simeq 1 - \frac{\alpha_k}{2}\left[\frac{\sigma_2(0) - \sigma_2(T)}{\sigma_2(0)}\right] \tag{5.76}$$

Therefore, one can rewrite Eq. 5.74 as [81, 92]

$$\frac{f_0(T) - f_0(0)}{f_0(0)} \simeq \alpha_k \frac{\sigma_2(T) - \sigma_2(0)}{2\sigma_2(0)}. \tag{5.77}$$

The quality factor of the resonator also depends on temperature due to the

change of the surface resistance and inductance. For a thin film, $R_s \sim \sigma_1/(\sigma_2)^2$ from Eq. 5.68 and $L_s \sim 1/(\omega\sigma_2)$ from Eq. 5.69. From Eq. 5.64, one can express the quality factor as

$$Q = \frac{\sigma_2(T)}{\alpha_k \sigma_1(T)}. \tag{5.78}$$

Considering other temperature-independent contributions to Q at zero temperature, one can show that [81, 92]

$$\frac{1}{Q(T)} \simeq \frac{1}{Q(0)} + \frac{\alpha_k \sigma_1(T)}{\sigma_2(T)}. \tag{5.79}$$

Figure 5.19 (a) shows the extracted quality factors for "Resonator1" as a function of temperature, corresponding to the data shown in Fig. 5.18. Blue and green squares are Q_L and Q_e, respectively. Red circles are Q_i, which was obtained from $1/Q_L = 1/Q_i + 1/Q_e$. The black solid curve is from Eq. 5.78 with σ_1 and σ_2 from the Mattis-Bardeen theory. The red and blue solid curves are from Eq. 5.79, where $Q_L(0)$ and $Q_e(0)$ were obtained from the data measured at 30 mK. Figure 5.19 (b) shows the measured resonance frequency (blue circles) as a function of temperature, from Fig. 5.18. The black solid curve is from Eq. 5.77. For the theoretical curves, I used three free parameters: the superconducting gap energy $\Delta_0 = 1.7\ k_B T_c$, the transition temperature $T_c = 1.3$ K, and the fractional kinetic inductance $\alpha_k = 0.035$.

Examination of Fig. 5.18 shows (see page 151) the measured temperature dependence of my device "Resonator1" followed the Mattis-Bardeen theory overall with the addition of a temperature independent loss term. This suggests the rapid decrease in f_0 and Q_L above 200 mK was due to "normal electrons" or thermal

quasiparticles. The main disagreement between the fit and the data is that the data shows less internal loss (higher Q_i) than the fit at 250 mK and 300 mK. This is actually consistent with the saturation of two-level systems at high temperatures [62], and suggests that further analysis of this data could reveal additional information about the "temperature independent" loss-term.

Table 5.1: Parameters of measured lumped-element resonators. There were two different wafer designs: "Wafer A" and "Wafer B". All the resonators were made of Al, had the same design, and did not go through e-beam lithography. The mask title of "Wafer A" and "Wafer B" was "LC resonator" and "QWCPWv3", respectively. Devices from "Wafer A" and "Wafer B" are shown in Fig. 5.3 (b) and Fig. 5.9 (a), respectively. Cu box and PCB are shown in Fig. 5.12 (a) and (b), respectively. P_i is the applied power in the transmission line on the device.

Parameters	"Resonator1"	"Resonator2"	"Resonator3"	"Resonator4"
Wafer type	A	A	A	B
Wafer fabrication date	May 22 '08	Nov 07 '08	March 04 '09	April 02 '09
Package type	Cu box	Cu box	Cu box	PCB
Refrigerator	He-3/He-4	He-3	He-3	He-3
Photoresist	NR7-1500PY	OiR 906-10	OiR 906-10	NR9-1000PY
e-beam resist	none	LOR/ZEP	MMA/ZEP	none
Al thickness	150 nm	150 nm	100 nm	100 nm
Temperature	30 mK	380 mK	380 mK	380 mK
P_i	-55 dBm	-55 dBm	-65 dBm	-70 dBm
f_0 (GHz)	5.578	5.601	5.531	5.582
Q_L	69,000	19,900	11,400	18,600
Q_e	72,700	27,000	25,300	40,700
Q_i	1,350,000	79,000	20,856	34,300

Chapter 6

Circuit Quantum Electrodynamics (CQED)

6.1 Overview

Investigations of the interaction between light and matter have revealed interesting quantum mechanical behavior. When a few photons are confined in a cavity and can interact with an atom many times before the system spontaneously decays, quantum electrodynamic effects can be observed. The cavity quantum electrodynamics (cavity QED) started with microwaves and Rydberg atoms. The initial experiments by Dan Kleppner at MIT were followed by S. Haroche in Paris and H. Walther in Munich [100]. The interaction between a neutral atom and a photon inside an optical cavity was explored in quantum optics [20] [see Fig. 1.3 (a)]. Recent circuit QED experiments [19] using a superconducting qubit (CPB) as an artificial atom and a resonator as a cavity have opened a way to explore solid state qubits [see Fig. 1.3 (b)] from a quantum optics perspective.

In this chapter, I discuss the physics of circuit QED and show measurements on resonator-CPB coupled system that I fabricated (see device pictures in Fig. 6.1).

6.2 Quantized LC Resonator

For a quantum mechanical description of the interaction between photons and an atom inside a cavity, one needs to quantize the states of the cavity or resonator.

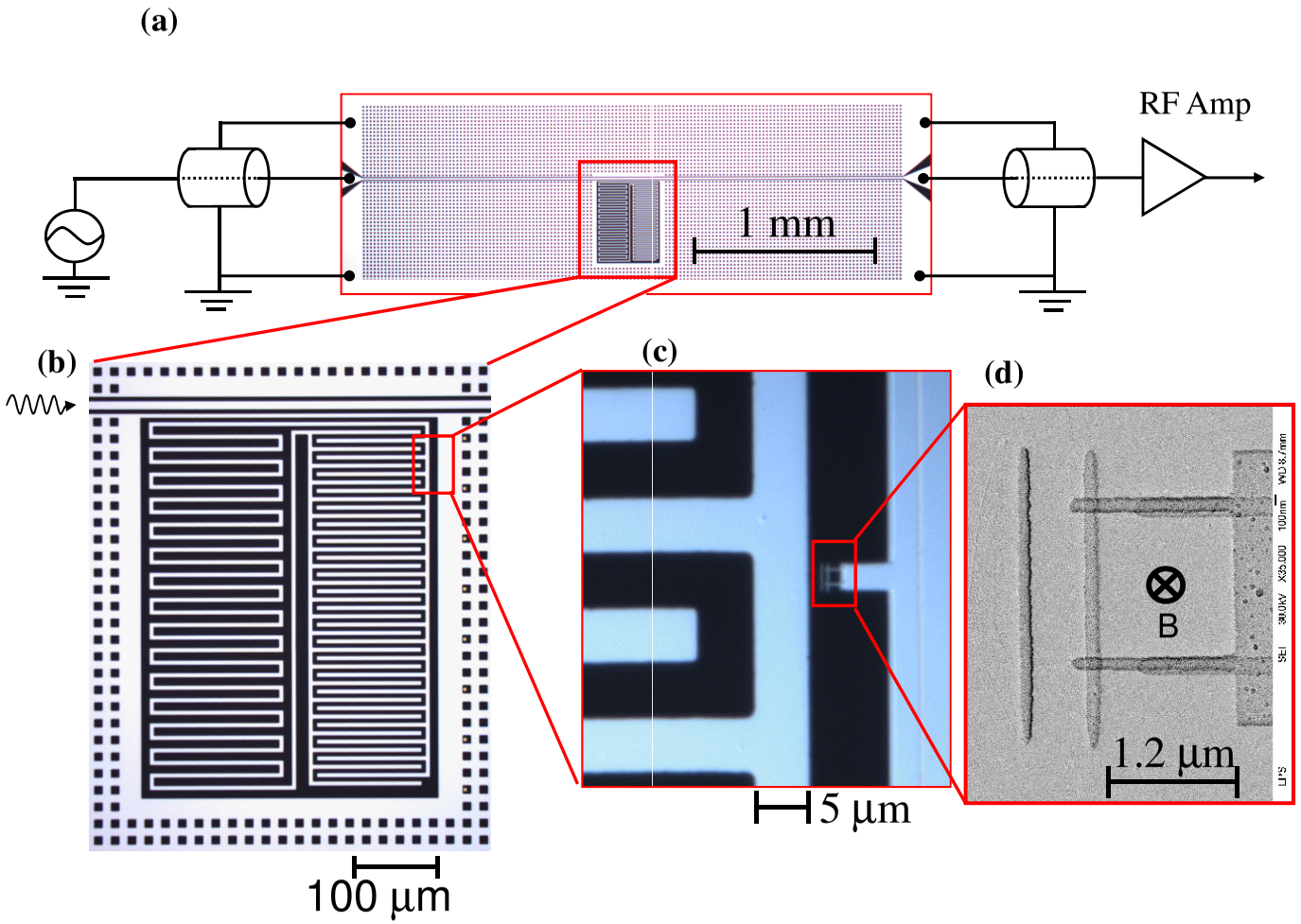

Figure 6.1: Device pictures. (a) Schematic of chip wired to coaxial cables. (b) Optical image of the resonator, (c) optical image of the resonator and CPB around the interdigital capacitor, and (d) scanning electron micrograph of a CPB.

To begin, I consider a simple harmonic oscillator, which has an oscillating mass m attached to a spring. The Hamiltonian is

$$H = \frac{p^2}{2m} + \frac{m\omega_r^2 x^2}{2}, \tag{6.1}$$

where p is the momentum of the mass, $\omega_r/2\pi$ is the frequency of the oscillator, and x is the displacement of the mass from the equilibrium position.

In quantum mechanics, x and p become operators that obey the commutation relation $[x, p] = i\hbar$. The Hamiltonian can be rewritten as

$$\begin{aligned} \hat{H} &= \hbar\omega_r \left(\hat{a}^\dagger \hat{a} + \frac{1}{2}\right) \\ &= \hbar\omega_r \left(\hat{n}_r + \frac{1}{2}\right) \end{aligned} \tag{6.2}$$

by defining the creation operator

$$\hat{a}^\dagger = \frac{m\omega_r}{2\hbar}\left(\hat{x} - \frac{i\hat{p}}{m\omega_r}\right) \tag{6.3}$$

the annihilation operator

$$\hat{a} = \frac{m\omega_r}{2\hbar}\left(\hat{x} + \frac{i\hat{p}}{m\omega_r}\right) \tag{6.4}$$

and the number operator $\hat{n}_r = \hat{a}^\dagger \hat{a}$.

In a lossless parallel LC resonator electrical circuit, the energy is

$$H = \frac{Q^2}{2C} + \frac{(\Phi - \Phi_a)^2}{2L}, \tag{6.5}$$

where Q is the charge stored on the capacitor with capacitance C, Φ is the total flux in the inductor with inductance L, and Φ_a is the applied flux. If the resonator is lossless, then one can model it as an ideal quantum resonator.

By analogy with the mass-and-spring oscillator in Eq. 6.1, one can make the transformation $p \rightarrow Q$, $m \rightarrow C$, $\Phi \rightarrow x$, and $\omega_r \rightarrow 1/\sqrt{LC}$. If Q and Φ are considered to be quantum operators, $\hat{Q}$ and $\hat{\Phi}$ satisfy the commutation relation $[\hat{\Phi}, \hat{Q}] = i\hbar$ [11]. Similarly the creation and annihilation operators in Eqs. 6.4 and 6.5 can be written as

$$\hat{a}^\dagger = \frac{1}{\sqrt{2\hbar Z_{LC}}} \left(\hat{\Phi} - i\hat{Q} Z_{LC} \right) \tag{6.6}$$

and

$$\hat{a} = \frac{1}{\sqrt{2\hbar Z_{LC}}} \left(\hat{\Phi} + i\hat{Q} Z_{LC} \right), \tag{6.7}$$

where $Z_{LC} = \sqrt{L/C}$ is the characteristic impedance of the LC resonator. Hence the Hamiltonian of a quantized LC resonator has the same form as Eq. 6.2, where ω_r is the resonator frequency and $\hat{n}_r = \hat{a}^\dagger \hat{a}$ is the number operator for photons stored in the resonator.

6.3 Jaynes-Cummings Hamiltonian

When an atom and photons are coupled by an interaction of strength g inside a cavity, their states become interdependent. As a result, one can no longer separate the properties of the atom completely from the properties of the photons; *i.e.* they are entangled. Such states are called dressed states [101] and the light will interact with the atom until either the photons in the cavity decay or the atom decays and the system returns to the ground state.

If we ignore both decay of the cavity and the atom and use the rotating wave approximation, the coupled system can be approximated by the Jaynes-Cummings

Hamiltonian [102, 21], which is given by

$$\hat{H} = \hbar\omega_r(\hat{a}^\dagger\hat{a} + \frac{1}{2}) + \frac{\hbar\omega_a}{2}\sigma_z + \hbar g(\hat{a}^\dagger\sigma^- + \hat{a}\sigma^+). \tag{6.8}$$

The first term represents the quantized energy levels of the uncoupled resonator. To get the second term, a two-level approximation was used for the Hamiltonian of the CPB:

$$\hat{H}_{CPB} = \frac{\hbar\omega_a}{2}\sigma_z, \tag{6.9}$$

where $\hbar\omega_a = \sqrt{[4E_C(1-n_g)]^2 + E_J^2}$ corresponds to the energy difference between E_e and E_g of a CPB (see Eq. 2.18). Note that $\hbar\omega_a = E_J$ at $n_g = 1$.

The third term in Eq. 6.8 describes the coupling between the resonator and CPB. Taking into account the n_g dependence of the CPB with $\theta = \arctan[E_J/4E_C(1-n_g)]$ [see Fig. 2.3 (b)], the coupling Hamiltonian is $\hbar g(a^\dagger + a)[1 - n_g - \cos(\theta)\sigma_z + \sin(\theta)\sigma_x]$ [21]. At $n_g = 1$, the maximum coupling strength between the resonator and CPB is defined as $g/2\pi$ in this thesis.

For capacitive coupling, $\hbar g = (eC_{g,r}/C_\Sigma)V_{vac,rms}$, where $C_{g,r}$ is the coupling capacitance between the CPB and resonator, C_Σ is the total capacitance of the CPB island, $V_{vac,rms} = \sqrt{\hbar\omega_r/2C}$ is the rms voltage amplitude for vacuum fluctuations, and C is the capacitance of the resonator [see Fig. 6.2 (a)]. If $\omega_r/2\pi = 5.5$ GHz and $C = 0.4$ pF, then $V_{vac,rms} = 2.13$ μV. Finally, σ^- and σ^+ annihilates and creates an excitation of the CPB, respectively.

The Jaynes-Cummings Hamiltonian can be represented in matrix form [103, 104] [see Figure 6.3 (a)]. It consists of the following n_r sub-matrices, $H^{(n_r)}$, given

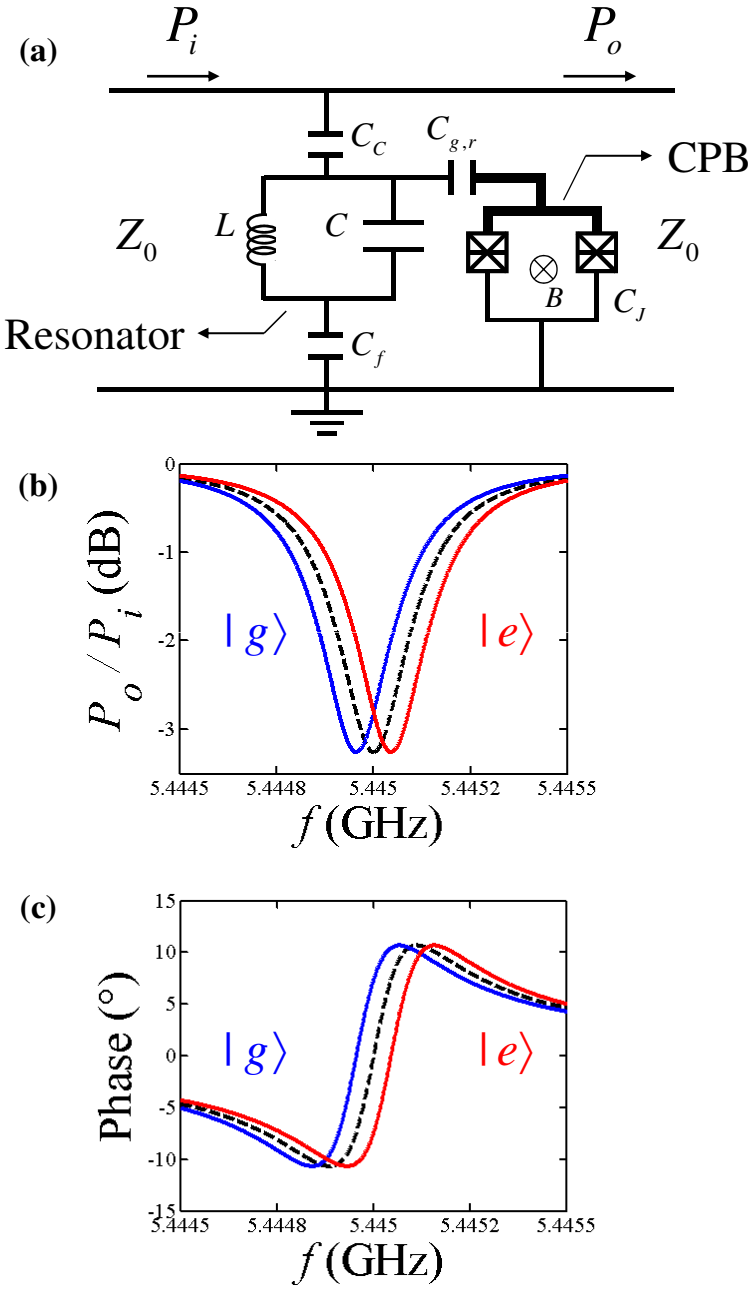

Figure 6.2: (a) Schematic of resonator and CPB coupled together through the coupling capacitance $C_{g,r}$. (b) Black dashed curve represents the transmitted power through the bare resonator or with $C_{g,r} = 0$. Assuming a positive detuning $\Delta/2\pi = 555$ MHz and the coupling strength $g/2\pi = 5$ MHz, the resonance frequency f_r increases by $\chi/2\pi = g^2/(2\pi\Delta) \approx 45$ kHz when the qubit is in the excited state (red curves) compared to the bare resonator. When the qubit is in the ground state, f_r decreases by the same amount of χ (blue curve). (c) Transmitted phase through the coupled system depending on the state of the qubit.

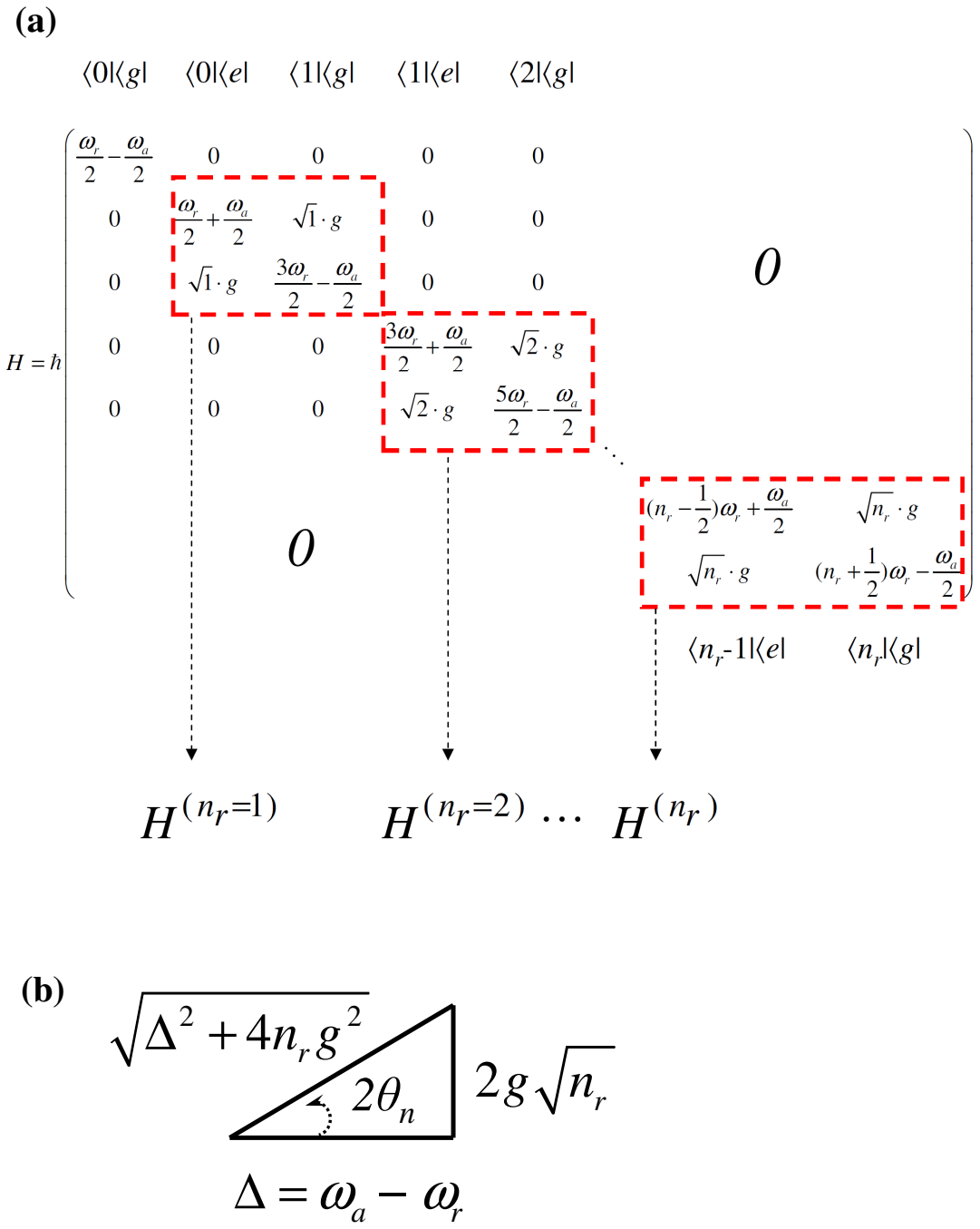

Figure 6.3: The Jaynes-Cummings Hamiltonian. (a) The matrix form of the Jaynes-Cummings Hamiltonian in Eq. 6.8. n_r is the number of photons stored in the resonator. The Jaynes-Cummings Hamiltonian H consists of n_r sub-matrices $H^{(n_r)}$ and zeros elsewhere. (b) The triangular relationship of θ_n (see Eq. 6.14).

by

$$H^{(n_r)} = \hbar \begin{pmatrix} (n_r - \frac{1}{2})\omega_r + \frac{\omega_a}{2} & \sqrt{n_r}g \\ \sqrt{n_r}g & (n_r + \frac{1}{2})\omega_r - \frac{\omega_a}{2} \end{pmatrix}. \tag{6.10}$$

The sub-matrix $H^{(n_r)}$ connects two bare states: $|n_r\rangle|g\rangle$ and $|n_r - 1\rangle|e\rangle$, which differ by the number of photons and excitation of the atom by ± 1. The energy eigenvalues of $H^{(n_r)}$ are

$$E_{n_r,\pm} = n_r\hbar\omega_r \pm \frac{\hbar}{2}\sqrt{(\omega_a - \omega_r)^2 + 4n_r g^2}. \tag{6.11}$$

For the lowest energy level, one finds $E_{0,g} = -\hbar\Delta/2$, where $\Delta \equiv \omega_a - \omega_r$ is the detuning between the resonator and the CPB. The second term in the square root in Eq. 6.11 yields an ac Stark shift when $g \neq 0$. Note that n_r in Eq. 6.11 is strictly speaking *not* the total number of photons in the system but rather the total number of excitations [21] in the coupled system.

The eigenstates [21, 103, 104] of $H^{(n_r)}$ in terms of the two bare states are given by

$$|n_r, +\rangle = \sin\theta_n|g\rangle|n_r\rangle + \cos\theta_n|e\rangle|n_r - 1\rangle \tag{6.12}$$

and

$$|n_r, -\rangle = \cos\theta_n|g\rangle|n_r\rangle - \sin\theta_n|e\rangle|n_r - 1\rangle, \tag{6.13}$$

where

$$\theta_n = \frac{1}{2}\arctan\left(\frac{2g\sqrt{n_r}}{\Delta}\right). \tag{6.14}$$

The triangular relationship of θ_n is shown in Fig. 6.3 (b).

On resonance, when $\Delta = \omega_a - \omega_r = 0$, the energy difference $(E_{n_r,+} - E_{n,-})$ between the coupled states scales with $2\hbar g\sqrt{n_r}$, which can be visualized by the

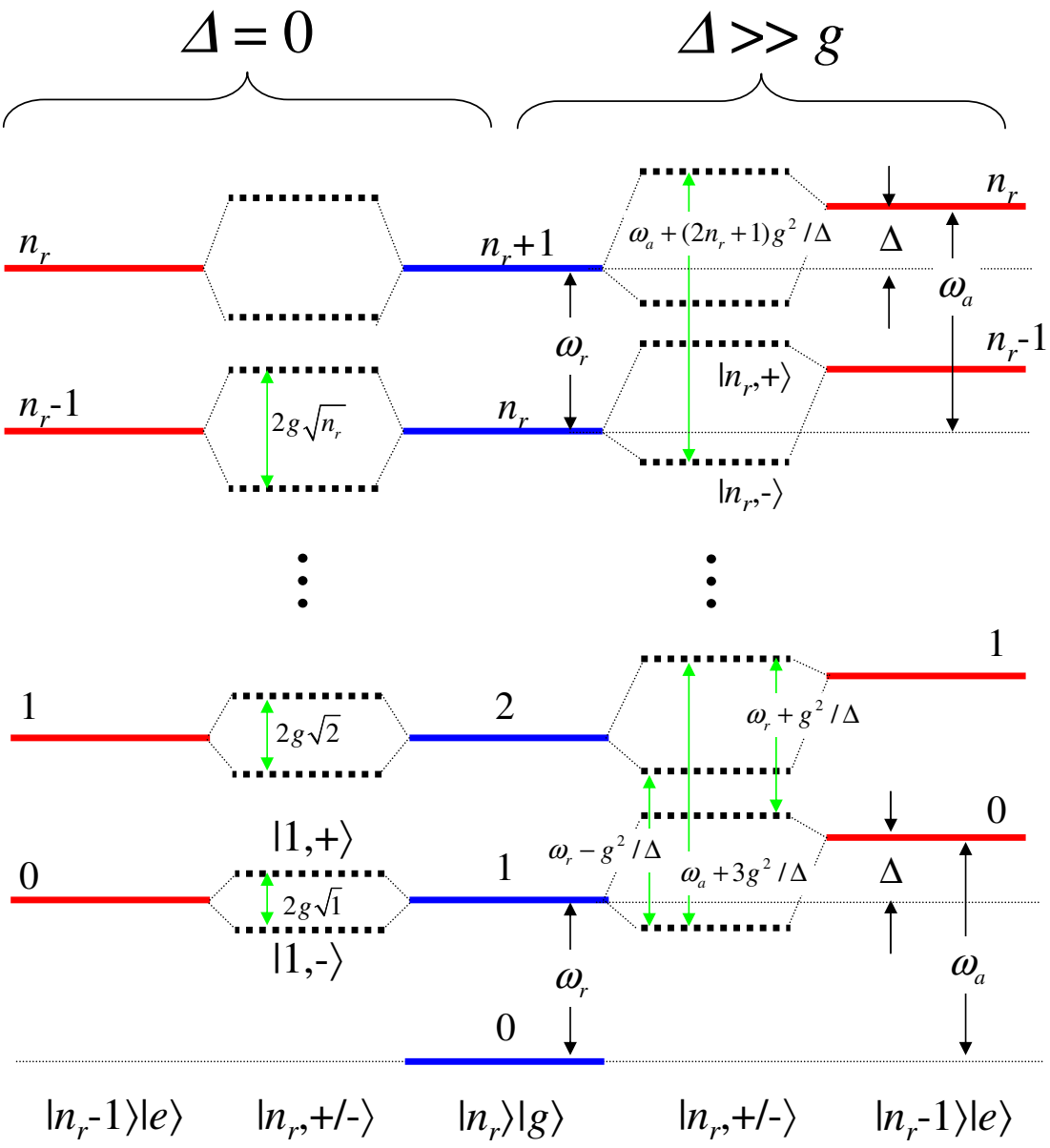

Figure 6.4: The Jaynes-Cummings ladder. One can climb up the ladder by increasing number of photons n_r. The ladder on the left-hand side is for zero detuning $\Delta = 0$ and the ladder on the right-hand side is for large detuning $\Delta \gg g$. Solid lines with blue and red colors represent energy levels of bare states $|n_r\rangle|g\rangle$ and $|n_r - 1\rangle|e\rangle$, respectively, where n_r is the number of photons stored in the resonator. Black dotted lines represent energy eigenvalues of coupled states; $|n_r, +\rangle$ and $|n_r, -\rangle$.

Jaynes-Cummings ladder on the left-hand side in Fig. 6.4. The Jaynes-Cummings ladder shows the energy levels of the atom-photon system. The bare states of the atom and photons are represented by solid lines and the coupled states of the atom and photons are represented by dashed lines. When $n_r = 1$, the energy difference between the coupled states corresponds to $2\hbar g$, which is called the vacuum Rabi splitting. This means that if the state $|g\rangle|1\rangle$ is created, it will oscillate back and forth between $|g\rangle|1\rangle$ and $|e\rangle|0\rangle$ at a frequency of g/π. Here "vacuum" means that the atom is in the vacuum state when the resonator absorbs one photon from the atom and vice versa.

The other limit of the Jaynes-Cummings Hamiltonian is the dispersive limit, when $\Delta \gg g$. In this limit, the Hamiltonian [102, 21, 103] is given by

$$\hat{H} \approx \hbar \left(\omega_r + \frac{g^2}{\Delta} \sigma_z \right) \left(\hat{a}^\dagger \hat{a} + \frac{1}{2} \right) + \frac{\hbar \omega_a}{2} \sigma_z, \tag{6.15}$$

where the first term yields the effective resonance frequency of the resonator. In the first term, one can see that the resonance frequency of the resonator is shifted by $\chi/2\pi = \pm g^2/(2\pi\Delta)$ depending on the state of the qubit. The Jaynes-Cummings ladder on the right-hand side in Figure 6.4 shows schematically the change of the resonance frequency from ω_r of the uncoupled bare states to $\omega_r - g^2/\Delta$ and $\omega_r + g^2/\Delta$ in the coupled states. Figures 6.2 (b) and (c) shows the qubit-state dependence of the resonance; the resonance frequency increases or decreases by the dispersive shift χ depending on the state of the qubit.

One can also obtain the change of resonator frequency from the energy eigenvalues in Eq. 6.11. In the dispersive limit, a Taylor's series expansion can be per-

formed in powers of $4n_r g^2/\Delta^2$. To first order, the energy eigenvalues are

$$E_{n_r,\pm} = n_r\hbar\omega_r \pm \left(\frac{\hbar\Delta}{2} + \frac{\hbar n_r g^2}{\Delta}\right). \tag{6.16}$$

This expansion is valid as long as $n_r \ll n_{crit}$, where

$$n_{crit} = \frac{\Delta^2}{4g^2}, \tag{6.17}$$

which defines a critical number of photons for the dispersive limit. For example, $n_{crit} = 100$ when $\Delta/2\pi = 100$ MHz and $g/2\pi = 5$ MHz.

In the dispersive limit, the excited state of the qubit $|e\rangle$ is close to $|+\rangle$. Hence, the energy difference between two neighboring photon states ($n_r + 1$ and n_r) with the qubit in the excited state is:

$$E_{n_r+1,+} - E_{n_r,+} = \hbar\omega_r + \frac{\hbar g^2}{\Delta}. \tag{6.18}$$

Also, the energy difference between two neighboring photon states ($n_r + 1$ and n_r) with the qubit in the ground state is:

$$E_{n_r+1,-} - E_{n_r,-} = \hbar\omega_r - \frac{\hbar g^2}{\Delta}. \tag{6.19}$$

This leads to a dispersive frequency shift of the resonator which does not depend on the number of excitation n_r as long as $n_r \ll n_{crit}$ is valid.

To see how the ac Stark shift effect [21, 106] arises in the coupled system in the dispersive limit, one can rewrite Eq. 6.15 as

$$\hat{H} \approx \hbar\omega_r\left(\hat{a}^\dagger\hat{a} + \frac{1}{2}\right) + \frac{\hbar}{2}\left(\omega_a + \frac{2g^2}{\Delta}\hat{a}^\dagger\hat{a} + \frac{g^2}{\Delta}\right)\sigma_z, \tag{6.20}$$

where the second term yields the effective qubit angular frequency, $2n_r g^2/\Delta$ is the ac Stark shift term, and g^2/Δ is the Lamb shift induced by the vacuum field. Using Eq. 6.16, the energy difference between two coupled states; $|n_r+1,+\rangle$ and $|n_r,-\rangle$, is given by

$$E_{n_r+1,+} - E_{n_r,-} = \hbar\omega_a + \hbar(2n_r+1)\frac{g^2}{\Delta}, \tag{6.21}$$

reproducing the effective qubit energy given in Eq. 6.20. The Jaynes-Cummings ladder on the right-hand side in Figure 6.4 shows the energy eigenvalues in the dispersive limit.

For small θ_n in the dispersive limit, $\tan(2\theta_n)$ in Eq. 6.14 becomes $2\theta_n$, leading to $\theta_n \simeq g\sqrt{n_r}/\Delta$. Since $\sin\theta_n \simeq \theta_n$ and $\cos\theta_n \simeq 1$, the eigenstates in Eqs. 6.12 and 6.13 can be approximated as

$$|n_r,+\rangle = \frac{g\sqrt{n_r}}{\Delta}|g\rangle|n_r\rangle + |e\rangle|n_r-1\rangle \tag{6.22}$$

and

$$|n_r,-\rangle = |g\rangle|n_r\rangle - \frac{g\sqrt{n_r}}{\Delta}|e\rangle|n_r-1\rangle. \tag{6.23}$$

6.4 Thermal Noise in a Resonator

In circuit QED experiments, it is important to prevent the resonator from being excited by thermal noise. Ideally, the number of thermally occupied photons in the resonator will be determined by the temperature of the bath and not by noise coming down the electrical leads. The probability for a resonator with resonance

frequency f and temperature T to be in the ground state is given by

$$\begin{aligned} P_g &= \frac{1}{\sum_{s=0}^{\infty} \exp(-s\frac{\hbar\omega_r}{k_B T})} \\ &= \frac{1}{Z}, \end{aligned} \tag{6.24}$$

where the denominator is the grand partition function Z for the system. Assuming a resonant frequency of $\omega_r/2\pi = 5.4$ GHz and a temperature $T = 50$ mK, the probability of being in the ground state is 99.5 %. For these parameters, Fig. 6.5 (a) shows a semi-log plot of the probability of the resonator in the ground state as a function of temperature.

We can also calculate the average number of excitations in the resonator as a function of temperature. This is given by,

$$\langle n_r \rangle = \sum_{n_r=0}^{\infty} \frac{n_r \exp(-n_r\frac{\hbar\omega_r}{k_B T})}{Z}. \tag{6.25}$$

Figure 6.5 (a) also shows a log-log plot of the expectation value of the number of resonator excitations as a function of temperature. Examination of this plot shows that to reach the limit where $\langle n_r \rangle < 1$ at $f_r = 5.4$ GHz, we need to cool below $T = 0.37$ K.

On the input side of our device we can put attenuators that thermalize incident noise (see "Microwaves In" in Fig. 6.6). Since we only need very small powers at the device we can put a fair amount of attenuation on this line. However, on the output line from the device, we have to be more careful; we want as little attenuation between the device and the first stage amplifier, otherwise the effective noise temperature of the amplifier goes up (see "Microwaves Out" in Fig. 6.6). To

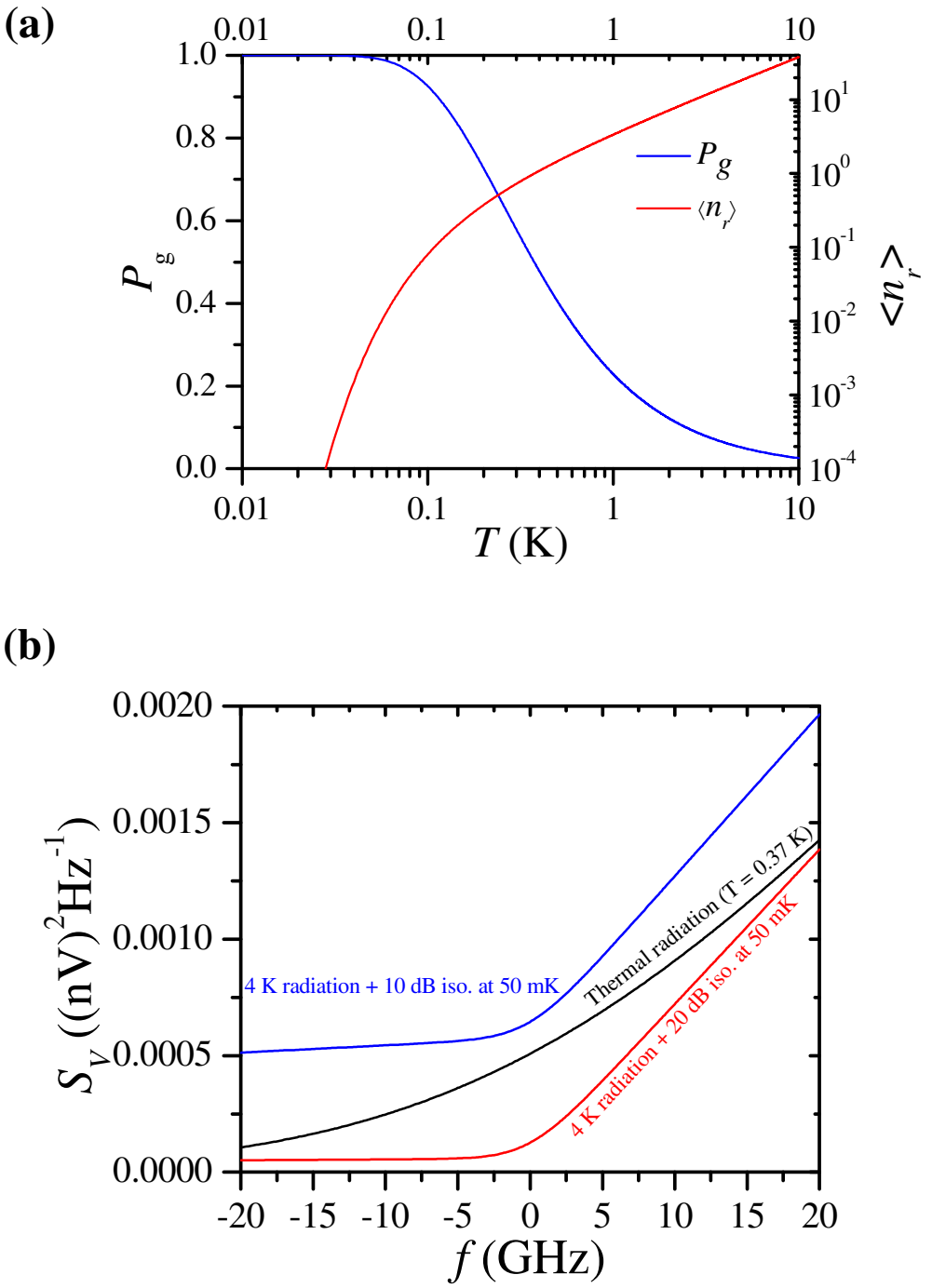

Figure 6.5: (a) Semi-log plot of the probability of the resonator being in the ground state as a function of temperatures (blue curve) and log-log plot of the number of excitations in the resonator as a function of temperature (red curve). (b) Power spectral density of voltage noise in $(\text{nV})^2/\text{Hz}$ from a 50 Ω resistor at $T = 0.37$ K (black curve), 4 K + 10 dB attenuator at 50 mK (blue curve), and 4 K + 20 dB attenuator at 50 mK (red curve).

isolate the device from noise at 4 K going down the output lines, I used isolators, which blocked noise coming down the lines, but not signal going up the lines.

To understand how much isolation we need, recall that the qubit transition rates are given by [29]

$$\Gamma_{\uparrow} = \left(\frac{A}{\hbar}\right)^2 S_V(-f) \tag{6.26}$$

$$\Gamma_{\downarrow} = \left(\frac{A}{\hbar}\right)^2 S_V(f), \tag{6.27}$$

where $\Gamma_{\uparrow}$ and $\Gamma_{\downarrow}$ represent the excitation and decay rate of the qubit, respectively, and A is a coupling factor from the qubit to the voltage fluctuations. Here S_V represents the "double-sided" spectral density of voltage noise (see discussion in sections 2.7 and 3.5). In thermal equilibrium at temperature T, the spectral density of voltage noise from a resistor R (e.g. 50 Ω) at a frequency f is given by Eq. 2.76 or Eq. 3.20. If we have a resistor (R) at temperature T_a and a coax cable that runs to an attenuator with attenuation α_b with the same effective resistance at temperature T_b, then the effective spectral density of voltage noise on the transmission line at the mixing chamber (see Eq. 3.19 and Fig. 3.10) is given by

$$S_V(f) = S_V(f, T_b) + \alpha_b S_V(f, T_a) \tag{6.28}$$

Figure 6.5 (b) shows a plot of the power spectral density of voltage noise as a function of frequency for a 50 Ω resistor at a temperature of $T = 0.37$ K (see the black curve). I also show the noise at $T_a = 4$ K with an $\alpha_b = 10^{-1} = 10$ dB attenuator at $T_b = 50$ mK (see the blue curve). For comparison, I also show noise from $T_a = 4$ K plus an $\alpha_b = 10^{-2} = 20$ dB attenuator at $T_b = 50$ mK (see the red curve). We see that in

order to make the noise temperature smaller than 0.37 K, one needs at least 20 dB of attenuation on the mixing chamber.

Because of that attenuator, however, the total noise that the device sees is not thermodynamic equilibrium noise; *i.e.* the spectral density does not obey

$$S_V(+f) = \exp\left[\frac{hf}{k_B T}\right] S_V(-f). \tag{6.29}$$

To understand the effect of non-equilibrium noise we need to calculate the steady state solution for the qubit to be in its excited state using the rate equations. We will assume that we have a resonator and that transitions can only occur between nearest neighbor levels. The rate of change of the probability of the ground state is given by

$$\frac{dP_0}{dt} = P_1\Gamma_\downarrow - P_0\Gamma_\uparrow. \tag{6.30}$$

The rate of change of the probability of the n_rth state, for $n_r > 0$, is given by

$$\frac{dP_{n_r}}{dt} = (n_r+1)P_{n_r+1}\Gamma_\downarrow + n_r P_{n_r-1}\Gamma_\uparrow - P_{n_r}(n_r\Gamma_\downarrow + (n_r+1)\Gamma_\uparrow). \tag{6.31}$$

Note the factor $n_r + 1$ and n_r in Eq. 6.31 come from the raising and lowering operators.

Since we are considering the steady state condition, the left hand side is zero. From Eq. 6.30 we have

$$P_1 = \frac{\Gamma_\uparrow}{\Gamma_\downarrow} P_0. \tag{6.32}$$

For the second state, we have

$$P_2 = (2\Gamma_\downarrow)^{-1}[P_1(\Gamma_\downarrow + 2\Gamma_\uparrow) - P_0\Gamma_\uparrow] \tag{6.33}$$

or

$$P_2 = \left(\frac{\Gamma_\uparrow}{\Gamma_\downarrow}\right)^2 P_0. \tag{6.34}$$

The recursion relation for the n_rth state is just

$$P_{n_r} = \left(\frac{\Gamma_\uparrow}{\Gamma_\downarrow}\right)^{n_r} P_0. \tag{6.35}$$

To solve for the probability of being in the ground state or the n_rth state we can use the normalization constraint

$$\sum_{n_r=0}^{\infty} P_{n_r} = 1. \tag{6.36}$$

Solving for P_0 we get

$$\begin{aligned} P_0 &= \frac{1}{\sum_{n_r=0}^{\infty}\left(\frac{\Gamma_\uparrow}{\Gamma_\downarrow}\right)^{n_r}} \\ &= \frac{1}{\left(\frac{1}{1-\Gamma_\uparrow/\Gamma_\downarrow}\right)} \\ &= 1 - \frac{\Gamma_\uparrow}{\Gamma_\downarrow}. \end{aligned} \tag{6.37}$$

The average number of photons can be found from Eqs. 6.35 and 6.37

$$\begin{aligned} \langle n_r \rangle &= \sum_{n_r=0}^{\infty} n_r P_{n_r} \\ &= \sum_{n_r=0}^{\infty} \left(\frac{n_r \left(\frac{\Gamma_\uparrow}{\Gamma_\downarrow}\right)^{n_r}}{\sum_{s=0}^{\infty}\left(\frac{\Gamma_\uparrow}{\Gamma_\downarrow}\right)^{s}} \right). \end{aligned} \tag{6.38}$$

Note that in the limit that the noise is thermal equilibrium noise (Eq. 6.29), Eq. 6.38 becomes Eq. 6.25. Using Eqs. 6.27, 6.28, and 6.38, I find that if there is one 10 dB isolator on the mixing chamber, then the average number of photons is on the order of 1.4 at $T_b = 50$ mK and 5.4 GHz. If we put a total of 20 dB of isolation on the

mixing chamber we get an average number of photons of 0.16. For $\langle n_r \rangle = 1$, one needs approximately 11.5 dB of isolation.

6.5 Experimental Setup

6.5.1 Dilution Refrigerator Setup

A schematic of cables and electrical components in the refrigerator is shown in Fig. 6.6; this set-up went through a few iterations and this arrangement is what I settled on in the end. A total of 60 dB attenuation was added to the microwave line feeding power to the resonator. The dc line for the CPB gate voltage was combined with microwaves using a bias T on the mixing chamber. There were no filters on the dc lines because it is very lossy and behaved as a filter going to the device. The total attenuation of the dc lines were about 27 dB at 0.5 GHz, 37 dB at 1 GHz, and 83 dB at 5 GHz [30]. To allow dc bias for the CPB, a dc block was placed right after the sample. Figure 6.7 shows photographs of the cold stage and 4 K stage.

As I discussed in the last section on thermal noise, we need to use less attenuation on the signal output line and still achieve high isolation from any noise going from the 4 K stage to the device. For that purpose, I used two isolators in series on the cold stage, with an isolation of 18 dB for each isolator between 4 and 8 GHz [see Figs. 6.6 and 6.7 (a)]. Figures 6.8 (a) and (b) show the transmission and isolation through each of the isolators, respectively. I measured each isolator individually by immersing it in liquid nitrogen and measuring the S-parameters using a network analyzer (Agilent E5071c). The transmission was flat with a small attenuation of

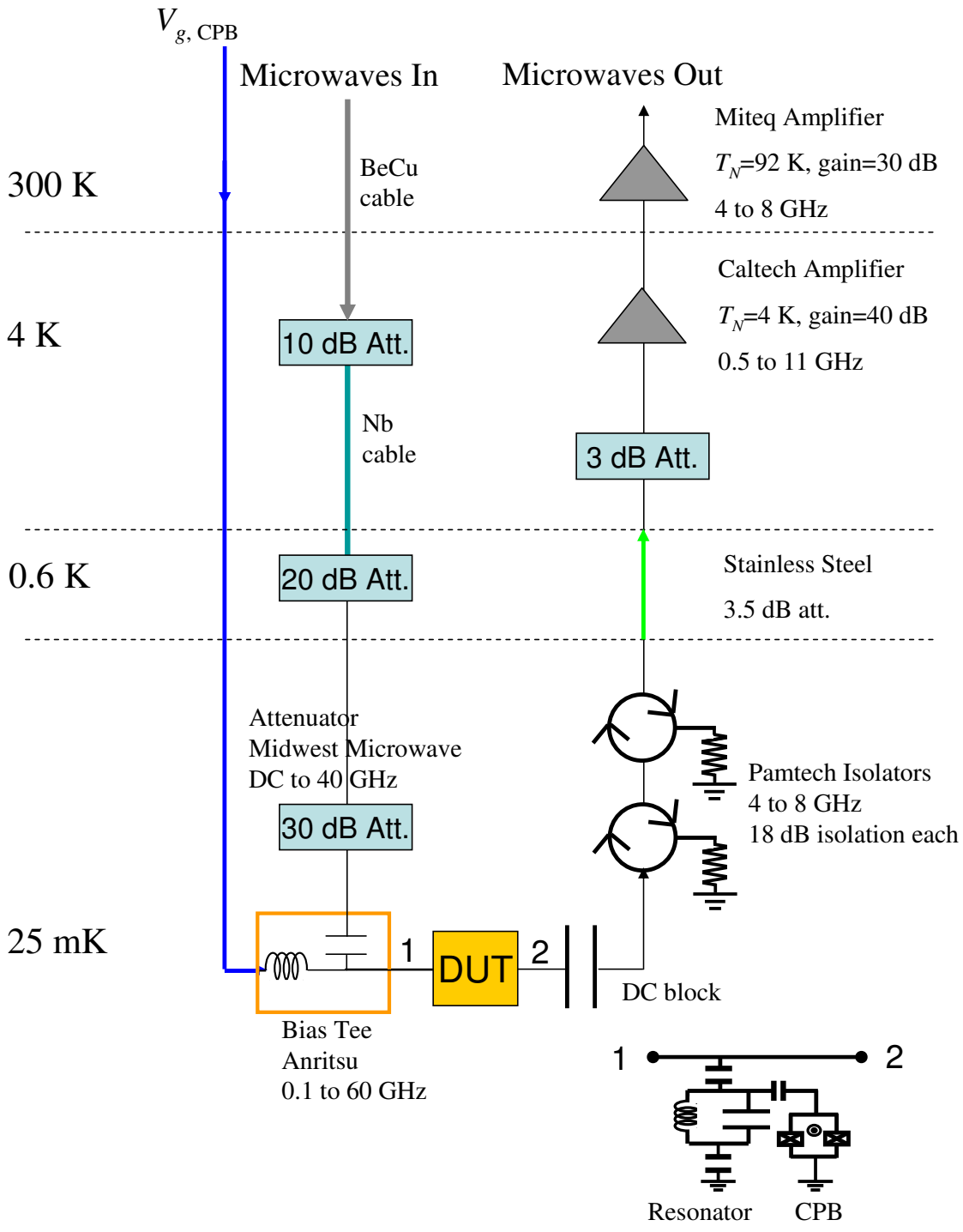

Figure 6.6: Dilution refrigerator wiring set-up. A dc cable is shown in blue. DUT means Device Under Test and its schematic is in the lower right-hand corner.

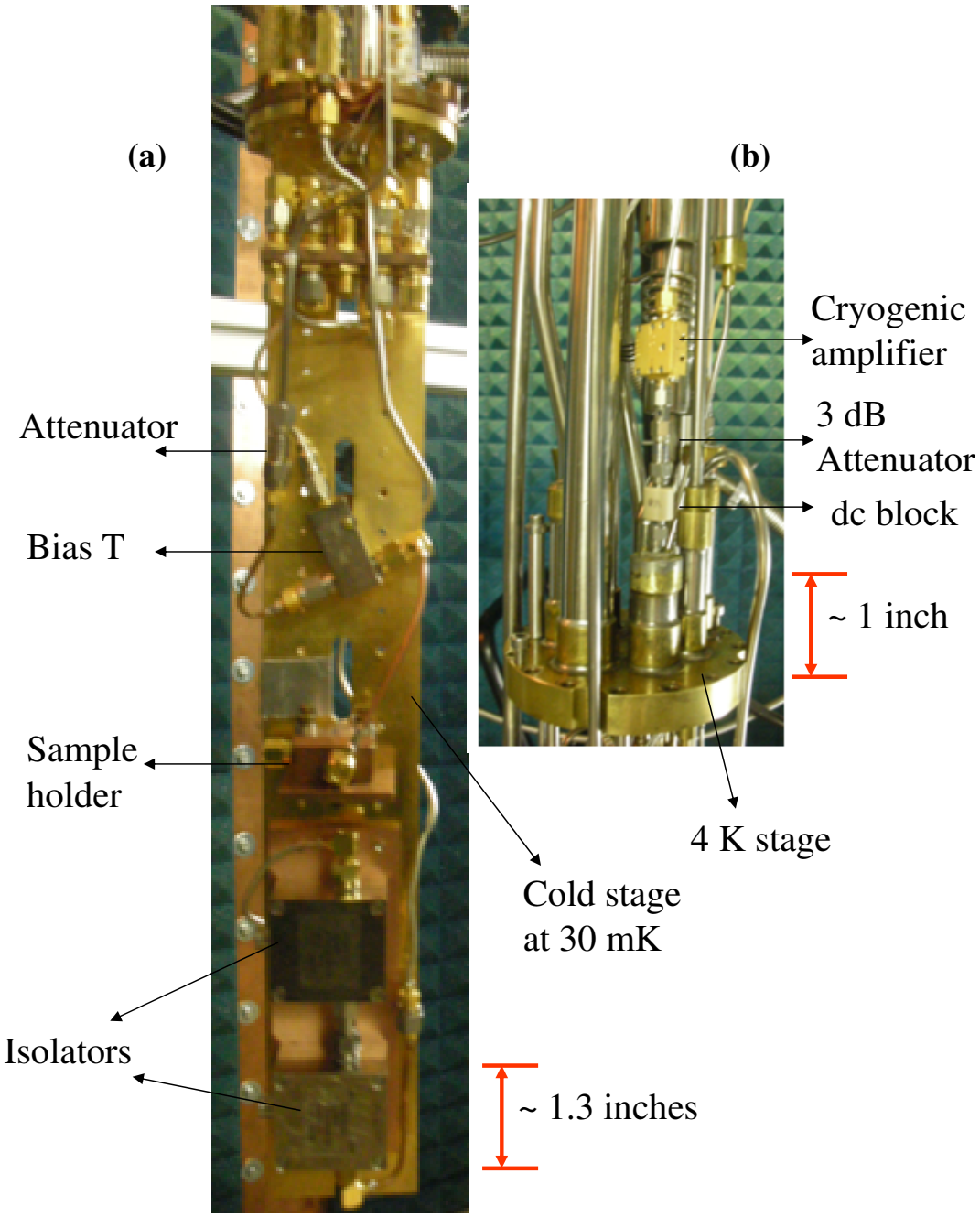

Figure 6.7: (a) Photograph of components at the cold stage and (b) photograph of components at the 4 K stage. For experiments after Dec 09 '09, the dc block was inserted between the device output and the isolator input on the cold stage.

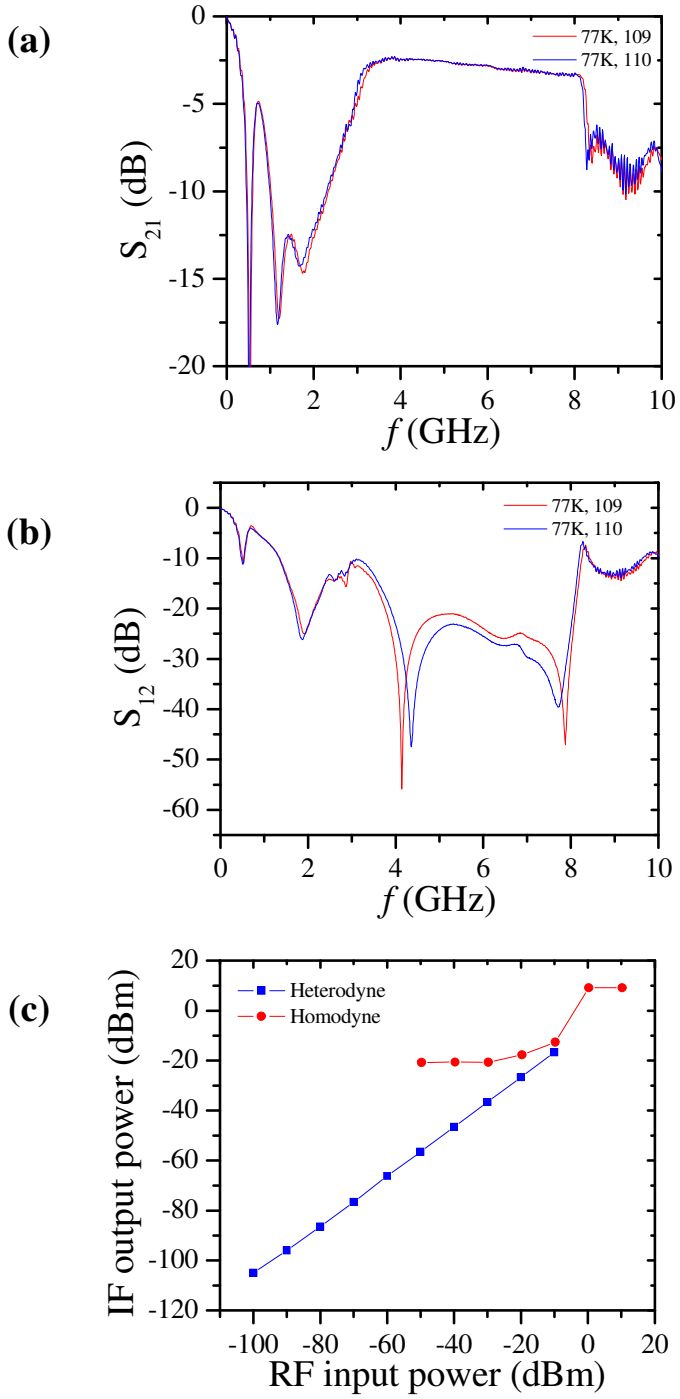

Figure 6.8: (a) Transmission of isolators at 77 K. Two isolators with the same design and specification were ordered: "109" and "110" are the serial numbers. (b) Isolation of isolators at 77 K. (c) The IF output of the single channel mixer as a function of the RF input power. Blue and red curves were measured by heterodyne and homodyne measurements, respectively.

about 2.5 dB between 4 to 8 GHz, which is the bandwidth of the isolator. The isolation was more than 20 dB from 4 to 8 GHz. The isolators also had magnetic shielding that allowed them to be used up to 1,000 Gauss; it was necessary to apply a magnetic field to vary E_J and it was best if this field did not affect the isolation.

After the device and isolators I used a stainless steel cable (UT85-SS-SS) with attenuation of 3.5 dB around 5.5 GHz to connect the mixing chamber and 4 K stage. We also tried to replace the lossy stainless steel cable with a BeCu cable to increase the signal-to-noise ratio; the BeCu cable had only a 0.6 dB loss. But we noticed that the refrigerator was only getting to 60 mK, probably due to heat flowing down the BeCu cable, so we went back to using UT85-SS-SS.

Our low noise cryogenic amplifier (Caltech: Model 210, see Appendix B), which is specified to have a noise temperature of 4 K around 5.5 GHz, was placed in the liquid helium bath. To prevent this amplifier from going into self-oscillation, we found we had to place a 3 dB attenuator right before the amplifier (see Fig. 6.6).

6.5.2 Measurement Setup

The set-up at the mixing chamber and 4 K stage were described in section 6.5.1. Here I describe the room temperature experimental setup. Figure 6.9 shows a schematic of the measurement set-up. The blue dashed lines are for the cold stage at 25 mK and red dashed lines are for the low noise amplifier at 4 K. Outside of the dashed boxes are parts that are at room temperature. On the left-hand side of the blue dashed box, one can see two microwave sources for two tones: the pump and probe.

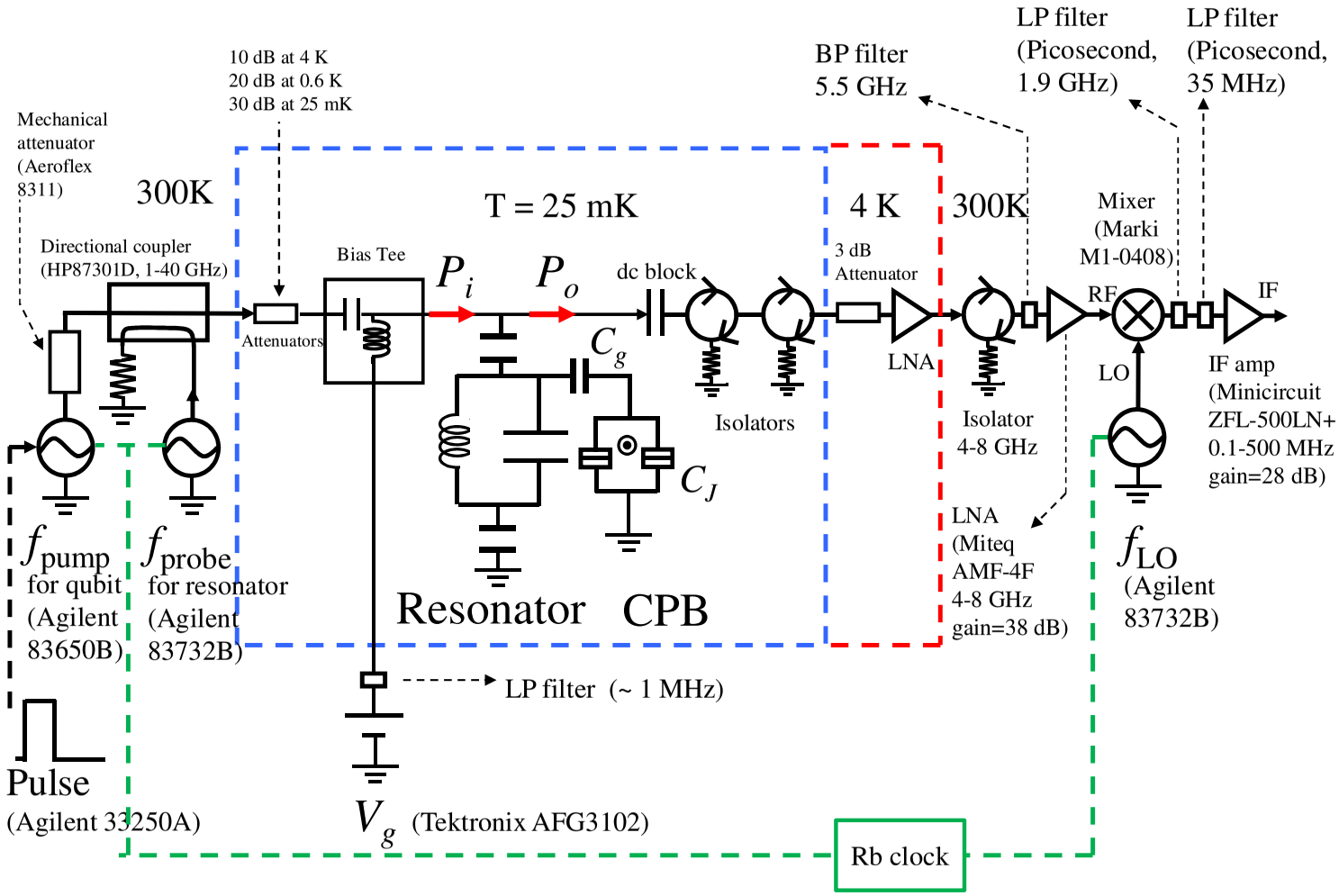

Figure 6.9: Schematic of the experimental set-up. The blue dashed box is the cold stage at the base temperature of 25 mK. The red dashed line is for the cryogenic amplifier at the 4 K stage. A Rubidium clock (Stanford Research Systems: FS725) [107] was used as a 10 MHz external clock for the signal generators.

The probe (the first tone) was used to measure the resonator while the pump (the second tone) was used to manipulate and excite the qubit. They were combined using a directional coupler (HP 87301D), which has a bandwidth from 1 GHz to 40 GHz. A Rubidium clock (Stanford Research Systems: FS725) [107] was used as a 10 MHz external clock for the signal generators. To sweep and dc bias the CPB gate voltage, I used an arbitrary waveform generator (Tektronix AFG3102)

After the cryogenic amplifier, the microwave signal went to a room temperature microwave isolator and bandpass filter with a center frequency of 5.5 GHz (see the right-hand side of the red dashed lines in Fig. 6.9). The isolator was used to reduce reflected signals while the bandpass filter was used to reduce the integrated signal to a smaller band around the probe frequency. Next, the microwave signal was amplified by a low noise amplifier (Miteq P/N: AMF-4F-04000800-12-10P), which had a gain of 38 dB over 4 GHz to 8 GHz.

After the LNA, the signal was passed through a mixer (Marki: M1-0408), where it was mixed down with a local oscillator (LO) to a low frequency signal, or IF signal. This mixer technique is discussed in section 6.5.3. To filter some leakage signal and reduce the integrated noise, the IF signal then passed through two absorptive low pass filters (Picosecond Pulse Labs) with cut-off frequencies at 1.9 GHz and 35 MHz.

Finally, the IF signal was amplified with an IF amplifier (Minicircuit) then sent to a digital oscilloscope (Agilent 54855A Infiniium), where we extracted the amplitude and phase of the probe signal by digitizing the IF signal (see next section).

Before the IF signal reached the digital oscilloscope, I filtered it with low pass

filters (Minicircuit) with cut-off frequencies at 1.9 MHz or 10 MHz. Next, the IF signal was sampled and averaged by the digital oscilloscope. I preferred to use this oscilloscope, rather than a conventional DAC because it has greater isolation between the input ports. For clean spectroscopy, the typical IF frequency was 400 kHz and I used a lower cut-off filter. For time-domain measurements, I used a higher IF frequency, up to 5 MHz.

6.5.3 Heterodyne Measurement

As I discussed in section 6.3, the resonator frequency changes depending on the qubit state, and changes in the resonance frequency are measurable by monitoring the transmitted amplitude and phase of a microwave signal [see Figs. 6.2 (b) and (c)]. To measure the response of a resonator, I initially used a vector network analyzer, which was convenient for measuring S_{21} over a wide frequency range quickly. For a qubit measurement, however, one needs a very accurate microwave source, ideally to an Hz, whereas the width from our network analyzer was on the order of 50 kHz. The measurement versatility of the network analyzer was also poor.

The resonance frequency of the resonator was $f_r = 5.5$ GHz, which is not convenient for measuring directly on an oscilloscope or DAC. One can convert the frequency down to dc or low frequency by making a homodyne or heterodyne measurement. Such frequency down-conversion can be performed by a microwave mixer; note that a similar technique is used internally in a vector network analyzer.

A single channel mixer consists of an RF input, local oscillator (LO) input,

and intermediate frequency (IF) output (see Fig. 6.9). The RF input voltage V_{RF} and LO input voltage V_{LO} are

$$V_{RF}(t) = A(t)\sin(\omega_{RF}t + \phi(t)) \tag{6.39}$$

$$V_{LO}(t) = B_0\sin(\omega_{LO}t), \tag{6.40}$$

where $A(t)$ and $\phi(t)$ represent the amplitude and phase of the probe signal from the resonator and B_0 is the constant voltage amplitude from the local oscillator, which we assume has constant zero phase offset. The mixer multiplies the input voltage signal with the voltage signal from the LO and produces an output voltage:

$$V_{IF}(t) = \frac{A(t)B_0}{2}[\cos((\omega_{RF} - \omega_{LO})t + \phi(t)) - \cos((\omega_{RF} + \omega_{LO})t + \phi(t))]. \tag{6.41}$$

Since we want an output that is the difference of two frequencies, we use a low-pass filter to remove the high frequency component at $\omega_{RF}+\omega_{LO}$. The resulting IF signal becomes

$$V_{IF}(t) = A^{'}(t)\cos[\omega_{IF}t + \phi(t)], \tag{6.42}$$

where $A^{'}(t) = A(t)B_0/2$ and $\omega_{IF} = \omega_{RF} - \omega_{LO}$.

For $\omega_{IF} = 0$, the IF signal is dc and this is a homodyne measurement. For a homodyne measurement, we noticed that there is a lower limit to the input rf power that can be used due to poor isolation between the LO and RF ports or due to self-mixing of the LO [see the red curve in Fig. 6.8 (c)]. In contrast, a heterodyne measurement ($\omega_{IF} \neq 0$) avoids this problem in the low rf power limit [see the blue curve in Fig. 6.8 (c)], but it requires two microwave sources with slightly different

frequencies. The circuit QED experiments require a small number of photons, hence we had to use a heterodyne measurement.

For a heterodyne measurement, the mixed down IF output $V_{IF}(t)$ is an ac signal having a frequency of ω_{IF}. In order to extract the in-phase $I(t)$ and out-of-phase $Q(t)$ components from $V_{IF}(t)$, we used the Fourier transform [103]:

$$I(t) = \frac{1}{T_{IF}} \int_{t}^{t+T_{IF}} \cos(\omega_{IF}\tau) V_{IF}(\tau) d\tau, \tag{6.43}$$

$$Q(t) = \frac{1}{T_{IF}} \int_{t}^{t+T_{IF}} \sin(\omega_{IF}\tau) V_{IF}(\tau) d\tau, \tag{6.44}$$

where $T_{IF} = 2\pi/\omega_{IF}$ is the period of the IF frequency. In actual measurements, we used a summation instead of an integral, hence Eqs. 6.43 and 6.44 become

$$I(t) = \frac{1}{T_{IF}} \sum_{n=0}^{N} \cos(\omega_{IF}\tau_n) V_{IF}(\tau_n) \Delta\tau, \tag{6.45}$$

$$Q(t) = \frac{1}{T_{IF}} \sum_{n=0}^{N} \sin(\omega_{IF}\tau_n) V_{IF}(\tau_n) \Delta\tau, \tag{6.46}$$

where $\tau_n = t + n\Delta\tau$, $\Delta\tau = T_{IF}/N$, and N is the number of data points in an IF period T_{IF}. Note that I used a sampling rate for my measurements equal to $N \times \omega_{IF}/2\pi$.

From $I(t)$ and $Q(t)$, I can get the time dependent amplitude $A^{'}(t)$ and phase $\phi(t)$:

$$A^{'}(t) = \sqrt{I(t)^2 + Q(t)^2} \tag{6.47}$$

$$\phi(t) = \arctan\left(\frac{Q(t)}{I(t)}\right). \tag{6.48}$$

6.6 Dispersive Limit

6.6.1 Dispersive Shift of the Resonator Resonance

The Jaynes-Cummings Hamiltonian (Eq. 6.15) predicts the dispersive frequency shift of the resonator when the resonator is coupled to the qubit even when the qubit ground state is far detuned. The corresponding dispersive shift of the resonator is $\chi/2\pi = g^2/(2\pi\Delta)$, where the detuning Δ is a function of E_J and n_g. Note that the amount of dispersive shift is the same regardless of whether the qubit is in the ground state or excited state, except that the sign will be opposite. Measuring $\chi/2\pi$ when the qubit is in the ground state turns out to be easier than when the qubit is in the excited state; for the excited state, we need to apply a second tone or pump frequency as well as the probe frequency. For single-tone spectroscopy, I measured the transmitted amplitude and phase of the probe signal through the resonator while sweeping the applied gate voltage to the CPB and stepping the microwave probe frequency.

Figure 6.10 shows single-tone spectroscopy of device "LEQED1" at two different magnetic fields. The source power was -70 dBm and the total loss from the directional coupler (17 dB) and attenuation in the refrigerator including cables (53.5 dB) was 70.5 dB from room temperature to the chip. Hence, the expected power of the probe signal on the transmission line in the chip was approximately -140.5 dBm or 8.9 aW. The relationship between the average power and number of photons in the resonator is $P_i = \kappa_r \langle n_r \rangle \hbar\omega_r$, where the energy decay rate of resonator is given by $\kappa_r/2\pi = f_r/Q_L = 0.18$ MHz (see Table 6.1). The average number of photons

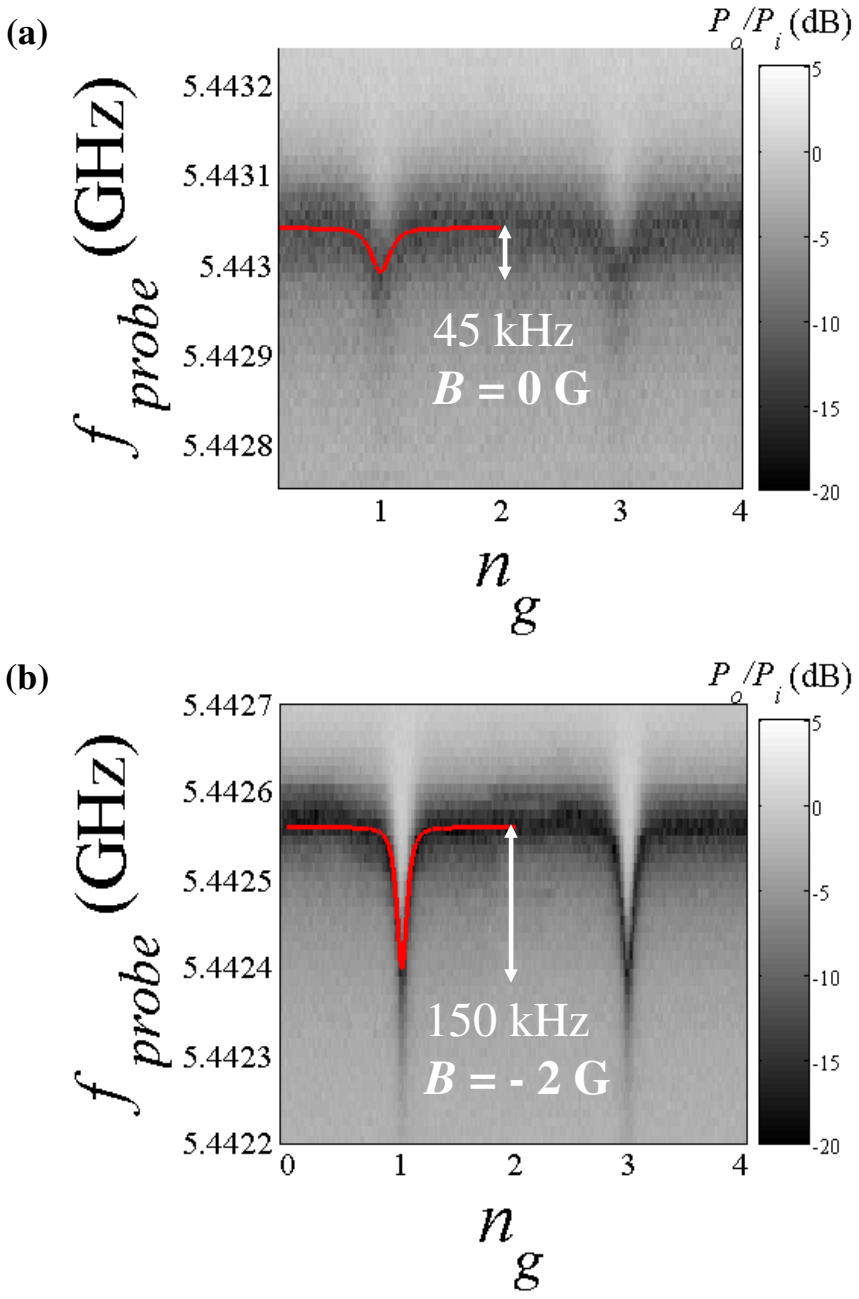

Figure 6.10: Single-tone spectroscopy of device "LEQED1". Measured transmitted probe amplitude (gray color) in the log scale as a function of the probe frequency f and n_g at B = 0 Gauss (a) and B = -2 Gauss (b). The red curves in (a) and (b) are the predicted spectrum from the Jaynes-Cummings Hamiltonian using the matrix in Fig. 6.3. Measured E_J/h of (a) and (b) was 8.15 GHz and 6.29 GHz, respectively from two-tone spectroscopy (see Fig. 6.13). From the detuning and dispersive frequency shift, I extracted $g/2\pi \simeq 11$ MHz.

in the resonator is expected to be approximately $\langle n_r \rangle = 2$. For this measurement, I ramped the gate voltage at 500 Hz and stepped the microwave frequency with a step size of 10 kHz. I averaged the IF signal 500 times at the oscilloscope and had Labview average them again 20 times. Thus, the total number of average was 10,000 for each frequency.

At zero magnetic field, a small resonance frequency shift of 45 kHz was measured at $n_g = 1$ and $n_g = 3$ [see Fig. 6.10 (a)]. This was smaller than the resonator width of 0.2 MHz [see Fig. 6.11 (a)]. The maximum E_J/h of the CPB "LEQED1", estimated from the SET resistance was 9 GHz and the measured E_J/h was 8.15 GHz at the same field used in this single-tone spectroscopy. As Eq. 6.19 predicts, the dispersive shift did not increase as I increased the number of photons as long as it was smaller than the critical number of photons, expected to be $n_{crit} = 15,000$ given $\Delta/2\pi = 2.7$ GHz and $g/2\pi = 11$ MHz. When I applied too much power, the dispersive frequency shift started to break down and the resonator showed strange behavior (see Fig. 7.2 and the discussion in section 7.1.3).

The observed dispersive shift has a periodicity in n_g of 2, which implies that there are no quasiparticles or at least a very small non-equilibrium quasiparticle population. To calibrate n_g, I warmed up the device to introduce thermal quasiparticles. I heated the mixing chamber and monitored the periodicity of the dispersive shift for temperatures of 30 mK, 150 mK, 200 mK, 250 mK, and 300 mK. When the temperature reached 250 mK, another dispersive shift appeared and doubled the periodicity due to thermal quasiparticles. In this way I calibrated n_g and verified 1-e periodicity at $T > 250$ mK. For $\Delta n_g = 2$, or a change of one excess Cooper-pair

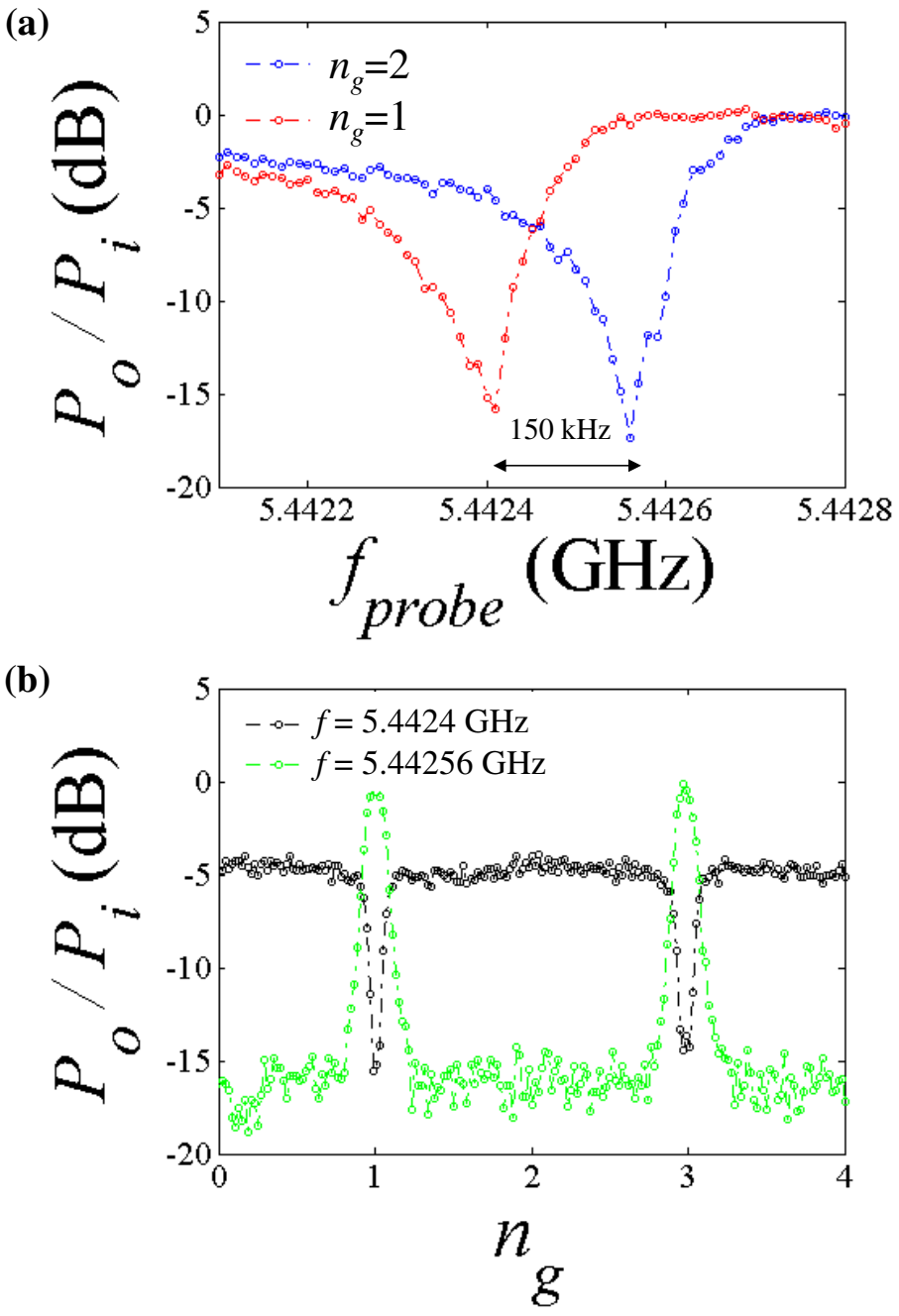

Figure 6.11: (a) Line cuts of Fig. 6.10 (b) at $n_g = 1$ and 2 along the probe frequency f. The resonator frequency was pulled down by 150 kHz at n_g=1, coupled with the qubit in the ground state (red curve). (b) Line cuts of Fig. 6.10 (b) at $f = 5.4424$ GHz (black curve) and $f = 5.44256$ GHz (green curve) along n_g.

(2e) on the island of the CPB, I applied a change in the dc gate voltage $\Delta V_g = 68$ mV. From $2e = C_{g,dc}\Delta V_g$, the dc gate capacitance was thus $C_{g,dc} = 4.7$ aF.

Increasing the B field increased the dispersive shift as expected [see Fig. 6.10 (b)]. At $B = -2$ Gauss, I observed a dispersive shift of $\chi/2\pi = 150$ kHz and E_J was found to be about 6.2 GHz. E_J and E_C of the CPB were measured by two-tone spectroscopy, which is discussed in the next section. From the measured dispersive shift $\chi/2\pi = 150$ kHz and detuning $\Delta/2\pi = 0.847$ GHz, I extracted a coupling strength $g/2\pi \simeq 11$ MHz. Using the Jaynes-Cummings Hamiltonian in matrix form (see Fig. 6.3) I was able to get a good fit to the dispersive shift of the resonator (see the red curve in Fig. 6.10).

Figure 6.11 (a) shows line cuts along f at $n_g = 1$ and 2 from Fig. 6.10 (b), showing the transmitted power through the resonator. The resonator resonance decreased by 150 kHz at $n_g = 1$, or the charge degeneracy point, where the coupling between the resonator and CPB was maximized since the detuning was minimized. At $n_g = 2$, the coupling was effectively off since the detuning was a maximum.

Figure 6.11 (b) shows line cuts along n_g for fixed probe frequency from Fig. 6.10 (b). The green curve is the transmitted power as a function of n_g when the probe frequency was fixed to the resonator's center frequency of $f = 5.44256$ GHz. At $n_g =$ 1 and 3, the transmitted power increased to 0 dB due to the dispersive shift of the resonator. As n_g moves away from those degeneracy points, the transmitted power decreased to -17 dB, which corresponded to the amplitude of the resonance. The black curve is the transmitted power as a function of n_g when the probe frequency was slightly detuned from the center frequency of the resonator and fixed to $f =$

5.4424 GHz. Since the resonance shifted down to $f = 5.4424$ GHz, the transmitted power dropped to -15 dB at $n_g = 1$ and 3. This is the opposite behavior from that of the green curve when the probe frequency was fixed to the center frequency of the resonator. But, due to the asymmetry of the resonance curve along f, the transmitted power for the black curve did not completely recover to 0 dB when n_g was away from the degeneracy points.

I was not able to observe the resonant limit, where $\Delta = 0$, directly by single tone spectroscopy, since I found it was hard to control the E_J of the CPB "LEQED1". We suspect magnetic vortices entered into the device or the ground plane, making it hard to change E_J smoothly. I also observed sudden drops in the quality factor of the resonator and substantial changes in the resonance frequency in nonzero magnetic fields. In those cases, I had to warm up above 1.3 K (T_c of the Al) with the magnetic field zero and cool back down to recover a sharp resonance.

Figure 6.12 shows single-tone spectroscopy of the second device "LEQED2". Since this device had an estimated maximum E_J of 19 GHz from the SET resistance, I could not observe the dispersive shift at zero magnetic field. Typically I applied a magnetic field between ± 4 and ± 2 Gauss in order to see a dispersive shift. Assuming the area of the CPB loop is $1\mu\text{m} \times 1\mu\text{m}$, under a magnetic field $B = 1$ Gauss, the ratio of the applied flux Φ_a to the flux quantum $\Phi_\circ$ is about 0.05. For $B = 3$ Gauss, $\Phi_a/\Phi_\circ \simeq 0.145$. Hence, one needs 20 Gauss for one flux quantum although this ignores flux shielding and focussing from the ground plane.

When a magnetic field $B = -2.855$ Gauss was applied to the device, I observed a dispersive shift of 150 kHz when the number of probe photons stored in the

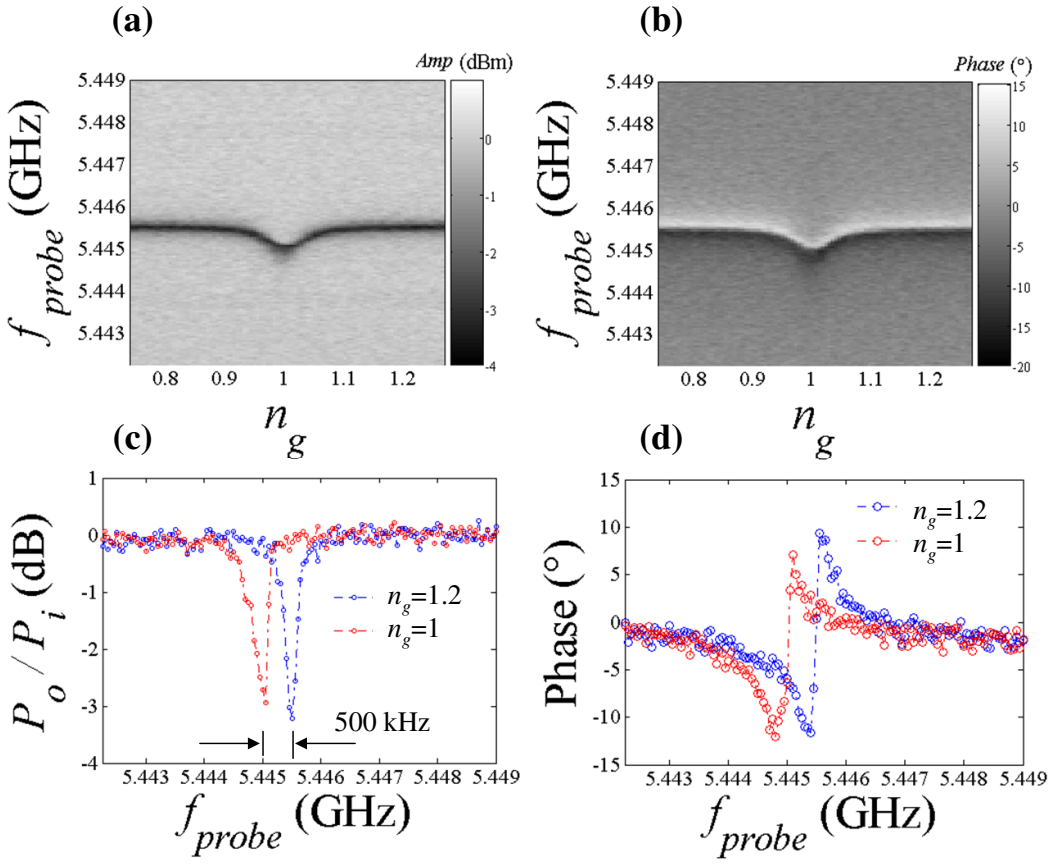

Figure 6.12: Single-tone spectroscopy of device "LEQED2". (a) Measured transmitted probe amplitude (gray color in a log scale) and (b) phase as a function of the probe frequency f and n_g at B = -2.855 Gauss. (c) The resonator frequency was pulled down by 500 kHz at n_g=1, when the qubit was in the ground state (red curve). (d) The transmitted phase through the resonator was also pulled down by 500 kHz at n_g=1 (red curve). Measured E_J/h was 5.495 GHz from two-tone spectroscopy. From the detuning and dispersive frequency shift, I extracted $g/2\pi \simeq 5$ MHz.

resonator was about 26. By measuring the CPB two-tone spectrum, I found $E_J/h =$ 5.495 GHz. From the detuning and dispersive shift, I extracted the coupling strength $g/2\pi \simeq 5$ MHz for device "LEQED2". From the 2-e periodicity of the dispersive shift, I found that the gate voltage $V_g = 71$ mV corresponded to $\Delta n_g = 2$ or one excess Cooper-pair ($2e$) on the island of the CPB. From $2e = C_{g,dc}V_g$, I found the dc gate capacitance $C_{g,dc}$ was about 4.5 aF, which was similar to that of device "LEQED1".

When we measured device "LEQED1", we found the phase fluctuated slowly by about 120° in 10 hours, even though the RF and LO were locked together by the external 10 MHz reference. To solve the phase problem, we decided to take a phase reference from the RF and LO. We added each directional coupler to the RF and LO output and divided the power for a second mixer. By mixing down the divided power from the RF and LO, we obtained the phase reference. Then, we subtracted the measured phase through the device "LEQED2" from the phase reference. This also required taking two IF signals from two mixers simultaneously through two channels on the digital oscilloscope. This method provided stable phase signals and we measured the phase signal instead of the transmitted power for device "LEQED2",

6.6.2 CPB Transition Spectrum

In order to measure the CPB spectrum in the dispersive limit, I had to apply a second microwave tone (pump) while measuring the transmitted signal of the first

microwave tone (probe). With the qubit in the ground state and biased at the degeneracy point, the probe frequency was fixed at the perturbed frequency of the resonator. If the qubit was excited, the resonator frequency would increase as the resonance curve shifted up. The resulting two-tone spectroscopy shows the change of transmitted probe amplitude as a function of the pump frequency f_{pump} and n_g.

The white parabola in Fig. 6.13 (a) is the CPB spectrum of device "LEQED1" at zero magnetic field. The step size in the pump frequency for (a) was 4 MHz and the number of probe photons stored in the resonator was approximately $\langle n_r \rangle = 22$. E_J/h was 8.43 GHz and I was able to see the spectrum up to 10 GHz though it was very faint. The horizontal white lines were due to charge fluctuations in the device. One can also see a faint second section of a parabola on the right-hand side (the spectrum looks like two curves). This was most likely due to a low frequency discrete charge fluctuator. At $B = -2$ Gauss, E_J/h decreased to 6.29 GHz [see the CPB spectrum in Fig. 6.13 (c)]. The step size in the pump frequency was 500 kHz and the number of probe photons stored in the resonator was about $\langle n_r \rangle = 2$. I found good fits to the model for both data (a) and (c), and found $E_C/k_B = 0.60$ K [see red curves in Fig. 6.13 (b) and (d)].

Fig. 6.14 (a) shows the CPB spectrum of device "LEQED2" at $B = -1.47$ Gauss. The step size in the pump frequency was 5 MHz and the number of probe photons stored in the resonator was about $\langle n_r \rangle = 18$. Baladitya Suri took this data by measuring the phase of the transmitted signal with the probe frequency fixed to the resonant frequency of the uncoupled resonator. One can also see a faint second parabola around $n_g = 1.1$ and $E_J = 6.35$ GHz caused by a charge fluctuator. By

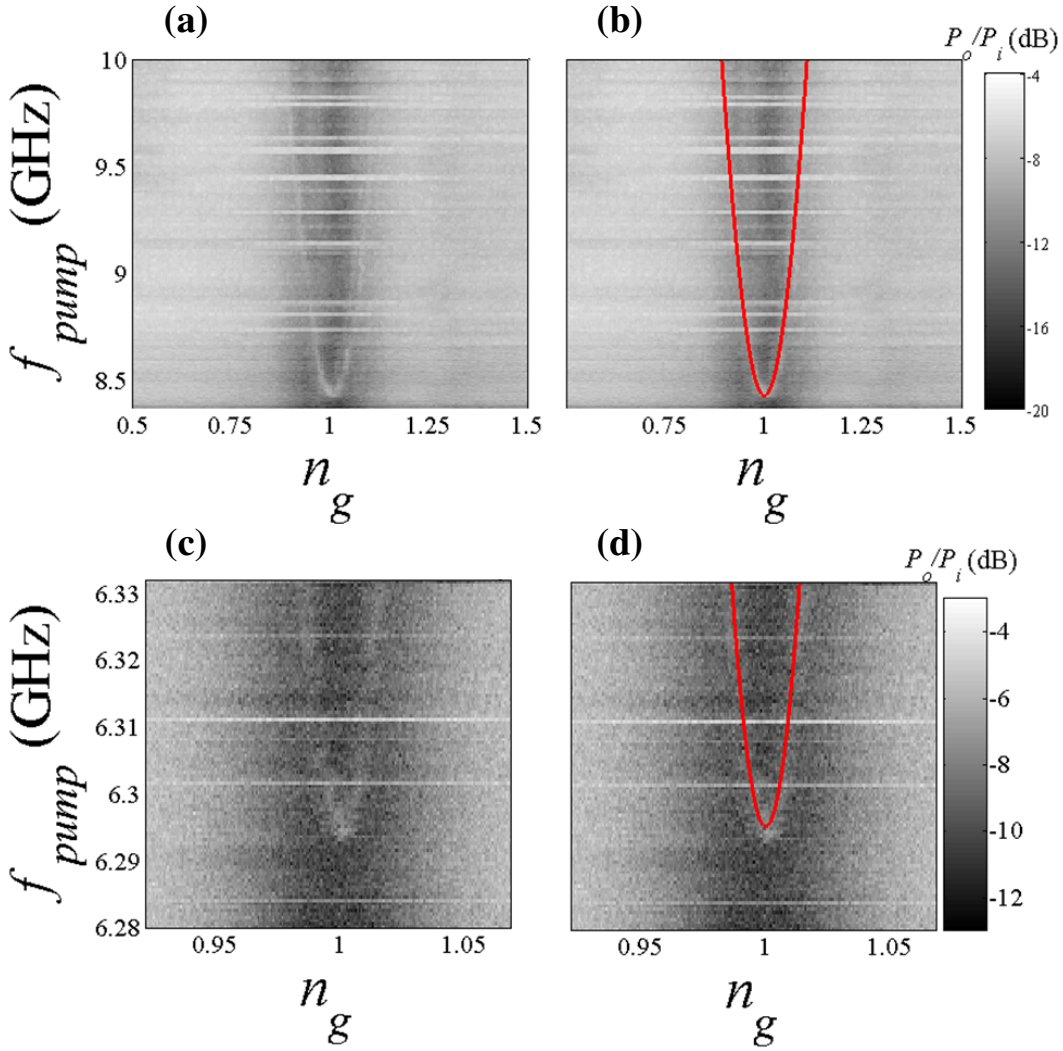

Figure 6.13: Two-tone spectroscopy of device "LEQED1". Measured transmitted probe amplitude (gray color log scale) as a function of the pump frequency f_{pump} and n_g at B = 0 Gauss (a) and B = -2 Gauss (b). The red curves in (b) and (d) are the predicted CPB spectrum from the Jaynes-Cummings Hamiltonian using the matrix in Fig. 6.3. $E_C/k_B = 0.60$ K was extracted by fitting CPB spectrums.

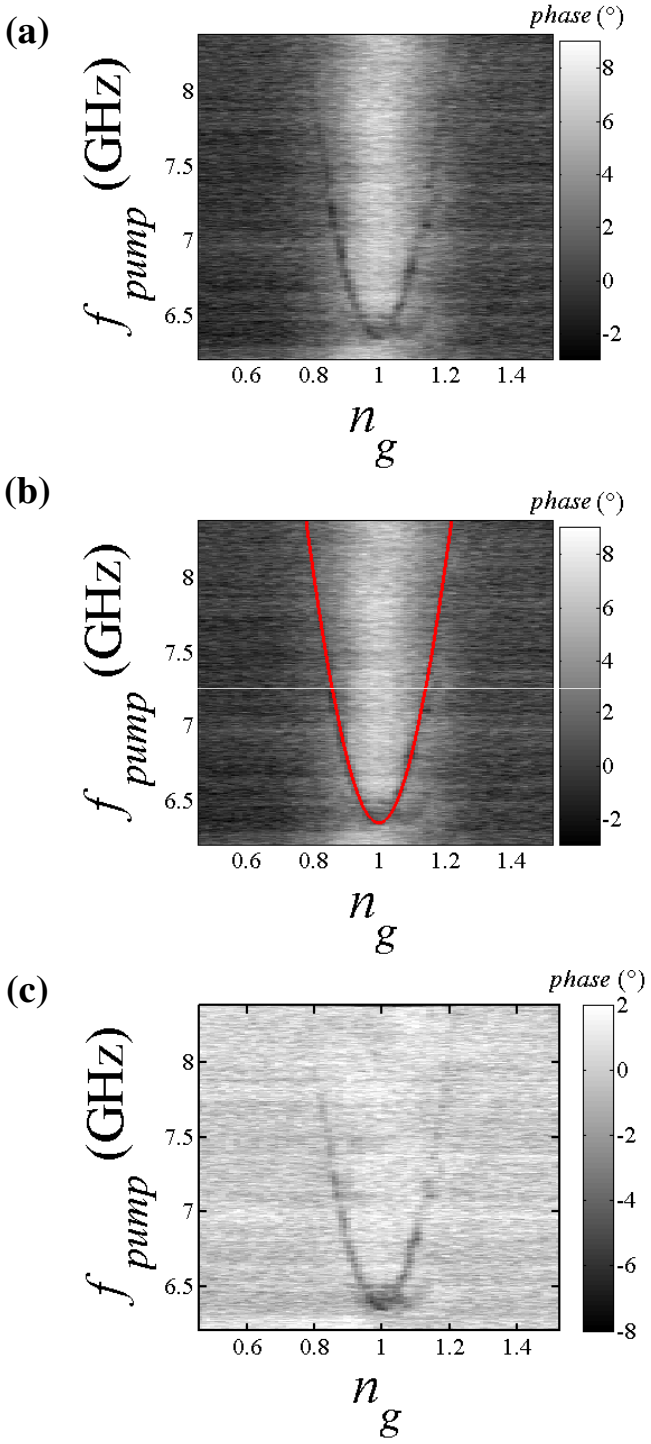

Figure 6.14: Two-tone spectroscopy of device "LEQED2". (a) Measured transmitted probe phase (gray color) as a function of the pump frequency f_{pump} and n_g at B = -1.47 Gauss. (b) Same data as (a) but fit to predicted spectrum (red curve). E_C/k_B = 0.30 K was extracted by fitting the spectrum. (c) The gray scale plot shows the net phase change of the transmitted probe after subtracting the average background phase from the data in (a). B. Suri took this data and I analyzed it.

fitting the spectrum, we extracted an $E_C/k_B = 0.30$ K [see red curves in Fig. 6.14 (b)].

6.6.3 Saturating the CPB

The expected excited state population P_e of the CPB due to the pump power can be found from the steady state solution of the Bloch equations [108, 109]. P_e is given by

$$P_e = \frac{\Omega^2 T_1 T_2/2}{1 + (\omega_{pump} - \omega_a)^2 T_2^2 + \Omega^2 T_1 T_2}, \tag{6.49}$$

where Ω is the bare Rabi flopping angular frequency. Ignoring inhomogeneous broadening, the half width at half maximum (HWHM) [108, 109] of the resonance is given by

$$2\pi\Delta f_{HWHM} = \frac{1}{T_2}\sqrt{1 + \Omega^2 T_1 T_2}. \tag{6.50}$$

In the limit of low power, we can also write

$$2\pi\Delta f_{HWHM} \equiv \frac{1}{T_2^*}, \tag{6.51}$$

where T_2^* is the spectroscopic coherence time of the qubit.

Since the Rabi frequency Ω is proportional to the amplitude of the pump voltage, the Δf_{HWHM} of the resonance will increase with power. This is known as "power broadening" [33]. If the pump power is very small, then the Ω term in Eq. 6.50 can be ignored, leading to $T_2^* \simeq T_2$, although this only holds, if we can ignore inhomogeneous broadening. Fig. 6.15 (a) shows the measured spectroscopic width of the CPB "LEQED1" at $n_g = 1$ as a function of pump frequency and power

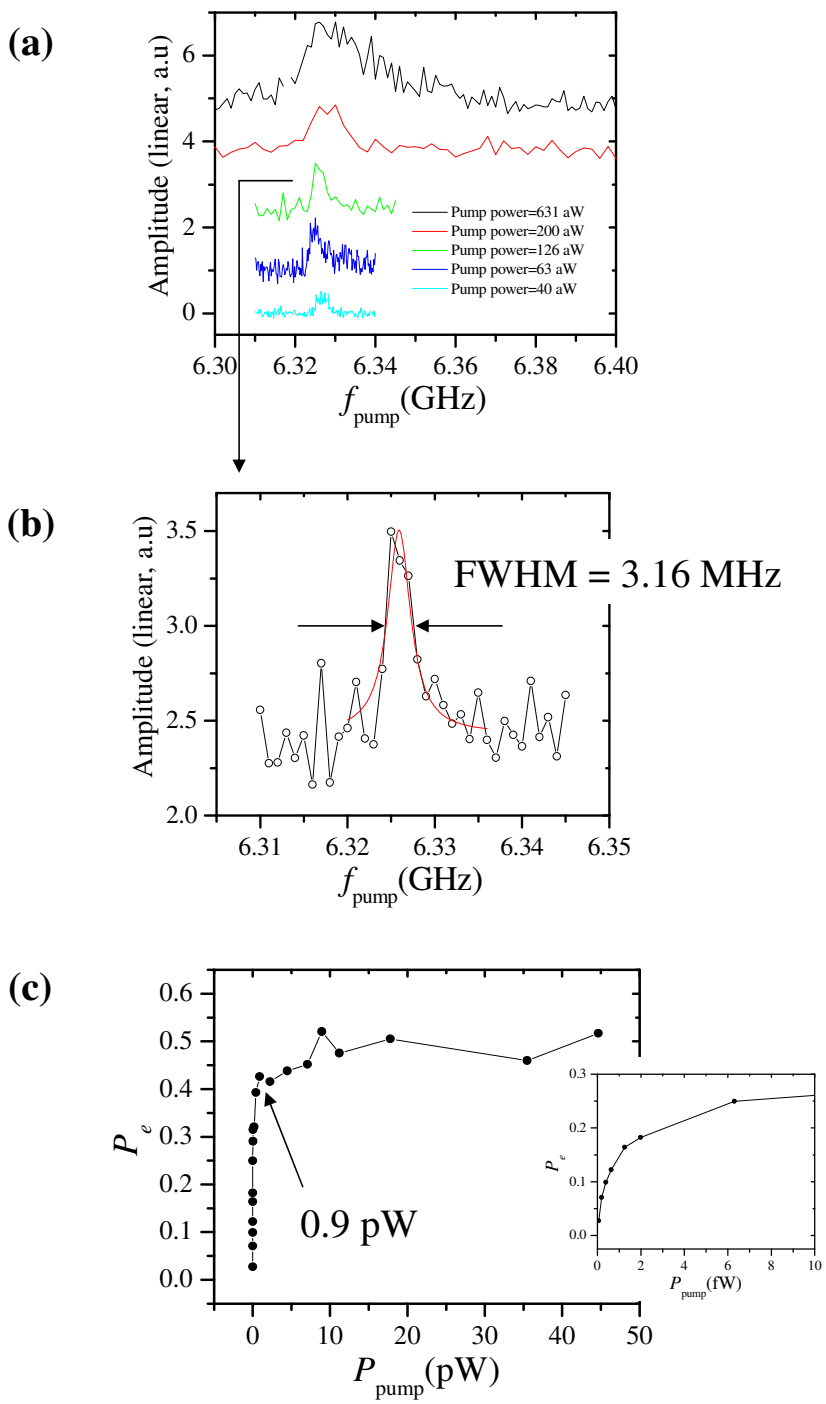

Figure 6.15: (a) The spectroscopic resonance of CPB "LEQED1" as a function of pump power at $E_J/h = 6.325$ GHz. The number of probe photons was about 2. (b) Lorentzian curve fit of the CPB resonance measured at a pump power of 0.4 fW. The Full Width Half Maximum (FWHM) was 3.16 MHz, which corresponds to T_2^* of 100 ns. (c) The population of the CPB in the excited state as a function of pump power at $n_g = 1$ and on resonance at $E_J/h = 6.22$ GHz. The number of probe photons was about 200. The inset shows a zoom in of (c) below the pump power of 10 fW.

while the number of probe photons was fixed to 2. As I increased the pump power, the width of the CPB resonance also increased. Below a pump power of 126 aW, the width did not decrease more. The minimum HWHM was about 1.58 MHz, which corresponds to a spectroscopic coherence time T_2^* of 100 ns [see the green curve in Fig. 6.15 (a) or Fig. 6.15 (b)]. Since T_2^* includes effects of inhomogeneous broadening as well as decoherence effects, this implies the coherence time T_2 of the CPB must be greater than or equal to 100 ns.

At high power on resonance ($\omega_{pump} = \omega_a$), one expects the population P_e to be saturated at 50 %. Fig. 6.15 (c) shows the measured P_e for $n_g = 1$ and on resonance, as I increased the pump power. I extracted P_e by measuring the amplitude of the CPB resonance and assuming $P_e = 0.5$ when the amplitude was saturated. P_e was saturated at pump powers of -90.5 dBm (0.9 pW) or larger. The inset in Fig. 6.15 (c) shows P_e for pump powers 10 fW or less. Due to charge fluctuations in the system, it was not always so easy to see a good quality CPB resonance. In particular, when I took the data in Fig. 6.15 (c), I biased the CPB at $n_g = 1$ and $E_J/h = 6.22$ GHz and measured the amplitude of the CPB resonance as a function of pump power for fast measurements. And for Fig. 6.15 (c), I did not measure the CPB resonance as a function of f_{pump} as Fig. 6.15 (a) since it took longer time and had more chances to be fluctuated by low frequency charge noise.

To extract the coherence time T_2 from the observed power broadening, we note that in general

$$\frac{1}{T_2^*} = \frac{1}{T_2^\dagger} + \frac{\sqrt{1 + \Omega^2 T_1 T_2}}{T_2}, \tag{6.52}$$

where $T_2^\dagger$ is the inhomogeneous broadening time [33]. At small pump power, we can ignore the Ω term and put the following bound on T_2:

$$\frac{1}{T_2^*} \simeq \frac{1}{T_2^\dagger} + \frac{1}{T_2} \geq \frac{1}{T_2}. \tag{6.53}$$

The measured T_2^* was 100 ns when the pump power was 126 aW [see Fig. 6.15 (b)]. P_e was less than 0.1 at the same power [see the inset in Fig. 6.15 (c)]. From Eq. 6.53, this means $T_2 \geq T_2^* = 100$ ns at the pump power of 126 aW. From T_1 and the bound on T_2, I could also extract a bound on the dephasing time T_φ using Eq. 2.32. As I discuss below, the measured T_1 of the CPB around $E_J = 6.29$ GHz was about 2.3 μs, which is much longer than T_2. Hence $T_\varphi \approx T_2 \geq 100$ ns.

6.6.4 ac Stark Shift

It is important to know the number of photons in the resonator so that you do not apply too much power to the device. One way to measure the number of photons is the ac Stark shift of the qubit. When the resonator is strongly coupled to the qubit, the ac Stark shift in the qubit energy level is observable and increases monotonically with power [105, 106]. I used the ac Stark shift to calibrate the number of photons in the resonator and extract the total attenuation on the input side of the microwave cables at the base temperature. I biased the CPB "LEQED1" at $n_g = 1$ and swept the pump frequency while monitoring the transmitted amplitude of the probe [see Fig. 6.16 (a)]. As I increased the power of the probe, E_J also increased. The pump power was fixed to -124 dBm or about 400 aW to excite the CPB; this was a low enough power (see previous section) not to saturate the CPB.

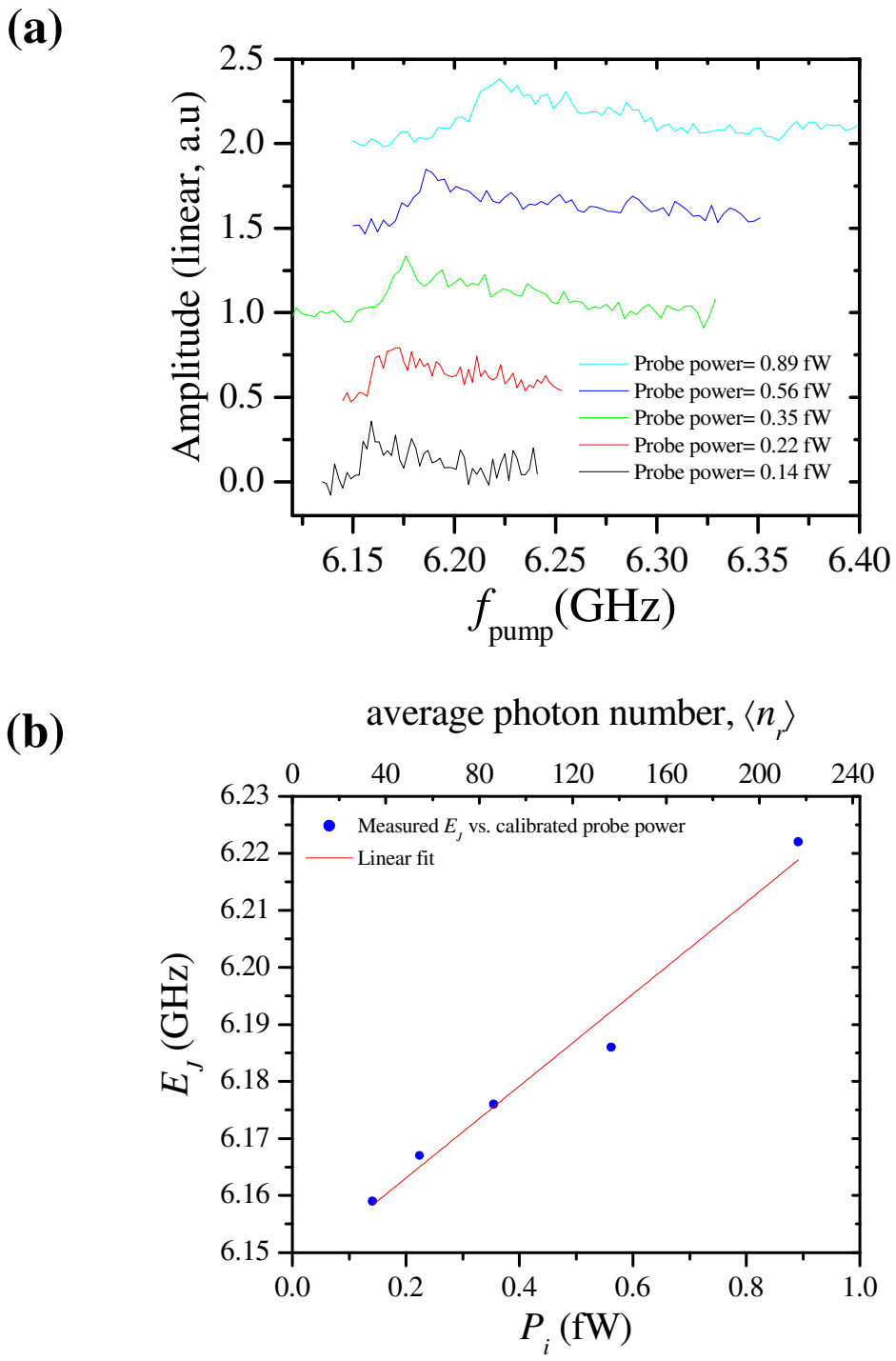

Figure 6.16: ac Stark shift of CPB "LEQED1". (a) Transmitted probe amplitude as a function of pump frequency at the degeneracy point for various probe powers. The asymmetric resonance could be due to the high pump power. (b) The probe power (P_i) was calibrated from ac Stark shift. I extracted the ac Stark shift of 0.34 MHz per photon in the resonator.

The CPB transition frequency f_a due to the ac Stark shift (Eq. 6.21) is given by

$$f_a = f_{a,0} + \frac{2g^2\langle n_r\rangle}{2\pi\Delta}, \tag{6.54}$$

where $\langle n_r\rangle$ is the average number of photons in the resonator, $f_{a,0}$ is the CPB transition frequency when $\langle n_r\rangle = 0$, and the detuning $\Delta/2\pi = f_{a,0} - f_r$. $f_{a,0} = 6.1469$ GHz was obtained by the linear fit of E_J versus probe power. From single-tone spectroscopy, I obtained a coupling strength $g/2\pi = 11$ MHz and the resonator frequency $f_r = 5.4428$ GHz. The factor $g^2/\pi\Delta$ leads to an ac Stark shift of 0.34 MHz per photon at $E_J/h = 6.1469$ GHz. Finally, the input power of the probe is related to the average number of photons in the resonator by

$$P_i = \kappa_r\langle n_r\rangle\hbar\omega_r, \tag{6.55}$$

where $\kappa_r = \omega_r/Q_L \simeq 2\pi(0.18\text{ MHz})$, given $Q_L = 30,000$. Combining Eqs. 6.54 and 6.55 yields

$$\begin{aligned} P_i &= \frac{\pi\Delta}{g^2}\frac{\omega_r}{Q_L}hf_r(f_a - f_{a,0}) \\ &= \frac{2\pi\times 0.18}{0.34}hf_r(f_a - f_{a,0}). \end{aligned} \tag{6.56}$$

For example, the probe power was about 1 fW for an ac Stark shift of 85 MHz. From this calibration and the known power at the source (and the fixed attenuators), I extracted the line attenuation of 3.5 dB in the input side of microwave cables in the refrigerator. I plot E_J versus the calibrated probe power and also $\langle n_r\rangle$ versus probe power in Fig. 6.16 (b).

Figure 6.17 shows the ac Stark shift in device "LEQED2". $f_{a,0} = 6.147$ GHz was obtained from a linear fit to E_J versus probe power. From single-tone spec-

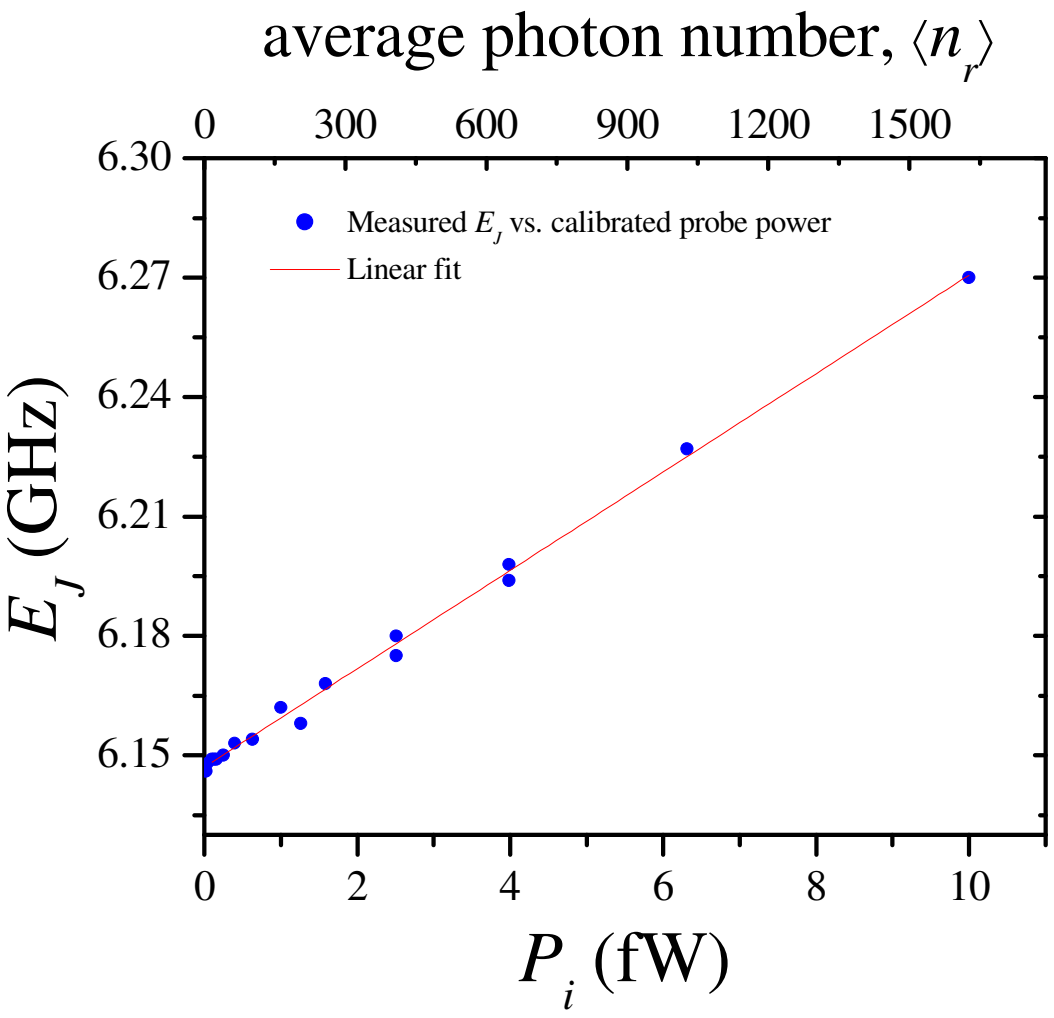

Figure 6.17: ac Stark shift of CPB "LEQED2". The probe power (P_i) was calibrated from the ac Stark shift. I extracted an ac Stark shift of 71 kHz per photon in the resonator. B. Suri assisted with taking this data.

troscopy, I obtained a coupling strength $g/2\pi = 5$ MHz and the resonator frequency $f_r = 5.44544$ GHz. The factor $g^2/\pi\Delta$ leads to an ac Stark shift of 71 kHz per photon. For this device $\kappa_r = \omega_r/Q_L \simeq 2\pi(0.272 \text{ MHz})$, given $Q_L = 20,000$. Then, the power at the device can be found from

$$P_i = \frac{2\pi 0.272}{0.071} h f_r (f_a - f_{a,0}). \tag{6.57}$$

For example, a probe power of about 10 fW was required to produce an ac Stark shift of 120 MHz. From this calibration, I was again able to extract the line attenuation of 3 dB in the input side of microwave cables in the refrigerator.

6.7 Near Resonant Limit

When the detuning Δ is zero, the vacuum Rabi splitting $g/2\pi$ will be observed in the resonator-CPB spectrum. Achieving $\Delta = 0$ requires smooth control of E_J. In device "LEQED1", I had difficulty changing E_J precisely, most likely due to the trapping of flux in the resonator. Nevertheless, I was able to reach a detuning of the CPB from the resonator as small as -83 MHz. Figure 6.18 shows the corresponding single-tone spectroscopy at $B = -1.8$ Gauss. By fitting the spectrum, I extracted E_J of 5.36 GHz, which was close to the resonator frequency of 5.44 GHz. From the fit to this data, I also confirmed $g/2\pi = 11$ MHz. Below $f = 5.441$ GHz and above $f = 5.446$ GHz, I was not able to observe the dispersive frequency shift; as can be seen in Fig. 6.18, the signal fades away.

Examination of Fig. 6.18 (a) shows that there is a parabola above the resonator

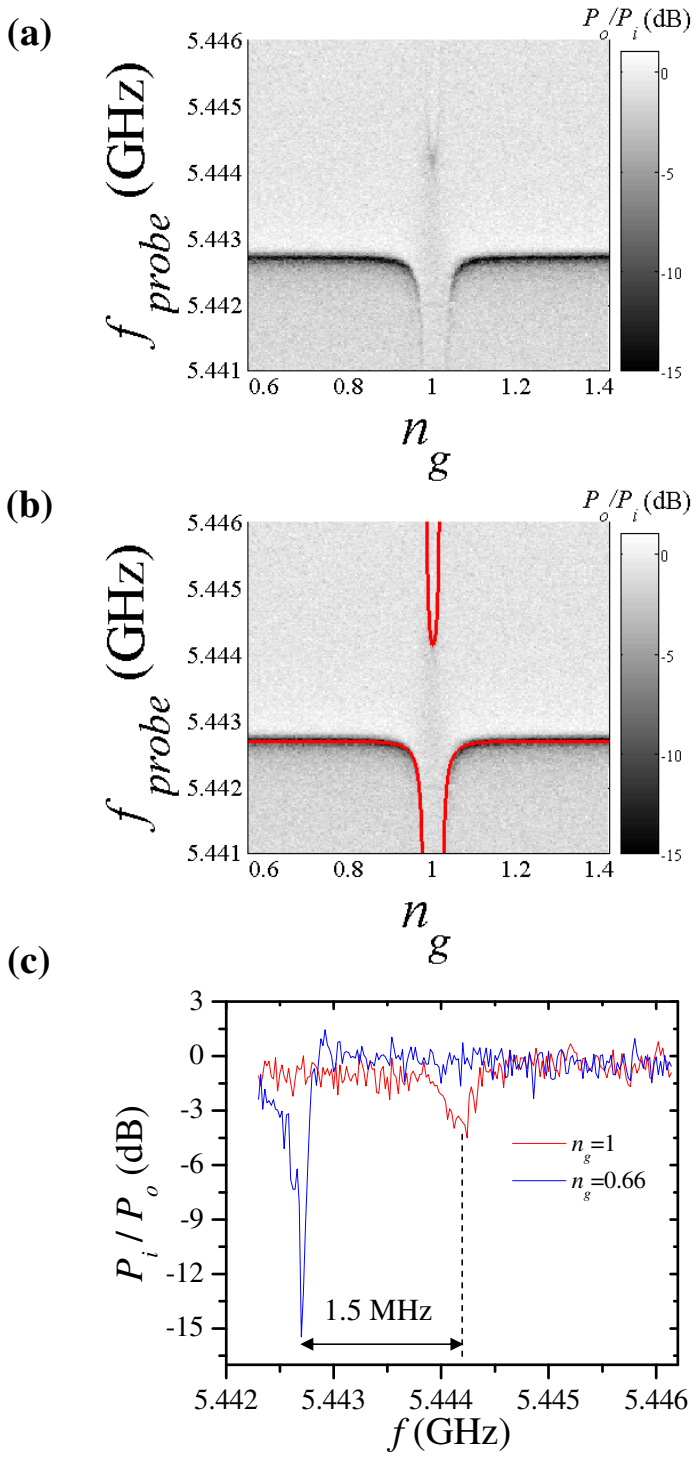

Figure 6.18: Single-tone spectroscopy of device "LEQED1" for relatively small detuning of the CPB from the resonator. (a) Single-tone spectroscopy when E_J was close to the resonator frequency at $B = -1.8$ Gauss. (b) Same as (a) with the predicted spectrum (red curves). By fitting the spectrum, I extracted E_J of 5.36 GHz. (c) Line cuts of (a) at $n_g = 1$ (red curve) and $n_g = 0.66$ (blue curve).

resonance frequency by 1.5 MHz. Fig. 6.18 (c) shows the amplitude line cuts at $n_g = 1$ (red curve) and $n_g = 0.66$ (blue curve) versus the probe frequency. By fitting the line cut at $n_g = 1$, I found the FWHM was about 600 kHz; this was only 3 times larger than the 200 kHz FWHM of the resonator resonance. This suggests that the state corresponding to points on the parabola was mainly composed of an excited state of the resonator, as would be expected theoretically from eigenstates of the system.

6.8 Charge noise

Since the CPB is sensitive to gate voltage, charge fluctuators can also couple to the CPB and change the effective n_g. 1-e charge fluctuations are commonly seen [see Fig. 6.19 (a)]. These fluctuations are random in time and required me to monitor and reset the gate voltage for the measurement as necessary.

Sub-electron fluctuations are also visible [see Fig. 6.19 (b)], which shows the phase shift of resonator "LEQED1" over time. I ran a program overnight to monitor the phase shift. For this measurement, I fixed the pump frequency to $E_J/h = 6.055$ GHz with a constant power. I then repeatedly swept the gate voltage over a small range, corresponding to n_g between 0.91 and 1.1, and monitored the CPB resonance along n_g [see Fig. 6.19 (b)].

Examination of Fig. 6.19 (b) reveals a lot of jitter along n_g. The fluctuations are very small in n_g and they appear to be occurring randomly. The line cut in Fig. 6.19 (c) shows the phase noise produced by the charge fluctuations. From

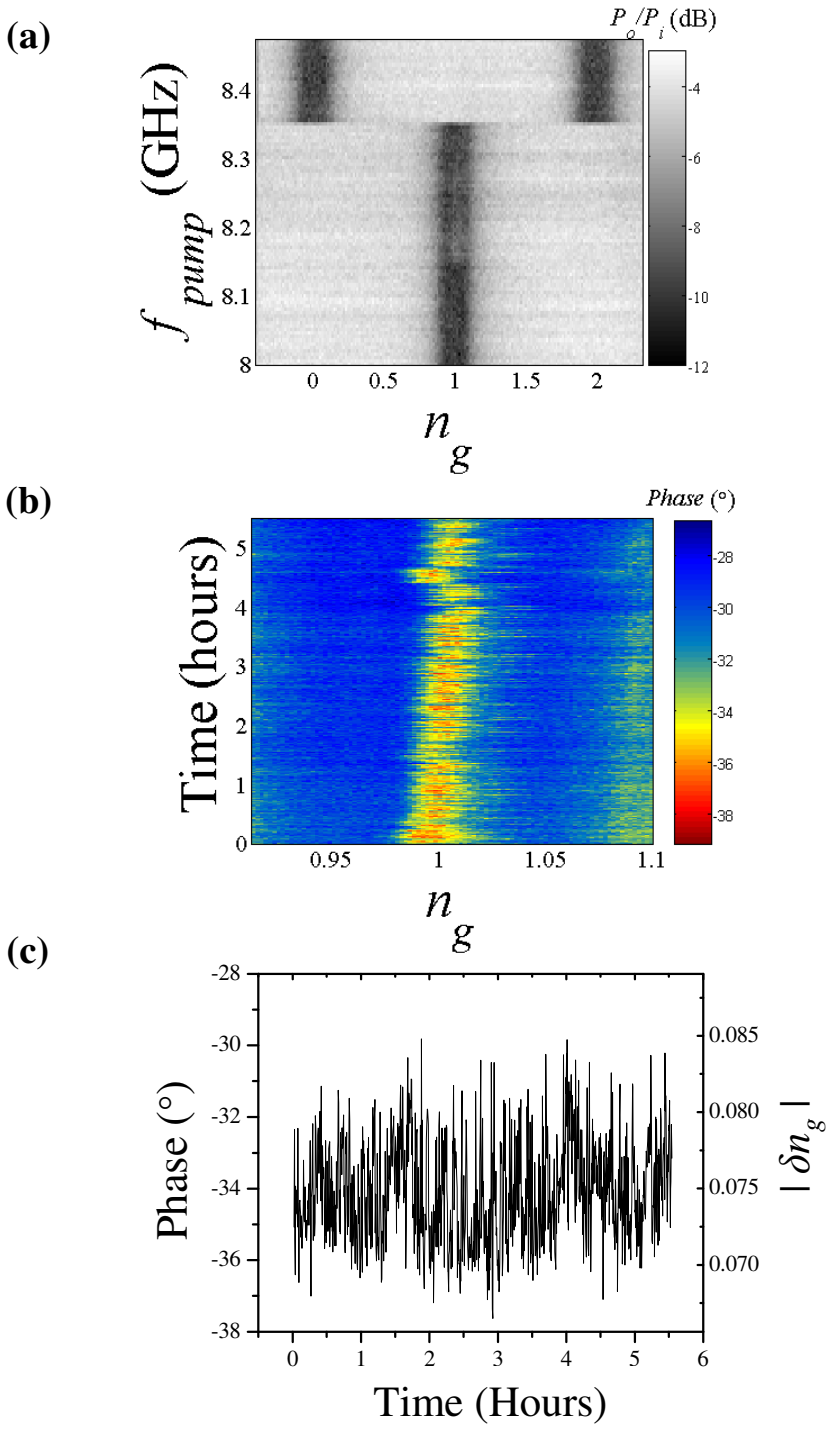

Figure 6.19: Charge noise in two devices. (a) Two-tone spectroscopy showing 1-e charge jump in device "LEQED1". (b) Sub-electron charge fluctuations in device "LEQED2" with the CPB excited at $E_J = 6.055$ GHz. False color represents the phase shift of the resonator due to the excitation of the CPB. (c) Line cut of (b) at $n_g = 1.004$.

the CPB resonance, the calibration factor $\delta n_g/\delta\phi$ was about 0.0023436 per degree. From this conversion factor, the standard deviation σ_q of charge fluctuation was about 0.00339 e. If the charge noise spectrum is $1/f$, *i.e.* $S_q(f) = A^2/f$, then I find $\sigma_q^2 = A^2 \ln(t_{max}/t_{min})$ [103] (also see Eq. 2.52), where $t_{max} = 5$ hours for all data, $t_{min} = 20$ seconds for one line scan, and $\sigma_q^2 = (0.00339\ e)^2$, hence $\ln(t_{max}/t_{min}) = 6.8$ and $A = 0.00339\ e/\sqrt{6.8} \simeq 1.3 \times 10^{-3}\ e$. This is similar value with typical measurements [45].

6.9 Extraction of Device Parameters

I summarized the parameters of two CQED devices in Table 6.1. The parameters of the resonator were found by analyzing S_{21} data found using the vector network analyzer with the resonator at 30 mK. Using a Lorentzian fit (see section 5.5.3) to $|S_{21}|$, I extracted the resonator center frequency f_r, loaded quality factor Q_L, external quality factor Q_e, internal quality factor Q_i, and effective coupling capacitance C_c. The resonator decay rate $\kappa_r/2\pi$ was calculated from $\kappa_r/2\pi = f_r/Q_L$.

Using 2-e periodicity in the single-tone spectroscopy, I also extracted the dc coupling capacitance $C_{g,dc}$ from $2e = C_{g,dc}V_g$, where V_g is the applied dc gate voltage. The CPB charging energy E_C was extracted by fitting the CPB spectrum obtained from two-tone spectroscopy. The total capacitance of the CPB island C_Σ was calculated from $E_C = e^2/2C_\Sigma$. I extracted the coupling strength $g/2\pi$ from the measured dispersive shift $\chi/2\pi = g^2/(2\pi\Delta)$ in the single-tone spectroscopy at $n_g = 1$. The resonator to CPB coupling capacitance $C_{g,r}$ was extracted from

Table 6.1: Parameters of two CQED devices measured at 25 mK. $E_{J,max}$ is from the resistance of an SET built on the same chip as the CQED device. See section 6.9 for the method of extracting parameters. $C_{g,rf}$ was extracted from the Rabi oscillation measurements (see section 6.11).

Parameters	"LEQED1" (LE1-68)	"LEQED2" (LE1-71)
f_r	5.443 GHz	5.446 GHz
$\kappa_r/2\pi$	0.18 MHz	0.3 MHz
Q_e	36,000	70,000
Q_i	180,000	32,000
Q_L	30,000	22,000
C_c	3.9 fF	3 fF
$E_{J,max}/h$	9 GHz	19 GHz
E_C/k_B	0.60 K	0.30 K
C_Σ	1.56 fF	3.12 fF
$g/2\pi$	11 MHz	5 MHz
$C_{g,r}$	33.3 aF	30.3 aF
$C_{g,dc}$	4.7 aF	4.5 aF
$C_{g,rf}$	not measured	10.5 aF

$\hbar g = eC_{g,r}/C_\Sigma\sqrt{\hbar\omega_r/2C}$, where C is the capacitance of the resonator (assumed to be about 400 fF based on the geometry [30] and [79]).

6.10 T_1 Measurement

To measure the energy relaxation time T_1 of the CPB in the first excited state (see Fig. 6.20), the CPB was excited as discussed in section 3.9, but here I used the resonator instead of the rf-SET to monitor the state of the CPB.

For a relaxation measurement, the CPB is first prepared in the ground state (no pump power). In this case, the resonator frequency at $n_g = 1$ is detuned by $-\chi/2\pi$ due to the dispersive shift when the detuning is positive (*i.e.* for $E_J > \hbar\omega_r$). I found the change of the amplitude or phase was linear for small frequency shifts in the dispersive limit. The resonator was continuously excited by the probe so that the amplitude or phase of the probe was continuously monitored as a function of time. When the qubit is excited, the resonant frequency of the resonator increases due to the change in the dispersive shift. When the pump power changes, there is a response time during which the resonator frequency settles to an equilibrium value. The response time is the ring-up or ring-down time of the resonator, which is determined by the decay rate of the resonator. If we turn off the pump power, then the qubit starts to relax to the ground state, causing the resonator frequency to relax back to the original frequency. As long as the qubit lifetime T_1 is longer than the ring-down time of the resonator, T_1 should be measurable.

Figure 6.21 (a) shows the measured T_1 as a function of E_J for devices "LEQED1"

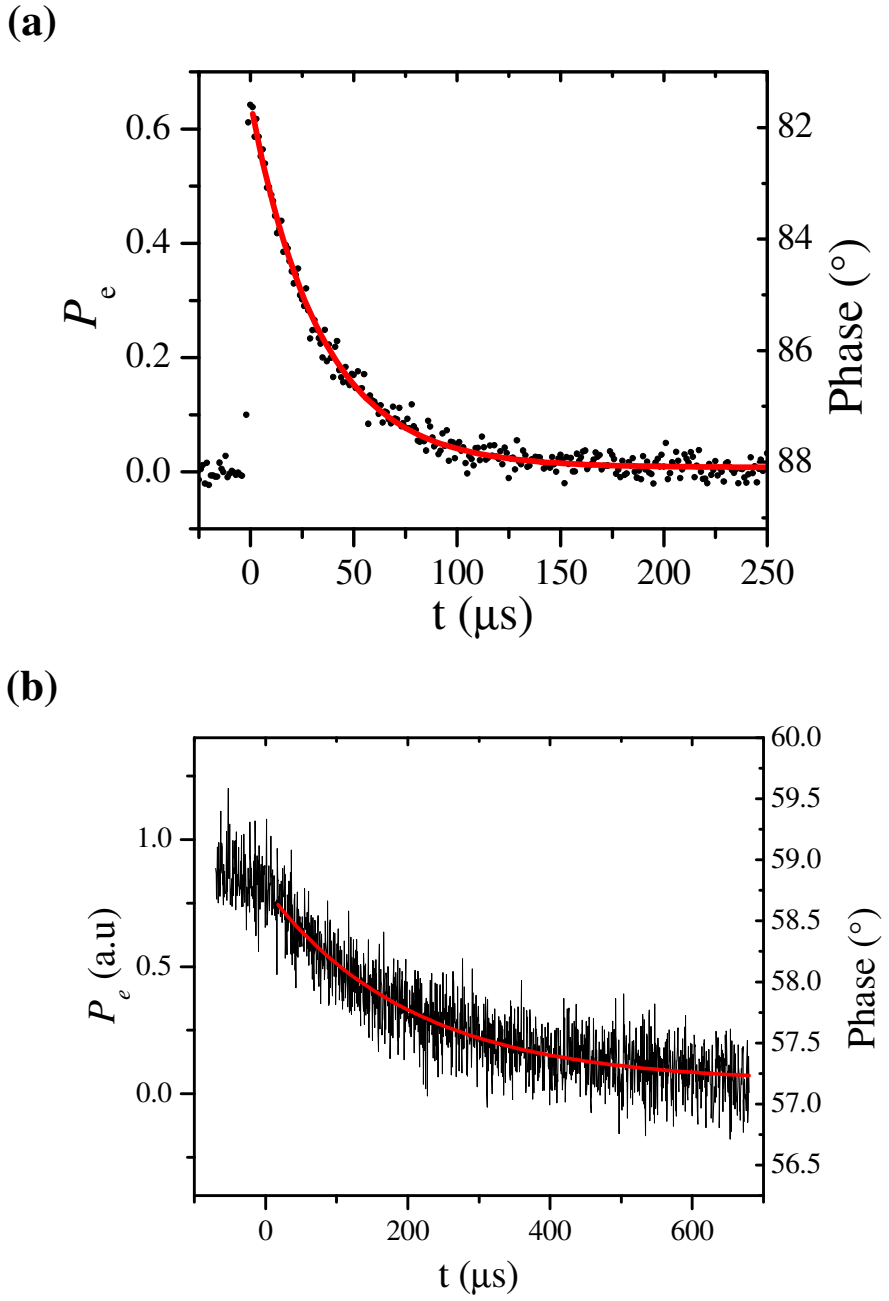

Figure 6.20: (a) Measured T_1 of CPB "LEQED2" at $n_g = 1$ and $E_J/h = 6.31$ GHz. The pump was turned on at the measurement time t=0 s for 190 ns. The red curve is the simple exponential curve fit to the decay after the pump switched off. From the fit (red curve), T_1 was about 33.8 μs $\pm$0.5 μs. The number of probe photons was about 20. (b) Measured T_1 of device "LEQED2" at $n_g = 1$ and $E_J/h = 4.497$ GHz. The pump was applied to the qubit for 750 μs and turned off at t=0 s. From the fit (red curve), the extracted T_1 was about 204.2 μs $\pm$8.9 μs.

and "LEQED2". The CPB was biased at the charge degeneracy point $n_g = 1$ for this T_1 data. Continuous microwaves were sent to the CPB for about 5 times T_1 and turned off for the same time. Since I applied a microwave pulse longer than the dephasing time of the qubit, the CPB was saturated to an incoherent mixed state of the ground state and the excited state.

For device "LEQED1", I only measured T_1 for a few values of E_J [see red curve in Fig. 6.21 (a)]. T_1 was about 10 μs at $E_J/h = 7$ GHz and dropped to 2.3 μs at $E_J/h = 6.29$ GHz. At $E_J/h = 6.29$ GHz, the CPB was detuned by more than 0.8 GHz from the resonator frequency of 5.443 GHz, which was much larger than $g/2\pi = 11$ MHz. I monitored the decay of the CPB by measuring the amplitude decrease of the probe, which was set to the dispersive shifted frequency so I could follow the linear change of the amplitude. The measured ring-up time of the resonator was about 1.7 μs, which set the limit for the shortest T_1 I could measure. The IF frequency of the mixer was 5 or 10 MHz, which was faster than the resonator decay rate. For "LEQED1", we did not use an IF amplifier after the mixer and absorption low-pass filters, while for device "LEQED2" we did use an IF amplifier (see Fig. 6.9). For device "LEQED1" I added a low-pass filter (Minicircuit) with a cut-off frequency of 30 MHz between the mixer and the oscilloscope (Agilent 54855A Infiniium) and there was only one isolator on the cold stage at 30 mK. The number of probe photons was $\langle n_r \rangle \cong 220$.

To monitor the decay of the CPB "LEQED2", I measured the phase change of the probe. I set the probe frequency to the center resonant frequency of the resonator, where the phase sensitivity was maximum and the phase change was

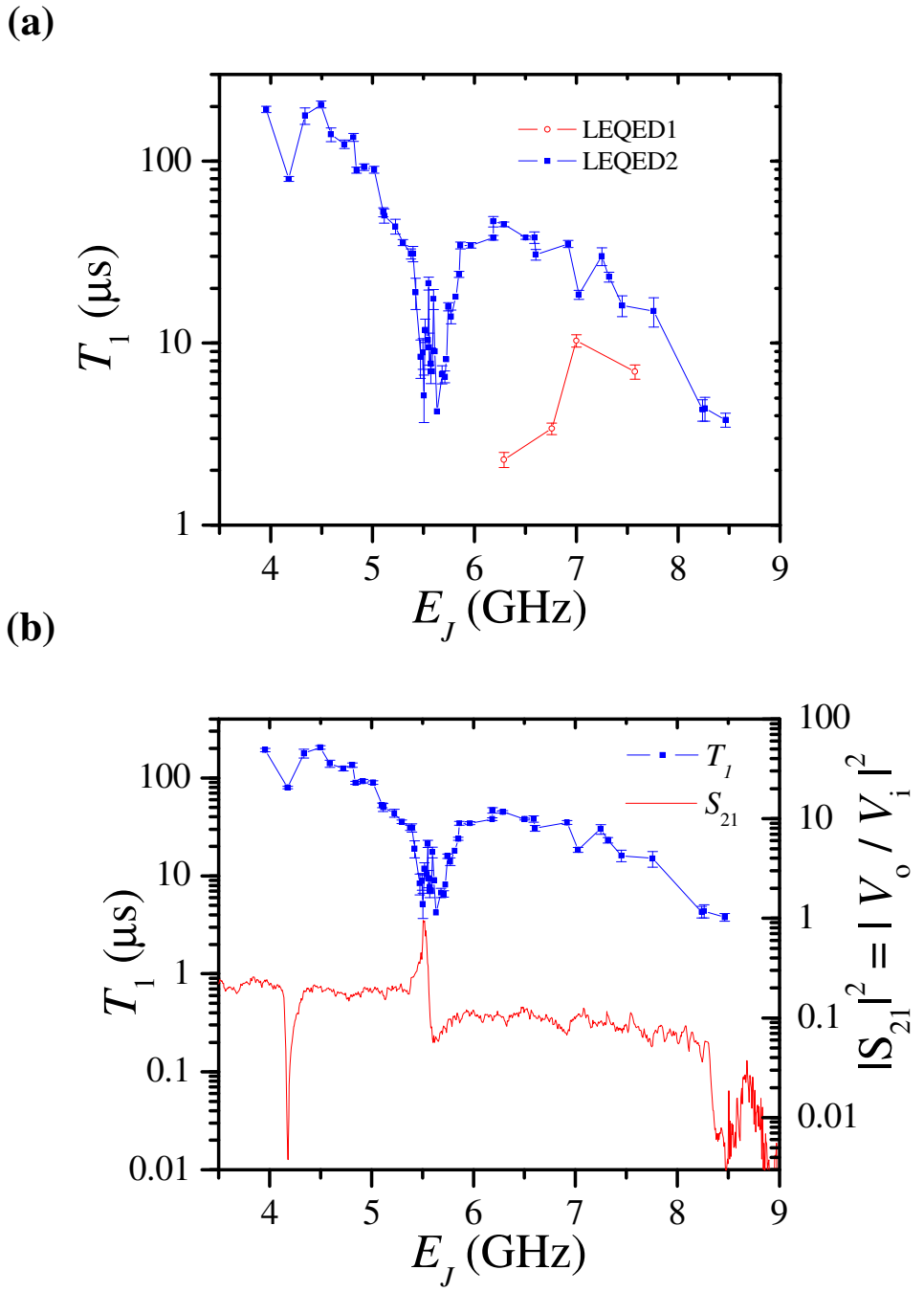

Figure 6.21: (a) Measured T_1 at $n_g = 1$ as a function of E_J of two CQED devices. The red and blue curves are T_1 of device "LEQED1" and "LEQED2", respectively. Baladitya Suri helped me take those data. (b) Comparison of T_1 of CPB "LEQED2" and S_{21} (red curve) of the system at 25 mK. The S_{21} of device "LEQED1" is not shown here.

linear in the frequency shift. The measured ring-up time of the resonator was about 2 μs. The measurement set-up is shown in Fig. 6.9. Typically the IF frequency of the mixer was 2 MHz. A low-pass filter (Minicircuit) with a cut-off frequency of 5 MHz was used after the IF amplifier. The number of probe photons was about $\langle n_r \rangle = 26$.

The blue curve in Fig. 6.21 (a) shows T_1 versus E_J for device "LEQED2". I observed a maximum T_1 of 200 μs at $E_J/h \simeq 4.5$ GHz and found that T_1 decreased to 3.8 μs at 8.5 GHz. There was also a depression in T_1 around the resonant frequency of the resonator.

From the measured T_1 versus frequency, one can extrapolate the spectral density of charge noise S_q in the CPB using Eq. 2.31. Since T_1 was taken at $n_g = 1$, S_q can be extracted from

$$\frac{1}{T_1} = \left(\frac{2E_C}{e\hbar}\right)^2 S_q(E_J/h). \tag{6.58}$$

Given $E_C/k_B = 0.3$ K, $S_q \simeq 1 \times 10^{-18}$ e^2/Hz from the maximum $T_1 \simeq 200$ μs at $E_J/h \simeq 4.5$ GHz and $S_q \simeq 4 \times 10^{-17}$ e^2/Hz from the minimum $T_1 \simeq 3.8$ μs at $E_J/h \simeq 8.5$ GHz.

If the charge noise power spectrum follows a $1/f$ distribution, *i.e.* $S_q = A^2/f$, where $A = 1.3 \times 10^{-3}$ e was found from sub-electron fluctuations in section 6.8, then $S_q(1\text{ Hz}) = (1.3 \times 10^{-3}\ e)^2$/Hz. For 4.5 GHz, this would imply $S_q(4.5\text{ GHz}) = 3.8 \times 10^{-16}$ e^2/Hz, and for 8.5 GHz, $S_q(8.5\text{ GHz}) = 2 \times 10^{-16}$ e^2/Hz. Hence, the estimated $1/f$ charge noise from low frequency S_q measurements is 1 to 2 orders of magnitude larger than inferred S_q from T_1 measurements.

Another figure of merit for T_1 is the loss tangent $\tan\delta$ from the dielectric material. We expect that in a simple RC system such as the CPB, the loss tangent is given by

$$\tan\delta = \frac{1}{\omega R C_\Sigma}, \tag{6.59}$$

where

$$R = \frac{T_1}{C_\Sigma}. \tag{6.60}$$

From the maximum $T_1 = 200\ \mu$s at $E_J/h = 4.5$ GHz and $C_\Sigma = 3.12$ fF, I find $R \simeq 64$ GΩ and $\tan\delta = 1.7 \times 10^{-7}$, which is extremely low for AlO_X tunnel junctions. This suggests that Eqs. 6.59 and 6.60 need to be examined more carefully for the CPB.

Noise on the transmission line can be indirectly coupled to the CPB through the resonator. When the CPB is far detuned from the resonance frequency of the resonator, we expect that the resonator will tend to filter out the noise [21]. In the dispersive limit, the energy relaxation rate due to the vacuum fluctuations in the resonator is given by [21]

$$\frac{1}{T_1} = \left(\frac{g}{\Delta}\right)^2 \kappa_r. \tag{6.61}$$

When $g/2\pi = 5$ MHz, $\kappa_r/2\pi = 0.18$ MHz, and $\Delta/2\pi = 100$ MHz, one gets $T_1 \simeq 354\ \mu$s. Eq.6.61 provides an expected upper bound for the lifetime, and my measured data does not violate this bound. Needless to say, this leaves open question of what is setting T_1 in the CPB.

6.11 Rabi Oscillation Measurements

The spectroscopic coherence time T_2^* of device "LEQED1" implies the coherence time T_2 must be at least 100 ns (see section 6.6.3). I was able to observe Rabi oscillations in the device, but unfortunately, it was damaged by an electrical shock before I was able to take much data.

After the electrical event, I had a problem with holding the CPB at the degeneracy point and maintaining the proper dispersive shift. We ran a number of diagnostics to determine if the problem was with the measuring electronics or with the device, and all our measurements suggested that the problem was in the device.

The main indication of a problem in device "LEQED1" was the response to gate voltage when probe power was applied. One test I did was to send a step function to the gate voltage from $n_g = 0$ to $n_g = 1$ and then measure the time it took for the dispersive shift to settle to the steady state dispersive shift at $n_g = 1$. The shift should have been very rapid, but in fact the maximum time constant was about 1.5 ms and the dispersive shift seemed to start out large and then disappear or settle to a relatively small value. This was quite unexpected. These measurements were done at different temperatures from (17 mK to 100 mK) and different average photon numbers (from 1 to 290 photons).

I also found that the steady state dispersive shift increased when the number of photons increased and when the temperature of the device increased. Even more puzzling was that the time constant for the decay decreased when the temperature increased. One hypothesis to explain my data was that the qubit at the base tem-

perature of the refrigerator was actually heated up due to TLSs. The dispersive shift disappeared because the qubit was being thermally excited by TLSs. When we increased the temperature of the mixing chamber, we were increasing the thermal conductivity of TLSs to the reservoir and that might effectively cool the TLSs. The increase in the conductivity could also explain the shorter time decay at higher temperatures. The strange part of my data was the dispersive shift improved when I increased the number of photons in the resonator. We were not able to completely understand this behavior. Hence, I decided to make another device "LEQED2" (see Table 6.1), and I went on to make many Rabi oscillation measurements on this device.

The way I did Rabi oscillation measurements is similar to the T_1 measurement, except the duration of the pump tone is varied. For a Rabi oscillation measurement, I applied a pump tone for a short pulse length. During the pulse, the qubit state rotates on the Bloch sphere and the system is left in a well-defined superposition state that depends on the pulse length. Due to dephasing, the excited state population will saturate to 0.5 if the pulse is sufficiently strong and the pulse length is much longer than the dephasing time. One can measure the excited state population P_e at the moment the pulse is turned off; thereafter the qubit begins to relax back to the ground state. By varying the pulse duration, one can map out P_e as a function of pulse length, and this tends to oscillate back and forth between 0 and 1 (see discussion in section 2.6).

In the CPB, the dephasing time decreases quickly away from $n_g = 1$ due to charge noise, as discussed in section 2.5 (Eq. 2.43). In other words, the dephasing

time is maximum at $n_g = 1$, and this is where I biased CPB "LEQED2" for Rabi oscillations. I used a small number of probe photons to excite the resonator continuously and set the probe frequency to the center frequency of the resonator so that I could calibrate the P_e by measuring the phase shift. In the dispersive limit, the phase shift was small and changed linearly as the qubit state decayed from 1 to 0.

When the CPB detuning from the resonator is positive, the resonator frequency increases as the CPB is driven into the excited state. This in turn caused a negative change of the phase, which is dependent on P_e. When the pulse is off, the resonator frequency returns to its original value within the qubit lifetime, causing a positive change of the phase. One has to wait for the full relaxation of the qubit before applying another pump pulse, otherwise the remnant excited state population of the qubit will affect the Rabi oscillation. I set the repetition time of the pump pulse to more than 5 times $T_1 \simeq 30$ μs.

The phase shift can be converted into a calibrated P_e by measuring the phase shift $\delta\phi$ versus the dispersive frequency shift $\chi/2\pi$. Suppose that for $n_g = 1$ the dispersive shift is $-\chi/2\pi$ when the CPB is in the ground state. Then when the qubit is pumped fully into the excited state, the resonator frequency will increase by $2 \times \chi/2\pi$ at $n_g = 1$. From single-tone spectroscopy, one can also measure the frequency and phase shift $\delta\phi$ of the uncoupled resonator by going away from $n_g = 1$; this corresponds to $\delta\phi$ for $P_e = 0.5$.

Figure 6.22 (a) shows a false color plot of the excited state population P_e of the CPB "LEQED2" as a function of the pump pulse length and measurement time. For this measurement, E_J was 6.15 GHz, the number of probe photons was

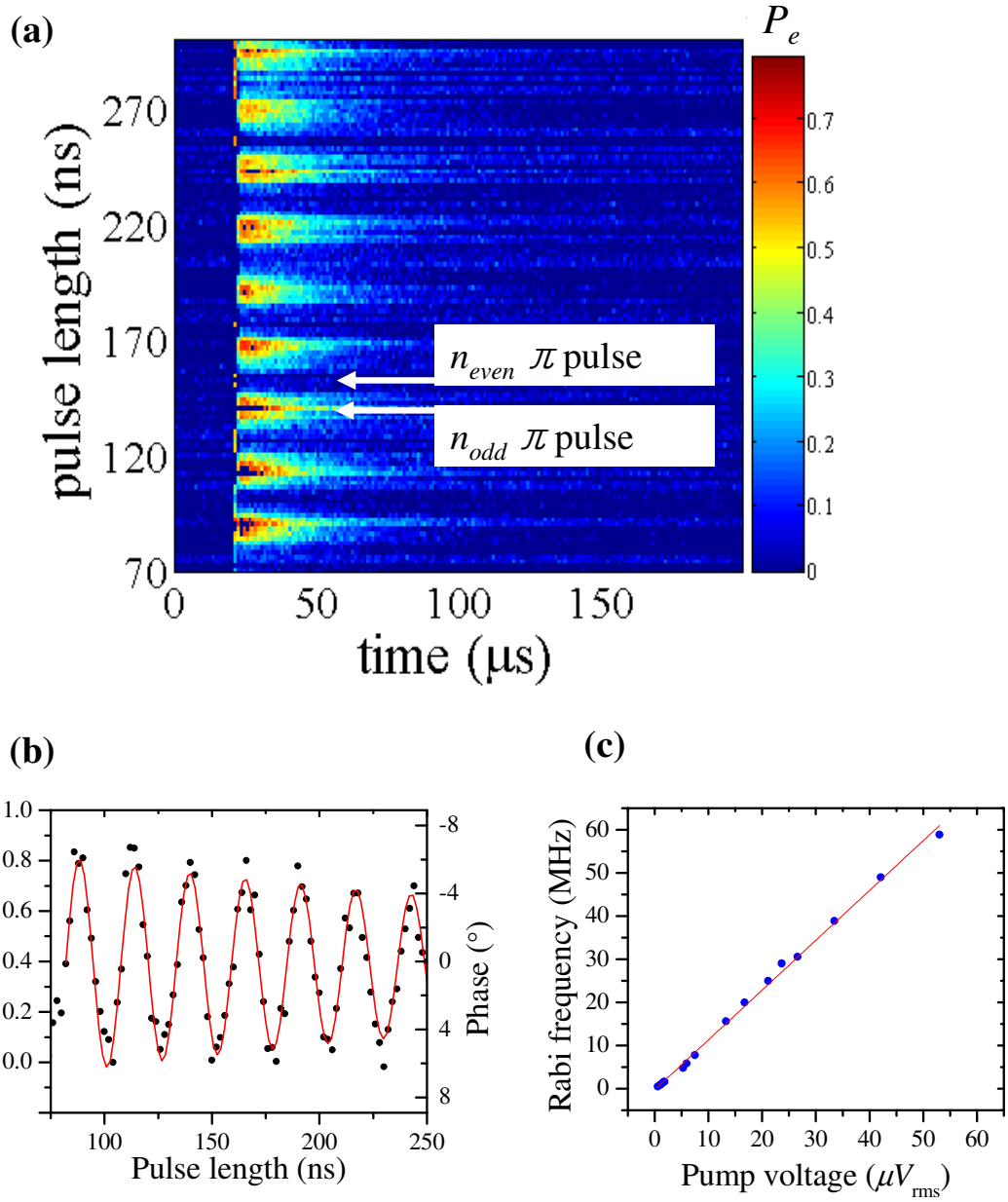

Figure 6.22: (a) Excited state population P_e of the CPB "LEQED2" as a function of the pump pulse length and measurement time. Red and blue represent the excited state and ground state of the CPB, respectively. The resolution in the measurement time was 1 μs. The number of probe photons was about 20, the pump voltage was 33.5 μV_{rms}, and E_J was 6.15 GHz. (b) Line cut along the pulse length at the measurement time of 23 μs. The maximum measured population in the excited state was about 80 %. From the fit (red curve), the extracted Rabi frequency was 39 MHz. (c) Measured Rabi frequency versus pump voltage applied. The red line is a linear fit. The number of probe photons was about 26. E_J was 6.3 GHz.

approximately 20, and I used a pump voltage of 33.5 μV_{rms}. The pump pulse repetition time was 200 μs, which was much longer than T_1 of 30 μs. For this plot, the pulse width of the pump microwaves was varied from 70 ns up to 300 ns with a pulse step size of 2 ns, and the response of the probe was measured from 0 to 200 μs.

Figure 6.22 (b) shows a line cut along the pulse length at the measurement time of 23 μs. I converted the phase change to excited state population P_e. The measurement contrast was about 80 % with the loss in contrast mainly being associated with the excited state. At the $n_{odd}\pi$ pulse points, I observed a maximum population of the qubit in the excited state. The Rabi frequency in this case was about 39 MHz. And at the $n_{even}\pi$ pulse points, the excited state population was almost zero. The loss of contrast may have been due to detuning, or it might have been caused by something in the measurement process, and it will take more experimental work to sort this out.

I next measured Rabi oscillations at different pump powers to verify that the Rabi frequency varied as expected with pump power. Figure 6.22 (c) shows the measured Rabi frequency versus the drive voltage at the on-chip transmission line. This data was taken at a slightly different E_J than the data in Fig. 6.22 (b). One sees from the plot that the Rabi frequency increased linearly with the drive (pump) voltage. This linear dependence of the Rabi frequency on the pump power was strong evidence that these were in fact Rabi oscillations; as discussed in section 2.6, the bare Rabi flopping frequency on resonance is linearly proportional to the drive voltage in the limit of low dissipation (see Eq. 2.74).

The relationship between the Rabi frequency f_R and drive voltage V_{rms} can also be used to extract the coupling $C_{g,rf}$ between the drive voltage and CPB. The harmonic perturbation is given by $n_g^{rf}\cos(\omega t)$, where $n_g^{rf} = C_{g,rf}V_{g,rf}/e$ is the drive amplitude for the qubit. The microwave source power is typically represented as an equivalent rms power P_{rms}. Assuming the transmission line is terminated with a matched load $R = 50\ \Omega$, the rms voltage V_{rms} is given by $\sqrt{RP_{rms}}$. Since the voltage amplitude $V_{g,rf}$ is equal to $V_{rms} \times \sqrt{2}$, the harmonic perturbation is given by

$$n_g^{rf} = \frac{C_{g,rf}V_{rms}\sqrt{2}}{e}. \tag{6.62}$$

For the simple case where the qubit is on resonance and there is no dissipation, one can combine Eq. 2.74 and 6.62 to get the coupling capacitance $C_{g,rf}$ as

$$C_{g,rf} = \frac{eh}{2\sqrt{2}E_C}\frac{f_R}{V_{rms}}, \tag{6.63}$$

where $f_R = \Omega_R/2\pi$ is the bare Rabi frequency. Using a linear fit, I extracted a slope of 1.16 MHz/μV_{rms} from the Rabi frequency data shown in Fig. 6.22 (c). Given $E_C/k_B = 0.3$ K or $E_C/h = 6.24$ GHz, I find $C_{g,rf} \simeq 10.5$ aF. This number is 2.3 times larger than $C_{g,dc} = 4.5$ aF. Additional measurements of Rabi frequency versus E_J (not shown in this thesis) revealed a frequency dependence to $C_{g,rf}$. The discrepancy between $C_{g,dc}$ and $C_{g,rf}$ could be related to the microwave circuit design of the floated resonator, and this possibility needs to be carefully examined.

The Rabi decay time provides more information about the coherence time, more directly than the spectroscopic coherence times T_2^*. However, I found it was

hard to observe the Rabi decay due to discrete low-frequency charge fluctuations. Figure 6.19 (b) shows how such a charge fluctuation can make measurements difficult by fluctuating the operating voltage of the qubit. This problem meant that we needed to complete the Rabi measurement in as short a time as possible. For example, the data in Fig. 6.22 (a) was averaged for 50,000 trials at each pulse length and took an hour. Hence, I decided to reduce the number of averages and the total measurement time while keeping the pulse repetition rate the same. Figure 6.23 shows a measured Rabi decay for 2,000 trials for each pulse length; this data took just a few minutes to acquire. I fit the data to:

$$P_e = A\sin(2\pi f_R(t-t_0))e^{-(t-t_0)/T'} + B \tag{6.64}$$

and extracted a Rabi decay time of $T' = 330$ ns. Since the measured T_1 at this E_J was about 30 μs, we can conclude that $T' \simeq 2T_2$ (from Eq. 2.71) and the resulting coherence time $T_2 = 165$ ns. Also using Eq. 2.32, we find $T_\varphi \sim T_2 \simeq 165$ ns. Thus the Rabi time is much shorter than $2T_1$ because of dephasing.

6.12 Discussion of T_1, T', T_2, and T_φ

The measured T_1 of CPB "LEQED2" ranged from a few μs up to 200 μs depending on E_J (see Fig. 6.21). I note that the largest T_1 I found is an order of magnitude larger than the largest times previously reported in CPB's [110]. The regularity of the dependence of T_1 on frequency suggested that this behavior was due to the microwave circuit. To test this idea, we did further measurements on Rabi

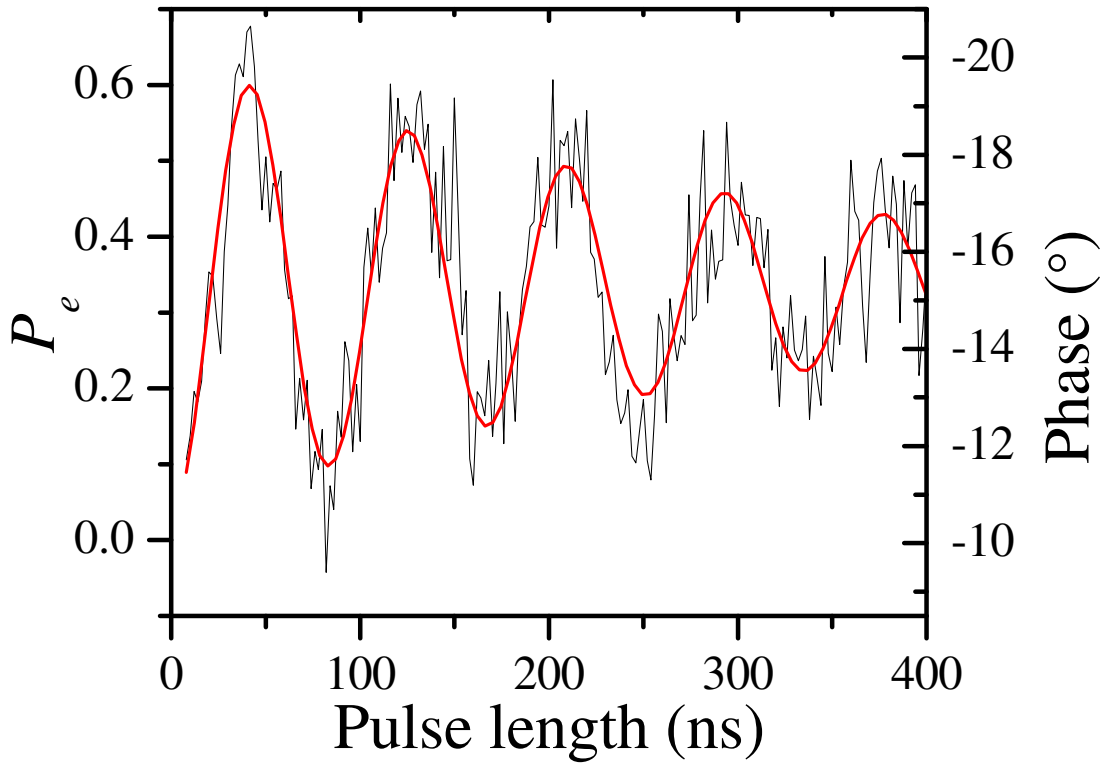

Figure 6.23: Decay of Rabi oscillation in CPB "LEQED2" at $n_g = 1$. The pump power was -87 dBm or 2 pW, and the pump frequency was resonant with the CPB at 6.05 GHz. The fit curve (red) yielded $T^{'} = 332$ ns ± 44 ns and $f_R = 11.92$ MHz ± 6 kHz. Baladitya took this data.

oscillations versus pump power and E_J. These revealed a frequency dependence in the coupling capacitance $C_{g,rf}$ between the pump tone and the CPB and we found that the frequency dependence of T_1 was strongly correlated to $C_{g,rf}$. In addition to the frequency dependence, we also observed two dips in T_1 around 4 GHz and 5.64 GHz. Interestingly, I found S_{21} through the resonator [see Fig. 6.21 (b)] also had two dips at similar frequencies. This suggests relaxation of the CPB qubit is very sensitive to the microwave environment. Also I note there is a decrease of T_1 around the resonator frequency, and this is expected due to the Purcell effect [24], which stimulates the qubit to decay.

I was able to extract estimates for the coherence time T_2 and dephasing time T_φ of both CQED devices. For device "LEQED1", I measured the spectroscopic width to extract T_2^*. From $T_2^* = 100$ ns and $T_1 = 2$ μs, I could find the bounds $T_\varphi \approx T_2 \geq 100$ ns. For device "LEQED2", we measured a Rabi decay time $T^{'} \approx 330$ ns. From $T^{'} = 330$ ns and $T_1 = 30$ μs, we extracted $T_\varphi \simeq T_2 = 165$ ns. Subsequent measurements by Vitaley, Sergey, and Baladitya on device "LEQED2" have revealed $T^{'}$s up to ~ 1.5 μs and this would imply $T_\varphi \simeq T_2 > 750$ ns at that bias point.

For comparison, previous T_1 and Ramsey fringe time T_2^* of a CPB measured by the Yale group were about 7 μs and 0.5 μs, respectively [110]. With Eqs. 2.32 and 6.53, their CPB's $T_\varphi \approx T_2 > T_2^* = 0.5$ μs. Recent T_1 and Ramsey fringe time T_2^* of a transmon measured by the Yale group were about 1.87 μs and 2.22 μs, respectively [67]. With Eqs. 2.32 and 6.53, their transmon's $T_2 \geq T_2^* = 2.22$ μs and $T_\varphi \geq 5.5$ μs.

Chapter 7

Conclusions

7.1 Future Work

7.1.1 Charge Qubits

Based on my results on charge qubits, I have a few suggestions for future work. Some of these recommendations are aimed at improving basic understanding of the physics of CPBs while others are aimed at improving the performance of the devices.

The first suggestion would be to continue measurements on device "LEQED2". In particular, measurements of $T^{'}$ versus E_J, spin-echo measurements of T_2, Ramsey measurements, and tomography measurements would be useful and interesting. Some of these measurements are underway as I write this. It would also be interesting to fabricate devices that are similar to "LEQED1" and "LEQED2" and measure them to see if T_1 depends systematically on E_C and the coupling (both g and C_c from the resonator to the transmission line). A systematic variation might provide better understanding of the main source of relaxation in the qubit.

The Yale group has argued that improving the dephasing time of these devices requires flattening the bands and decreasing the charging energy. This argument has yet to yield devices with substantially better T_φ than I have reported here. Decreasing the charging energy E_C of the CPB to $E_C/k_B = 0.030$ K and studying

the dephasing in those devices would be interesting. This will also probably require increasing the coupling capacitance $C_{g,r}$ by a factor of 10 to keep the coupling strength $g/2\pi$ on the order of 5 MHz. These changes would make devices similar to the transmon [111] and in fact might produce worse performance than in my current devices; the use of a larger $C_{g,r}$ means greater sensitivity to noise in the input transmission line and resonator and an increase in C_Σ means an increase in the dielectric loss.

7.1.2 Read-out Schemes

A better understanding of the coupling between the transmission line and resonator might explain how the qubit couples to the environment or reveal how to improve the isolation of the qubit from the environment. This suggests it would be useful to examine some other resonator designs.

The resonator in Fig. 7.1 (a) could be implemented to read out a CPB in a bandpass mode (by measuring S_{23} or S_{14}) or a notch style mode (S_{21} or S_{34}). This resonator is coupled to two transmission lines, while the notch style resonator I used was coupled to one transmission line. The second transmission line could also provide better isolation between the pump and probe tones. Multiplexing resonators is also possible by putting many resonators between two transmission lines.

The quarter wavelength ($\lambda/4$) CPW resonator [see Fig. 7.1 (b)] could be used to read out the CPB. It would be interesting to see if there are any discernable differences from my measurements on lumped-element LC resonators. The advantage

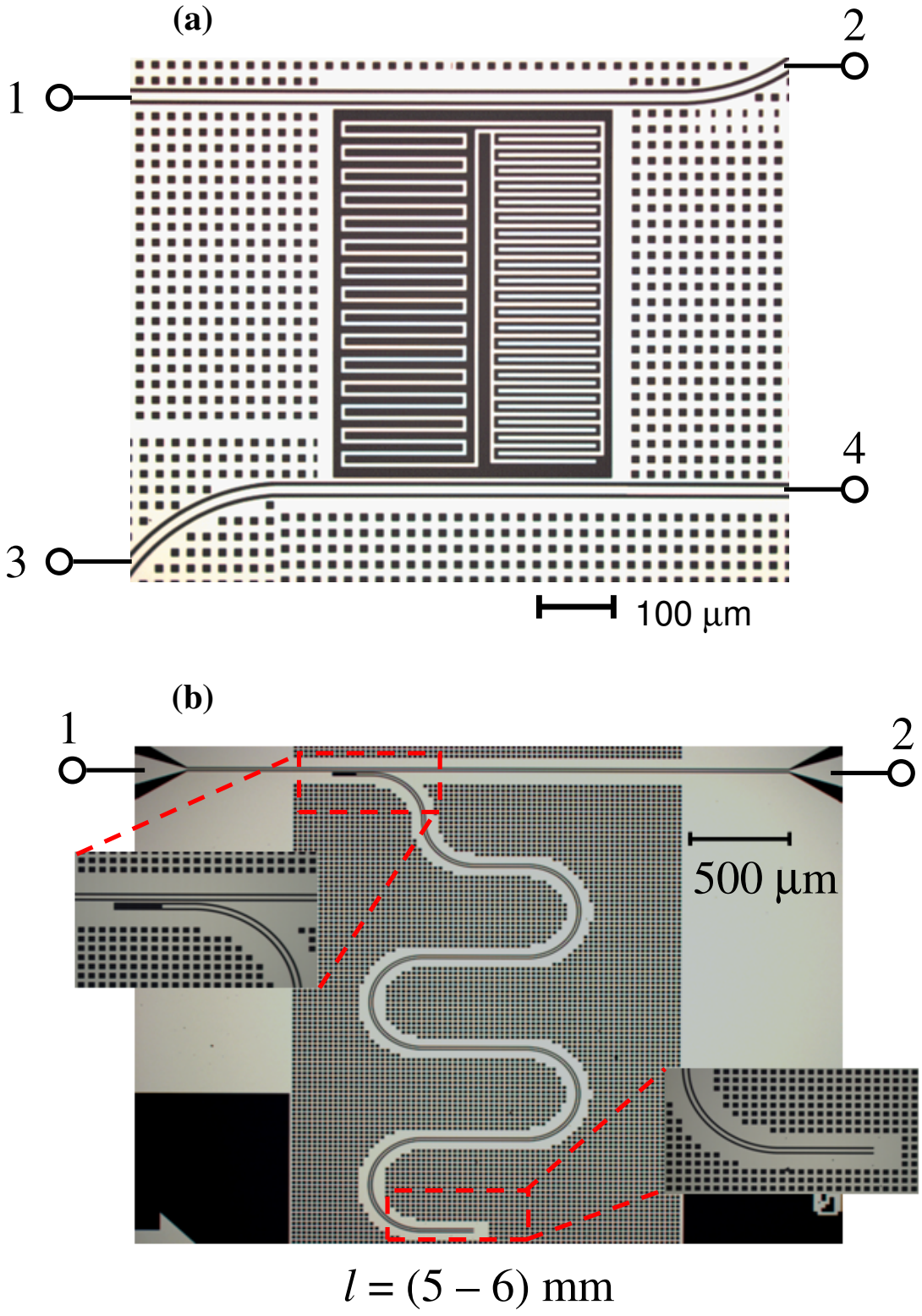

Figure 7.1: New resonator designs for a CPB read-out. (a) Both bandpass and notch style resonator with four ports and (b) a quarter wavelength resonator.

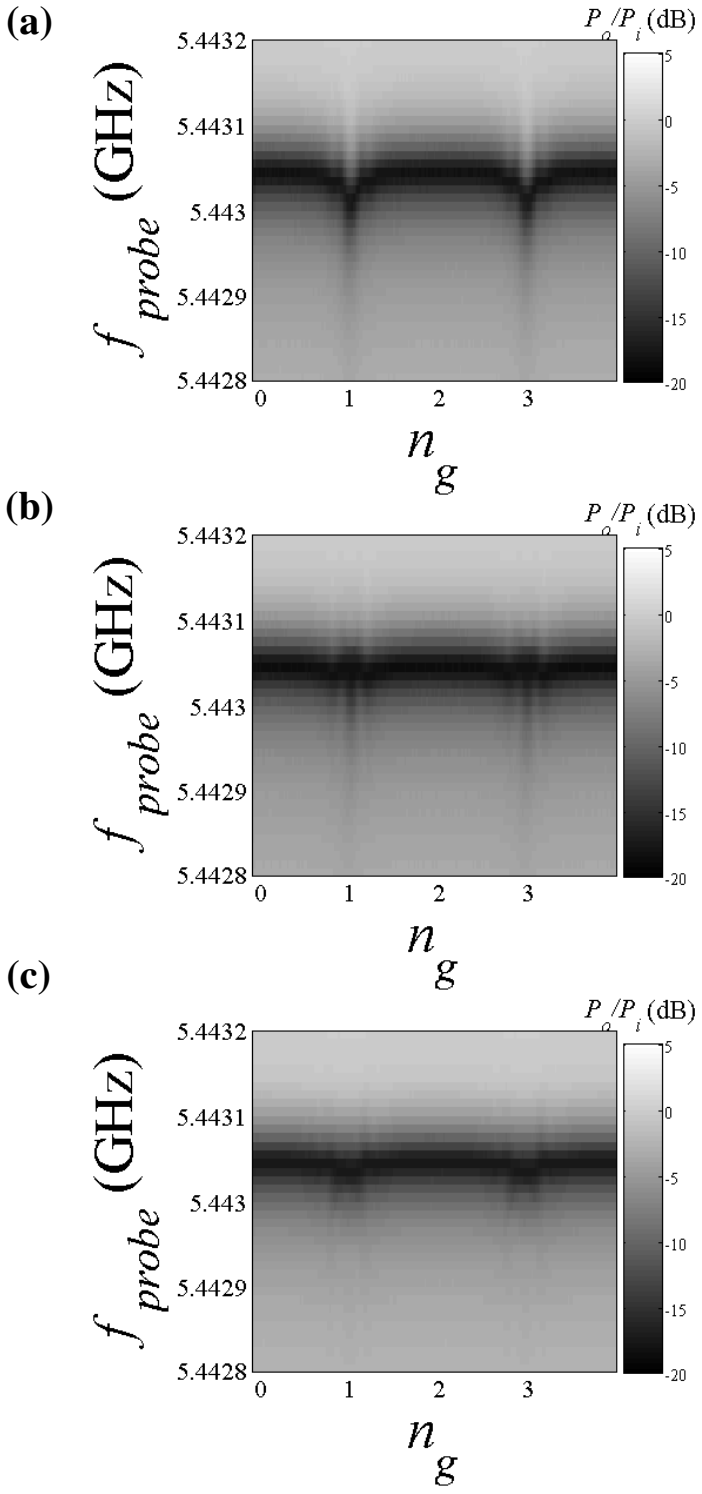

Figure 7.2: Single-tone spectroscopy of device "LEQED1" with number of photons of (a) 7,000, (b) 22,000, and (c) 70,000 in the resonator. E_J was about 8.45 GHz at zero magnetic field.

of the $\lambda/4$ resonator is perhaps a more controllable external Q of the resonator. By increasing (decreasing) the length of the coupling strip, one can decrease (increase) the Q_e. For fast measurements of the CPB, one needs smaller Q_e. The $\lambda/4$ resonator could also be used as a tunable resonator by placing a Josephson junction in the resonator where it is terminated to the ground. A tunable resonator would be interesting because it would act as a tunable coupling element between two qubits.

7.1.3 Many Photons in the Resonator

Figure 7.2 shows single-tone spectroscopy of device "LEQED1" as a function of the number of photons stored in the resonator at E_J of 8.45 GHz. I started from single photons and increased to 2, 7, 22, 70, 220, 2,200, 7,000, 22,000, and 70,000 photons. When 7,000 photons were stored in the resonator, the dispersive shift of the resonator started to be distorted. The frequency shift pattern changed as I increased the probe power. A complete understanding of this phenomenon is lacking, although some of the behavior appears similar to dressed state effects observed by C. M. Wilson *et al.* [112].

7.2 Summary of Key Results

Using an rf-SET to measure the charge on a CPB, I was able to observe the CPB energy level spectrum and also a few avoided level crossings in the CPB spectrum. I showed that each splitting was due to coupling between the qubit and a charged two-level fluctuator located in the Josephson tunnel junction of the qubit.

From fitting the spectrum, I was able to determine the parameters of the CPB and charge fluctuators. I also observed a strong correlation of T_1 with the location of each avoided level crossing, which revealed that these discrete anomalous charge fluctuators are a source of dissipation for our qubit.

Perhaps the most intriguing results reported in this thesis are of T_1 for the CPB measured using two read-out schemes: the rf-SET and microwave resonator technique. With the rf-SET, I was not able to measure the CPB at $n_g = 1$ due to non-equilibrium quasiparticles [see the small step at $n_g = 1$ in Fig. 3.17 (a)] and because our read-out was not sensitive at this gate voltage. But, I was able to measure T_1 away from the charge degeneracy point, and at frequencies up to 50 GHz, where n_g was close to 1.9. The maximum T_1 was about 4 μs (see Fig. 3.19) and an extrapolation of the spectral density of noise yields $S_q \sim 10^{-12}\ e^2/\text{Hz}$ at 27 GHz.

By coupling the CPB to a high-Q lumped-element resonator, I was able to bias the CPB at or near $n_g = 1$, measure the state of the qubit, and perform T_1 and Rabi measurements. My measurements at $n_g = 1$ revealed a maximum $T_1 = 200$ μs for $E_J/h = 4.5$ GHz [see Fig. 6.21 (a)] and a minimum $T_1 \simeq 3.8$ μs for $E_J/h \simeq 8.5$ GHz. This places an upper bound on the spectral density of charge noise $S_q \leq 4 \times 10^{-17}\ e^2/\text{Hz}$ at 8.5 GHz. A strong frequency dependence of the qubit lifetime was also observed: I noticed there were a few dips in T_1 as a function of E_J and these dips coincided with dips in S_{21} of the system. From these results, I concluded that the dispersive read-out using the resonator enhanced the qubit relaxation time by a factor of 30 and decreased S_q by a factor of 10^6 compared with

the dissipative read-out using the rf-SET.

Being able to bias the CPB at $n_g = 1$ was also a major step forward in increasing the coherence time. At $n_g = 1$, I was able to measure Rabi oscillations of the CPB. By measuring the Rabi flopping frequency as a function of the pump power and E_J, we were able to extract the coupling capacitance $C_{g,rf}$ between the pump tone and CPB. The extracted $C_{g,rf}$ showed a strong frequency dependence from 1.25 aF at $E_J/h = 4.467$ GHz to 10.5 aF at $E_J/h = 6.04$ GHz. We noticed this frequency dependence of T_1 was strongly related to $C_{g,rf}$'s frequency dependence. Preliminary measurements of Rabi oscillation revealed Rabi decay times on the order of 330 ns, which leads to an estimated coherence time $T_2 = 165$ ns. This value is about 1/2 the dephasing time of 310 ns expected from the discussion in section 2.5 (see Eq. 2.54). The coherence time reported in this thesis is still smaller than that of other CPB ($T_2 \geq 500$ ns) [110] and transmon ($T_2 \geq 2.2$ μs) [67], but ongoing and preliminary measurements have revealed Rabi decay times up to 1.5 μs. Further measurements are likely to reveal still larger times at specific biases, although this is to be seen.

Appendix A

Device Fabrication Recipes

For building the resonator and CPB, I used recipes that were developed by Vitaley Zaretskey and Ben Palmer.

- Photo lithography: Futurrex NR9-1000PY (negative lift-off resist)
  1. Blow away any dust on the 3-inch sapphire wafer using compressed N_2 (if the wafer was clean in the dry box in the clean room).
  2. Put wafer on the 3-inch chuck in the spinner and test-run the programmed spinner.
  3. Spin NR9-1000PY on the wafer at 3000 rpm for 60 sec and ramp down at 1000 rpm/s. Make sure the back side of wafer is clean. If needed, clean it by a Q-tip with Acetone on it.
  4. Prebake wafer at 160°C for 3 minutes 30 sec (use hot plate).
  5. Expose wafer in the contact aligner for 8 sec.
  6. Postbake wafer at 120°C for 3 minutes 30 sec.
  7. Develop the photo resist by RD6 for 12 sec in a beaker and then dispose RD6 in the Acid/Base sink.
  8. Rinse wafer by D.I. water in a beaker for 1 minute.
  9. Blow dry wafer.
  10. Check the developed resist under the optical microscope.

- Lift-off of NR9-1000PY after Al deposition.
  1. Pour 450 mL of RR5 in a 500 mL beaker.
  2. Place wafer in a teflon wafer holder and leave the wafer in RR5 for about two hours at room temperature.
  3. Ultrasound the beaker for 15 minutes.
  4. Prepare another 500 mL beaker with 450 mL Acetone.
  5. Remove wafer from RR5 and immediately immerse it in the Acetone.
  6. Ultrasound the beaker for 15 minutes.
  7. Rinse wafer by Acetone, Methanol, and IPA for 1 minute each.
  8. Blow dry wafer on the teflon holder.
  9. Check the metal pattern using an optical microscope.

◦ Spin the protective (blue) resist (FSC-M) for the wafer dicing.

1. Blow wafer to remove any dust on it.
2. Put wafer on the 3-inch chuck in the spinner.
3. Spin FSC-M on the wafer at 2000 rpm for 60 sec and ramp down at 500 rpm/s.
4. Bake wafer at 120°C for 3 minutes 30 sec.

◦ Photolithography: Etching Al with OiR 906-10 (positive resist)

1. Clean and blow dry wafer, which has Al deposited. One needs to prepare large Al etchant to be warm up.
2. Pour Aluminum etchant in a big and wider beaker with a magnetic stir bar (wear double gloves, plastic gown, and face protection / hat).
3. Heat up the beaker on the hot plate at 55°C and set the magnetic stir spin to 600 rpm. Cover the beaker with a dish.
4. Put wafer on the 3-inch chuck in the spinner and test-run the programmed spinner.
5. Spin HMDS at 2000 rpm for 60 sec and ramp down at 500 rpm/s.
6. Spin OiR 906-10 at 3500 rpm for 60 sec and ramp down at 1000 rpm/s. Make sure the back side of wafer is clean. If needed, clean it using a Q-tip and Acetone.
7. Prebake wafer at 90°C for 1 minute.
8. Expose wafer in the contact aligner for 5 sec.
9. Postbake wafer at 120°C for 1 minute.
10. Develop the photoresist by OPD 4262 in a beaker for 1 minute at room temperature and later dispose OPD 4262 in the Acid/Base sink.
11. Rinse wafer by D.I. water in a beaker for 1 minute.
12. Blow dry wafer.
13. Check the developed resist under an optical microscope.
14. Use the teflon holder and place the wafer in the Al etchant. The wafer will spin slowly with the magnetic stir bar. Later dispose the Al etchant in the Acid sink.
15. Within one or two minutes, the parts of the wafer become transparent at which point remove and rinse the wafer in D.I. water in another beaker.
16. Rinse wafer by Acetone, Methanol, and IPA for 1 minute each (be sure the Al etchant is gone since it reacts with Acetone).
17. Blow dry wafer.
18. Check the metal patterning under the optical microscope.

◦ Electron beam lithography: MMA/ZEP spin-on

1. Clean and blow dry wafer, which has only Al pattern on it after the optical lithography.
2. Spin MMA(8.5)MAA EL11 on the wafer at 1000 rpm for 60 sec and ramp down at 500 rpm/s. The thickness should be approximately 940 nm.
3. Prebake wafer at 180°C for 5 minutes.
4. Put wafer on the 3-inch chuck in the spinner and test-run the programmed spinner.
5. Spin ZEP 520A DR2.3 at 5000 rpm for 60 sec and ramp down at 500 rpm/s.
6. Prebake wafer at 180°C for 5 minutes. The thickness should be approximately 120 nm.
7. One should do another prebake at 180°C for 30 minutes in the oven. It will strengthen the resist by further baking out the solvent.

◦ Electron beam lithography: MMA/ZEP develop after E-beam writing

1. Place chip in OPD 4262 for 1 minute to strip the Al anti-charging layer.
2. Rinse chip by D.I. water for 1 minute.
3. Develop ZEP layer in ZED-N50 for 3 minutes and later dispose ZED-N50 in a storage bottle.
4. Rinse chip by IPA for 1 minute.
5. Develop MMA layer by IPA:D.I. water of 5:1 (IPA of 50 mL and D.I. water of 10 mL).
6. Rinse chip using IPA for 1 minute.
7. Blow dry chip.

◦ Electron beam lithography: MMA lift-off after Al deposition

1. Prepare NMP in two small beakers and put chip on one beaker.
2. Place two beakers on the hot plate at 120°C in the fume hood for 30 minutes. One needs to be careful of the flash point of NMP (120°C). Since actual temperature inside the solution is lower than the temperature on the hot plate surface, I increased up to 120°C.
3. Agitate the chip in NMP using tweezers to shake off metal pieces.
4. Put chip quickly into another beaker.
5. Place the beaker on the hot plate at 120°C of NMP for 10 minutes.
6. Quickly dip and rinse chip in a beaker of IPA before NMP dries out and leaves residue on the chip.
7. Blow dry chip.

Appendix B
Caltech Amplifier Kit

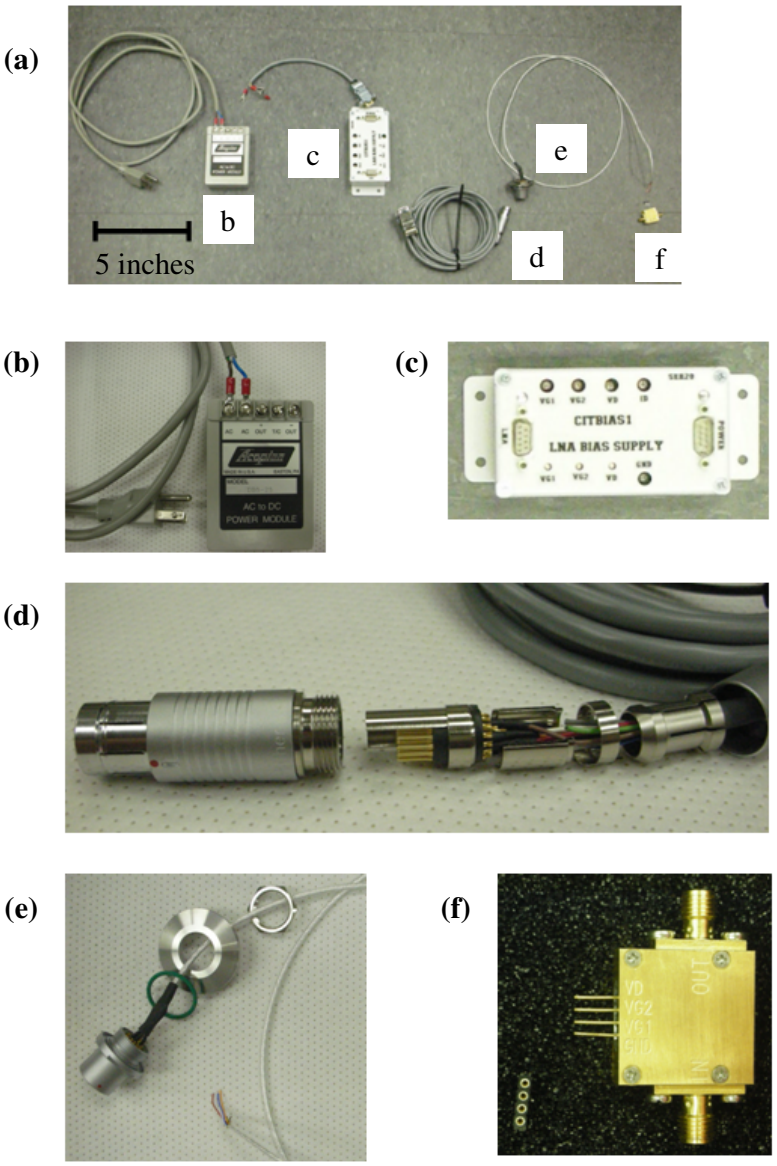

Figure B.1: (a) Caltech Amplifier kit. (b) AC to DC (+/- 5 V) power supply module (Acopian). (c) DC bias regulator module (Caltech: CITBias1). I used the recommended bias setting for our specified LNA (S/N:210): $V_d = 1.2$ V, $V_{g1} = 2.1$ V, and $V_{g2} = 2.1$ V. (d) and (e) Fischer connector assemblies. (f) A Caltech amplifier.

Bibliography

[1] R. P. Feynman, Int. J. Theor. Phys. **21**, 467 (1982).

[2] D. Deutsch and R. Jozsa, Proceedings of the Royal Society of London A **439**, p. 553 (1992).

[3] P. W. Shor, SIAM **41**(2), 303332 (1999).

[4] L. K. Grover, Proceedings, 28th Annual ACM Symposium on the Theory of Computing, p. 212 (1996); arXiv:quant-ph/9605043 (1996).

[5] W. K. Wootters and W. H. Zurek, Nature **299**, 802 (1982).

[6] P. W. Shor, Phys. Rev. A **52**, R2493 (1995).

[7] E. Knill and R. Laflamme, Phys. Rev. A **55**, 900 (1997).

[8] B. B. Blinov, D. L. Moehring, L.- M. Duan, and C. Monroe, Nature **428**, 153 (2004).

[9] S. Shapiro, Phys. Rev. Lett. **11(2)**, 80 (1963).

[10] B. D. Josephson, Phys. Lett. **1**(7), 251 (1962).

[11] M. Devoret, A. Wallraff and J. Martinis, arXiv:cond-mat/0411174 (2004).

[12] M. Tinkham, *Introduction to Superconductivity*, 2nd ed. (McGraw-Hill, New York, 1996).

[13] V. Bouchiat, D. Vion, P. Joyez, D. Esteve, and M. H. Devoret, Phys. Script. **T76**, 165 (1998).

[14] R. J. Schoelkopf, P. Wahlgren, A. A. Kozhevnikov, P. Delsing, and D. E. Prober, Science **280**, 1238 (1998).

[15] Y. Nakamura, Yu. A. Pashkin, and J. S. Tsai, Nature **398**, 786 (1999).

[16] K. Bladh, D. Gunnarsson, G. Johansson, A. Käck, G. Wendin, A. Aassime, M. Taslakov, and P. Delsing, Phys. Script. **T102**, 167 (2002).

[17] D. Vion, A. Aassime, A. Cottet, P. Joyez, H. Pothier, C. Urbina, D. Esteve, M. H. Devoret, Science **296**, 886 (2002).

[18] I. Siddiqi, R. Vijay, F. Pierre, C. M. Wilson, M. Metcalfe, C. Rigetti, L. Frunzio, M. H. Devoret, Phys. Rev. Lett. **93**, 207002 (2004).

[19] A. Wallraff, D. I. Schuster, A. Blais, L. Frunzio, R.- S. Huang, J. Majer, S. Kumar, S. M. Girvin and R. J. Schoelkopf, Nature **431**, 162 (2004).

[20] R. J. Thompson, G. Rempe, and H. J. Kimble, Phy. Rev. Lett. **68**, 1132 (1992).

[21] A. Blais, R. Huang, A. Wallraff, S. M. Girvin, and R. J. Schoelkopf, Phys. Rev. A **69**, 062320 (2004).

[22] A. Aassime, G. Johansson, G. Wendin, R. J. Schoelkopf, and P. Delsing, Phys. Rev. Lett. **86**, 3376 (2001).

[23] B. A. Turek, K. W. Lehnert, A. Clerk, D. Gunnarsson, K. Bladh, P. Delsing, and R. J. Schoelkopf Phys. Rev. B. **71** 193304 (2005).

[24] A. A. Houck, J. A. Schreier, B. R. Johnson, J. M. Chow, Jens Koch, J. M. Gambetta, D. I. Schuster, L. Frunzio, M. H. Devoret, S. M. Girvin, and R. J. Schoelkopf, Phys. Rev. Lett. **101**, 080502 (2008).

[25] M. Büttiker, Phys. Rev. B **36**, 3548 (1987).

[26] B. S. Palmer, C. A. Sanchez, A. Naik, M. A. Manheimer, J. F. Schneiderman, P. M. Echternach, and F. C. Wellstood, Phys. Rev. B **76**, 054501 (2007).

[27] J. Aumentado, M. Keller, J. Martinis, and M. Devoret, Phys. Rev. Lett. **92**, 066802 (2004).

[28] Y. Makhlin, G. Schön, and A. Shnirman, Rev. Mod. Phys. **73**, 357 (2001).

[29] R. J. Schoelkopf, A. A. Clerk, S. M. Girvin, K.M. Lehnert, and M. H. Devoret, arXiv:cond-mat/0210247v1 (2002).

[30] C. A. Sanchez, *Towards Single Shot Measurements of a Cooper Pair Box Qubit Using an rf-set*, Ph.D. thesis, University of Maryland (2005).

[31] D. J. Griffiths, *Introduction to Quamtum Mechanics*, (Prentice-Hall, Inc., New Jersey, 1995), p. 305.

[32] M. Fox, *Quantum Optics*, (Oxford University Press Inc., New Jersey, 2006), p. 168.

[33] L. Allen and J. H. Eberly, *Optical Resonance and Two-Level Atoms* (Dover, New York, 1987), p. 61.

[34] H. Paik, *Coherence in dc Squid Phase Qubits*, Ph.D. thesis, University of Maryland (2007).

[35] A. Cottet, *Implementation of a Quantum Bit in a Superconducting Circuit*, Ph.D. thesis, Université Paris (2002).

[36] A. Cottet, D. Vion, P. Joyez, D. Esteve, and M.H. Devoret, *International Workshop on Superconducting Nano-electronics Devices*, (J. Pekola, B. Ruggiero, and P. Silvestrini eds., Kluwer Academic, Plenum Publishers, New York, 2002), p. 73.

[37] J. M. Martinis, S. Nam, J. Aumentado, K. M. Lang, and C. Urbina, Phys. Rev. B. **67** 094510 (2003).

[38] F. Yoshihara, K. Harrabi, A. O. Niskanen, Y. Nakamura, and J. S. Tsai, Phys. Rev. Lett. **97**, 167001 (2006).

[39] K. Bladh, T. Duty, D. Gunnarsson, and P. Delsing, New Journal of Physics **7**, 180 (2005).

[40] A. Aassime, D. Gunnarsson, K. Bladh, and P. Delsing, Appl. Phys. Lett. **79**, 4031 (2001).

[41] A. Guillaume, J. F. Schneiderman, P. Delsing, H. M. Bozler and P. M. Echternach, Phys. Rev. B. **69** 132504 (2004).

[42] J. F. Schneiderman, *Progress in Measurement Techniques for the Single Cooper-Pair Box Qubit*, Ph.D. thesis, University of Southern California (2007).

[43] M. D. Shaw, *Quasiparticle Tunneling and Quantum Coherence in the Single Cooper-Pair Box*, Ph.D. thesis, University of Southern California (2009).

[44] A. N. Korotkov, Phys. Rev. B. **49**, 10381 (1994).

[45] O. Astafiev, Yu. A. Pashkin, Y. Nakamura, T. Yamamoto, and J. S. Tsai, Phys. Rev. Lett. **93**, 267007 (2004).

[46] R. J. Schoelkopf, A. A. Clerk, S. M. Girvin, K.M. Lehnert, and M. H. Devoret, in Quantum Noise in Mesoscopic Physics, edited by Y. V. Nazarov (Kluwer Academic Publishers, Netherlands, 2003) pp. 175-203; R. J. Schoelkopf, A. A. Clerk, S. M. Girvin, K.M. Lehnert, and M. H. Devoret, arXiv:cond-mat/0210247v1 (2002).

[47] P. Dutta, P. Dimon, and P. M. Horn, Phys. Rev. Lett. **43**, 646 (1979).

[48] C. T. Rogers and R. A. Buhrman, Phys. Rev. Lett. **55**, 859 (1985).

[49] M. Constantin and C. C. Yu, Phys. Rev. Lett. **99**, 207001 (2007).

[50] M. Mück, M. Korn, C. G. A. Mugford, J. B. Kycia and J. Clarke, Appl. Phys. Lett. **86**, 012510 (2005).

[51] F. C. Wellstood, C. Urbina, and John Clarke, Appl. Phys. Lett. **85**, 5296 (2004).

[52] D. J. Van Harlingen, T. L. Robertson, B. L. T. Plourde, P. A. Reichardt, T. A. Crane, and J. Clarke, Phys. Rev. B **70** 064517 (2004).

[53] R. H. Koch, J. Clarke, W. M. Goubau, J. M. Martinis, C. M. Pegrum and D. J. Harlingen, J. Low Temp. Phys. **51**, 207 (1983).

[54] I. Chiorescu, Y. Nakamura, C. J. P. M. Harmans, and J. E. Mooij, Science **299**, 1869 (2003).

[55] Y. A. Pashkin, T. Yamamoto, O. Astafiev, Y. Nakamura, D. V. Averin, and J. S. Tsai, Nature **421**, 823 (2003).

[56] L. J. Geerligs, V. F. Anderegg, J. E. Mooij, Physica B **165**, 973 (1990).

[57] G. Zimmerli, T. M. Eiles, R. L. Kautz, and J. Martinis, Phys. Lett. **61**, 237 (1992).

[58] L. Ji, P. D. Dresselhaus, S. Han. K. Lin, W. Zheng and J. E. Lukens, J. Vac. Sci. Technol. B. **12**, 3619 (1994).

[59] M. Kenyon, C. J. Lobb, and F. C. Wellstood, J. Appl. Phys. **88**, 6536 (2000).

[60] S. Machlup, J. Appl. Phys. **25**, 341 (1954).

[61] R. W. Simmonds, K. M. Lang, D. A. Hite, S. Nam, D. P. Pappas, and J. M. Martinis, Phys. Rev. Lett. **93**, 077003 (2004).

[62] J. M. Martinis, K. B. Cooper, R. McDermott, M. Steffen, M. Ansmann, K. D. Osborn, K. Cicak, S. Oh, D. P. Pappas, R. W. Simmonds, and C. C. Yu, Phys. Rev. Lett. **95**, 210503 (2005).

[63] L. Tian and R. W. Simmonds, Phys. Rev. Lett. 99, 137002 (2007).

[64] B. L. T. Plourde, T. L. Robertson, P. A. Reichardt, T. Hime, S. Linzen, C.-E. Wu, and John Clarke, Phys. Rev. B **72**, 060506(R) (2005).

[65] G. Ithier, E. Collin, P. Joyez, P. J. Meeson, D. Vion, D. Esteve, F. Chiarello, A. Shnirman, Y. Makhlin, J. Schriefl, and G. Schön, Phys. Rev. B **72**, 134519 (2005).

[66] F. Deppe, M. Mariantoni, E. P. Menzel, S. Saito, K. Kakuyanagi, H. Tanaka, T. Meno, K. Semba, H. Takayanagi, and R. Gross, Phys. Rev. B **76**, 214503 (2007).

[67] J. A. Schreier, A. A. Houck, Jens Koch, D. I. Schuster, B. R. Johnson, J. M. Chow, J. M. Gambetta, J. Majer, L. Frunzio, M. H. Devoret, S. M. Girvin, and R. J. Schoelkopf, Phys. Rev. B **77**, 180502(R) (2008).

[68] Z. Kim, V. Zaretskey, Y. Yoon, J. F. Schneiderman, M. D. Shaw, P. M. Echternach, F. C. Wellstood, and B. S. Palmer, Phys. Rev. B **78**, 144506 (2008).

[69] F. C. Wellstood, Z. Kim, and B. S. Palmer, arXiv:0805.4429 (2008).

[70] A. A. Clerk, S. M. Girvin, A. K. Nguyen and A. D. Stone, Phys. Rev. Lett. **89**, 176804-1 (2002).

[71] T. A. Fulton and G. J. Dolan, Phys. Rev. Lett. **59**, 109 (1987).

[72] T. A. Fulton, P. L. Gammel, D. J. Bishop, L. N. Dunkleberger, and G. J. Dolan, Phys. Rev. Lett. **63**, 1307 (1989).

[73] J. D. Jackson, *Classical Electrodynamics*, 2nd ed. (John Wiley & Sons, New York, 1975), p. 51.

[74] K. B. Cooper, Matthias Steffen, R. McDermott, R. W. Simmonds, Seongshik Oh, D. A. Hite, D. P. Pappas, and John M. Martinis, Phys. Rev. Lett. **93**, 180401 (2004).

[75] L. Faoro, J. Bergli, B. L. Altshuler, and Y. M. Galperin, Phys. Rev. Lett. **95**, 046805 (2005).

[76] A. M. Zagoskin, S. Ashhab, J. R. Johansson, and Franco Nori, Phys. Rev. Lett. **97**, 077001 (2006).

[77] D. M. Pozar, *Microwave Engineering*, 3rd ed. (John Wiley & Sons, New York, 2005).

[78] Rainee N. Simons, *Coplanar Waveguide Circuits, Components, and Systems*, (John Wiley & Sons, New York, 2001).

[79] K. C. Gupta, *Microstrip Line and Slotlines* revised 2nd ed. (Artech House, 1996).

[80] Peter K. Day, Henry G. LeDuc, Benjamin A. Mazin, Anastasios Vayonakis, and Jonas Zmuidzinas, Nature **425**, 817 (2003).

[81] B. A. Mazin, *Microwave Kinetic Inductance Detectors*, Ph.D. thesis, California Institute of Technology (2004).

[82] L. Frunzio, A. Wallraff, D. Schuster, J. Majer, and R. Schoelkopf, IEEE Transactions on Applied Superconductivity **15(2)**, 860, (2005).

[83] M. Sandberg, C. M. Wilson, F. Persson, T. Bauch, G. Johansson, V. Shumeiko, T. Duty, and P. Delsing, Appl. Phys. Lett. **92**, 203501 (2008).

[84] E. M. Purcell, Phys. Rev. **69(11-1)** 681 (1946).

[85] AWR Corporation, 1960 E. Grand Avenue Suite 430, El Segundo, CA 90245, http://web.awrcorp.com

[86] Ansoft, 225 West Station Square Drive Suite 200, Pittsburgh, PA 15219, http://www.ansoft.com

[87] Microtronics, Inc., 103 Penns Trail, Newtown, PA 18940, http://www.microtronicsinc.com

[88] JC Nabity Lithography Systems, P.O. Box 5354, Bozeman, MT 59717, http://www.jcnabity.com

[89] D. V. Averin and Yu. V. Nazarov, Phys. Rev. Lett. 69, 1993 (1992).

[90] V. Ambegaokar and A. Baratoff, Phys. Rev. Lett. 10, 486 (1963).

[91] P. J. Petersan and S. M. Anlage, J. Appl. Phys. **84**, 3392 (1998).

[92] J. Gao, *The Physics of Superconducting Microwave Resonators*, Ph.D. thesis, California Institute of Technology (2008).

[93] H. Paik and K. D. Osborn, Appl. Phys. Lett. **96**, 072505 (2010).

[94] A. D. OConnell, M. Ansmann, R. C. Bialczak, M. Hofheinz, N. Katz, Erik Lucero, C. McKenney, M. Neeley, H. Wang, E. M. Weig, A. N. Cleland, and J. M. Martinis, Appl. Phys. Lett. **92**, 112903 (2008).

[95] A. L. Schawlow and G. E. Devlin, Phys. Rev. **113**, 120 (1959).

[96] D. C. Mattis and J. Bardeen, Phys. Rev. **111**, no.2, 412-417 (1958).

[97] J. Gao, J. Zmuidzinas, A. Vayonakis, P. K. Day, B. A. Mazin, and H. G. Leduc, J. Low Temp. Phys. **151**, 557 (2008).

[98] M. A. Biondi and M. P. Garfunkel, Phys. Rev. **116**, 853 (1959).

[99] B. Mühlschlegel, Zeitschrift fr Physik A Hadrons and Nuclei **155**, 313-327 (1959).

[100] D. Kleppner and S. Haroche, *Cavity quantum electrodynamics*, Physics Today **42**, 24 (January 1989).

[101] Claude Cohen-Tannoudji, Jacques Dupont-Roc, and Gilbert Grynberg, *Atom-Photon Interactions*, (John Wiley & Sons, New York, 1992).

[102] E. T. Jaynes and F. W. Cummings, Proc. IEEE **51**, 89 (1963).

[103] D. I. Schuster, *Circuit Quantum Electrodynamics*, Ph.D. thesis, Yale University (2007).

[104] C. Gerry and P. Knight , *Introductory Quantum Optics*, (Cambridge University Press, New York, 2005).

[105] M. Brune, P. Nussenzveig, F. Schmidt-Kaler, F. Bernardot, A. Maali, J. M. Raimond, and S. Haroche, Phy. Rev. Lett. **72**, 3339 (1994).

[106] D. I. Schuster, A. Wallraff, A. Blais, L. Frunzio, R. S. Huang, J. Majer, S. M. Girvin, and R. J. Schoelkopf, Phy. Rev. Lett. **94**, 123602 (2005).

[107] Stanford Research Systems, Inc., 1290-D Reamwood Avenue, Sunnyvale, CA 94089, http://www.thinksrs.com

[108] A. Abragam, *The Principles of Nuclear Magnetism* (Oxford, London, 1961).

[109] R. A. Smith, Proceedings of the Royal Society of London A **362**, 1 (1978).

[110] A. Wallraff, D. I. Schuster, A. Blais, L. Frunzio, J. Majer, M.H. Devoret, S. M. Girvin, and R. J. Schoelkopf, Phy. Rev. Lett. **95**, 060501 (2005).

[111] Jens Koch, Terri M. Yu, Jay Gambetta, A. A. Houck, D. I. Schuster, J. Majer, Alexandre Blais, M. H. Devoret, S. M. Girvin, and R. J. Schoelkopf, Phy. Rev. A. **76**, 042319 (2007).

[112] C. M. Wilson, G. Johansson, T. Duty,y and F. Persson, M. Sandberg, P. Delsing, Phys. Rev. B. **81** 024520 (2010).